Blowdown simulation of CO_2 pipelines

A thesis submitted to University College London for the degree of Doctor of Philosophy

By

Alexander Collard

Department of Chemical Engineering
University College London
Torrington Place
London WC1E 7JE

April 2015

I, Alexander Collard, confirm that the work presented in this thesis is my own. Where information has been derived from other sources, I confirm that this has been indicated in the thesis.

Abstract

Pipelines are the most practical option for transporting large volumes of captured CO_2 to appropriate storage sites as part of the Carbon Capture and Storage (CCS) process. Proper maintenance, including periodic blowdown of pipelines or pipeline sections, is necessary for their safe operation, a pre-requisite for the public acceptance of CCS.

Given the relatively high Joule-Thomson coefficient of CO_2, blowdown can present significant risks to pipeline infrastructure. Depressurisation will result in rapid cooling of the inventory, potentially to below the CO_2 triple point temperature (216 °K); and adjoining pipe wall, which may cool below its ductile to brittle transition temperature, resulting in a significant decrease in its resistance to brittle fracture.

In this thesis a rigorous CFD model for pipeline outflow, based on the Euler equations, is coupled with a Finite Element model of heat conduction (referred to hereafter as FEM-O) in order to predict transient pipe wall temperatures during the depressurisation of CO_2 pipelines. The Peng Robinson Equation of State (EoS) is selected from a range of EoS including the Soave-Redlich-Kwong, Span and Wagner and GERG 2008 for use with FEM-O. The selection was based on a review of the literature, the accepted computational efficiency of cubic EoS and a comparison of outflow predictions with large-scale experimental data generated by the UK National Grid. New formulations of two and three pipe junction boundary conditions are developed for FEM-O in order to model controlled venting of CO_2 pipelines.

FEM-O is validated against data gathered from various large-scale dense phase CO_2 release experiments conducted by the UK National Grid. These included two full bore rupture experiments of a 144 m long, 0.15 m diameter shock tube, a pseudo-steady state release through two 0.05 m diameter pipes joined in series and the blowdown of a large CO_2 pipe system through a 5.88 m long, 0.08 m diameter vertical vent pipe connected to

a T-junction. One shock tube experiment utilised a binary mixture of dense phase CO_2 with N_2. The rest of the tests employed pure, dense phase CO_2.

Allowing for uncertainty in the experimental data, FEM-O predicted the range and rate of outer pipe wall cooling to ± 4 °C throughout each decompression test. Outer pipe wall temperatures were observed and predicted to fall from ambient temperatures to as low as 247 K over ca. 25 s. Fluid pressure and rapid transient predictions closely matched the experimental data. Fluid temperature was consistently under predicted by FEM-O. For the pseudo steady-state experiment, fluid pressure around the junction of the pipes was under predicted by ca. 5 bara (12 %) and fluid temperature predictions by less than 1 %. No experimental wall temperature data was recorded. For the venting of a pipeline system through a T-junction; FEM-O significantly over predicted fluid and pipe wall temperatures compared to the experimental data. This resulted from the assumption of isentropic fluid flow through the T-junction, which in this experiment caused the model to converge on an unrealistic solution for fluid entropy in the fitting.

A verification study was also performed to investigate the performance of the FEM steady state pipe wall temperature calculation algorithm, the sensitivity of the pipe wall temperature predictions to the discretisation of the solution domain and to various different boundary conditions applied. Further, the performance of the newly formulated junction boundary conditions was verified. Lastly a large scale venting experiment was simulated to investigate flow regimes in the inventory. The results demonstrate the minimum requirements for the discretisation of the solution domain in order to maintain accuracy. The uninsulated boundary condition appears to under predict transient wall temperature while the insulated and buried boundary conditions display the expected performance. The new pipeline junction boundary conditions display the expected performance. The large scale venting simulation results suggest the inventory stratifies within seconds of the initiation of venting.

The accuracy of FEM-O wall temperature predictions are shown to be dependent on the applicability of the fluid model to the blowdown scenario. For FBR scenarios transient pipe wall temperature predictions agree well with the available experimental data.

However improvements cannot be claimed when simulating venting scenarios. The Finite Element computer code has been prepared in modular form and may be readily integrated with other blowdown models.

Acknowledgements

I would like to offer my heartfelt thanks to all who have given me the chance to carry out this work and whose wisdom and patience has made this thesis possible.

To the UK National grid for their sponsorship of the COOLTRANS project, to which my work contributed.

The Don Valley Power Project is co-financed by the European Union's European Energy Programme for Recovery
The sole responsibility of this publication lies with the author.
The European Union is not responsible for any use that may be made of the information contained therein.

My supervisor, Prof. Haroun Mahgerefteh, for the opportunity, and for taking the risk.

To my family (all of you) for helping me through the last few years.

To my fellow researchers in the office, Serg, Sols, Peng, Vik, Navid, Shirin, Aisha and Mozhdeh. You've made this a very interesting few years.

To Louis and OJ for their unique perspective and patience.

The technical and admin. staff of the Department of Chemical engineering, UCL.

Finally to Maria, who knows why.

Contents

Chapter 1: Introduction

The release of anthropogenic greenhouse gases (GHG) is now accepted as the main driver for the observed changes in global climate (United Nations, 2014a), including higher average global temperatures, changes in rainfall patterns and extreme weather events. The United Nations Framework Convention on Climate Change commits signatories to stabilising atmospheric GHG concentrations "at a level that would prevent dangerous anthropogenic interference with the climate system" (United Nations, 2014b).

The burning of fossil fuels for energy and in other industrial processes contributes significantly to emissions of GHGs. In 2010 alone ca. 31.85 Gt of CO_2 was released to the atmosphere, of which ca. 13.2 Gt of CO_2 (40 %) was derived from the energy sector (IPCC, 2014). CO_2 emissions from the energy sector are expected to rise to ca. 15.4 Gt between 2010 and 2040 while retaining a share of 40 % of global CO_2 emissions over the same period. This is despite an expected increase in uptake of renewable energy technologies, especially in the developing world (IEA, 2013, 2014).

Given the continued use of fossil fuels for generating energy and in industry, Carbon Capture and Storage (CCS) has attracted increasing attention as a method of reducing the resulting CO_2 emissions. CCS involves the capture of waste CO_2 from large fixed emitters, its transportation via pipeline to deep geological storage sites and its long term sequestration ($\geq 10^3$ years) (Bachu et al., 2007).

The effective deployment of CCS will require the development of extensive high pressure pipeline networks linking CO_2 emitters to storage sites. As CCS pipelines will inevitably run close to population centres their safe operation is paramount. Given their huge capacity (typically several hundred tonnes), even a small puncture could result in the release of a significant mass of inventory. Gaseous CO_2 is odourless, colourless, more dense than air and at concentrations ≥ 10 % v/v causes instantaneous

unconsciousness and rapidly results in death (Kruse and Tekiela, 1996). Thus any leak from a CO_2 pipeline represents a significant hazard.

An essential part of the hazard assessment for any pipeline carrying a pressurised inventory is the analysis of the consequences of pipeline rupture and of outflow from the pipeline. Prediction of the transient outflow rate is central to assessing all consequences for the pipeline system once outflow begins. For CO_2 pipelines these include cooling in the pipe wall and the associated risk of brittle fracture, the possible formation of solid inventory and its ejection from the pipeline and the atmospheric dispersion of the escaping inventory (Bilio et al., 2009).

During outflow from a CO_2 pipeline significant cooling of the inventory will increase the probability of the pipe wall cooling below its Ductile to Brittle Transition Temperature (DBTT), at which point its resistance to brittle fracture decreases significantly (P. Zhang, 2014). Propagation of a brittle fracture will result in the relocation of the CO_2 release point, the effective escalation of the release to a Full Bore Rupture (FBR) and the release of a massive amount of inventory in a very short space of time.

The formation of solid inventory in the pipeline during outflow may result in the fouling of equipment, such as valves, impairing their normal operation. Ejection of solid CO_2 will alter the behaviour of the dispersing inventory cloud.

Therefore, a model for predicting outflow from CO_2 pipelines should accurately predict discharge rate and cooling in the inventory and pipe wall. Additionally, given the potential geographical extent of a CCS pipeline network, the model should also account for network characteristics such as junctions and changes in pipeline geometry and inclination.

Significant research effort has been directed toward the development of accurate and robust mathematical models for predicting transient discharge rates from pressurised pipelines. More rigorous models, such as the two fluid model OLGA (Bendiksen et al.,

1991), account for thermal and mechanical non-equilibrium effects in the inventory. OLGA has been shown to be of limited use in modelling unsteady flows in ruptured hydrocarbon pipelines (Shoup et al., 1998) due to its reliance on certain empirical data, such as for the transition between the various flow regimes, and numerical stability issues. There is also little information concerning the formulation of the choking condition at the rupture plane, vital for modelling transient outflow. Additionally, OLGA accounts for heat transfer between the ambient and pipe wall using a constant heat transfer coefficient. This severely limits its applicability to modelling CO_2 pipeline blowdown as phase changes in the inventory during blowdown would result in significant changes to the heat transfer coefficient with time.

For failure scenarios where a high degree of turbulence is expected in the inventory less rigorous models may be suitable. Brown et al. (2013) developed a Homogeneous Relaxation Model (HRM) of pipeline blowdown in which mechanical equilibrium in the inventory is assumed, non-equilibrium liquid-vapour mass transfer is accounted for by relaxation to thermodynamic equilibrium. As the model does not account for phase slip its application is limited to modelling of Full Bore Rupture (FBR), the most catastrophic and least common type of failure.

Mahgerefteh and co-workers (see for example Mahgerefteh and Atti, 2006; Mahgerefteh and Wong, 1999; Oke et al., 2003) developed a pipeline outflow model based on the Homogeneous Equilibrium Model (HEM). The model accounts for rapid pressure and thermal transients in the fluid during depressurisation and frictional effects. Heat transfer between the inventory and ambient is modelled using an energy balance across the pipe wall. Comparison of the simulated results with corresponding experiments and real pipeline failure events, such as the Piper Alpha tragedy, show very good agreement.

In reviewing the literature it was observed that heat transfer between a pipeline and the ambient is not always accounted for in discharge models. Predictions from such models may therefore be expected to diverge from reality. This is a particular problem for CO_2 pipeline modelling, where prolonged cooling of the inventory during outflow can have a

significant impact on transient fluid properties. Where external heat transfer is accounted for, the pipe wall conduction models used have not been validated due to a lack of appropriate experimental data.

The aim of this work is to develop a mathematical model to better assess the hazards associated with the blowdown of CO_2 pipeline networks. The specific objectives are:

- to develop a heat conduction model for calculating transient pipe wall temperatures and heat transfer between the ambient and pipeline inventory during outflow;
    - to integrate the above model with an appropriate outflow model and validate its performance;
- to formulate and validate flexible models for two and three pipe junctions which minimise runtime while maintaining accuracy;
- to investigate the applicability of the model to simulating CO_2 pipeline outflow under a number of scenarios.

This thesis is divided into nine chapters.

In chapter 2 relevant literature is reviewed. The chapter includes brief discussions of the transportation of CO_2 by pipeline and the risks associated with venting of such pipelines. Mathematical models for pipeline outflow reported in the literature are reviewed with specific consideration of their ability to predict discharge rate, rapid fluid transients and pipe wall temperatures. Modelling of network features such as junctions are also considered. Pipe wall heat conduction models are discussed. In addition, a review of the work investigating Equations of State (EoS) for modelling CO_2 properties is presented.

In chapter 3 the theoretical background and formulation of the pipeline blowdown model OUTFLOW (see section 2.4.4) employed in this study is presented. A complete description of the previously reported heat transfer model and associated correlations is included.

In chapter 4 the Method of Characteristics (MOC), the numerical solution technique used in OUTFLOW, is presented. Boundary conditions for modelling pipeline blowdown are described.

In chapter 5 OUTFLOW is first used to model CO_2 shock tube decompression using a range of EoS. Based on a comparison of predicted and experimental data an EoS is selected for the modelling work in this thesis. OUTFLOW pipe wall temperature predictions are then validated against experimental shock tube data.

In chapter 6 the formulation of a Finite Element heat conduction model and its integration with OUTFLOW to create the composite model FEM-O is presented. FEM-O fluid and pipe wall temperature predictions are then validated against experimental shock tube data.

In chapter 7 new pipeline junction boundary conditions are proposed for two and three pipe junctions. The new boundary conditions are implemented in FEM-O and validated against appropriate experimental data.

In chapter 8 a verification study of FEM-O is presented. The sensitivity and accuracy of the FEM calculations to factors including the solution domain discretisation and FEM boundary conditions are investigated. In addition, a verification study is performed on the new junction boundary conditions presented and validated in chapter 7. Finally, venting of a long CO_2 pipeline is simulated and the flow regime within the inventory (e.g. annular, stratified, turbulent) during outflow investigated by comparison with experimentally derived flow regime data.

Chapter 9 presents the conclusions of this thesis and suggestions for future work.

Chapter 2: Literature Review

2.1 Introduction

Pipelines provide the means to move large quantities of fluid inventories over long distances with relative ease. Proper maintenance, including periodic emptying of whole pipelines or pipeline sections for inspection and possible repair, is central to their continued safe operation. Emptying of a pipeline must be carried out in a controlled fashion to avoid infrastructure damage and to minimise process risks.

The UK Pipeline Safety Regulations 1996 (HSE, 1996) require that the risks associated with the construction and operation of major accident hazard (MAH) pipelines, which include CO_2 pipelines (Shuter et al., 2011), are as Low As Reasonably Practicable (ALARP). In the context of CO_2 pipelines outflow models can contribute significantly to understanding the outflow process and to minimising process risks.

In this chapter a range of topics relevant to modelling the blowdown of pipelines are reviewed. First, a brief discussion of the transportation of CO_2 for Carbon Capture and Storage (CCS) is presented. The pipeline blowdown process is then addressed and important phenomena and risks specific to CO_2 pipelines are identified.

In the next section a review of published outflow models is presented and their applicability to modelling outflow from CO_2 pipelines is discussed. In particular, their accuracy in predicting depressurisation rate, rapid transients in the inventory, discharge rate and pipe wall temperatures are highlighted. This is followed with a discussion of the modelling of heat exchange in pipeline models.

Finally, a brief review of work to identify a suitable Equations of State (EoS) for use in modelling CO_2 pipeline venting is presented.

2.2 CO_2 transportation for Carbon Capture and Storage (CCS)

It has been assumed in the preceding text that land based transportation of CO_2 for CCS will be by pipeline, however in offshore transportation scenarios this may not be the most practicable method. In this section a brief discussion of the transportation of CO_2 is presented.

CCS is a bridging technology being researched in order to reduce CO_2 emissions from large scale emitters while replacement low carbon technologies are developed and introduced. CCS research has focussed overwhelmingly on the application of the technology to fossil fuel power stations.

While fossil fuel power stations emit a continuous flow of CO_2, and any CO_2 injection site for deep underground storage will rely on such a continuous stream, power stations have not been built with any regard to the proximity of suitable long term CO_2 storage sites. Pipelines therefore represent the ideal transportation method, allowing for continuous transportation of large volumes of CO_2 from fixed sources to storage sites over long distances. Pipeline transportation is limited however by the availability of land, the topography (see also section 7.1) and, given the potential for off-shore CO_2 storage, the depth of water in which pipelines can currently be built (see for example Golomb, 1993). Transportation by ship, or a combination of pipeline and ship transport, may thus be considered when warranted (Svensson et al., 2004). Road or rail transport of CO_2 has not been seriously considered for CCS (Golomb, 1997; Skovholt, 1993).

The economics of CO_2 transportation by pipeline have been studied by many researchers. McCoy and Rubin (2008) reported the development of a sophisticated engineering-economic model for estimating the cost of transporting varying amounts of CO_2 over a range of distances in the USA. The model accounted for construction, operation and maintenance of the pipeline in the transportation cost. Other studies have

relied on the use of commercially available software such as ASPEN PLUS (Zhang et al., 2006).

Shafeen et al. (2004) presented transportation cost estimates for CO_2 from the Nanticoke power plant (Ontario) to a local geological storage site below Lake Erie. In this example an appropriate injection site was fortuitously close to Nanticoke; only 112 km for a direct pipeline. For many power stations however, this will not be the case. Additionally, as the costs associated with CO_2 storage will vary geographically the most economic storage solution may not be the closest. Skovholt (1993) reported the financial advantages of using larger diameter pipelines, even after investment and operational costs are accounted for. Chandel et al. (2010) further demonstrated the economies of scale a trunk pipeline could achieve.

Minimising the risks associated with CO_2 transport will be vitally important to the public acceptability of CCS; public opposition to one large-scale CCS storage experiment in Hawaii resulted in its relocation to Norway and subsequent cancellation (IPCC, 2005). Deliberate blowdown of a pipeline presents significant risks to the public and pipeline itself. In the next section this process is briefly discussed to illustrate key risks.

2.3 CO_2 pipeline blowdown and associated risks

Unless otherwise stated, the terms blowdown and venting are used interchangeably in this thesis to refer to the controlled emptying of a pipeline. Where relevant, depressurisation through an accidental rupture (puncture or full bore (guillotine) rupture (FBR)) is specified.

Bilio et al. (2009) presented an excellent discussion of key factors expected to affect the safe operation of a CO_2 pipeline. Of particular relevance to pipeline blowdown are the purity of the inventory and the associated risk of solids formation during blowdown, the

risk of fracture and the risks posed by the dispersing inventory cloud. In this section these factors are discussed within the context of a pipe undergoing blowdown.

Based on the description provided by Fairuzov (1998), the blowdown process in CO_2 pipelines may be divided into three stages:

1) Decompression wave propagation – rapid depressurisation of the fluid occurs upon rupture of the pipeline. The resultant decompression wave propagates along the pipe at the local speed of sound. Outflow is choked.
2) Flashing boundary propagation – a flashing boundary subsequently propagates along the pipeline at the local speed of sound. Depressurisation continues at a reduced rate and significant cooling will be observed in the CO_2 inventory and the pipe wall in contact with it.
3) Two phase discharge – two phase discharge occurs, the flashing front travels throughout the fluid, resulting in flashing along the full length of the pipe. Possible stratification of the inventory. Inventory and pipe wall temperatures continue to drop.

Introducing impurities to a CO_2 inventory will change the fluid's properties; different behaviour at every stage of the blowdown process will be seen as a result. Of particular significance for ductile fracture and dispersion behaviour respectively will be changes in the speed of sound in the fluid and to the composition and properties of the inventory as it is discharged.

A pipeline is at risk of ductile fracture formation during stage 1 of blowdown only. Ductile fractures evolve from small cracks in the pipe wall originating at a rupture; if the pressure exerted on a crack tip exceeds the material crack arrest pressure a ductile fracture will be initiated. If the crack velocity then exceeds the decompression wave velocity a long running fracture will result (Mahgerefteh et al., 2012a). Fluid properties therefore directly affect the formation and behaviour of ductile fractures.

A pipeline undergoing venting is at risk from brittle fractures during stage 3 of blowdown; prolonged cooling of the pipe wall may result in it falling below its Ductile

to Brittle Transition Temperature (DBTT). At this point a significant drop in the wall fracture toughness occurs and the risk of brittle fracture increases significantly. Brittle fracture propagation depends on both thermal stresses in the pipe wall and pressure stresses exerted on it by the fluid (Mahgerefteh and Atti, 2006; Zhang, 2014).

A further risk for the pipeline during stage 3 of blowdown is that the fluid properties may pass the inventory triple point, resulting in the formation of solids. Solids may foul the internal surfaces of pipeline infrastructure such as valves, inhibiting their function.

Evidence for CO_2 pipeline failure

CO_2 pipelines are an established technology. In the mid-western USA more than 2500 km of pipelines carry 50 $MtCO_2$ y^{-1} for enhanced oil recovery (IPCC, 2005). Gale (2004) presented data for the number of reported incidents in CO_2 pipelines in the USA between 1990 and 2001. In this period 10 incidents were reported: 4 involving relief valve failure, 3 involving weld/gasket/valve packing failure, 2 due to corrosion and 1 due to outside force. Gale (2004) concluded that CO_2 and natural gas pipelines were equally prone to incidents. It was noted that the CO_2 pipeline incident data was limited based on the small sample size.

In the absence of historical experience modelling studies can provide legitimacy to concerns over ductile and brittle fracture in CO_2 pipelines. Mahgerefteh et al. (2012a) predicted the formation of long running ductile fractures following FBR of CO_2 pipelines operating at a range of conditions and with various inventories.

Zhang (2014) presented a model for the prediction of brittle fracture propagation following the puncture of buried CO_2 pipelines, reporting that under certain circumstances the pipe wall could cool below its DBTT and brittle fractures propagate. Unfortunately however, appropriate experimental data was not available to validate this model.

2.4 Review of outflow models

In the previous section the blowdown process in CO_2 pipelines was described and key risks associated with it were discussed. The relationship between the fluid properties, wall temperatures and ductile and brittle fracture during venting/blowdown of CO_2 pipelines was presented. The significance of the chemical composition of the inventory was also discussed.

In order to model depressurisation of a CO_2 pipeline and hence accurately illustrate the risks associated with the process, an outflow model must produce accurate transient fluid property and pipe wall temperature predictions. It should also account for heat transfer between the ambient and inventory.

In this section models for simulating outflow from pipelines are reviewed and their methods of accounting for heat transfer discussed. Where available, data for the validation of the discussed models is presented.

2.4.1 Summary of published outflow models

Denton (2009) reviewed the reported state of the art pipeline outflow models. More recently Brown (2011) expanded and updated this review. Relevant models reviewed by Brown (2011), and some recently reported models, are summarised in table 2.1. Included in the table are their methods of calculating pipe wall heat conduction. Models that neglect pipe wall heat conduction are not included in the review.

Table 2.1: State of the art outflow models with details of their mechanisms for modelling pipe wall heat conduction.

Model	Heat conduction calculation
OLGA (Bendiksen et al., 1991)	Heat conduction in the pipe wall not discussed, fluid/wall heat transfer coefficient calculated internally, user specified pipe wall/ambient heat transfer coefficient
FaNM (Fairuzov, 1998a, 1998b, 1999, 2000)	Heat conduction in pipe wall not calculated, fluid/pipe wall/ambient heat transfer calculated using modified energy conservation equation
University College London model OUTFLOW (Atti, 2006; Mahgerefteh et al., 1999 to 2012; Oke et al., 2003)	Heat conduction in pipe wall calculated using transient energy balance, fluid/pipe wall/ambient heat transfer accounted for
SLURP_HEM_HT (Cumber, 2007)	Fluid/pipe wall heat transfer accounted for
Machnet (Terenzi, 2005)	Fluid/pipe wall/ambient heat transfer calculated by solving the Fourier equation in cylindrical geometry
GasDECOM (Botros et al., 2004 to 2013)	No published details found
Brown et al. (2014)	2-D heat conduction in pipe wall cross-section calculated using Finite Difference method, assumed perfect insulation for this publication
Burlutskiy (2013, 2014)	Neglects heat transfer
CFD-DECOM (Xu et al., 2014)	Heat conduction in pipe wall calculated using Finite Volume method, assumed perfect insulation for this publication

2.4.2 OLGA (Bendiksen et al., 1991)

OLGA is a two-phase flow model based on the solution of the conservation equations for mass, momentum and energy. Separate continuity equations are applied for gas, liquid bulk and liquid droplets, these may be coupled through interfacial mass transfer. Two momentum equations are used for either liquid films or gas with possible liquid droplets. One energy equation is applied for the whole mixture. An equation of state such as the Peng-Robinson (PR) (Peng and Robinson, 1976) or Soave-Redlich-Kwong (SRK) (Soave, 1972) is employed to calculate fluid properties. An implicit finite difference scheme is used to solve the relevant conservation equations.

Heat transfer between the pipe wall and inventory is calculated within OLGA. A pipe wall composed of multiple materials of varying heat transfer properties can be simulated, the wall description along different lengths of the pipe can be varied. The pipe can be simulated as totally insulated using the user specified heat transfer coefficient between the pipe wall and ambient. Different frictional factors are used for the various flow regimes.

OLGA was originally developed to model the slow transients associated with terrain-induced slugging, pipeline start-up, shut-in and variable production rates. Successive iterations addressed the simulation of stratified/annular flow regimes and extended the model for hydrocarbon mixtures (Bendiksen et al., 1991). The numerical solution scheme employed gave rise to numerical diffusion of sharp slug fronts and tails, resulting in the incorrect prediction of slug size. This was addressed by introducing a Lagrangian type front tracking scheme (Nordsveen and Haerdig, 1997).

Validation

OLGA was validated by Shoup et al. (1998) against field data obtained by Deepstar for blowdown of a 5.28 km, 0.102 m internal diameter (ID) onshore pipeline with varying inclination and containing gas condensate at 4.8 MPa (700 psig). The precise mixture composition was not given. The pipeline was blown down through a 2.54 cm choked

opening. In order to simulate blowdown it was assumed that release occurs through a valve situated at the end of the pipeline.

Figures 2.1 and 2.2 present the observed and predicted pressure history and gas flow rate respectively at the release end of the pipeline. As may be observed, while OLGA was able to predict the trends in behaviour, it was not able to precisely predict the real pressure or flow rate at the release end. However, better agreement between observed and predicted pressure data was achieved further from the release point during the first minutes of blowdown.

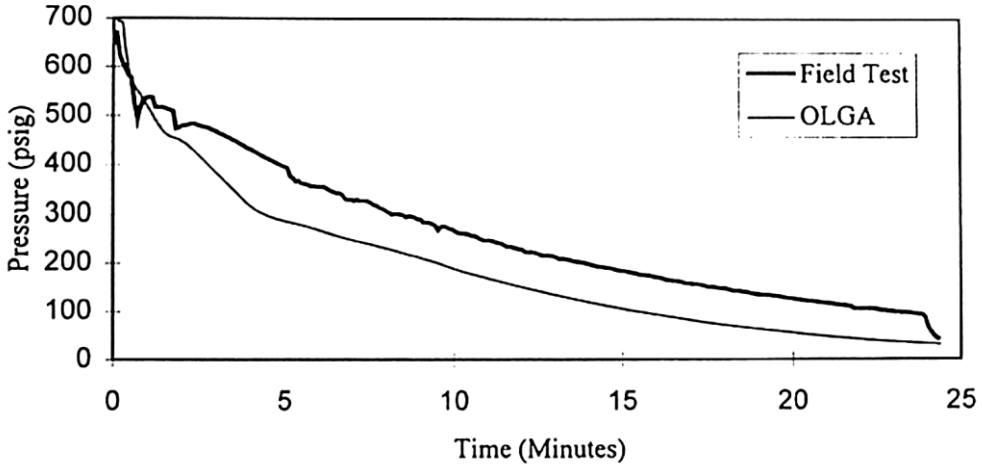

Figure 2.1: Pressure at the release end of the pipe. OLGA Simulations versus Field Test (Shoup et al., 1998).

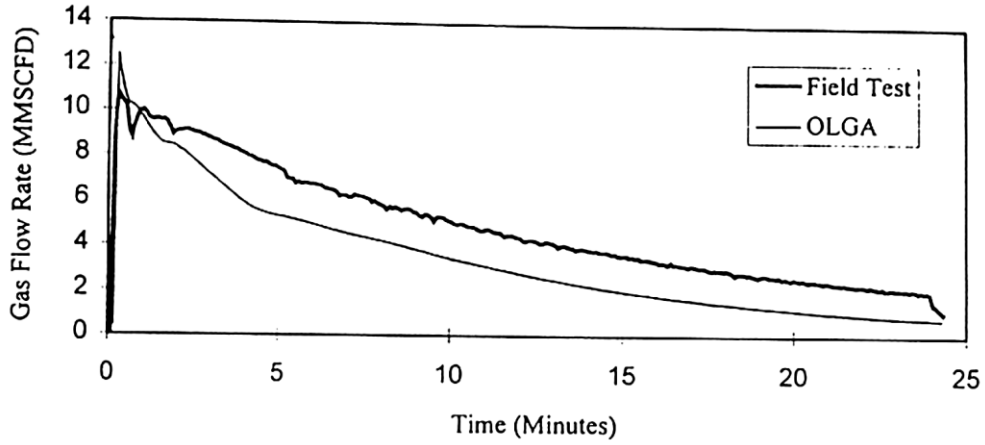

Figure 2.2: Gas flow rate at the release end of the pipe. OLGA Simulations versus Field Test (MMSCFD – million standard cubic feet per day) (Shoup et al., 1998).

OLGA was used to simulate experimental decompression tests by Botros et al. (2007). The tests were performed using a 172 m long, 49.5 mm ID instrumented shock-tube rig. Decompression of the pipeline was initiated upon failure of a rupture disc.

Figure 2.3 shows the variation of pressure with time during the first 1000 ms of discharge for Case 2: a conventional gas mixture (ca. 95.6 % methane) at an initial pressure and temperature of 105.8 bara and -25.6 °C. Data is shown from instruments located 23.1 m (P14), 47.1 m (P19) and 71.1 m (P24) from the rupture point. As was observed by Botros et al. (2007), the predicted speed of the decompression wave is significantly slower than observed experimentally, the predicted pressure drop is also greater.

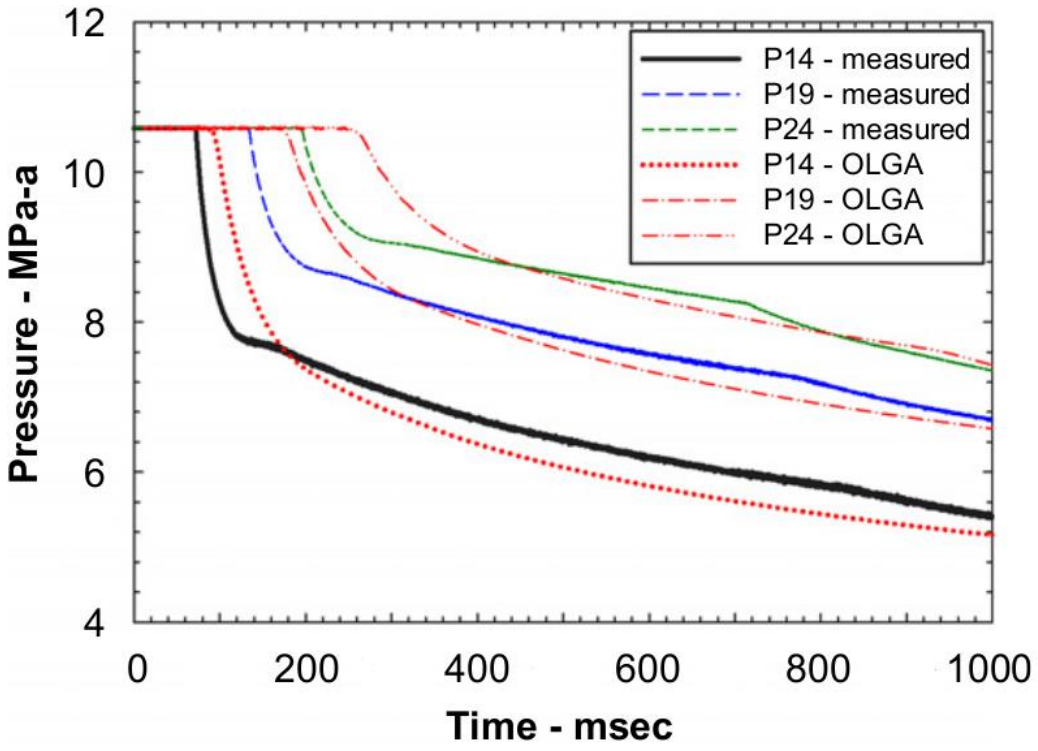

Figure 2.3: Comparison between OLGA and experimental data for Case 2 at P14, P19 and P24 (Botros et al., 2007).

2.4.3 Fairuzov (1998a, 1998b, 1999, 2000)

Fairuzov (1998a) reported that, of the pipeline outflow models reviewed for that publication, all neglected the thermal capacitance of the pipe wall and most assumed that fluid flow in the pipeline was adiabatic.

In a later publication (Fairuzov, 2000) it was observed that the traditional approach to solving the two phase conjugate heat transfer problems in pipelines was to couple separate models for fluid flow and transient heat conduction in the wall using experimentally derived correlations for boiling heat transfer. However in a pressurised pipeline undergoing blowdown the flashing of the inventory occurs due to depressurization, rather than heating of the fluid.

Fairuzov (1998a) presented a new approach to solving the problem of transient conjugate heat transfer in flashing liquid flows in pipelines to address these issues. The outflow model developed is based on equations for the conservation of mass, momentum and energy. A novel formulation of the energy equation accounts for the heat capacitance of the pipe wall. Conjugate heat transfer calculations for predicting fluid/pipe wall heat transfer are not required. The external heat flux is calculated from Newton's cooling law. The thermodynamic and transport properties of the fluid were calculated with a computer code developed by Solorzano et al. (1996), which utilised the SRK EoS. The governing equations were solved using the Gear method (Gear, 1971). The model assumed:

- flow is one-dimensional;
- homogeneous equilibrium in the inventory at saturation conditions;
- the fluid and pipe wall were in local thermal equilibrium;
- axial heat transfer in the pipe wall was negligible.

The model was validated against experimental data reported by Tam and Cowley (1988). The experiment considered was the FBR of a 100 m long pipeline with an ID of 150 mm. The pipeline was suspended on 20 load cells spaced at 5 m intervals to measure discharge rate, fluid temperature and pressure was measured along the full

length of the pipe using 10 thermocouples and 10 pressure sensors. The pipeline inventory was pressurised LPG (95 mole% propane with 5 mole% butane) at initial conditions of 11.25 bar and 19.9 °C. Given the short length of the pipeline the assumption of thermal equilibrium between the fluid and pipe wall was not achieved. Nonetheless it was assumed that a small part of the inner wall was in thermal equilibrium with the fluid, the thickness of this thermally penetrated layer was estimated to be ca. 1 mm.

Figure 2.4 presents the variation of predicted and experimental pipeline inventory with time. Figures 2.5 and 2.6 present the variation of predicted and experimental fluid pressures and temperatures respectively at the open and closed ends of the pipeline. As may be observed, in all cases the agreement of the model with the experimental data is reasonable.

Referring to figure 2.5, predicted fluid pressures are presented assuming a thermally penetrated layer of 1 mm or adiabatic expansion of the inventory. As may be observed, adiabatic expansion results in significant under prediction of the fluid pressure at the closed end in the later stages of blowdown.

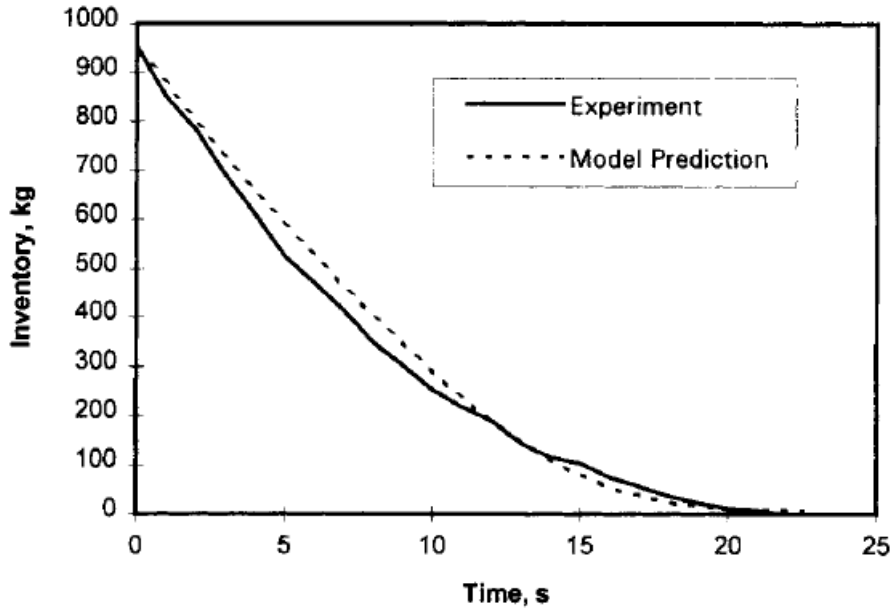

Figure 2.4: Predicted and experimental pipeline inventory during blowdown of a 100 m pipeline containing LPG (Fairuzov, 1998a).

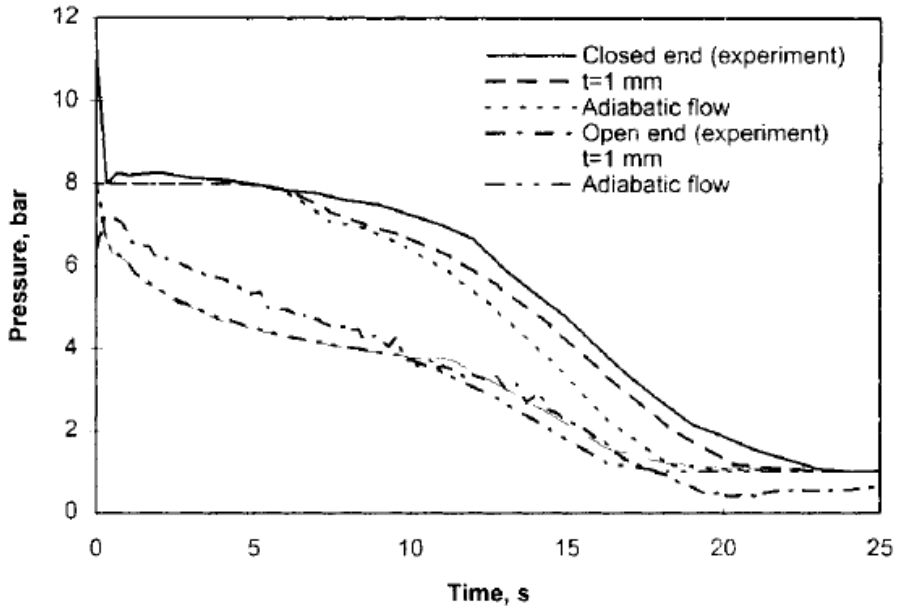

Figure 2.5: Predicted and experimental fluid pressures during blowdown of a 100 m pipeline containing LPG (Fairuzov, 1998a).

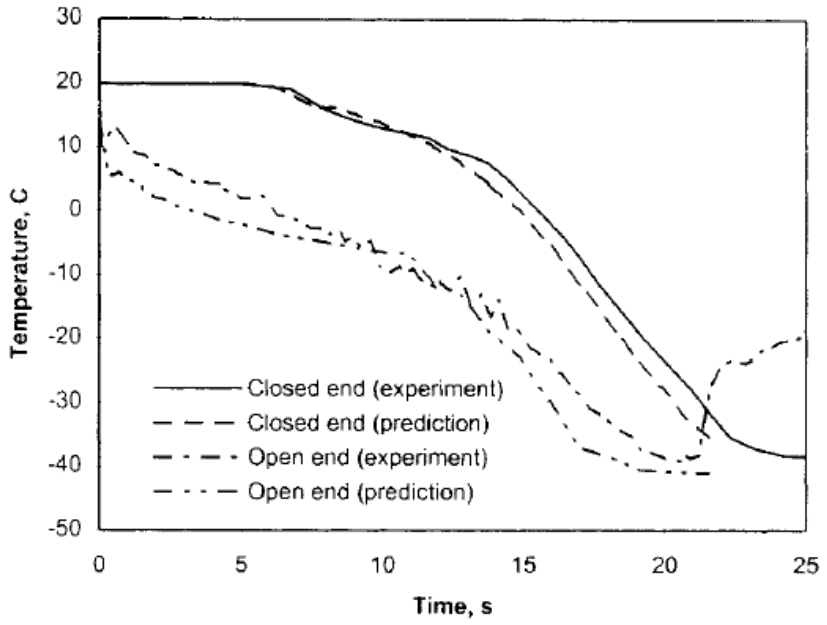

Figure 2.6: Predicted and experimental fluid temperatures during blowdown of a 100 m pipeline containing LPG (Fairuzov, 1998a).

Given the assumption of a thermally penetrated layer on the inner pipe wall, no wall temperature predictions were reported.

Fairuzov (1998b) subsequently reformulated the model using the Euler equations for conservation of mass, momentum and energy. The model assumptions remained the same as presented above and the energy equation was formulated to account for the heat capacitance of the pipe wall. A new dimensionless term governing the effect of thermal capacity of the pipe wall on the behaviour of the flashing liquid flow was also introduced into the energy equation. The governing equations were solved via their conversion into a system of finite difference equations using the RELAP5 numerical solution scheme (Ransom and Trapp, 1978). The reformulated model does not consider the dynamics of the depressurisation wave (Fairuzov, 1998b). The new model (hereafter referred to as FaNM) was successfully validated against the same experimental data used previously (Fairuzov, 1998a).

In two subsequent publications the range of applicability of FaNM (Fairuzov, 1998b) was investigated by comparison with another outflow model (referred to hereafter as FaCon). FaCon (Fairuzov, 2000) was formulated in an identical fashion to FaNM with the exception of using a conventional formulation of the energy equation. The source term for heat flux in the energy equation is calculated from Newton's cooling law. Heat conduction in the pipe wall was calculated separately by solving the heat conduction equation in one (radial) dimension using the Finite Volume method (FVM). FaCon was successfully validated using the same experimental data used previously (Fairuzov, 1998a). It was demonstrated (Fairuzov, 2000) that for long pipes (fL/D = 200) undergoing FBR the relative error between FaNM and FaCon predictions for fluid temperature, fluid/wall interface temperature and outer wall temperature were consistently small (<2 %). For shorter pipe lengths (fL/D = 2) the blowdown was too fast to achieve local thermal equilibrium between the pipe wall and fluid. FaNM is therefore inappropriate for modelling blowdown of short pipes. Fairuzov (1999) also demonstrated the capability of FaNM to accurately model blowdown following either FBR or puncture (A_dC_d/A = 0.05) of a long pipeline (fL/D = 200).

2.4.4 University College London outflow model (Atti, 2006; Mahgerefteh et al., 1999 to 2012; Oke et al., 2003)

The UCL outflow model, referred to hereafter as OUTFLOW, was developed over a number of years to model transient outflow from ruptured pipelines. The historical development of the model is given by Brown (2011).

In this section the ability of OUTFLOW to accurately model pipeline depressurisation, fluid properties and discharge rate is demonstrated by comparison with experimental data. Development of this model for pipeline network simulation is also discussed.

OUTFLOW solves the conservation equations for mass, momentum and energy for one dimensional fluid flow in a pipeline using the Method of Characteristics (MOC). A cubic EoS is used to calculate fluid properties (Mahgerefteh et al., 2007; Mahgerefteh et al., 2006b; Mahgerefteh et al., 1999). The constituent phases in the inventory are assumed to be in mechanical and thermal equilibrium. Heat transfer between the ambient and pipe wall is accounted for through a transient energy balance (Atti, 2006) from which the pipe wall temperature was calculated. Newton's cooling law is applied to calculate heat flux to the inventory.

Oke et al. (2003) developed OUTFLOW to model punctures in long pipelines and validated it against appropriate field data from the Isle of Grain depressurisation test P40 (Richardson and Saville, 1996). This test involved the depressurisation of an isolated 100 m long, 0.154 m ID pipeline containing commercial LPG through a 0.150 m diameter puncture located at the end of the pipe. The inventory had an initial pressure and temperature of 21.6 bara and 293.15 K respectively.

Simulated fluid pressure data from the closed and open ends of the pipeline is compared with the corresponding experimental data in figure 2.7. Variation in the predicted and experimental total pipe inventory is shown in figure 2.8.

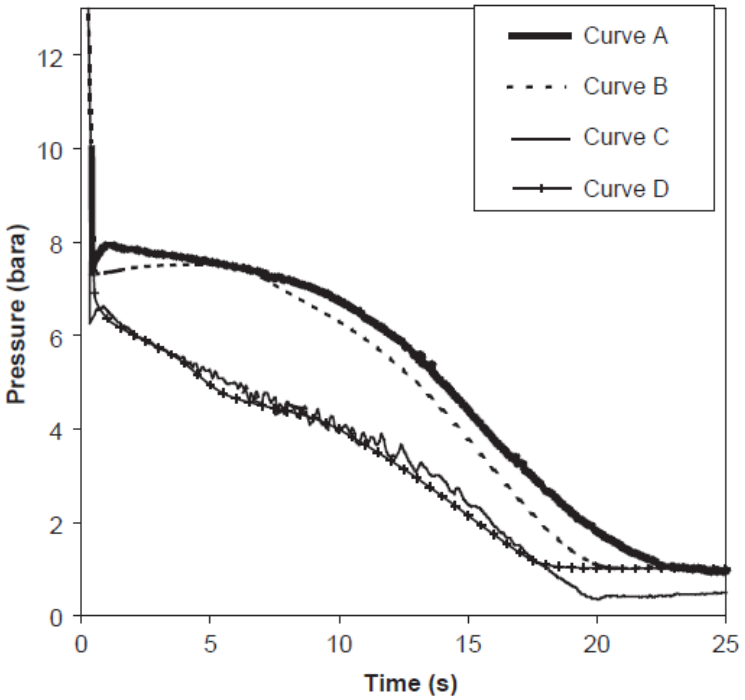

Figure 2.7: Experimental and OUTFLOW simulated pressure histories at the closed and open ends of the pipe for Isle of Grain test P40 (Oke et al., 2003).

Curve A – experimental data (closed end)

Curve B – OUTFLOW predictions (closed end)

Curve C – experimental data (open end)

Curve D – OUTFLOW predictions (open end)

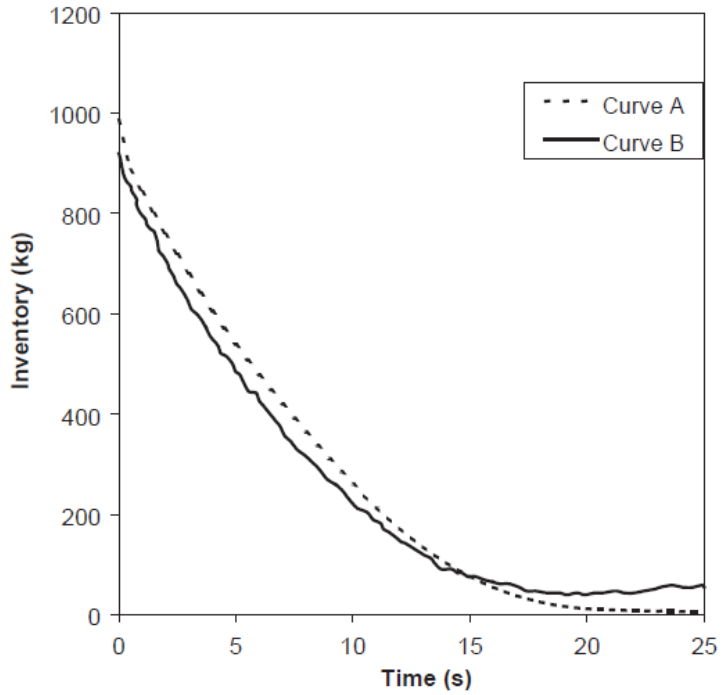

Figure 2.8: Experimental and OUTFLOW simulated total line inventory for Isle of Grain test P40 (Oke et al., 2003).

Curve A – experimental data

Curve B – OUTFLOW predictions

As may be observed, the OUTFLOW pressure predictions agree reasonably well with the experimental data, especially at the open end of the pipeline. Reasonable agreement between the simulated and observed line inventory is also observed during the first ca. 15 s of discharge.

More recently Mahgerefteh et al. (2012b) used OUTFLOW to simulate decompression wave speeds in gas phase CO_2 inventories during FBR of a shock tube. Predicted data was compared against the corresponding experimental data, reported by Cosham et al. (2011). The shock tube used was insulated, 144 m long with an internal diameter of 146 mm (a complete description of the experimental setup is presented in section 5.2.1). Cosham et al. (2011) reported that a variety of inventories were investigated, including pure CO_2 and CO_2 with impurities relevant to CCS.

Figures 2.9 and 2.10 compare the OUTFLOW simulated decompression wave speeds for pure CO_2 and CO_2 with 4.03 mole% N_2 respectively with the corresponding experimental data. Simulated decompression wave speeds are calculated at transducers P13 and P14 (paired, located 1.84 m from the rupture plane) and transducers P15 and P16 (paired, located 2.44 m from the rupture plane). The PR EoS (Peng and Robinson, 1976) was used in simulations.

As may be observed, reasonable agreement is obtained between the experimental and simulated data down to ca. 15 barg. Small differences between the simulated and experimental data were reported to be due to inaccurate prediction of fluid speed of sound by the EoS. In both figures, plateaux in curves C (associated with a phase change from gaseous to a two phase inventory) occur at significantly lower pressures than predicted by OUTFLOW. This was ascribed to delayed nucleation by Cosham et al. (2011), which OUTFLOW is unable to account for.

Within the limits of the model, therefore, OUTFLOW is able to simulate fluid properties in an inventory with reasonable accuracy during pipeline blowdown.

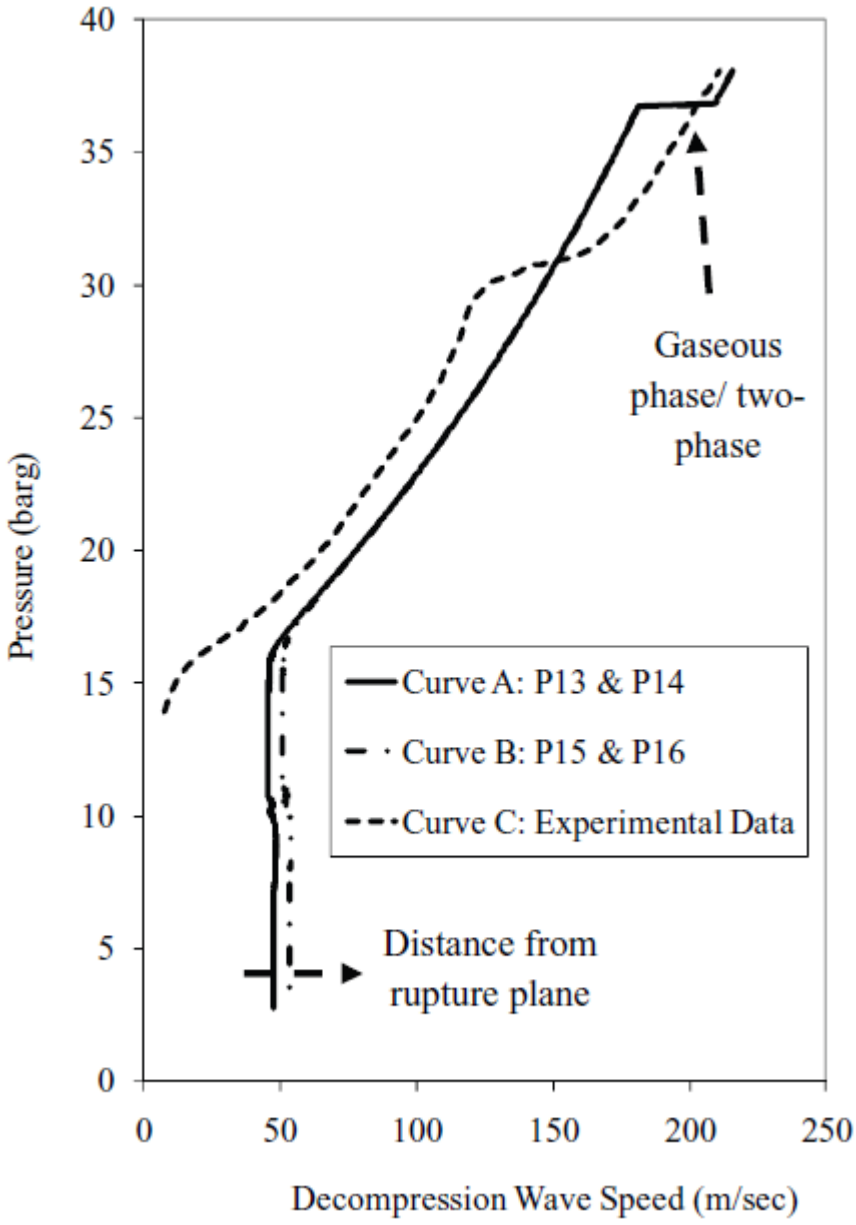

Figure 2.9: Comparison of fluid pressure with decompression wave speed for pure CO_2 (initial conditions: 38.1 barg, 278.15 K) (Mahgerefteh et al., 2012a).

Curve A: data from transducers P13 and P14 (1.84 m from rupture plane).

Curve B: data from transducers P15 and P16 (2.44 m from rupture plane).

Curve C: experimental data.

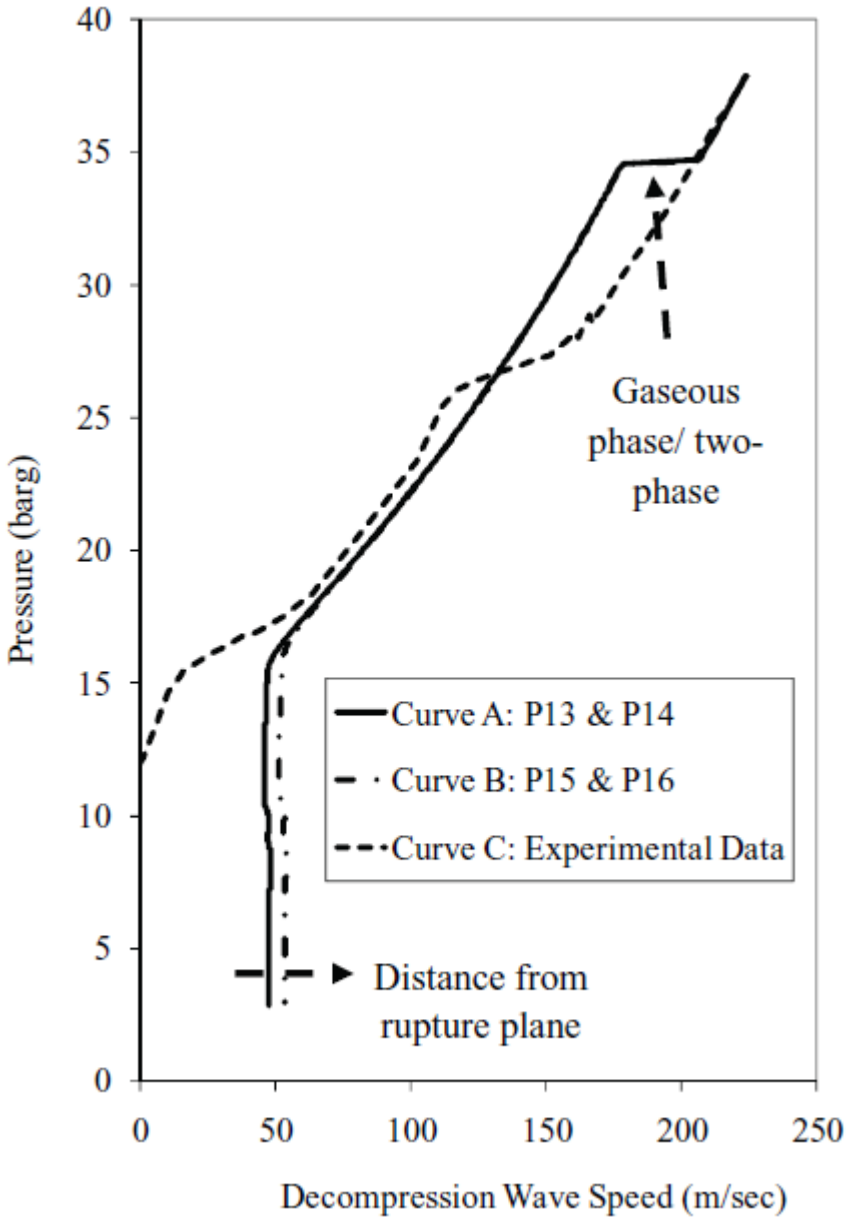

Figure 2.10: Comparison of fluid pressure with decompression wave speed for 95.97 mole% CO_2 with 4.03 mole% N_2 (initial conditions: 37.9 barg, 278.35 K) (Mahgerefteh et al., 2012a).

Curve A: data from transducers P13 and P14 (1.84 m from rupture plane).

Curve B: data from transducers P15 and P16 (2.44 m from rupture plane).

Curve C: experimental data.

Mahgerefteh et al., (2006a) further developed OUTFLOW to model outflow following rupture in pipeline networks. A detailed description of the boundary conditions used to model fluid flow through junctions is presented in section 4.3.3.

In the absence of suitable real data, OUTFLOW simulations were performed to investigate the effects of pipeline configuration on the discharge process. Three configurations of a 25 km pipeline were simulated; these are shown in figure 2.11.

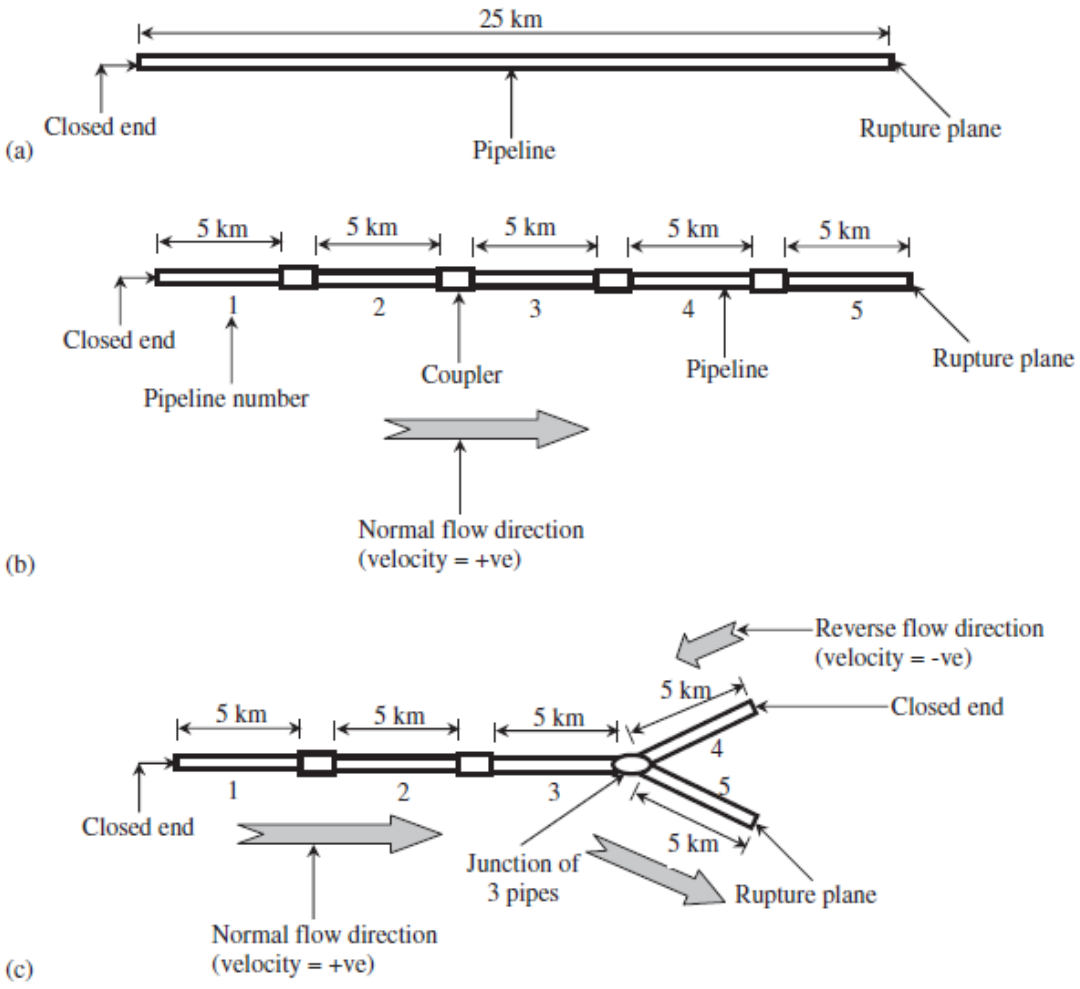

Figure 2.11: Pipeline network configurations simulated by Mahgerefteh et al., (2006a).

Maintaining an overall length of 25 km, the pipeline ID and wall thickness was 0.419 and 0.019 m respectively in every subsection. The pipeline was modelled as fully

insulated in each configuration; each pipeline and subsection was horizontal. The inventory was 90 mole% CH_4 and 10 mole% C_2H_6 at an initial temperature and pressure of 283 K and 117 bara and at rest prior to rupture.

Fluid pressures at the rupture plane and intact ends were compared for all configurations, as shown in figure 2.12.

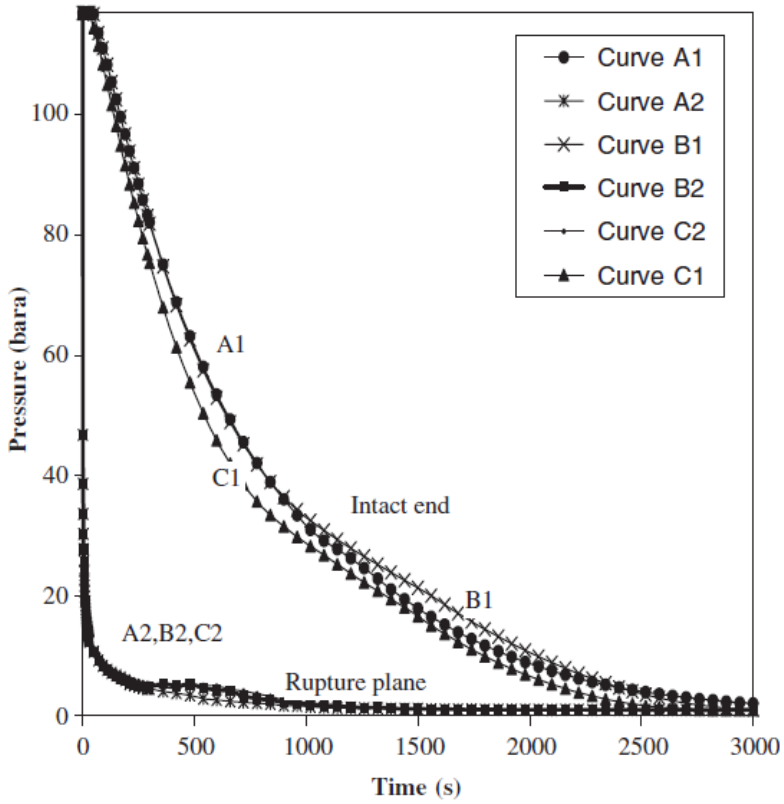

Figure 2.12: Fluid pressures at the rupture plane and intact ends of the pipeline for all configurations (Mahgerefteh et al., 2006a).

Curves A1 and 2: intact and rupture plane data respectively, configuration A
Curves B1 and 2: intact and rupture plane data respectively, configuration B
Curves C1 and 2: intact and rupture plane data respectively, configuration C

As may be observed from curve C1, depressurisation is predicted to occur fastest for pipe configuration C. Comparison of the rupture plane fluid velocities supports this conclusion, with fluid velocity beginning to decline significantly earlier than observed for the other configurations. However, no significant differences were reported in the

discharge rates from each configuration. The total mass discharged from each configuration was not reported, nor was a discussion of mass conservation in the study. Additionally, very limited data for fluid properties at the inlet or outlet of any junction was reported (only fluid velocity data at the T-junction, pipe configuration C).

In summary, OUTFLOW has been developed over a number of years to model outflow from pipelines. The model's accuracy in predicting depressurisation rate, discharge rate and rapid transients in the inventory has been demonstrated. Development of the model to simulate outflow from pipeline networks has also been discussed.

2.4.5 SLURP (Cleaver et al., 2003; Cumber, 2007)

Cleaver et al. (2003) developed SLURP for simulating the outflow rate from ruptured pipelines transporting compressed volatile liquids. The mathematical basis of SLURP is the same as that originally developed by Morrow (1982) with the extension of the thermodynamic property model to account for a wide range of fluids with a consistent degree of accuracy (Cleaver et al., 2003).

The main assumptions in SLURP include; for failure along the pipe length, outflow from each ruptured end is not affected by outflow from the other, the pipeline is infinitely long and the outflow from the pipeline is always choked. Cleaver et al. (2003) do not report that heat transfer between the ambient and the pipeline is accounted for.

Cumber (2007) extended SLURP (SLURP_FAUSKE) by reverting to the homogeneous equilibrium flow assumption (SLURP_HEM) by assuming no phase slip and accounting for fluid/wall heat transfer (SLURP_HEM_HT).

To study the impact of these extensions to SLURP a number of propane outflow scenarios were modelled and the results compared against PROFES predictions. Heat transfer through the pipe wall was not accounted for in the PROFES predictions. Table 2.2 shows the failure scenarios examined.

Table 2.2: Failure scenarios used in the comparison of predicted outflow of propane at 15 °C from a pipeline using SLURP and PROFES (Cumber, 2007).

Case	Initial pressure (barg)	Pipe diameter (mm)
P1	45	250
P2	70	250
P3	20	250

Figure 2.13 shows the comparison of the variation of mass flow rate with time for case P1. As it may be observed, the SLURP models predict a higher flow rate than that given by PROFES, with SLURP_FAUSKE giving the closest agreement. It is also observed that the inclusion of heat transfer effects (SLURP_HEM_HT) has little impact on the predicted outflow. Cumber (2007) stated that this was consistent with the findings of Webber et al. (1999) where including wall heat transfer tended to improve predictions of temperature and pressure profiles but not the discharge rate as compared to measured data.

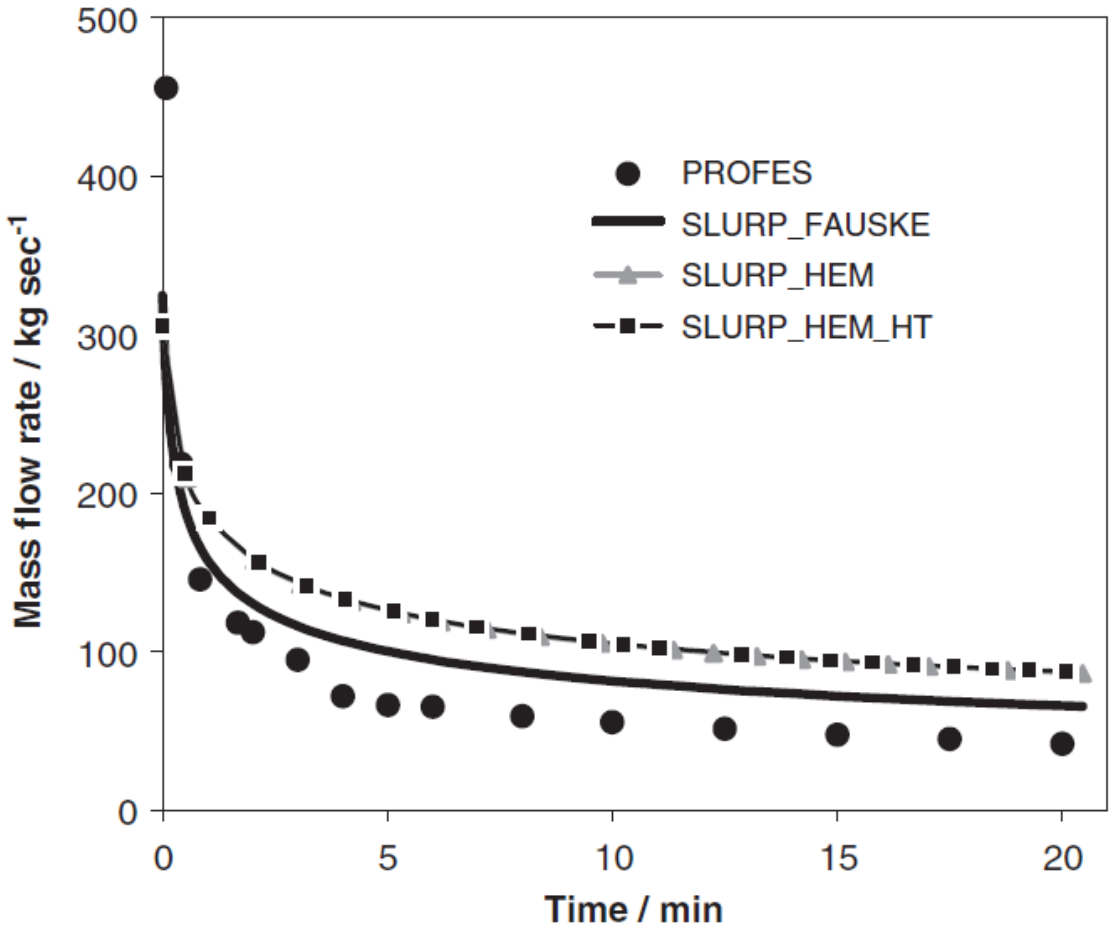

Figure 2.13: Comparison of predicted release rate for a propane pipeline at an initial pressure of 46 bara and 15 °C (Cumber, 2007).

While Cleaver et al. (2003) validated SLURP against various Isle of Grain tests when originally presenting their model, Cumber (2007) compared the upgraded SLURP against PROFES simulations only.

2.4.6 Machnet (Terenzi, 2005)

Terenzi (2005) presented Machnet (Machnet_Real) developed to investigate the impact of real gas behaviour on the interaction between pipeline decompression and ductile fracture propagation. Homogeneous equilibrium is assumed between gas and liquid. Thermodynamic properties, such as the void fraction, are determined by linear

interpolation using a look up table with the density and specific internal energy as independent variables. Fluid/wall heat transfer is calculated by solving the Fourier equation in cylindrical geometry between the external environment and the fluid. The Colebrook-White correlation (Keenan and Neumann, 1946) is used to account for frictional effects along the pipeline. The resulting governing system of equations is resolved using Roe's method, a Finite Volume conservative scheme of the Godunov-type (Godunov et al., 1979).

Terenzi (2005) also developed a model for the decompression of a pipeline transporting an ideal gas (Machnet_Ideal) by assuming zero heat transfer and frictionless flow to derive a solution for the pressure at the exit plane and decompression wave speed.

Machnet_ideal and Machnet_real predictions were compared with the results of tests conducted at the Foothills Pipelines Northern Alberta Burst Test Facility (NABT) (Picard and Bishnoi, 1988). Terenzi (2005) presented a comparison of experimental and simulated data for NABT test 5 only; this test involved the release of natural gas (ca. 85 % methane) at 7.544 MPa and 18.5 °C from a pipeline with ID 1422 mm and ca. 60 m long.

Figure 2.14 presents data for the variation of the ratio of pressure to initial pressure and void fraction, both as a function of expansion wave velocity. Machnet_Ideal and Machnet_Real predictions (using the PR and SRK EoS) are compared with experimental data. As may be observed, Machnet_Real predictions using both EoS show reasonable agreement with the experimental data. Machnet_Ideal over-predicts the wave speed throughout the decompression process. Additionally, the fluid void fraction falls slightly from unity when the pressure ratio reaches ca. 0.55. At this point Machnet_Real predictions using the PR and SRK EoS begin to diverge from the experimental data.

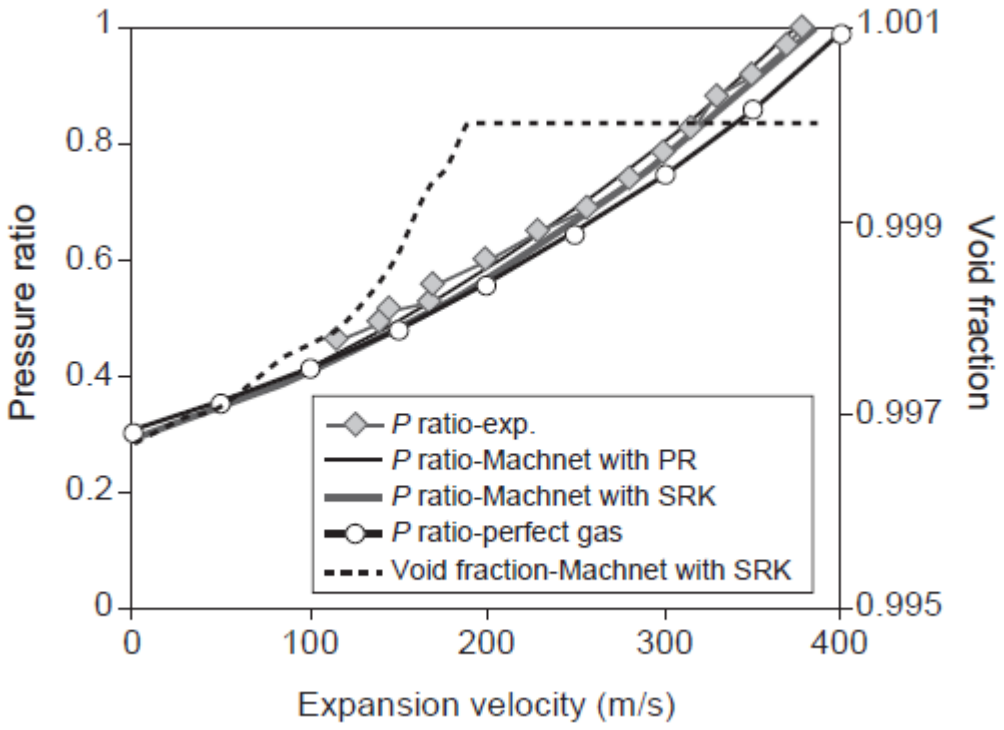

Figure 2.14: Measured and calculated decompression wave speed results of NABT Test 5 (Picard and Bishnoi, 1988).

No further experimental comparisons were conducted by Terenzi (2005) and figure 2.14 was the only quantitative validation data presented. Therefore the ability of Machnet_Ideal to model outflow and de-pressurisation of pipelines cannot be verified.

2.4.7 Two-phase fluid model of Brown et al. (2014)

CCS pipelines are expected to transport CO_2 in the liquid phase in order to maximise mass flow rate. Consequently two phase flow is to be expected as a pipeline is vented or blown down, with the potential for the inventory to stratify. In fact recent work conducted as part of the CO2PipeHaz project ("CO2PipeHaz," 2012) has demonstrated that stratification occurs only when the pipeline is punctured. High speed video recording of fluid flow through a transparent section of a pipe undergoing blowdown demonstrates that the greater turbulence within the fluid during FBR ensures the complete entrainment of the evolving vapour within the liquid (see figure 2.15).

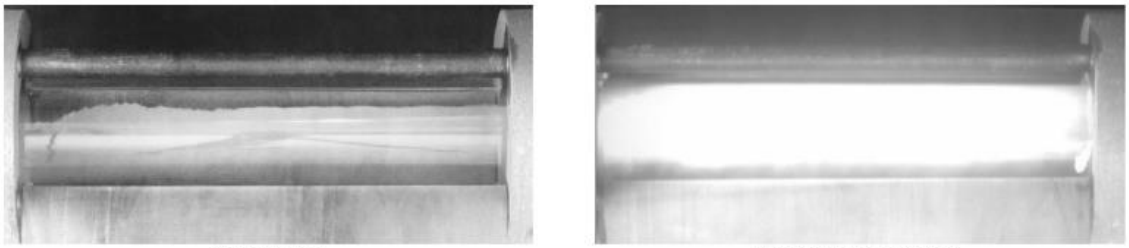

Figure 2.15: Fluid flow patterns captured following puncture (a) and FBR (b) of a pipeline containing dense phase CO_2 (Brown et al., 2013).

To model outflow following failure of a high pressure CO_2 pipeline Brown et al. (2014) developed a two-fluid transient flow model. The model was based on the single pressure two-fluid model described by, for example, Stewart and Wendroff (1984). Phase interaction terms were modelled using simple constitutive relations which assumed a constant thermal relaxation time and interphase drag coefficient. Pipe wall temperature is calculated by solving the transient heat conduction equation in two dimensions using a Finite Difference method, the heat transfer rate between it and each fluid phase is calculated using the Dittus-Boelter (1985) correlation. It was assumed that only forced convective heat transfer occurs within the pipe and the pipe was perfectly insulated.

The model was validated against experimental data gathered from the FBR of a 256 m long, 233 mm ID pipeline filled with CO_2 containing ca. 0.2 % v/v of air to a pressure of 36 bara and 274 K. The pipeline was insulated with 50 mm thick glass wool along its entire length. The validation was used to study the impact of the model's constitutive parameters on simulated temperature and pressure profiles.

Figure 2.16 presents the experimental and simulated fluid pressures from 6 m upstream of the rupture plane. Simulations were conducted using a variety of thermal relaxation times (τ). Predicted data generated using a homogeneous equilibrium model is also included for reference (Brown et al., 2013). As may be observed the two-fluid model is able to predict trends in the experimental data. However, no single relaxation time was able to predict fluid pressure over the whole time period presented.

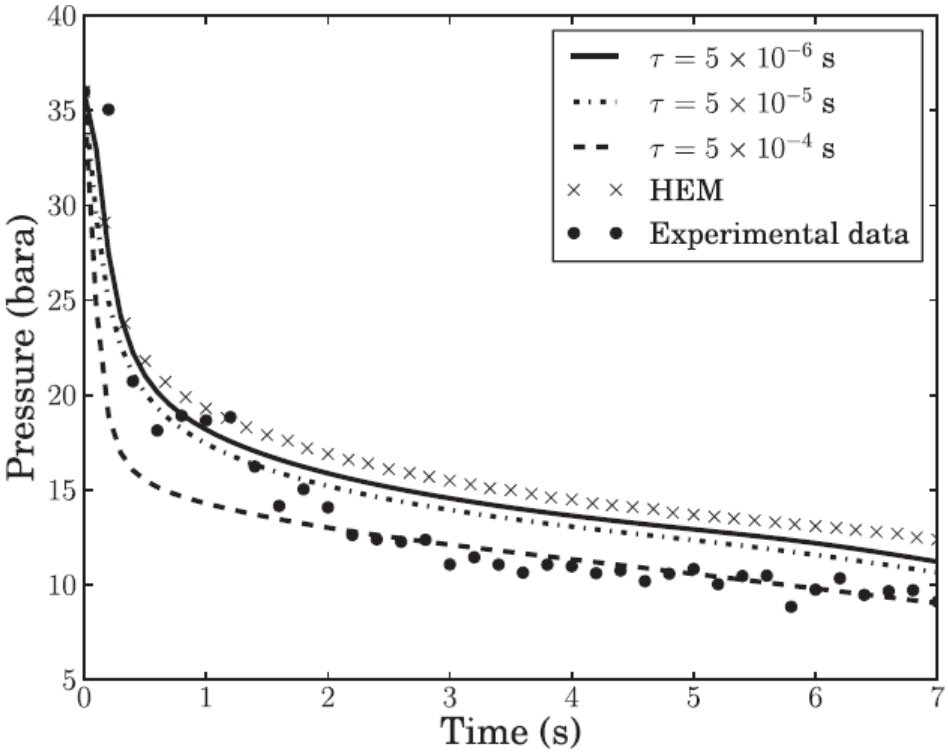

Figure 2.16: Variation of experimental and predicted fluid pressure using various thermal relaxation times (τ) 6 m upstream of the rupture plane (Brown et al., 2014).

Figure 2.17 presents a comparison of the experimental and predicted liquid and vapour temperatures from 6 m upstream of the rupture plane. Simulations were conducted using a variety of thermal relaxation times (τ). As for the fluid pressure predictions, with an appropriate relaxation time the temperature of both fluid phases may be predicted. However, when compared with figure 2.16 it may be observed that while a relaxation time of $5x10^{-4}$ s produces the best pressure predictions following passage of the decompression wave, it consistently produces the worst temperature predictions in both phases.

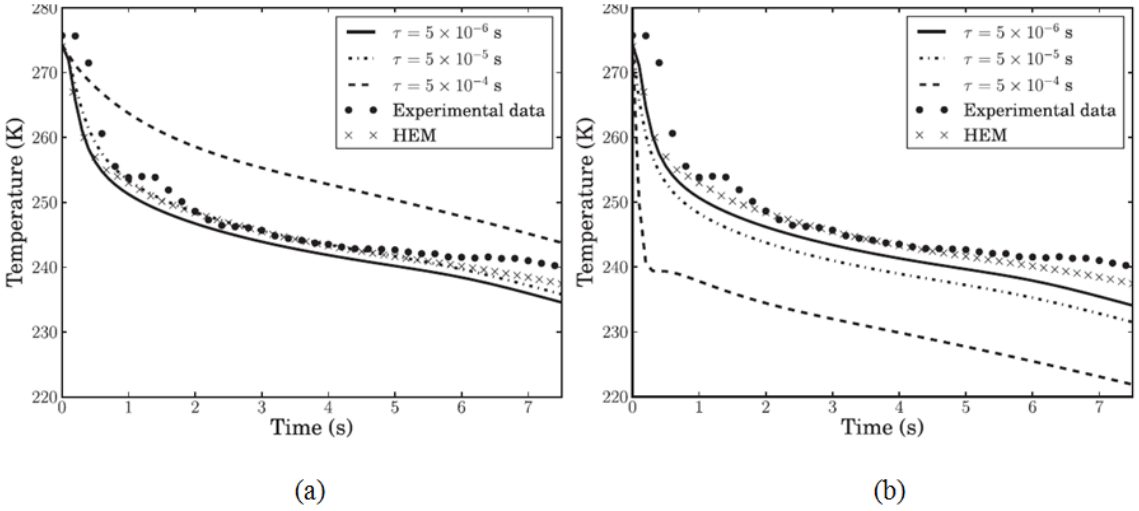

Figure 2.17: Variation of experimental and predicted liquid (a) and vapour (b) temperatures using various thermal relaxation times (τ) 6 m upstream of the rupture plane (Brown et al., 2014).

A comparison of the predicted and experimental wall temperatures was not presented.

2.4.8 CFD-DECOM (Xu et al., 2014)

The model CFD-DECOM was developed to model both fast depressurisation as well as slow blowdown of pipelines. The model is based in the conservation equations for mass, momentum and energy, which are solved using a finite volume approach based on the arbitrary Lagrangian-Eulerian method (ALE) (Xu et al., 2014). Homogeneous equilibrium in the inventory is assumed. The Peng-Robinson EoS (1976) was employed to calculate thermodynamic properties and phase equilibrium data for the fluid. Pipe wall heat conduction is calculated in two dimensions using a method "similar to Fairuzov's (2000) approach" (Xu et al., 2014). The source term for heat flux in the energy equation is calculated from Newton's cooling law. Two-dimensional heat conduction in the pipe wall was calculated separately.

CFD-DECOM was successfully validated against pipeline decompression data reported by Botros et al. (2007) and the Isle of Grain tests P40, 42, 61 and 65. Selected validation results against the former are reproduced below.

The pipeline modelled was 172 m long with an ID of 49 mm, the wall thickness was 5 mm and the roughness 0.05 mm. As the real pipe was insulated it was modelled assuming no heat transfer between the pipe wall and ambient. The inventory consisted of a rich gas mixture (ca. 69 % CH_4, 21 % C_2H_6, 9 % C_3H_8) at an initial temperature and pressure of 268.2 K and 9.95 MPa respectively.

Figures 2.18 and 2.19 present the experimental pressure and temperature data from the vicinity of the rupture plane respectively, together with the corresponding CFD-DECOM data. As may be observed, the predicted time at which the decompression wave arrives at the transducers agrees well with the experimental pressure data, fractionally poorer agreement is seen in the temperature comparison at transducer T14. Referring to figure 2.18, from 0.1 s differences of up to ca. 1 MPa may be observed between the experimental and predicted fluid pressures at both P8 and P10.

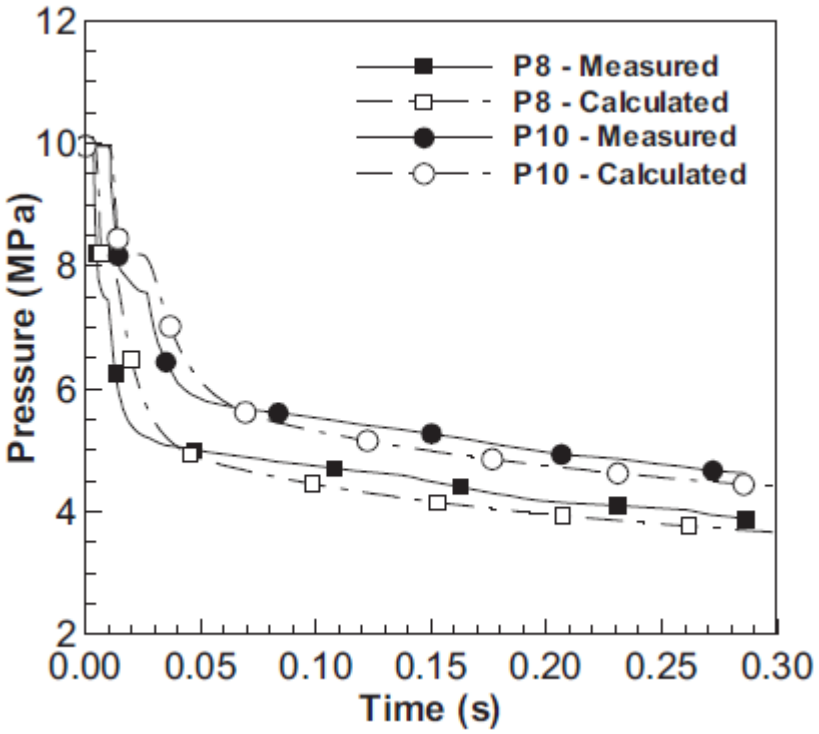

Figure 2.18: Experimental and CFD-DECOM predicted fluid pressures near the rupture plane (transducers P8 and P10 are 1.64 m and 4.04 m from the rupture plane respectively) (Xu et al., 2014).

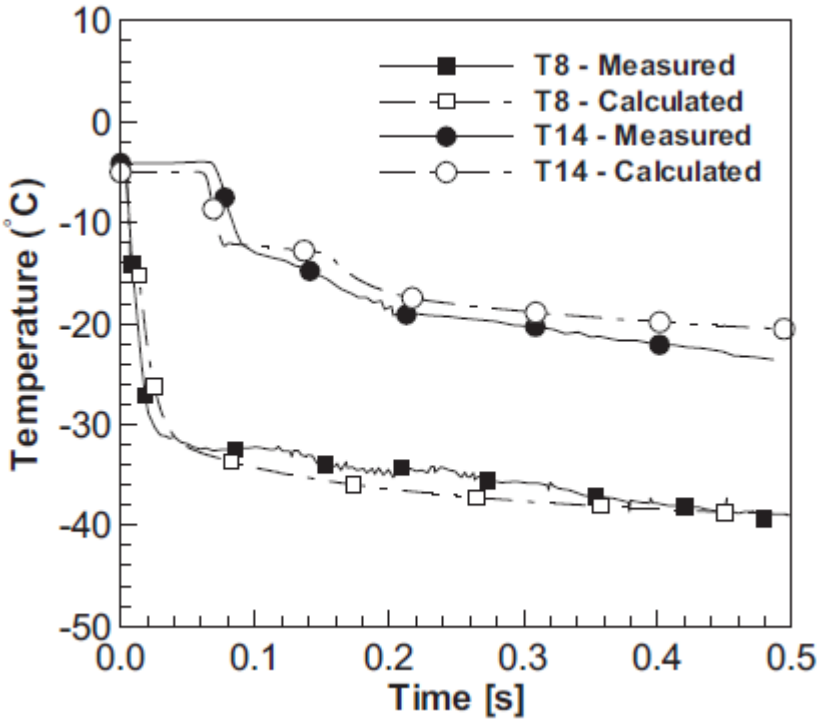

Figure 2.19: Experimental and CFD-DECOM predicted fluid temperatures near the rupture plane (transducers T8 and T14 are 1.64 m and 23.05 m from the rupture plane respectively) (Xu et al., 2014).

The authors concluded that for all five experimental comparisons performed to validate CFD-DECOM, the predicted pressure, temperature and inventory data vs. time were all in reasonably good agreement with the experimental data.

2.4.9 Conclusions of reviewed outflow models

In this section various pipeline outflow models have been reviewed with reference to the model requirements for simulating of CO_2 pipeline venting. These were the necessity to accurately model transient fluid properties and wall temperatures, and account for fluid/pipe wall/ambient heat transfer. It is notable that for each model no wall temperature calculations were published, the implications of which will be discussed in section 2.5.

For the models SLURP_HEM_HT and Machnet_Real insufficient data was reported by the researchers to properly assess their suitability for modelling venting. GasDECOM was not considered as no data was found concerning the model's formulation. The model of Burlutskiy (2013, 2014) neglected heat transfer with the wall. The models of Brown et al. (2014) and Xu et al. (2014) were reported after the work described in this thesis was begun.

Of the models formulated around the conservation equations for mass, momentum and energy, OLGA tended to under-predict pressure at the rupture plane, occasionally by significant margins. Further, OLGA predictions for pipeline discharge and rapid transients were not consistently accurate. OUTFLOW and FaNM predictions for pipeline inventory and fluid properties were shown to be accurate. OUTFLOW was shown to predict rapid transients in the fluid with acceptable accuracy; no equivalent data was reported for FaNM. A further advantage of OUTFLOW is the reported ability to model pipeline junctions.

The model OUTFLOW is selected for use in this work based on the above review. Based on the conservation equations, it requires an EoS to calculate the thermodynamic and phase properties of the inventory. In section 2.6 a brief review of the literature is presented regarding work to identify an EoS appropriate for modelling CCS processes.

2.5 Discussion of pipeline wall temperature modelling

In reviewing the literature concerning pipeline outflow models it is notable that none presented data concerning transient pipe wall temperatures during outflow. The conjugation of the fluid and associated pipe wall heat conduction models was also not described in detail. When reviewing the literature no suitable experimental data to validate wall temperature predictions was discovered, indicating the past importance of this information when modelling outflow from hydrocarbon pipelines. However as discussed in section 2.3, significant cooling of a CO_2 pipeline wall can occur during venting/blowdown. Thus at the very least the validation of a pipe wall temperature

model is necessary before it may be reliably used to investigate the hazards associated with CO_2 pipeline blowdown.

As part of the COOLTRANS research project National Grid UK recorded pipe wall temperature and fluid data from large scale CO_2 blowdown experiments. This data was used to validate the pipe wall temperature predictions from OUTFLOW, a description of the experiments and comparison of predicted and experimental results is presented in sections 5.2 and 5.4 respectively. As may be observed, cooling in the pipe wall is significantly over-predicted by OUTFLOW. The development of OUTFLOW to model CO_2 pipeline venting/ blowdown therefore requires the implementation of an accurate heat conduction model to calculate transient pipe wall temperatures. This model must be compatible with the Method of Characteristics (MOC).

Zhang (2014) developed and integrated a brittle fracture model with OUTFLOW. This model replaced the transient energy balance model of Atti (2006) with the heat conduction equation, written in three dimensions and solved using the Finite Volume method (FVM). Wall stresses in the vicinity of a rupture were calculated using the Finite Element analysis tool ABAQUS (SIMULIA, 2011). The wall temperature predictions of this model were not validated against experimental data.

Pipe wall heat conduction also plays a significant role in the steady state operation of pipelines. Zhu et al. (2013) investigated the factors affecting the thermal performance of two pipelines carrying crude and refined oil which were buried in the same trench. Incompressible fluid flow was modelled using the Navier-Stokes equations. Heat conduction in two dimensions was calculated for a cross section of the two pipe walls and surrounding soil at various distances along the length of the pipes. The cross-sectional area was discretised using a progressive triangular array generated with GAMBIT 2.3. All computations were carried out by with the FVM commercial CFD code FLUENT 13.0 (Ansys, n.d.).

The model was successfully validated using steady state fluid temperature data recorded from a pipeline carrying crude oil, located 1.2 m from a refined oil pipeline buried in the

same trench. A comparison of the simulated and observed steady state crude oil temperatures are shown in figure 2.20 along a 300 km length of pipeline.

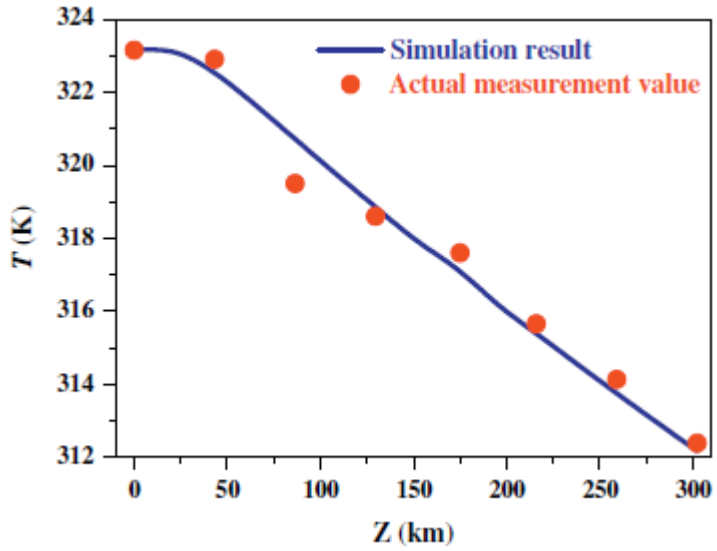

Figure 2.20: Comparison of simulated and actual steady state crude oil temperatures along a 300 km length of pipeline (Zhu et al., 2013).

Neither predicted nor recorded pipe wall temperature data was reported by Zhu et al. (2013).

Yapıcı and Albayrak (2004) investigated heat conduction and thermal stresses in a pipe contained flowing fluid (fully developed laminar regime) and subject to uniform and non-uniform external heat flux. Fluid flow was modelled using equations for continuity, momentum and energy; heat conduction in the pipe wall was calculated in two dimensions (axial and radial). The governing equations were solved by FDM using FLUENT 4.5 (Ansys, n.d.). Simulation results were not compared against experimental data.

Al-Zaharnah et al. (2000) investigated thermal stresses in a pipe system in which a pipe containing flowing fluid in a fully developed laminar regime was subjected to a uniform external heat flux on the outer pipe wall. Fluid flow was modelled using equations to describe continuity, momentum and energy. The pipe wall conduction equation was

written in two dimensions (axial and radial). The governing fluid equations and conduction equation were solved using an FVM approach. Simulation results were not compared with experimental data.

As discussed above, the Finite Volume and Finite Difference methods (FVM and FDM respectively) are used extensively in modelling pipeline systems. FDM involves the discretisation of a problem such that dependent variables exist only at discrete points in the domain, thus a problem involving calculus is transformed into an algebraic problem. FVM is a variation on the FDM, where the equation(s) governing the problem are applied in integral form to control volumes within the domain (Tannehill et al., 1997). This allows the calculation of properties at the centre of the control volume and on its boundaries.

The FDM requires the domain to be discretised in a regular fashion throughout, although for the FVM nodes need not be at the centre of the control volume. FDM type methods become difficult to use when the solution domain possess irregular geometry, such as might be found on the valve and pipe infrastructure connecting a vent pipe to a main pipe section.

The Finite Element method (FEM) has also found extensive applications in modelling heat conduction in domains with complex geometry (Lewis et al., 2004). The method discretises the domain into a mesh of interconnected elements. The partial differential equations describing the domain are reduced to a system of linear or non-linear simultaneous equations, thus a continuous problem is reduced to one with a finite number of unknowns at specified points, referred to as nodes. There is no requirement for element shapes to be regular or nodes to conform to a regular grid pattern, thus complex surface geometries on the domain boundary may be easily represented.

Given the flexibility of the FEM in discretising the solution domain it is selected for integration with OUTFLOW to model pipe wall temperatures during venting of CO_2 pipelines. The greater flexibility of this model compared to the FDM allows significant

potential for further development of OUTFLOW to model heat conduction in complex pipeline infrastructure, such as valves.

2.6 Equations of State for modelling CO_2 pipeline outflow

Equations of state (EoS) are algebraic expressions that relate the temperature, pressure and molar volume of real fluids (Sinnott, 1999). They are often developed and optimised in order to model specific systems; such as solids formation during CO_2 pipeline blowdown (Martynov et al., 2014, 2013), or CO_2 pipelines during normal operation (Demetriades et al., 2013). Selection of the most appropriate EoS for CFD work can improve the accuracy of any data generated (Li and Yan, 2009a).

2.6.1 Criteria for selecting an Equation of State

An EoS for modelling blowdown of CO_2 pipelines should not be so complex as to present numerical or analytical difficulties in application. It should accurately represent the fluid properties over the range of conditions expected during blowdown (ca. 150 to 1 bara and ambient temperatures to at least 216 K), and especially the vapour-liquid equilibrium (VLE) properties. Accuracy should be maintained when any relevant impurities are added to the fluid. The suitability of a proposed EoS should be assessed by comparison of calculated properties with real data.

The available CO_2 experimental data useful for validating EoS predictions has been recorded over the last 111 years (see Li et al., 2011). Inevitably some of this work has been carried out with equipment and to standards that are now obsolete, use of some experimental data must therefore be carefully considered. Figure 2.21 represents graphically the areas of the P/T phase diagram for which VLE experimental data exists, and indicates which CO_2 mixture the data is associated with. Figure 2.22 presents the same information for experimentally measured mixture volume (Li et al., 2011).

Li et al. (2011) identified various knowledge gaps in the published experimental data. Referring to figure 2.21, the available data for CO_2/H_2S, CO_2/CO and CO_2/SO_2 does not consistently extend to lower pressures and temperatures surrounding the saturation line of pure CO_2. Additionally, little VLE data is available for multi-component CO_2 mixtures such as $CO_2/CH_4/N_2$, $CO_2/N_2/O_2$, $CO_2/CH_4/H_2S$ and $CO_2/CO/H_2$. For the volume property, Li et al. (2011) found no data for CO_2/O_2 and CO_2/CO. Referring to figure 2.22, it may be observed that data for mixtures containing H_2, Ar and H_2S is limited.

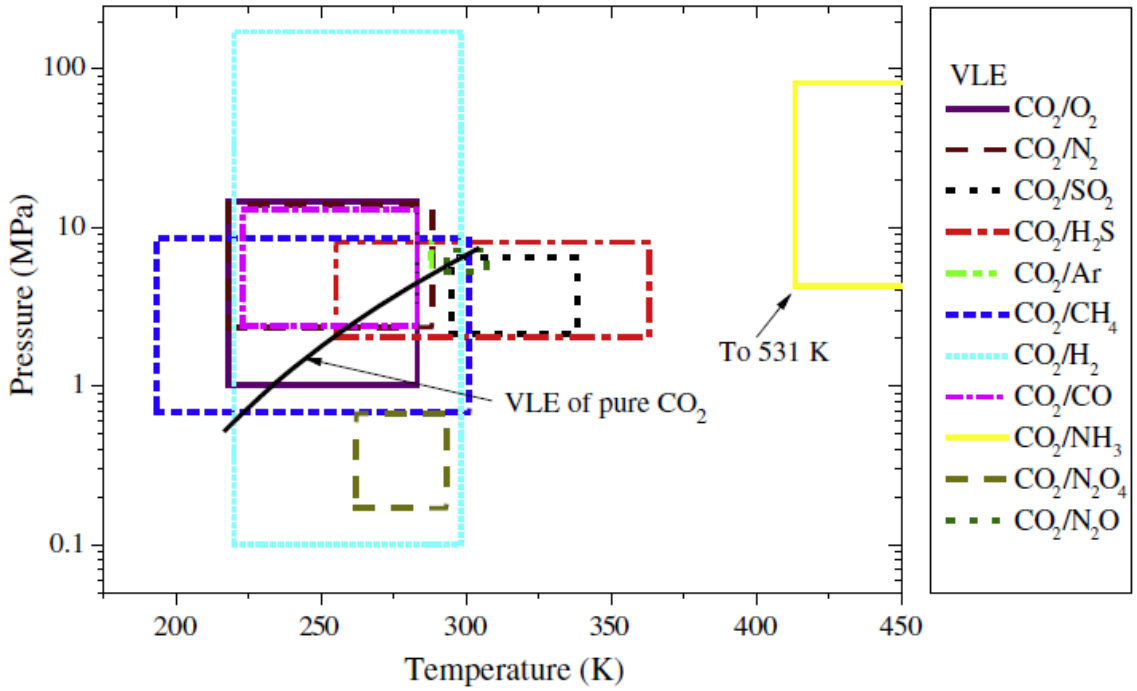

Figure 2.21: T/P ranges for which experimental VLE data for various CO_2 mixtures relevant to CCS is available (Li et al., 2011).

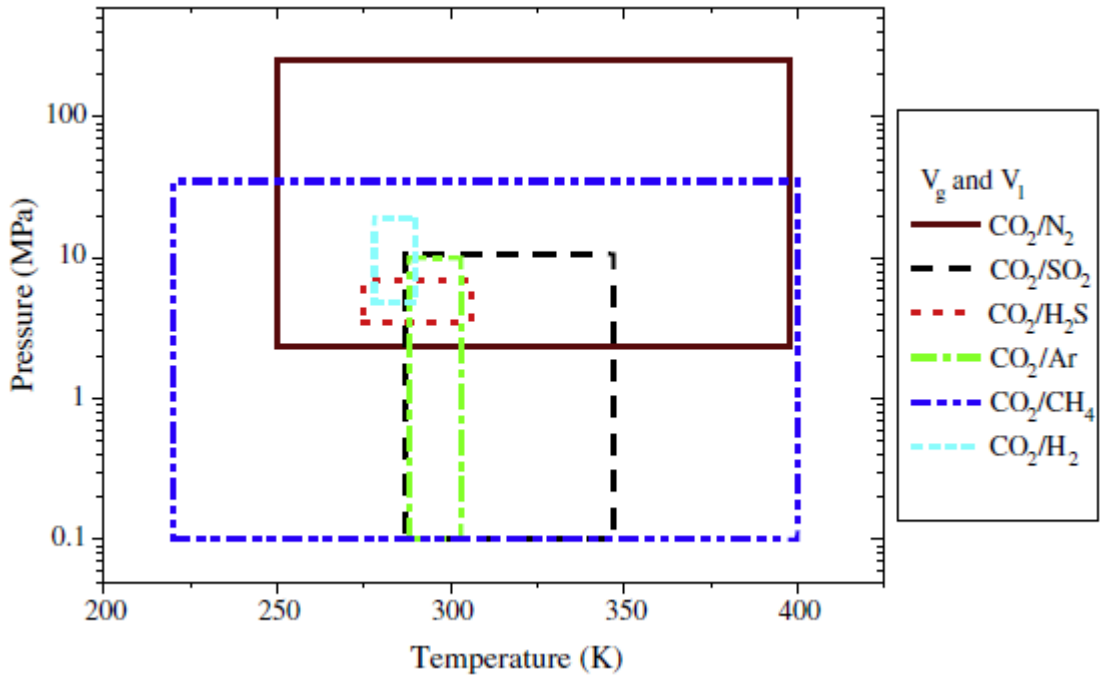

Figure 2.22: T/P ranges for which experimental mixture volume data for various CO_2 mixtures relevant to CCS is available (Li et al., 2011).

2.6.2 Li and Yan (2009a, 2009b)

Two recent studies investigated the applicability of eight EoS for calculating the VLE and volume data of CO_2 mixtures with impurities relevant to CCS (Li and Yan, 2009a, 2009b). The EoS investigated are shown in table 2.3 together with the mixing rules used with each.

In the equations presented in table 2.3; P, R, T and V represent the pressure, universal gas constant, temperature and molar volume respectively. The a, b and c terms are parameters of the EoS. The parameters i and j are the component indices, a_i, a_j, b_i and c_i are parameters in the mixing rule equations, x_i and x_j are the mole fractions in the liquid phase for components i and j, k_{ij} is the binary interaction parameter. For the PT EoS the equation set 2.3 was used in (Li & Yan, 2009a) and set 2.4 in (Li & Yan, 2009b).

Inappropriate k_{ij} values can result in poor EoS calculation accuracy, see for example Ikeda and Schaefer (2011). The optimum value of k_{ij} for a mixture can vary depending on the property being calculated. Li and Yan (2009a, 2009b) determined optimum values of k_{ij} for calculating VLE, gas and liquid volumes for each mixture investigated using the available experimental data. These values of k_{ij} were used for all calculations.

Table 2.3: The EoS and associated mixing rules use in the studies of Li and Yan (2009a, 2009b).

Equation of State	Formulation	Mixing Rule set	Set number
Peng-Robinson (PR) (Peng and Robinson, 1976)	$P = \frac{RT}{V-b} - \frac{a(T)}{V(V+b)+b(V-b)}$	$a = \sum_i \sum_j x_i x_j a_i^{\frac{1}{2}} a_j^{\frac{1}{2}} (1-k_{ij})$; $b = \sum_i x_i b_i$; $k_{ij} = k_{ji}$	**2.1**
modified PR (MPR1) (Li and Yan, 2009b)	$P = \frac{RT}{V-b} - \frac{a}{(V+c)(V+b+2c)+(b+c)(V-b)}$	$a = \sum_i \sum_j x_i x_j a_i^{\frac{1}{2}} a_j^{\frac{1}{2}} (1-k_{ij})$; $b = \sum_i x_i b_i$; $c = \sum_i x_i c_i$; $k_{ij} = k_{ji}$	**2.2**
Patel-Teja (PT) (Patel and Teja, 1982)	$P = \frac{RT}{V-b} - \frac{a(T)}{V(V+b)+c(V-b)}$	$a = \sum_i \sum_j x_i x_j a_i^{\frac{1}{2}} a_j^{\frac{1}{2}} (1-k_{ij})$; $b = \sum_i x_i b_i$; $c = \sum_i x_i c_i$; $k_{ij} = k_{ji}$	**2.3**
		$a = \sum_i \sum_j x_i x_j a_i^{\frac{1}{2}} a_j^{\frac{1}{2}} k_{ij}$; $b = \sum_i x_i b_i$; $c = \sum_i x_i c_i$; $k_{ij} = k_{ji}$	**2.4**
Redlich-Kwong (RK) (Redlich and Kwong, 1949)	$P = \frac{RT}{V-b} - \frac{a/T^{0.5}}{V(V+b)}$	$a = \sum_i \sum_j x_i x_j a_i^{\frac{1}{2}} a_j^{\frac{1}{2}} (1-k_{ij})$; $b = \sum_i x_i b_i$; $k_{ij} = k_{ji}$	**2.5**
Soave-Redlich-Kwong (SRK) (Soave, 1972)	$P = \frac{RT}{V-b} - \frac{a(T)}{V(V+b)}$	$a = \sum_i \sum_j x_i x_j a_i^{\frac{1}{2}} a_j^{\frac{1}{2}} (1-k_{ij})$; $b = \sum_i x_i b_i$; $k_{ij} = k_{ji}$	**2.6**

Table 2.3 (cont.):

Equation of State	Formulation	Mixing Rule set	Set number
modified SRK (MSRK) (Peneloux and Rauzy, 1982)	$P = \frac{RT}{V-b} - \frac{a}{(V+c)(V+b+2c)}$	$a = \sum_i \sum_j x_i x_j a_i^{\frac{1}{2}} a_j^{\frac{1}{2}} (1-k_{ij})$; $b = \sum_i x_i b_i$; $c = \sum_i x_i c_i$; $k_{ij} = k_{ji}$	**2.7**
improved SRK (ISRK) (Ji and Lempe, 1997)	$P = \frac{RT}{V+c-b} - \frac{a(T)}{(V+c)(V+b+c)}$	$a = \sum_i \sum_j x_i x_j a_i^{\frac{1}{2}} a_j^{\frac{1}{2}} (1-k_{ij})$; $b = \sum_i \sum_j x_i x_j \left(\frac{b_{ii}+b_{jj}}{2}\right)(1-l_{ij})$; $c = \sum_i x_i c_i$; $k_{ij} = k_{ji}$; $l_{ij} = l_{ji}$	**2.8**
3P1T (Yu et al., 1987)	$P = \frac{RT}{V-b} - \frac{a(T)}{V(V+c)+b(3V+c)}$	$a = \sum_i \sum_j x_i x_j a_i^{\frac{1}{2}} a_j^{\frac{1}{2}} (1-k_{ij})$; $b = \sum_i x_i b_i$; $c = \sum_i x_i c_i$; $k_{ij} = k_{ji}$	**2.9**

Li and Yan (2009b) used EoS equation sets 2.1, 2.2 and 2.4 to 2.8 to calculate the volumes of CO_2 mixtures with varying concentrations of CH_4, H_2S, SO_2, Ar and N_2. Calculations for each mixture were also made over a range of temperatures and pressures corresponding to the available experimental data. Calculated data was compared to experimental data in terms of Absolute Average Deviation (AAD). A summary of which EoS predicted vapour and liquid volumes with the lowest and highest overall AAD for each mixture is given in table 2.4.

Table 2.4: Summary of the EoS with the lowest and highest AAD for calculating liquid volume (V_l) and gas volume (V_g) properties of each mixture (Li and Yan, 2009b).

Mixture	EoS with lowest AAD		EoS with highest AAD	
	V_l	V_g	V_l	V_g
CO_2/CH_4	PT	PT	ISRK	ISRK
CO_2/H_2S	PT	MPR	ISRK	RK
CO_2/N_2	PR	PT	ISRK	ISRK
CO_2/Ar	PT	PR	MSRK	MPR
CO_2/SO_2	PT	ISRK	ISRK	RK

Li and Yan (2009b) investigated the effect of using different values of k_{ij} on the AAD of the volume calculations for the mixtures discussed. It was observed that the AAD could be very high, especially if the calculation involved a saturated gas/liquid. In the absence of the large amount of data required to calculate k_{ij} a value of 0 (zero) can be used (or 1 for the PT EoS), this would have the effect of ignoring attractive forces between particles. It was reported that in this scenario the PR and PT EoS were generally superior to the other EoS investigated for calculating vapour and liquid phase densities.

It was concluded that the PR and PT EoS (equation sets 2.1 and 2.4 respectively) were generally superior to the others considered for calculating the volume properties for each mixture (Li and Yan, 2009b).

Li and Yan (2009a) also evaluated the ability of various cubic EoS to calculate the VLE of pure CO_2 and CO_2 with various impurities relevant to CCS. The mixtures considered were CO_2 with CH_4, H_2S, SO_2, Ar, N_2 and O_2. The EoS investigated were the PR, PT, RK, SRK and 3P1T (equation sets 2.1, 2.3, 2.5, 2.6 and 2.9 respectively).

Calculated and experimental data was compared and the results summarised in terms of AAD. For pure CO_2 all the EoS, with the exception of the RK, were able to calculate the saturation pressure with an AAD less than 3 %, the SRK EoS was the best with an AAD of 1.05 %. Table 2.5 summarises the AAD of the EoS for the calculation of saturation pressure (P_s) and mole fraction of CO_2 in the vapour phase ($y_{s,CO2}$) for each mixture (Li and Yan, 2009a). From the data presented it was concluded that the PR, PT and SRK are superior to the RK and 3P1T for the calculation of VLE data for the CO_2 mixtures investigated.

Table 2.5: AAD of the EoS when calculating the VLE properties of binary CO_2 mixtures (saturation pressure, P_s, mole fraction of CO_2 in the vapour phase, $y_{s,CO2}$) (Li and Yan, 2009a). For some mixtures no data was reported, this is denoted by –.

		PR	PT	RK	SRK	3P1T
CO_2/CH_4	P_s	1.68	2.00	5.73	1.87	20.74
	$y_{s,CO2}$	2.63	3.14	16.71	2.79	26.95
CO_2/O_2	P_s	4.17	3.62	4.08	4.02	3.50
	$y_{s,CO2}$	2.89	2.74	14.90	3.44	14.13
CO_2/H_2S	P_s	1.22	1.48	3.41	1.32	3.32
	$y_{s,CO2}$	4.54	4.28	9.28	4.49	4.79
CO_2/N_2	P_s	2.08	1.62	4.08	1.79	3.10
	$y_{s,CO2}$	2.23	2.17	5.25	2.83	13.15
CO_2/Ar	P_s	2.88	2.85	5.43	3.36	9.79
	$y_{s,CO2}$	–	–	–	–	–
CO_2/SO_2	P_s	4.64	4.67	10.62	4.28	4.17
	$y_{s,CO2}$	–	–	–	–	–

The authors further investigated the effects of changing the k_{ij} on the calculation accuracy of the EoSs. It was concluded that the calibrated k_{ij} values did not necessarily improve calculation accuracy for saturated pressure compared with literature values, however the accuracy of calculated saturated vapour compositions were improved (Li and Yan, 2009a).

2.6.3 Non cubic Equations of State

Non cubic EoS have also been considered for modelling of CCS processes. A review of the available research is given in Li et al. (2011) and a brief summary is given here.

Li et al. (2011) discussed the investigation of various virial and extended virial equations for modelling the thermodynamic properties of CO_2 with impurities. From the evidence reviewed it was observed that their performance in modelling CO_2 fluids was not significantly greater than that seen for cubic EoS.

The Statistical Associating Fluid Theory (SAFT) EoS has been considered for modelling of CCS processes including transport and storage because it is capable of modelling the thermodynamic properties of several complex fluids. SAFT can also be used to reliably explore areas of a phase diagram some distance from areas with supporting experimental data (Li et al., 2011). Ji et al. (2005) have studied the interaction of CO_2/H_2O and $CO_2/H_2O/NaCl$ systems using a SAFT type EoS, concluding that the EoS was able to represent the density and equilibrium concentration data for both mixtures.

The GERG EoS (Kunz et al., 2007) has also been considered for modelling of CCS systems (Li et al., 2011). Its formulation is explicit in the reduced Helmholtz energy; this allows for the calculation of all thermodynamic properties from combinations of the Helmholtz derivatives but also makes its implementation into simulation tools complex. A limitation of the EoS is that it cannot be used with mixtures that contain sulphur. In one study (Li et al., 2007) the accuracy ascribed to the GERG was not obtained when

calculating volume or VLE data for CO_2 rich mixtures. In this study the AAD of the calculated liquid volume of CO_2 mixtures could reach as high as 18 %, a considerably higher AAD than that reported by the GERG manual

2.6.4 Summary

In this section a brief review of the literature investigating the suitability of various EoS for modelling CCS processes was presented. Among the cubic EoS considered, the SRK was identified as producing the most accurate predictions for the saturation pressure of pure CO_2 between ca. 300 to 220 K. When compared with experimental data, among the EoS considered the SRK, PR and PT were reported as generally superior for calculating the VLE properties and the PR and PT EoS for calculating volume properties of CO_2 mixtures.

The importance of a calibrated binary interaction parameter for accuracy of the EoS was identified. In the absence of calibration data the binary interaction parameter may be assigned a value of 0 (zero) or 1. When a value of "0" is used with the PR, or "1" with the PT, these EoS were identified as more likely to produce accurate data compared to the other EoS considered in table 2.3.

2.7 Conclusion

In this chapter a brief discussion of the pipeline transportation of CO_2 for CCS and the necessity and risks associated with venting/blowdown of such pipes was presented. The depressurisation rate, propagation of rapid transients, discharge rate and pipe wall temperature were identified as key parameters of the process that any outflow model must be capable of capturing to properly model the outflow of CO_2 from a pipeline. Various outflow models were reviewed and the model OUTFLOW was selected for use in this thesis based on its demonstrated accuracy in modelling the above phenomena.

None of the pipeline outflow models reviewed, including OUTFLOW, had had wall temperature predictions validated against experimental data. Comparison of wall temperature predictions from OUTFLOW against experimental data recently generated by National Grid UK revealed the inaccuracy of these predictions. Therefore a review of wall temperature models reported in the literature was presented and an FEM model of heat conduction selected for implementation in OUTFLOW. This model was selected based on its flexibility in modelling complex geometries and potential for development to model complex pipeline infrastructure such as valves.

Finally, a brief review of the reported work to identify an EoS for modelling pipeline transport of CO_2 was presented. The PR and PT EoS were identified from a selection of cubic EoS as most consistently accurate in calculating VLE and fluid volume properties of pure CO_2 and binary CO_2 mixtures.

In the following two chapters the formulation of the model OUTFLOW is presented.

Chapter 3: Background theory for the transient pipeline flow model OUTFLOW

3.1 Introduction

For the accurate prediction of fluid flow from a pressurised pipeline a simulation model must account for:

- rapid transients in a single and/or two phase flowing fluid;
- the thermo-physical behaviour of the fluid mixture;
- the interaction of the fluid with the pipe wall.

The Navier-Stokes conservation equations represent the most complete formulation that describes any fluid flow situation. These equations allow for the variation of fluid properties in three dimensions in space, as well as in time. However, as every term in the equations must be resolved when solving the full system of equations their use is computationally demanding. Depending on the type of flow, certain terms in the equations will have a negligible effect on the final solution and so may be safely ignored.

The final form of the Navier-Stokes equations, depending on the assumptions and simplifications made, may be linear, quasilinear or nonlinear, parabolic or hyperbolic in nature. Consequently, the method of their numerical resolution must be selected appropriately.

This chapter presents the governing model assumptions and the mathematical formulation of the model OUTFLOW, reviewed in section 2.4.4.

3.2 Model assumptions

The most important underlying assumptions in the formulation of OUTFLOW are:

- steady state flow exists prior to rupture;
- flow is predominantly one-dimensional, except in the vicinity of a puncture where it is assumed to be two-dimensional;
- for full bore rupture (FBR) the Homogeneous Equilibrium Model (HEM) is applied, this treats the constituent phases as if they are in thermal and mechanical equilibrium;
- each pipeline segment (in individual pipelines or networks) is rigidly clamped, of uniform cross sectional area and possess inelastic walls.

3.3 Formulation of the governing conservation equations

The governing equations for generalised, unsteady, one-dimensional fluid flow may be expressed in terms of combinations of primitive parameters e.g. pressure, entropy, density, enthalpy. For OUTFLOW these equations are formulated in terms of pressure, entropy and fluid velocity.

The mass, momentum and energy conservation equations are thus given by Oke (2004):

$$\left(\frac{\partial P}{\partial t} + u\frac{\partial P}{\partial x}\right) - \varphi\left(\frac{\partial s}{\partial t} + u\frac{\partial s}{\partial x}\right) + \rho a^2 \frac{\partial u}{\partial x} = 0 \qquad \textbf{3.1}$$

$$\rho\left(\frac{\partial u}{\partial t} + u\frac{\partial u}{\partial x}\right) + \frac{\partial P}{\partial x} = \beta_x - \rho g \sin(\theta) \qquad \textbf{3.2}$$

$$\rho T\left(\frac{\partial s}{\partial t} + u\frac{\partial s}{\partial x}\right) = Q_h - u\beta_x \qquad \textbf{3.3}$$

Where *P*, *u and s* are the pressure, velocity and entropy as a function of time, *t*, and space, *x*. ρ, *a*, *T* and φ are the density, speed of sound, temperature and isochoric thermodynamic function (see section 3.5.3) of the homogeneous fluid. Q_h, θ and g are

the heat transferred through the pipe wall to the fluid, the angle of inclination of the pipeline relative to the horizontal and the acceleration due to gravity respectively. β_x is the frictional force term, given by:

$$\beta_x = -\frac{2\rho u|u|f_w}{D} \quad \textbf{3.4}$$

Where f_w is the Fanning friction factor and D is the pipeline diameter.

3.4 Cubic Equations of State (EoS)

The conservation equations contain more than three independent variables and must therefore be solved in conjunction with a fourth equation. For this an appropriate EoS is used, as well as for calculating fluid thermodynamic and phase equilibrium data.

In the model OUTFLOW three cubic EoS are available: the Soave-Redlich-Kwong (SRK) (Soave, 1972), the Peng-Robinson (PR) (Peng and Robinson, 1976) and the Modified Peng-Robinson (MPR) (Wu and Chen, 1997). These are given below in equations 3.5, 3.6 and 3.7 respectively.

$$P = \frac{RT}{V-b} - \frac{a(T)\alpha}{V(V+b)} \quad \textbf{3.5}$$

$$P = \frac{RT}{V-b} - \frac{a(T)\alpha}{V^2+2bV-b^2} \quad \textbf{3.6}$$

$$P = \frac{RT}{V-b} - \frac{a(T)\alpha}{V(V+b)+0.645b(V-b)} \quad \textbf{3.7}$$

Where:

$$a(T) = \Omega_a \frac{R^2 T_c^2}{P_c^2} \quad \textbf{3.8}$$

$$b(T) = \Omega_b \frac{RT_c}{P_c} \quad \textbf{3.9}$$

For the SRK Ω_a = 0.42747 and Ω_b = 0.08664. For the PR Ω_a = 0.45724 and Ω_b = 0.07780. For the MPR Ω_a = 0.44720 and Ω_b = 0.08070.

For mixtures:

$$a = \sum_i \sum_j y_i y_j a_{ij} \quad \textbf{3.10}$$

$$a_{ij} = \left(1 - K_{ij}\right)\sqrt{a_i a_j} \quad \textbf{3.11}$$

$$b = \sum_i y_i b_{V\,i} \quad \textbf{3.12}$$

Where P_c, T_c and V are the critical pressure (kN/m^2), critical temperature (K) and molar volume (m^3/kmol) respectively. In addition, R and α are the universal gas constant (kJ/(kmol.-K)) and alpha function, while K_{ij}, y_i and y_j are the binary interaction parameter and component mole fractions respectively.

Given the fluid molecular weight (M_W) (kg/kmol), the fluid density is given by:

$$\rho = \frac{M_W}{V} \quad \textbf{3.13}$$

The form of the generalised alpha function used in conjunction with the SRK, PR and MPR EoS is given by:

$$\alpha = \left(1 + \kappa(1 - T_r^{0.5})\right)^2 \quad \textbf{3.14}$$

Where for each EoS:

SRK: $$\kappa = 0.480 + 1.574\omega - 0.176\omega^2$$ **3.15**

PR: $$\kappa = 0.37464 + 1.54226\omega - 0.26992\omega^2$$ **3.16**

MPR: $$\kappa = 0.41510 + 1.52174\omega - 0.22170\omega^2$$ **3.17**

T_r is the reduced temperature and ω the accentric factor.

3.5 Hydrodynamic and thermodynamic relations for the HEM

Comparisons with experimental data have shown that the HEM assumption is applicable to the modelling of outflow from long (>100 m) pipelines undergoing full bore rupture (Chen, 1995; Mahgerefteh et al., 1999).

The main equations used in the calculation of two-phase fluid density, speed of sound, the heat transferred to the fluid (Q_h) and the pertinent hydrodynamic relations are presented in the following sections.

3.5.1 Two-phase fluid density

Based on the HEM assumption the pseudo-mixture density is given by:

$$\rho = \frac{\rho_g \rho_l}{\rho_g(1-\chi) + \rho_l \chi}$$ **3.18**

$$\rho_g = \frac{PM_g}{Z_g RT}$$ **3.19**

$$\rho_l = \frac{PM_l}{Z_l RT} \quad \textbf{3.20}$$

Where ρ_l and ρ_g are the liquid and gas densities respectively. χ is the fluid quality, defined as the mass of vapour per unit mass of the bulk fluid. Z is the fluid compressibility.

3.5.2 Single and two-phase speed of sound (Atti, 2006)

For single-phase real fluids, the speed of sound (a) in the fluid may be expressed analytically (Picard and Bishnoi, 1987):

$$a^2 = \frac{\gamma}{\kappa\rho} \quad \textbf{3.21}$$

Where γ is the ratio of specific heats and κ the isothermal coefficient of volumetric expansion, given by (Walas, 1985):

$$\gamma = \frac{C_P}{C_V} \quad \textbf{3.22}$$

$$\kappa = -\rho\left(\frac{\partial V}{\partial P}\right)_T \quad \textbf{3.23}$$

C_p and C_v are the specific heats at constant pressure and volume respectively. V is the specific volume of the fluid and the term $\left(\frac{\partial V}{\partial P}\right)_T$ in equation 3.23 can be obtained by differentiating the PR and MPR EoS (equations 3.6 and 3.7 respectively):

$$\left(\frac{\partial V}{\partial P}\right)_T = \left(\frac{-RT}{(V-b)^2} - \frac{2a(T)\alpha(V+b)}{(V^2+2bV-b^2)^2}\right)^{-1} \quad \textbf{3.24}$$

$$\left(\frac{\partial V}{\partial P}\right)_T = \left(\frac{-RT}{(V-b)^2} - \frac{a(T)\alpha(2V+1.645b)}{\left(V(V+b)+0.645b(V-b)\right)^2}\right)^{-1} \quad \textbf{3.25}$$

For two-phase flows equation 3.21 is evaluated numerically (Mahgerefteh et al., 2000):

$$a^2 = \left(\frac{\Delta P}{\rho(T,P) - \rho(T^*, P - \Delta P)}\right)_s \quad \textbf{3.26}$$

Where the subscript *s* denotes a constant entropy condition and ΔP denotes an incremental change in the fluid pressure (ΔP = 1x10^{-6} bar). T^* is the fluid temperature obtained from a pressure-entropy flash at the incremented pressure.

3.5.3 Evaluation of the thermodynamic function φ

The isochoric thermodynamic function φ for single-phase fluids (see equation 3.1) is given by (Picard and Bishnoi, 1987):

$$\varphi = \left(\frac{\partial P}{\partial s}\right)_\rho = \frac{\rho \xi T a^2}{C_P} \quad \textbf{3.27}$$

Where ξ is the isobaric coefficient of volumetric expansion and is equal to $\frac{1}{V}\left(\frac{\partial V}{\partial T}\right)_P$. In the case of two-phase flows φ is calculated numerically as shown below, given that:

$$\varphi = \left(\frac{\partial P}{\partial s}\right)_\rho \stackrel{\text{def}}{=} \left(\frac{\partial P}{\partial s}\right)_V \quad \textbf{3.28}$$

Using one of Maxwell's relations (Walas, 1985):

$$\left(\frac{\partial P}{\partial s}\right)_\rho = -\left(\frac{\partial T}{\partial V}\right)_S \quad \textbf{3.29}$$

Since $V = {}^1/_\rho$:

$$\frac{dV}{d\rho} = -\frac{1}{\rho^2} \quad \textbf{3.30}$$

Equation 3.29 becomes:

$$\left(\frac{\partial P}{\partial s}\right)_{\rho} = \rho^2 \left(\frac{\partial T}{\partial \rho}\right)_{S} \quad \textbf{3.31}$$

Therefore, from equation 3.28:

$$\varphi = \rho^2 \left(\frac{\partial T}{\partial \rho}\right)_{S} = \rho^2 \left(\frac{\Delta T}{\Delta \rho}\right)_{S} \quad \textbf{3.32}$$

Equation 3.32 can be solved using the same numerical algorithm as that used for the solution of equation 3.26.

3.5.4 Fanning Friction Factor (f_w)

The fanning friction factor, f_w, is required for calculating the frictional force in the momentum equation (equation 3.2). For transitional and turbulent flows in rough pipes f_w is determined from (N. H. Chen, 1979):

$$\frac{1}{\sqrt{f_w}} = 3.48 - 1.7372\, ln\left(\frac{\varepsilon}{r_{in}} - \frac{16.2446}{Re} ln\, A\right) \quad \textbf{3.33}$$

Where:

$$A = \frac{\left(\frac{\varepsilon}{r_{in}}\right)^{1.0198}}{6.0983} + \left(\frac{7.149}{Re}\right)^{0.8981} \quad \textbf{3.34}$$

ε, r_{in} and Re represent the pipe roughness, pipe inner radius and Reynolds number respectively.

For turbulent flow in smooth pipelines Rohsenow et al. (1998) recommend the correlation proposed by Techo (1965) for determining f_w:

$$\frac{1}{\sqrt{f_w}} = 1.7372 \ln \frac{Re}{1.964 \ln Re - 3.8215} \quad \textbf{3.35}$$

According to Rohsenow et al. (1998) the above correlation gives predictions within 2 % of experimental data.

The fanning friction factor for laminar fully developed flow is given by Rohsenow et al. (1998):

$$f_W = \frac{16}{Re} \quad \textbf{3.36}$$

3.5.5 Thermal conductivity and viscosity calculations

The vapour thermal conductivity and viscosity needed for determining the Nusselt, Reynolds and Prandtl numbers are calculated using the principle of corresponding states using methane as a reference fluid. The method is that described by Ely and Hanley (1981, 1983) for non-polar gases. It is claimed (Assael et al., 1996) that this method (Ely and Hanley, 1981) is one of the few schemes able to predict the viscosity and thermal conductivity for a wide range of non-polar components with reasonable accuracy.

In the case of liquid mixtures containing alkanes, viscosities and thermal conductivities are determined from a semi-empirical scheme presented by Assael et al. (1996). The range of applicability of the scheme is between 280 K to 400 K and from saturation pressures up to 990 atms where the uncertainty in the predictions is less than 5 % (Assael et al., 1996).

For mixtures containing two-phase fluids correlations proposed by the Design Institute for Physical Property Data (DIPPR) (Daubert and Danner, 1990) are applied due to their claimed accuracy. For two-phase fluids, the mixture thermal conductivity and viscosity is given by:

$$\frac{1}{c_m} = \frac{\chi}{c_g} + \frac{1-\chi}{c_l} \qquad \textbf{3.37}$$

Where c_m is the mixture property to be determined and c_g and c_l are the gas and liquid properties respectively.

3.6 Fluid/wall heat transfer (Atti, 2006)

3.6.1 Calculation of heat flux

Heat transferred to or from a flowing pipeline inventory must pass through the enclosing wall. The process will be affected by the pipe wall properties and ambient conditions unless the pipe is perfectly insulated

Newton's cooling law (Fairuzov, 1998; Mahgerefteh et al., 1999) is commonly used for determining the heat transferred to a fluid flowing in a pipe. It is given by:

$$Q_h = \frac{4}{D_{in}} U_h \left(T_{amb} - T_f\right) \qquad \textbf{3.38}$$

Where U_h, D_{in}, T_{amb}, T_f and Q_h denote the overall heat transfer coefficient, the pipeline inner diameter, the ambient and fluid temperatures and the quantity of heat transferred to the fluid respectively.

Equation 3.38 lumps the pipe wall and the ambient as a single heat source with a constant heat transfer coefficient. This ignores the pipe wall as a heat repository and as a

conducting medium. Additionally, the use of a constant heat transfer coefficient is unrealistic when phase changes in the inventory are likely to occur during outflow.

Therefore a transient energy balance, based on a lumped body approach (Myers, 1987), is applied across the fluid/wall/ambient interfaces to model the transient heat transfer process. The wall temperatures are updated at a given time step and used to estimate the heat input to the fluid in the next time interval. Figure 3.1 shows a schematic representation of the important heat transfer parameters.

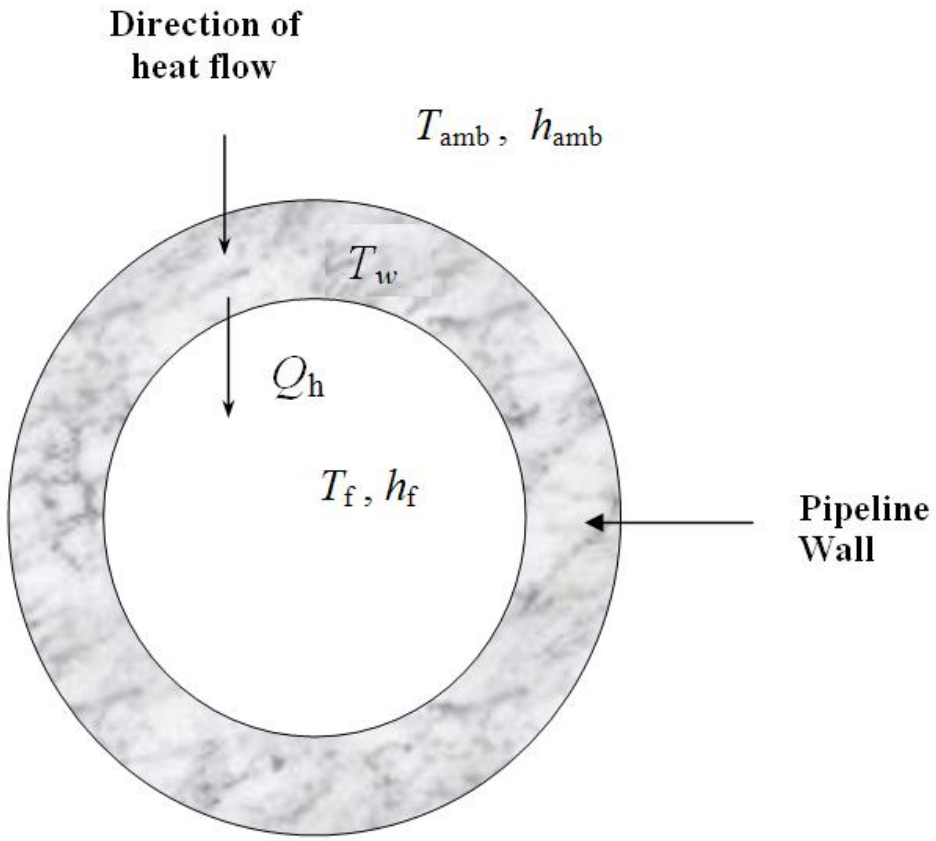

Figure 3.1: Schematic representation of the heat flow across the pipeline wall based on the lumped body approach (Atti, 2006).

T_{amb}, h_{amb} and T_w in figure 3.1 represent the ambient temperature, heat transfer coefficient of the ambient and wall temperature respectively. T_f, h_f and Q_h represent the fluid temperature, fluid heat transfer coefficient and the quantity of heat transferred to the fluid respectively.

The following assumptions are made in the lumped body approach:

- there is no temperature stratification within the pipe wall;
- the heat transfer coefficient between the pipe wall and either the ambient (h_{amb}) or the flowing fluid (h_f) is determined from the system properties at the beginning of a given time step and remains constant during the time step;
- the ambient and fluid temperature employed in the energy balance are constant over a given time step;
- the wall density (ρ_w), specific heat capacity (C_{pw}) and thermal conductivity (κ_w) are constant with respect to time and space;
- heat transfer in the pipe wall is predominantly in the radial direction, longitudinal and tangential heat conduction in the pipe wall is neglected.

Based on figure 3.1 and the above assumptions the transient energy balance across the pipe wall can be written as (Myers, 1987):

$$h_{amb}^{i-1} A_{out} (T_{amb} - T_w) - h_f^{i-1} A_{in} \left(T_w - T_f\right) = \rho_w C_{pw} V_w \frac{dT_w}{dt} \qquad \textbf{3.39}$$

Where T_w is the wall temperature at the end of a given time step Δt, *i-1* refers to property values at the beginning of the given time step, V_w is the pipe volume per unit length, A_{out} and A_{in} are the outer and inner pipe wall surface areas per unit length respectively. For a cylindrical pipeline V_w, A_{out} and A_{in} may be expressed as:

$$V_w = \pi \left(\frac{D_{out}^2 - D_{in}^2}{4} \right) \qquad \textbf{3.40}$$

$$A_{out} = \pi D_{out} \qquad \textbf{3.41}$$

$$A_{in} = \pi D_{in} \qquad \textbf{3.42}$$

Where D_{out} and D_{in} are the outer and inner diameters of the pipe respectively.

By multiplying out, collecting like terms and rearranging, equation 3.39 can be rewritten:

$$\frac{dT_w}{dt} + \left(\frac{h_{amb}^{i-1}A_{out} + h_f^{i-1}A_{in}}{\rho_w C_{pw} V_w}\right) T_w = \frac{h_{amb}^{i-1}A_{out}T_{amb} + h_f^{i-1}A_{in}T_f}{\rho_w C_{pw} V_w} \quad \textbf{3.43}$$

Equation 3.43 can be expressed as:

$$\frac{dT_w}{dt} + LT_w = M \quad \textbf{3.44}$$

Where:

$$L = \frac{h_{amb}^{i-1}A_{out} + h_f^{i-1}A_{in}}{\rho_w C_{pw} V_w} \quad \textbf{3.45}$$

$$M = \frac{h_{amb}^{i-1}A_{out}T_{amb} + h_f^{i-1}A_{in}T_f}{\rho_w C_{pw} V_w} \quad \textbf{3.46}$$

Equation 3.44 is a linear first order differential equation, and has a general solution given by (Stroud, 1995):

$$T_w e^{\int L dt} = \int M e^{\int L dt}\, dt \quad \textbf{3.47}$$

The evaluation of equation 3.47 is subject to the following boundary condition:

$$T_w = T_w^{i-1} \; when \; \Delta t = 0 \quad \textbf{3.48}$$

Since the parameters *L* and *M* (equations 3.45 and 3.46) contain variables that are assumed to be constants within a given time step (Δt), integrating equation 3.47 gives:

$$T_w e^{L\Delta t} = \frac{M}{L} e^{L\Delta t} + MC \quad \textbf{3.49}$$

Where *C* is the constant of integration. By applying the boundary condition given in equation 3.48, *C* can be evaluated as:

$$C = \frac{T_w^{i-1}}{M} - \frac{1}{L} \quad \textbf{3.50}$$

Substituting equation 3.50 into equation 3.49 and rearranging:

$$T_w = \frac{M}{L} + \left(T_w^{i-1} - \frac{M}{L}\right) e^{-L\Delta t} \quad \textbf{3.51}$$

Using the expressions for *L* and *M* given in equations 3.45 and 3.46 the updated wall temperature at the end of a time step Δt can be obtained.

Applying Newton's cooling law, the heat transferred to the fluid (Q_h) in a given time step may then be calculated by (Atti, 2006):

$$Q_h = \frac{4}{D_{in}} h_f \left(T_w - T_f\right) \quad \textbf{3.52}$$

3.6.2 Fluid/wall heat transfer coefficients (FHTC)

Two heat transfer correlations are used depending on the nature of the flowing fluid. For single phase fully developed flow in rough pipes the correlation of Bhatti and Shah (1987) is used:

$$Nu = \frac{RePr(f/2)}{1 + (f/2)^{0.5}[4.5Re_\varepsilon^{0.2}Pr^{0.5} - 8.48]} \quad \textbf{3.53}$$

The roughness Reynolds number (Re_ε) is given by:

$$Re_\varepsilon = \frac{\rho \varepsilon u}{\mu_f}\sqrt{\frac{f}{2}} \qquad \textbf{3.54}$$

The fanning friction factor, *f*, employed in equations 3.53 and 3.54 is calculated from the correlation proposed by Nikuradse (1933) and is given by:

$$\frac{1}{\sqrt{f}} = 3.48 - 1.737 \ln\left(\frac{\varepsilon}{r}\right) \qquad \textbf{3.55}$$

Where *Re*, *Pr*, *Nu*, ρ, μ_f, ε and *r* represent the Reynolds number, Prandtl number, Nusselt number, fluid density, fluid viscosity, pipe wall roughness and pipe radius respectively.

For two phase flow in pipelines heat transfer is assumed to be by forced convection only, the correlation of Steiner and Taborek (1992) is used:

$$\frac{h_{FC}}{h_l} = F_{tp} = \left((1-x)^{1.5} + 1.9x^{0.6}\left(\frac{\rho_l}{\rho_v}\right)^{0.35}\right)^{1.1} \qquad \textbf{3.56}$$

Where h_{FC} is the fluid heat transfer coefficient (adjusted for forced convection in the inventory), *x* is the flow quality (i.e. vapour fraction), ρ_v and ρ_l are the vapour and liquid densities respectively and F_{tp} is the two phase flow convective factor. h_l is the heat transfer coefficient for the liquid phase in the pipeline, given by Rohsenow et al. (1998):

$$\frac{h_l D_{in}}{\kappa_l} = 0.023\left[\frac{\rho_{mix} u(1-x)D_{in}}{\mu_l}\right]^{0.8}\left[\frac{\mu_l C_{pl}}{\kappa_l}\right]^{0.4} \qquad \textbf{3.57}$$

Where the two-phase mixture density, ρ_{mix}, is given by:

$$\rho_{mix} = \frac{\rho_v \rho_l}{\rho_v(1-x) + \rho_l x} \qquad \textbf{3.58}$$

The subscript *l* represents liquid phase properties. κ, D_{in}, u, μ, and C_p represent the thermal conductivity, inner pipe diameter, fluid velocity, viscosity and specific heat of the liquid respectively.

3.6.3 Pipe wall/ambient heat transfer coefficients

For insulated or buried pipelines a constant heat transfer coefficient between the pipe wall and the ambient (h_{amb}) is used over the full length of the pipeline. For pipelines exposed to the open air both natural and/or forced convection are accounted for, the heat transfer coefficient is given by (Incropera and DeWitt, 1996; Rohsenow et al., 1998):

$$h_{amb} = \left(h_{nat}^3 + h_{for}^3\right)^{\frac{1}{3}} \quad \textbf{3.59}$$

Where h_{amb}, h_{nat} and h_{for} are the total convective, natural and forced convection heat transfer coefficients respectively.

Natural convection

For natural convection the correlation proposed by Churchill and Chu (1975) for flow over horizontal cylinders is used:

$$\frac{h_{nat} D_{out}}{\kappa_{film}} = \left[0.60 + \frac{0.387 Ra_D^{1/6}}{\left[1 + \left(0.559/Pr_{film}\right)^{9/16}\right]^{8/27}}\right]^2 \quad \textbf{3.60}$$

Where D_{out} is the outer diameter of the pipe, κ the thermal conductivity and the subscript *film* represents ambient fluid properties evaluated at the film temperature, T_{film}:

$$T_{film} = \frac{(T_s + T_{amb})}{2} \quad \textbf{3.61}$$

T_s represents the surface temperature (i.e. T_w). The Rayleigh, Prandtl and Grashof numbers are respectively defined as:

$$Ra_D = Gr_{film}Pr_{film} \quad \textbf{3.62}$$

$$Pr_{film} = \frac{C_{pfilm}\mu_{film}}{\kappa_{film}} \quad \textbf{3.63}$$

$$Gr_{film} = \frac{\rho_{film}^2 g \xi_{film}(T_s - T_{amb})D_{out}^3}{\mu_{film}^2} \quad \textbf{3.64}$$

Where C_p, μ and g represent the specific heat at constant pressure, viscosity and gravitational acceleration. ξ_{film} is the isobaric volumetric expansion coefficient, given by (Incropera and DeWitt, 1996):

$$\xi_{film} = -\frac{1}{\rho_{film}}\left(\frac{\delta\rho_{film}}{\delta T_{film}}\right)_p \quad \textbf{3.65}$$

Forced convection

For forced convection over a cylinder the heat transfer correlation proposed by Churchill and Bernstein (1977) is used. The correlation is recommended for $Re \times Pr > 0.2$ and is given by:

$$\frac{h_{for}D_{out}}{\kappa_{film}} = \left[0.30 + \frac{0.62 Re_{film}^{1/2} Pr_{film}^{1/3}}{\left[1 + \left(0.4/Pr_{film}\right)^{2/3}\right]^{1/4}}\left[1 + \left(\frac{Re_{film}}{282000}\right)^{5/8}\right]^{4/5}\right] \quad \textbf{3.66}$$

3.7 The Steady State Isothermal Flow Model (Oke, 2004)

The steady state isothermal flow model presented here is based on the one-dimensional continuity and momentum equations presented in section 3.3.

From equation 3.1, the steady state expression is obtained by setting the time derivatives to zero and can be written as:

$$\frac{\partial \rho u}{\partial x} = 0 \qquad \textbf{3.67}$$

Integrating equation 3.67 gives (Oke, 2004):

$$\rho_i u_i = \rho_{i-1} u_{i-1} \qquad \textbf{3.68}$$

Where the subscripts *i-1* and *i* represent the previous and current grid points under consideration respectively. Equation 3.68 is the governing equation for mass conservation during steady state flow in a constant diameter pipeline.

From equation 3.2 the steady state momentum equation in one-dimension can be expressed as:

$$\rho u \frac{du}{dx} = -\frac{dP}{dx} - \rho g \sin(\theta) + \beta \qquad \textbf{3.69}$$

Where, the steady state frictional force term β is given by equation 3.4 (see also section 3.5.4). Substituting the expression for β into equation 3.69 and rearranging gives (Oke, 2004):

$$\rho dP - (\rho u)^2 \frac{d\rho}{\rho} = -\left(\frac{2 f_w (\rho u)^2}{D} + \rho^2 g \sin(\theta)\right) dx \qquad \textbf{3.70}$$

The above equation can be expressed as:

$$\rho dP + K_1 \frac{d\rho}{\rho} = (K_2 + \rho^2 K_3) dx \quad \textbf{3.71}$$

Where:

$$K_1 = -(\rho u)^2 \quad \textbf{3.72}$$

$$K_2 = -\frac{2 f_w (\rho u)^2}{D} \quad \textbf{3.73}$$

$$K_3 = -g \sin(\theta) \quad \textbf{3.74}$$

Rearranging equation 3.71 and taking the limits results in (Oke, 2004):

$$\int_{P_{i-1}}^{P_i} \frac{\rho}{(K_2 + \rho^2 K_3)} dP + K_1 \int_{\rho_{i-1}}^{\rho_i} \frac{\rho}{\rho(K_2 + \rho^2 K_3)} d\rho = \int_{x_{i-1}}^{x_i} dx \quad \textbf{3.75}$$

After resolving the integrals on the LHS the final form of equation 3.75 is given by (Oke, 2004):

$$\frac{1}{2}\left[\frac{\rho}{(K_2 + \rho^2 K_3)_{P_i}} + \frac{\rho}{(K_2 + \rho^2 K_3)_{P_{i-1}}}\right] + \frac{K_1}{2K_2}\left[2ln\left(\frac{\rho_i}{\rho_{i-1}}\right) - ln\left(\frac{(K_2 + \rho_i^2 K_3)}{(K_2 + \rho_{i-1}^2 K_3)}\right)\right] = x_i - x_{i-1} \quad \textbf{3.76}$$

The following outlines the algorithm used in OUTFLOW for calculating the isothermal steady state drop (as summarised by Denton, (2009)):

1. Collate data at pipeline inlet (e.g. fluid pressure, temperature, velocity, etc.)

2. Divide the pipeline into sections (grids) with the distance between the grids being $\Delta = x_i - x_{i-1}$;
3. Guess the downstream pressure at the next grid point i.e. P_i;
4. In conjunction with an EoS, evaluate the expression on the LHS of equation 3.76;
5. If equation 3.76 is satisfied, then the guessed downstream pressure is adopted as the solution. The fluid velocity u_i can then be obtained by applying equation 3.68. If the equation is not satisfied, go back to step 3 and update the guessed P_i;
6. Update the flow properties at this grid point and calculate the pressure drop at the next grid using steps 3-5 until the variables at the final grid is calculated.

3.8 Hyperbolicity of the governing conservation equations

The partial differential equations (PDEs) which describe the conservation of mass, momentum and energy, coupled with an appropriate EoS, constitute a system of equations that are essentially the Euler equations with additional terms due to friction and heat transfer in the momentum and energy equations respectively.

The selection of an appropriate numerical technique for the solution of the governing PDEs is dependent on their mathematical nature. It is shown below that the system of conservation equations are quasilinear and hyperbolic.

A partial differential equation is said to be quasilinear if all derivatives of the dependent function *f(x,t)* are linear, while their corresponding coefficients may contain non-linear terms (Prasad and Ravindran, 1985), i.e. it is in the following form:

$$a(x,t,u)f_t + b(x,t,u)f_x = c(x,t,u) \qquad \textbf{3.77}$$

Where f_t and f_x are the partial derivatives of the function u in terms of t and x respectively.

Writing equations 3.1, 3.2 and 3.3 as:

$$\left(\frac{\partial P}{\partial t}+u\frac{\partial P}{\partial x}\right)-\varphi\left(\frac{\partial s}{\partial t}+u\frac{\partial s}{\partial x}\right)+\rho a^2\frac{\partial u}{\partial x}=0 \qquad \textbf{3.78}$$

$$\rho\left(\frac{\partial u}{\partial t}+u\frac{\partial u}{\partial x}\right)+\frac{\partial P}{\partial x}=\alpha \qquad \textbf{3.79}$$

$$\rho T\left(\frac{\partial s}{\partial t}+u\frac{\partial s}{\partial x}\right)=\psi \qquad \textbf{3.80}$$

Where:

$$\alpha=\beta_x-\rho g\sin(\theta) \qquad \textbf{3.81}$$

$$\psi=Q_h-u\beta_x \qquad \textbf{3.82}$$

It may be observed that equations 3.78 to 3.80 are linear in the partial derivative terms. Additionally, terms that are coefficients of the partial derivatives, such as the density, ρ, or the fluid speed of sound, a, are nonlinear functions of P, s and u. The governing equations therefore possess a quasilinear structure.

Equations 3.78 to 3.80 may also be written in the general form:

$$A\frac{\partial U}{\partial t}+B\frac{\partial U}{\partial x}=C \qquad \textbf{3.83}$$

Where A, U, B and C are given by:

$$U=\begin{pmatrix}P\\ s\\ u\end{pmatrix} \qquad \textbf{3.84}$$

$$A=\begin{pmatrix}1 & -\varphi & 0\\ 0 & 0 & \rho\\ 0 & \rho T & 0\end{pmatrix} \qquad \textbf{3.85}$$

$$B = \begin{pmatrix} u & -\varphi u & \rho a^2 \\ 1 & 0 & \rho u \\ 0 & \rho T u & 0 \end{pmatrix} \quad \textbf{3.86}$$

$$C = \begin{pmatrix} 0 \\ \alpha \\ \psi \end{pmatrix} \quad \textbf{3.87}$$

A system of PDEs, as given by equation 3.83, is said to be hyperbolic if the eigenvalues, satisfying equation 3.88, are real and distinct (Prasad and Ravindran, 1985):

$$|B - \lambda A| = 0 \quad \textbf{3.88}$$

Thus for the conservation equations the above equation may be expressed as:

$$|B - \lambda A| = \begin{vmatrix} (u-\lambda) & \varphi(\lambda - u) & \rho a^2 \\ 1 & 0 & \rho(u-\lambda) \\ 0 & \rho T(u-\lambda) & 0 \end{vmatrix} = 0 \quad \textbf{3.89}$$

Hence the determinant is:

$$(u-\lambda)[0 - \rho^2 T(u-\lambda)^2] - \varphi(\lambda - u)[0-0] + \rho a^2[\rho T(u-\lambda) - 0] = 0 \quad \textbf{3.90}$$

Factorising equation 3.90 and dividing through by $\rho^2 T$ gives:

$$(u-\lambda)[a^2 - (u-\lambda)^2] = 0 \quad \textbf{3.91}$$

Solving equation 3.91 to obtain the roots gives:

$$\lambda_1 = u \quad \textbf{3.92}$$

$$\lambda_2 = u - a \quad \textbf{3.93}$$

$$\lambda_3 = u + a \qquad \textbf{3.94}$$

It can be seen that the eigenvalues (λ_i) are real and distinct, therefore the quasilinear governing equations are hyperbolic. This implies that the behaviour of the physical system described by these equations will be dominated by wave-like phenomena (Prasad and Ravindran, 1985).

3.9 Conclusion

In this chapter the mass, momentum and energy conservation equations for transient fluid flow in a pipeline following its failure were presented. These were expressed in terms of pressure, entropy and velocity due to the proven accuracy and computational efficiency of this formulation. These equations were shown to be quasilinear and hyperbolic.

The conservation equations coupled with a cubic Equation of State represent the core of the model OUTFLOW. The various hydrodynamic and thermodynamic relations for predicting pertinent fluid properties such as the fluid speed of sound, viscosity and phase dependent friction factor were presented.

The main features of the lumped body approach for modelling heat transfer effects between the fluid/pipe wall and pipe wall/ambient were presented. The correlations used to account for the varying heat transfer contribution from different fluid phases are also presented.

Finally, the steady state isothermal model based on a real fluid was presented.

Chapter 4: Application of the Method of Characteristics (MOC) to the modelling of fluid flow in pipelines

4.1 Introduction

The Euler equations for unsteady real fluid flow were first presented in chapter 3 (equations 3.1 to 3.3 respectively), where they were shown to be hyperbolic and quasilinear. These equations cannot be solved analytically as they contain terms that are unknown or non-linear functions of their dependent and independent variables (see Flatt, 1986; Mahgerefteh et al., 1999).

Three numerical techniques are commonly employed for resolving hyperbolic partial differential equations. These are:

1. Finite Difference Methods (FDM)
2. Finite Volume Methods (FVM)
3. Method of Characteristics (MOC)

The FDM is a general mathematical technique that is widely applied to PDEs. It involves discretising the spatial domain into a series of nodes forming a grid. Finite approximations are then substituted for the derivatives in the PDEs to produce a system of algebraic relations to calculate fluid properties at all grid points. However, numerical diffusion associated with the FDM makes it unsuitable for modelling the transient flow following pipeline failure (Mahgerefteh et al., 2009).

Similarly, the FVM breaks the system up into a set of discrete cells. The integral of the PDEs over each cell is approximated to produce a system of algebraic relations. The application of the FVM to hyperbolic PDEs has received significant attention in recent

years (Brown, 2011; Leveque, 2002; Toro, 2009). The development of a FVM specifically for the resolution of governing conservation equations in OUTFLOW was addressed by Brown (2011). In this work it was demonstrated that the FVM generally performed well except when simulating FBR of an initially liquid state inventory. This makes an FVM solution to the Euler equations of limited use for a CO_2 pipeline outflow model.

The MOC is a mathematical technique that is particularly suited to solving systems of hyperbolic PDEs with two independent variables such as distance and time. The MOC resolves the system of PDEs into a system of ordinary differential equations (compatibility equations) through a particular co-ordinate change. These co-ordinates represent curves (characteristic lines) in the space-time plane along which the compatibility equations hold. The compatibility equations can be solved using finite-difference methods. The method is particularly suitable for systems containing complex boundary conditions as each boundary condition may be applied individually to each characteristic curve moving into the computational domain.

In this chapter, the formulation and implementation of the MOC used to solve the conservation equations governing single/two-phase homogeneous flow in pipeline networks is outlined. Various boundary conditions required to simulate blowdown of a pipeline are presented.

4.2 Formulation of the MOC

4.2.1 Discretisation methods of the space-time plane

There are two main grid discretisation methods for the MOC. These are the Characteristic Grid method (CG) (Wylie and Streeter, 1993) and the Inverse Marching method or the Method of Specified Time Intervals (MST) (Flatt, 1986).

In the case of the CG method, the position of the new solution is not known *a priori*. This is determined by the intersection of the left and right running characteristics with the origins located at points where the solution is already known or obtained from the initial data. A free-floating grid is developed in the $x - t$ plane as shown in figure 4.1. This method is particularly accurate as the solution progresses naturally along the characteristic lines. In the case where more than two characteristic lines are present, i.e. when an energy equation is solved, the intersection of the path line between the known initial points requires interpolation.

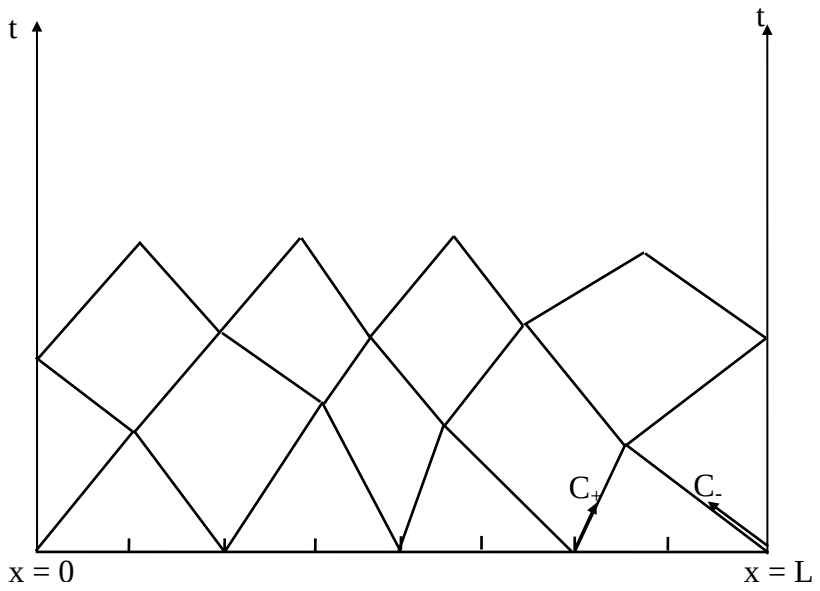

Figure 4.1: The Characteristic Grid.

In the MST (see figure 4.2) the location of the solution points in the space-time grid is specified *a priori* and the characteristic lines are traced backwards in time to their origin in the previous time line. This method requires interpolation to locate the intersection of all three characteristic lines on the previous time line and as a result can lead to a greater loss of accuracy than the CG method.

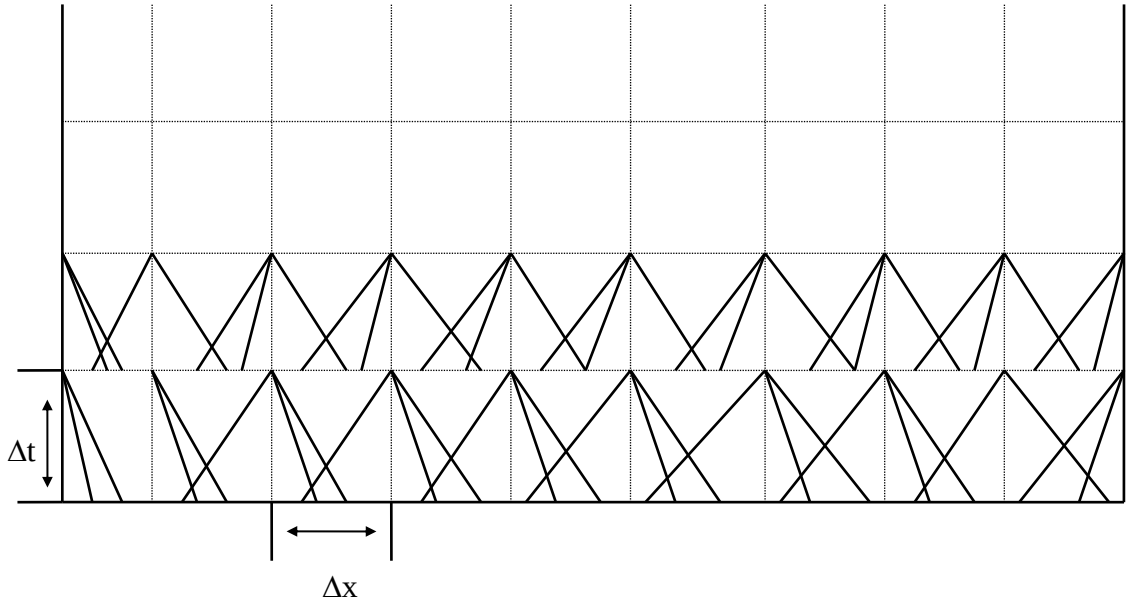

Figure 4.2: The Method of Specified Time Intervals.

While the CG method may be more accurate it does not allow for the introduction of boundary conditions at predefined times. In contrast, the MST method allows control of the time at which input variables are given at boundaries. This means that the implementation of models for systems that commonly prevail in reality, such as valve closure or pump shutdown, is much less cumbersome. For this reason, the MST is used in implementing the Euler equations in OUTFLOW.

4.2.2 Numerical formulation of the MOC

The solution of PDEs using the MOC comprises two steps:

1. Conversion of the PDEs into a system of ordinary differential equations (ODEs) called the compatibility equations.
2. Solution of the compatibility equations based on the MST method employing an Euler predictor-corrector technique (Zucrow and Hoffman, 1975) .

Step 1 – Conversion of the PDEs to ODEs

The governing conservation equations (continuity, momentum and energy) for unsteady fluid flow were presented in chapter 3 and are repeated below.

$$\left(\frac{\partial P}{\partial t}+u\frac{\partial P}{\partial x}\right)-\varphi\left(\frac{\partial s}{\partial t}+u\frac{\partial s}{\partial x}\right)+\rho a^2\frac{\partial u}{\partial x}=0 \qquad \textbf{3.78}$$

$$\rho\left(\frac{\partial u}{\partial t}+u\frac{\partial u}{\partial x}\right)+\frac{\partial P}{\partial x}=\alpha \qquad \textbf{3.79}$$

$$\rho T\left(\frac{\partial s}{\partial t}+u\frac{\partial s}{\partial x}\right)=\psi \qquad \textbf{3.80}$$

Where:

$$\alpha=\beta_x-\rho g\sin(\theta) \qquad \textbf{3.81}$$

$$\psi=Q_h-u\beta_x \qquad \textbf{3.82}$$

Following Atti (2006), the conservation equations may be replaced by three compatibility equations (equations 4.1, 4.3 and 4.5), which are valid only along the corresponding characteristic curves (equations 4.2, 4.4 and 4.6 respectively). For the Path line (C_0) the compatibility and characteristic curve equations are respectively given by:

$$d_0 s=\frac{\psi}{\rho T}d_0 t \qquad \textbf{4.1}$$

$$\frac{d_0 t}{d_0 x}=\frac{1}{u} \qquad \textbf{4.2}$$

For the positive Mach line (C_+) the compatibility and characteristic curve equations are respectively given by:

$$d_+P + \rho a d_+u = \left(a\alpha + \frac{\varphi\psi}{\rho T}\right) d_+t \qquad \textbf{4.3}$$

$$\frac{d_+t}{d_+x} = \frac{1}{u + a} \qquad \textbf{4.4}$$

For the negative Mach line (C_-) the compatibility and characteristic curve equations are respectively given by:

$$\rho a d\_u - d\_P = \left(a\alpha - \frac{\varphi\psi}{\rho T}\right) d\_t \qquad \textbf{4.5}$$

$$\frac{d\_t}{d\_x} = \frac{1}{u - a} \qquad \textbf{4.6}$$

The positive (C_+) and negative (C_-) Mach lines govern the speed at which expansion and compression waves propagate, while the path line (C_0) dictates the rate of flow through any given point along the pipeline.

Step 2 – Solution of the compatibility equations

As described above, the solution of the compatibility equations requires the tracing of the characteristic lines in a discretised *x – t* plane as shown in figure 4.3.

It is assumed that the fluid properties are already known at grid points *i-1*, *i* and *i+1* at time t_1. The initial conditions at points *p*, *o* and *n* are evaluated by linear interpolation. The compatibility equations are solved using a finite difference method to predict the flow variables *P*, *h* and *u* at point *j* (the intersection point of the characteristic curves at the next time step, $t_1 + \Delta t_1$).

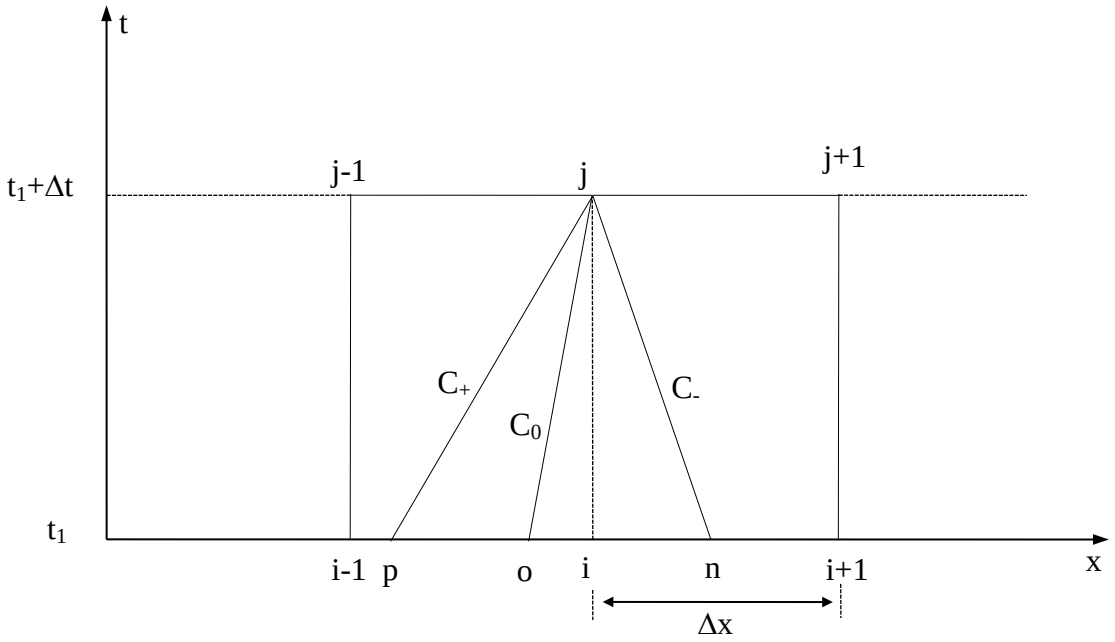

Figure 4.3: A schematic representation of Path line (C_0) and Mach lines (C_+, C_-) characteristics at a grid point along the time (*t*) and space (*x*) axes.

The time step (Δt) employed is calculated subject to the Courant-Friedrichs-Lewy (CFL) criterion (Courant et al., 1967; Mahgerefteh et al., 2009). This criterion is a requirement for the stability of the numerical scheme employed. It is given by:

$$\Delta t \leq \frac{\Delta x}{|u+a|_{max}} \qquad \textbf{4.7}$$

4.2.3 Finite difference solution of the compatibility equations

A full description of the finite difference method used to resolve the compatibility equations is given by Atti (2006). A summary of the key points is given here.

An Euler predictor-corrector finite difference technique is used to numerically solve the compatibility and characteristic equations 4.1 to 4.6. The method consists of an explicit predictor step (first order approximation), which is used as an estimate of the fluid

properties at the solution point. As the characteristics lines are curved rather than linear it is necessary to minimise any error introduced in this step. This is achieved with a corrector step (second order approximation) which refines the initial estimate for an implicit approximation of the time step.

First order approximation – predictor step

In the predictor step the Path line, positive and negative Mach line compatibility equations (equations 4.1, 4.3 and 4.5) are respectively expressed in finite difference form as (Atti, 2006):

$$(s_j - s_0) = \left(\frac{\psi}{\rho T}\right)_0 (t_j - t_0) \quad \textbf{4.8}$$

$$(\rho a)_p (u_j - u_p) + (P_j - P_p) = \left(a\alpha + \frac{\varphi\psi}{\rho T}\right)_p (t_j - t_p) \quad \textbf{4.9}$$

$$(\rho a)_n (u_j - u_n) - (P_j - P_n) = \left(a\alpha - \frac{\varphi\psi}{\rho T}\right)_n (t_j - t_n) \quad \textbf{4.10}$$

The subscripts assigned to the various properties in equations 4.8 to 4.10 denote the location in space and time, as shown in figure 4.3.

To calculate the points x_p, x_o and x_n the characteristic line equations 4.2, 4.4 and 4.6 are written in first order finite difference form (equations 4.11, 4.12 and 4.13). Linear interpolation formulae for *u* and *a* at points *p*, *o* and *n* (see figure 4.3) are then combined with the corresponding equations 4.11, 4.12 and 4.13 to produce a pair of equations for each point, these are solved simultaneously to yield values for *u* and *a*. Substituting the calculated values for u_p, a_p, u_n, a_n, and u_o into their corresponding equations 4.11, 4.12 or 4.13 yields the locations of points x_p, x_o and x_n.

$$\lambda_0 = u_o = \frac{x_i - x_o}{\Delta t} \Rightarrow x_o = x_i - u_o \Delta t \quad \textbf{4.11}$$

$$\lambda_+ = u_p + a_p = \frac{x_i - x_p}{\Delta t} \Rightarrow x_p = x_i - (u_p + a_p)\Delta t \quad \textbf{4.12}$$

$$\lambda_- = u_n - a_n = \frac{x_i - x_n}{\Delta t} \Rightarrow x_n = x_i - (u_n + a_n)\Delta t \quad \textbf{4.13}$$

The fluid properties (*P*, *S* and *u*) are then linearly interpolated from those at the grid points *i-1*, *i* and *i+1*(Atti, 2006).

With all the necessary values calculated at *t1* the fluid properties at point *j* are then calculated using equations 4.8 to 4.10.

Second order approximation – corrector step

In order to improve the accuracy of the first order solution, a second order approximation to the compatibility equations is employed. The second order finite difference form of the Path line, positive and negative Mach line compatibility equations (equations 4.1, 4.3 and 4.5) are respectively expressed as (Atti, 2006):

$$(s_j - s_0) = \frac{1}{2}\left[\left(\frac{\psi}{\rho T}\right)_0 + \left(\frac{\psi}{\rho T}\right)_j\right](t_j - t_0) \quad \textbf{4.14}$$

$$\frac{1}{2}((\rho a)_p + (\rho a)_j)(u_j - u_p) + (P_j - P_p) = \frac{1}{2}\left(\left(a\alpha + \frac{\varphi\psi}{\rho T}\right)_p + \left(a\alpha + \frac{\varphi\psi}{\rho T}\right)_j\right)(t_j - t_p) \quad \textbf{4.15}$$

$$\frac{1}{2}((\rho a)_n + (\rho a)_j)(u_j - u_n) - (P_j - P_n) = \frac{1}{2}\left(\left(a\alpha - \frac{\varphi\psi}{\rho T}\right)_n + \left(a\alpha - \frac{\varphi\psi}{\rho T}\right)_j\right)(t_j - t_n) \quad \textbf{4.16}$$

The second order approximations to the characteristic equations 4.2, 4.4 and 4.6 are respectively given by:

$$\frac{1}{2}(\lambda_0 + \lambda_j) = \frac{1}{2}(u_o + u_j^r) = \frac{x_i - x_o}{\Delta t} \Rightarrow x_o = x_i - \frac{\Delta t}{2}(u_o + u_j^r) \quad \textbf{4.17}$$

$$\frac{1}{2}(\lambda_+ + \lambda_j) = \frac{1}{2}(u_p + u_j^r) + \frac{1}{2}(a_p + a_j^r) = \frac{x_i - x_p}{\Delta t} \Rightarrow x_p$$
$$= x_i - \frac{\Delta t}{2}(u_p + u_j^r + a_p + a_j^r) \quad \textbf{4.18}$$

$$\frac{1}{2}(\lambda_- + \lambda_j) = \frac{1}{2}(u_n + u_j^r) - \frac{1}{2}(a_n + a_j^r) = \frac{x_i - x_n}{\Delta t} \Rightarrow x_n$$
$$= x_i - \frac{\Delta t}{2}(u_n + u_j^r - a_n - a_j^r) \quad \textbf{4.19}$$

The subscript *j* together with superscript *r* refer to the solution condition at the previous iteration step, *r*.

In a similar manner employed in the predictor step, the positions x_p, x_o and x_n are calculated using equations 4.17, 4.18 and 4.19. The fluid properties at these points are then found by linear interpolation. Fluid properties at point *j* are then determined using equations 4.14 to 4.16. This calculation is repeated until a certain tolerance (ca. 10^{-5}) is satisfied for the three independent flow variables, i.e. *P*, *S* and *u*.

4.3 Boundary conditions for simulating outflow from pipelines

In this section the boundary conditions required to simulate outflow from a multi-segment pipeline following failure are presented. These include:

- intact pipeline end;
- reservoir at the pipe inlet;
- junction of multiple pipelines;
- full-bore rupture/orifice at pipeline end.

4.3.1 The intact end boundary condition

At the intact end of the pipeline, only the negative Mach line (C_-) and Path line (C_0) characteristics are applicable and so only two compatibility equations are valid. In this case one boundary condition must be supplied in order to determine the pertinent flow variables *P*, *S* and *u*. Figure 4.4 shows the grid scheme at the intact end point.

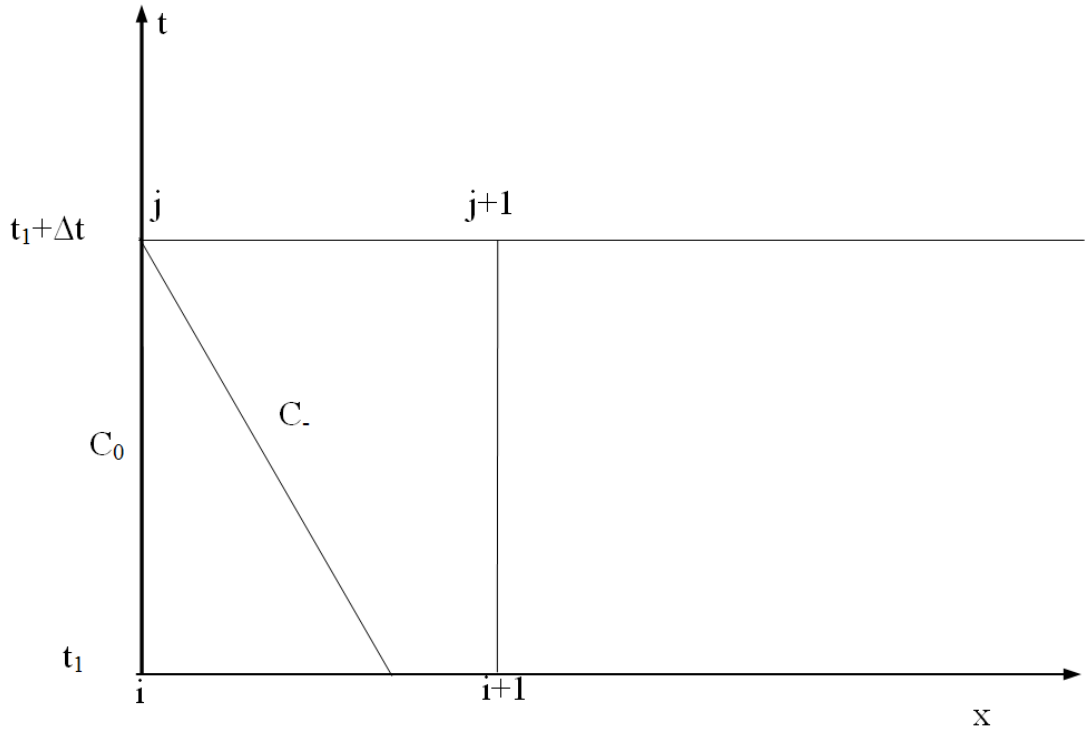

Figure 4.4: Grid scheme showing the active characteristic lines (C_0 and C_-) at the inlet intact end point.

The first order finite difference approximation of the negative characteristic equation, C_- (equation 4.10), can be written as:

$$P_j = K_2 + (\rho a)_n(u_j - u_n) + P_n \qquad \textbf{4.20}$$

Where, K_2 is given by:

$$K_2 = \left(\frac{\varphi\psi}{\rho T} - a\alpha\right)_n \Delta t \qquad \textbf{4.21}$$

Applying the boundary condition that the velocity at the closed end is equal to zero to equation 4.20 gives:

$$P_j = K_2 + (\rho a u)_n + P_n \qquad \textbf{4.22}$$

The upstream entropy may then be calculated using the path line characteristic (equation 4.8):

$$s_j = \left(\frac{\psi}{\rho T}\right)_0 \Delta t + s_0 \qquad \textbf{4.23}$$

The corrector step as described in section 4.2.3 is then employed to calculate the flow variables at the intact end.

4.3.2 Reservoir at the pipe inlet

The reservoir boundary condition is similar to the intact end boundary condition presented above. The reservoir is assumed to be infinite, therefore the net fluid movement within it is assumed to be nil and the fluid pressure at the inlet to the attached pipeline is constant.

As fluid only flows out of the reservoir the Path and positive Mach line would both be traced into the reservoir, this however takes them out of the computational domain and so two boundary conditions must be supplied instead:

$$P_j = P_{\text{res}} \qquad \textbf{4.24}$$

$$u_j = 0 \qquad \textbf{4.25}$$

Where P_{res} is the reservoir pressure. Fluid entropy at the pipeline inlet is then calculated at each time interval from the Path line characteristic, equation 4.8.

4.3.3 Junction of multiple pipe sections

Two pipe junctions

Denton's (2009) model for the effect of pressure losses between segments in pipeline networks is applied in this study and outlined below. Figure 4.5 is a schematic representation of the characteristic lines at a typical bend or connector. B_1 and B_2 refer to the flow boundaries at the common junction associated with pipeline 1 and 2 respectively.

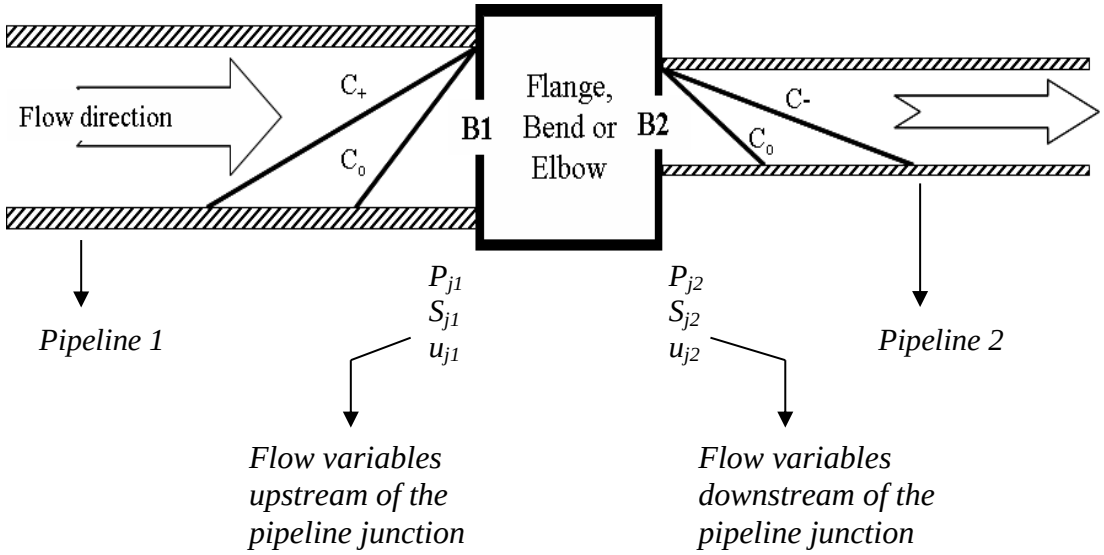

Figure 4.5: Schematic representation of characteristic lines upstream and downstream of a 2-way junction.

At the boundary B_1, only the positive Mach line (C_+) and Path line (C_0) characteristics lie within the computational domain. Similarly, at B_2 only the negative Mach line (C_-) and the Path line (C_0) are applied. The solution at points B_1 and B_2 are denoted by j_1 and

j_2 respectively. K_{loss} coefficients are used to account for pressure losses due to friction or changes in flow direction across the fitting (Perry et al., 2008). These coefficients are determined empirically for different types of fittings, and are employed in calculating the pressure drop resulting from flow across a given fitting (Perry et al., 2008).

The pressure drop at the pipeline junction is given by:

$$P_{j1} = P_{j2} + K_{pl} \quad \textbf{4.26}$$

Where:

$$K_{pl} = 0.5\left(\rho_{j1} u_{j1} \left|u_{j1}\right| - \rho_{j2}(1 + K_{loss}) u_{j2} \left|u_{j2}\right|\right) \quad \textbf{4.27}$$

And ρ_j, u_j and P_j are the density, velocity and pressure at junction j.

The coefficient K_{loss} accounts for the pressure drop resulting from the losses described above. Its values are obtained from the literature (Perry et al., 2008). These loss coefficients are relatively insensitive to the Reynolds number for $Re \geq 500$ (Perry et al., 2008). As flow conditions where $Re \geq 20{,}000$ are likely to be prevalent at pipeline junctions during the depressurisation process, constant loss coefficients are utilised in this study. These are summarised in table 4.1.

Table 4.1: K_{loss} for turbulent flow through fittings and valves (Perry et al., 2008).

Type of fitting	K_{loss}
45° elbow (standard)	0.35
90° elbow (standard)	0.75
Coupling/Union	0.04
Tee (standard, branch blanked off)	0.40
Gate valve (open)	0.17
Angle valve (open)	2

Taking the junction as a control volume, assuming no mass accumulation and considering flow into the junction as positive, applying a continuity equation gives:

$$\rho_{j1} u_{j1} A_{j1} + \rho_{j2} u_{j2} A_{j2} = 0 \qquad \textbf{4.28}$$

Where, A_j is the cross-sectional area of the pipeline.

If continuity is satisfied across the boundaries, the flow transport properties obtained are adopted as the required solution.

Junction of three pipes (Oke, 2004)

This boundary condition assumes the flow is split from a trunk pipeline into two downstream pipelines. Analysis of the flow is similar to that across the junction of two pipes. Figure 4.6 is a schematic representation of characteristic lines at a three pipe junction. B_1, B_2, and B_3 represent the flow boundaries at the common junction associated with pipelines 1, 2 and 3 respectively.

At B_1 the positive Mach (C_+) and Path line (C_0) compatibility equations are active, while at B_2 and B_3 the negative Mach (C_-) and Path line (C_0) compatibility equations are applied. As for the two pipeline junction, pressure losses across the junction are accounted for using the coefficient K_{loss}, pressure drop across the junction is therefore calculated separately for flow between pipes 1 and 2 and pipes 1 and 3:

$$P_{j1} = P_{j2} + K_{pl12} \qquad \textbf{4.29}$$

$$P_{j1} = P_{j3} + K_{pl13} \qquad \textbf{4.30}$$

Where K_{pl} is calculated from equation 4.27 and values of K_{loss} are given in table 4.1.

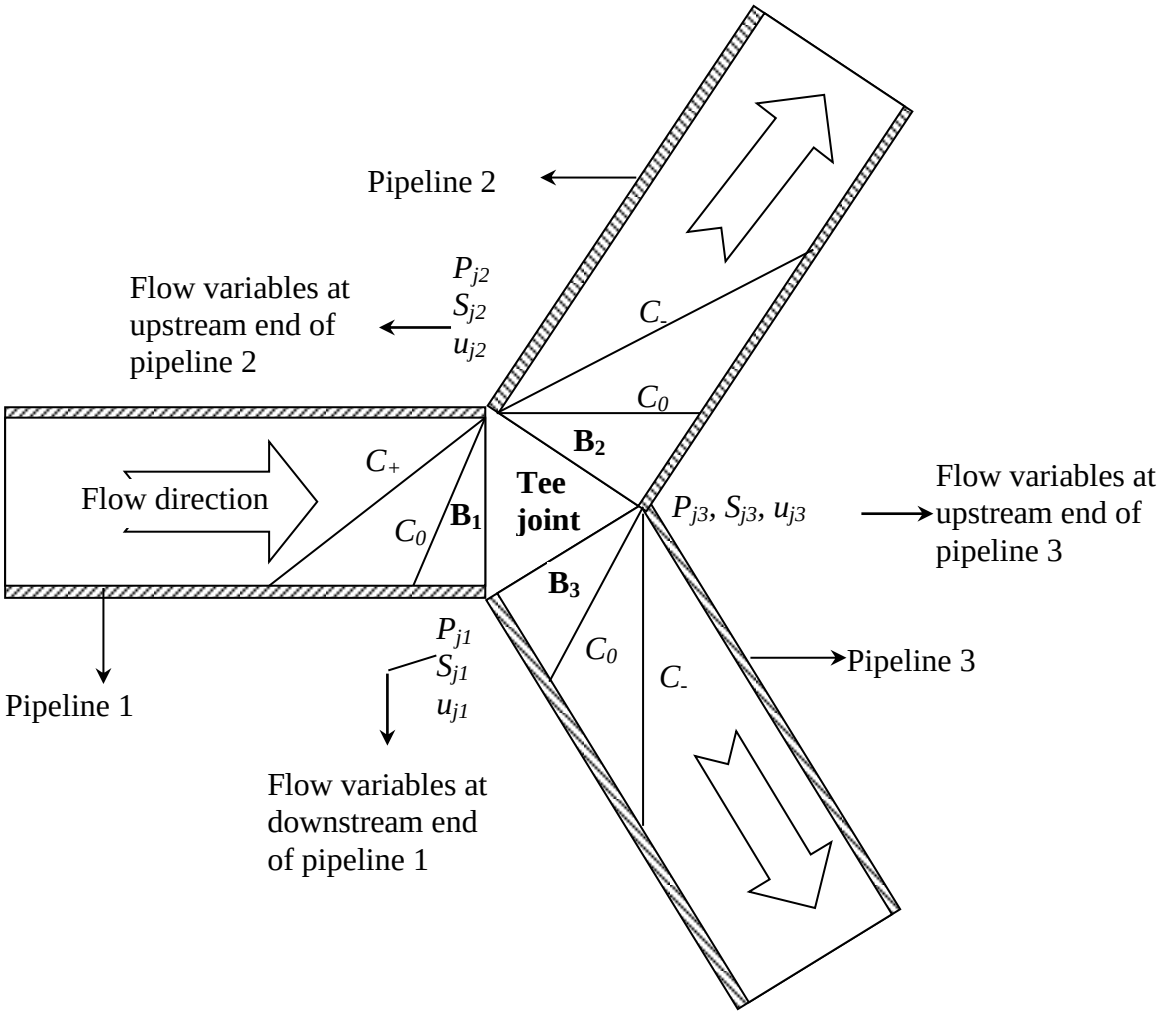

Figure 4.6: Schematic representation of characteristic lines upstream and downstream of a junction of three pipelines.

Assuming no mass accumulation in the junction, the continuity of flow through the junction is given by:

$$\rho_{j1}u_{j1}A_{j1} - \left(\rho_{j2}u_{j2}A_{j2} + \rho_3 u_{j3}A_{j3}\right) = 0 \qquad \textbf{4.31}$$

Where A_{jn} is the cross-sectional area of the pipe.

The two and three pipe boundary conditions account for variation in the direction of fluid flow as well as for pressure losses in the junction fitting and differing pipeline diameters between the pipes connected to the junctions.

4.3.4 Full bore rupture at the downstream end

Two distinct types of flow are assumed to occur at the release plane during outflow from a pipeline:

1. Critical/choked flow
2. Non-choked flow.

During choked flow the release flow rate is at a maximum and the fluid at the orifice is assumed to undergo an isentropic expansion from a pressure above the ambient. For single-phase flow the release velocity is equal to the sonic velocity at the prevailing pressure.

Once the pressure at the release plane has reached the ambient pressure the flow is no longer choked. The release velocity in this case is subsonic and the discharge is driven only by the momentum of the remaining fluid inventory.

At the rupture plane only the C_+ and C_0 characteristics are applicable. In the absence of a simple analytical relationship expressing the expansion process across the release plane, a 'ghost' cell adjacent to the boundary cell, as depicted in figure 4.7, is used to apply suitable conditions to the C_- characteristic. The ghost cell is a fictitious node ($i+1$) lying at the same position as node i as illustrated in figure 4.7.

The introduction of this extra node allows the solution along the negative characteristic. The flow properties at point j are then obtained just as for interior points. Interpolation is not required within the ghost cell as all the properties within it are spatially invariant.

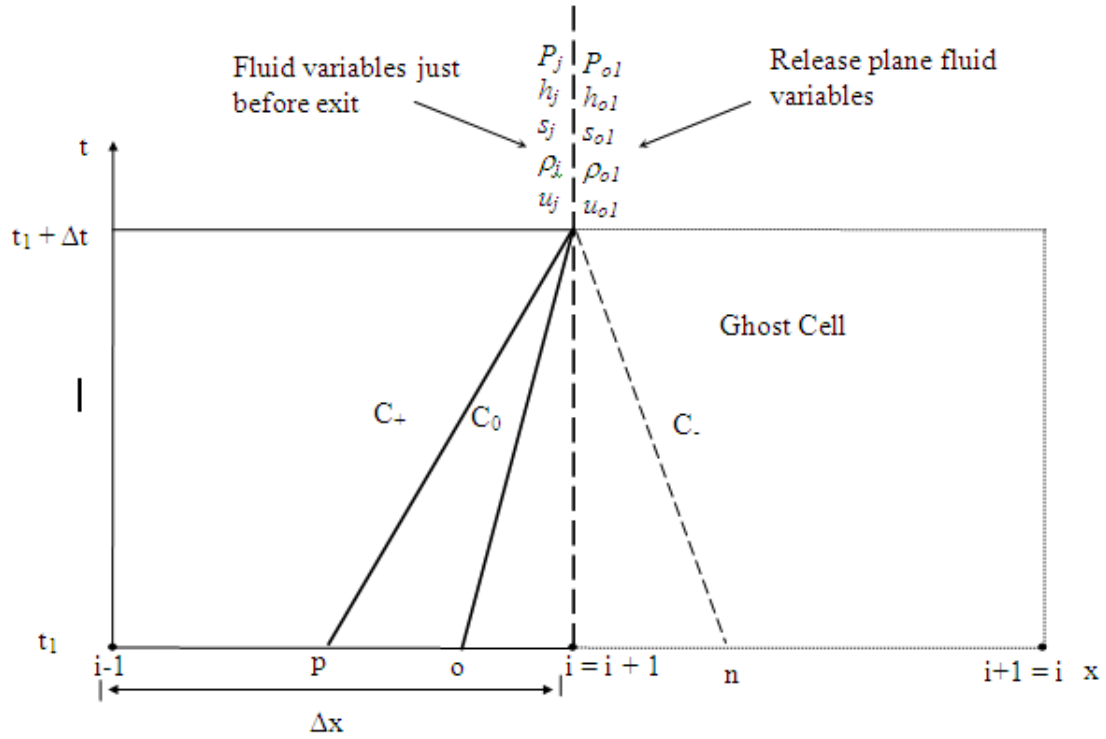

Figure 4.7: Diagram illustrating characteristic lines at the rupture plane based on the concept of a ghost cell.

The flow variables P_{o1}, S_{o1} and u_{o1} (see figure 4.7) at the release plane are calculated using the method described in section 4.3.5.

Mass flow rate is conserved across the release plane. While the expansion process at the release plane is assumed to be isentropic, non-isentropic effects may occur during puncture due to the hydraulic resistance posed by the release orifice. Hence, the actual flow rate of the exiting fluid may be smaller than the assumed isentropic flow rate with the ratio between the two being equal to the discharge coefficient C_d.

Therefore the mass flow rate both approaching and leaving the release plane can be expressed as:

$$u_j \rho_j A_{pipe} = C_d \rho_{o1} u_{o1} A_{o1} \qquad \textbf{4.32}$$

Where A_{o1} and A_{pipe} are the orifice area and pipe areas respectively. P_{o1} and u_{o1} are the fluid density and fluid velocity respectively.

4.3.5 Discharge rate calculation algorithm

As discussed in the previous section, while the discharge pressure is above the downstream pressure the flow is choked and the mass flow rate at the release plane is at a maximum. When the pressure at the release plane drops to the downstream pressure, the flow is no longer choked and the release rate is calculated accordingly.

Figure 4.8 shows the relevant pressures at the release plane that govern the discharge process. P_j, P_{o1} and P_d represent the pressure of the fluid approaching the release plane, the discharge pressure and the downstream or ambient pressure respectively.

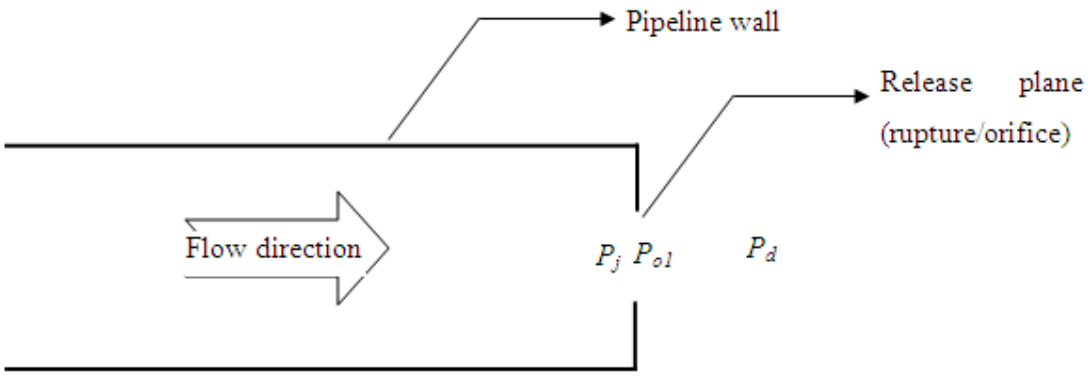

Figure 4.8: A schematic representation of pertinent pressures at the rupture plane governing the discharge rate.

The choked and non-choked discharge rates are calculated by applying an energy balance across the release plane. As mentioned previously the expansion process is assumed to be isentropic. Any additional non-isentropic effects are accounted for by introducing a discharge coefficient (C_d; see equation 4.32).

The energy balance across the release plane, ignoring changes in potential energy between the flow approaching and exiting the failure plane, is given by:

$$h_j + \frac{1}{2}u_j^2 = h_{o1} + \frac{1}{2}u_{o1}^2 \qquad \textbf{4.33}$$

Where the subscripts *j* and *o1* represent the upstream and release plane conditions respectively.

In the case of choked/critical flow the velocity u_{o1} is replaced by the local single/two-phase speed of sound, a_{o1}. The release pressure (P_{o1}) is then obtained by solving equation 4.33 using Brent's (2002) algorithm. The iterative solution of equation 4.33 involves guessing and updating the discharge pressure, P_{o1}, in conjunction with pressure-entropy (isentropic) flash calculations until equation 4.33 is satisfied. Once a solution is obtained, other flow variables at the release plane (ρ_{o1}, T_{o1} and h_{o1}) are determined from a corresponding pressure-entropy (P_{o1}-s_j) flash calculation.

For non-critical flow the release pressure, P_{o1}, is equal to the ambient pressure, P_d. The remaining outflow variables, such as ρ_{o1}, T_{o1} and h_{o1}, may be calculated using a pressure-entropy (P_{o1}-s_j) flash calculation. The release velocity u_{o1} may then be obtained from equation 4.33.

Once the release plane flow conditions are determined u_j is updated using equation 4.32 and employed in the corrector steps (see section 4.2.3) until convergence is achieved. The corresponding calculation flow logic diagram for determining the discharge rate is shown in figure 4.9.

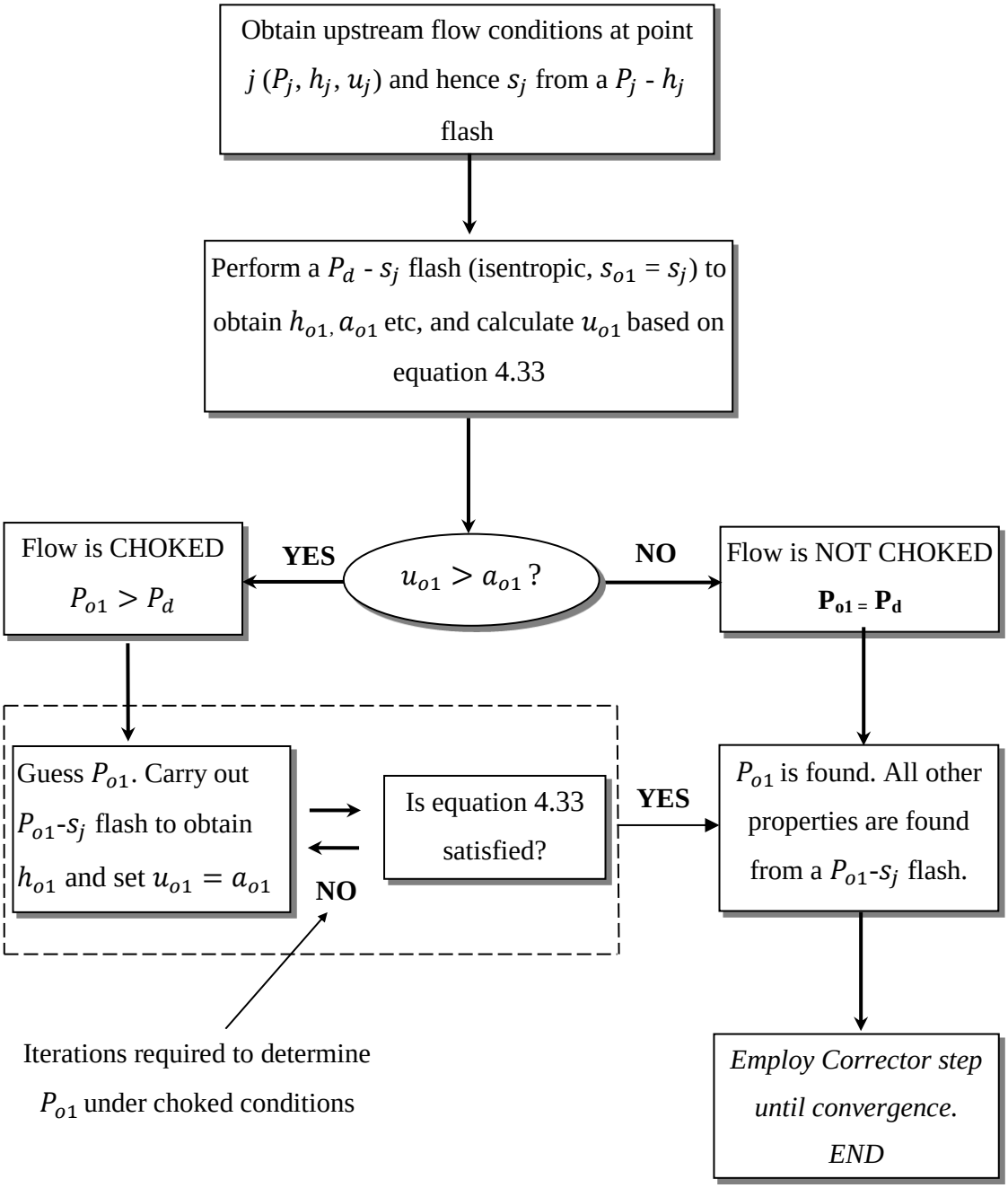

Figure 4.9: Calculation algorithm for obtaining flow variables at the discharge plane (Brown, 2011).

4.4 Conclusion

In this chapter the formulation of the MOC based on the Method of Specified Time intervals (MST) was presented. The governing conservation equations were converted into compatibility and characteristic equations. These were then discretised using the Euler predictor-corrector technique. By assuming that the fluid properties varied linearly between grid points algebraic expressions for the fluid variables at the next time step along the pipeline length were obtained.

The compatibility equations were combined with appropriate boundary conditions to model the fluid dynamics following the failure of multi-segment pipeline networks. The frictional losses due to fittings, changes in pipeline diameter and changes in elevation were accounted for by the introduction of a loss coefficient, K_{loss}.

Chapter 5: Validation of OUTFLOW for CO_2 pipeline modelling

5.1 Introduction

Mathematical simulation models can make a significant contribution to the design and safe operation of industrial processes. However, the predictive accuracy of such models must first be demonstrated against relevant experimental data. In section 2.4.4 the accuracy of the model OUTFLOW in predicting depressurisation rate, discharge rate and rapid transients in the inventory was demonstrated. OUTFLOW pipe wall temperature predictions have not been validated previously due to a lack of appropriate experimental data.

A review of EoS for calculating the properties of CO_2 and CO_2 mixtures was also presented in chapter 2. For models such as OUTFLOW, which are based on the solution of the mass, momentum and energy conservation equations, an appropriate EoS must be used to determine the thermodynamic properties and phase split of the inventory. For CO_2 inventories, a particular requirement is that the EoS is able to accurately calculate the fluid critical and triple point conditions and thermodynamic properties along the fluid saturation line.

Various studies have investigated the accuracy of several EoS for calculating CO_2 fluid properties, as discussed in section 2.6. However, these studies have focused on binary and ternary mixtures and have not considered the full range of impurities expected from the various potential CCS capture technologies in a single mixture. Additionally there is no reported work systematically investigating the impact of these various EoS on the predictive accuracy of any transient outflow models.

The work presented in this chapter therefore addresses the following objectives:

- the identification of an appropriate EoS for modelling CO_2 pipeline blowdown with OUTFLOW;
- the validation of OUTFLOW pipe wall temperature predictions.

The work presented in this chapter comprises three parts. In the first a detailed description of four large scale CO_2 shock tube blowdown experiments is presented. The transient fluid property and pipe wall temperature data recorded during these experiments is used extensively in this chapter and in chapter 6 to assess the accuracy of simulation results. The experiments described were conducted by the UK National Grid as part of the COOLTRANS research programme (UKCCSRC, 2012).

In the second section simulation data of CO_2 shock tube blowdown, generated using OUTFLOW incorporating various EoS, is compared against corresponding experimental data. Based on the degree of agreement between data sets an appropriate EoS is selected for all the subsequent simulation work presented in this thesis.

In the third part of this chapter OUTFLOW pipe wall temperature predictions during pipeline blowdown are validated against experimental data.

5.2 Description of the National Grid shock tube experiments (Cosham et al., 2011, 2012)

5.2.1 Experimental setup

The shock tube used was 144 m long and built from carbon steel. Average values for the pipeline internal diameter (ID), wall thickness and roughness were reported as 146.36 mm, 10.97 mm and 0.005 mm respectively. The shock tube had a downward slope of 0.5° towards the open end and was insulated with a 25 mm thick layer of closed-cell rubber foam. The downward slope was ignored in simulations due to its small magnitude.

Figure 5.1 shows a photograph of the shock tube taken from the rupture end. As may be observed, the shock tube was anchored at this end using a large concrete block that fully surrounded the pipe. Smaller anchor blocks were also placed at regular intervals along the length of the shock tube. A smaller diameter recirculation pipe (ca. 100 mm ID), used to maintain the homogeneity of the inventory and isolated prior to blowdown, was connected to the shock tube at both ends. The rear end of the shock tube was sealed with a domed cap and the rupture end with a bursting disk. Blowdown was initiated by explosively cutting the bursting disk to produce a clean Full Bore Rupture (FBR).

Figure 5.1: An image of the shock tube test rig from the rupture end, the primary anchor block and re-circulation pipe are visible in the left foreground.

The shock tube was instrumented with various transducers distributed along its full length. The type and technical specifications of the instruments used are detailed in table 5.1; their locations and numbering on the shock tube are detailed in table 5.2.

Transducers FP01 to FP35 were temperature compensated Kulite CT-375M fast response pressure transducers mounted flush to the internal bore of the shock tube. These were installed at 12 and 3 o'clock positions in locations 1 to 9 (see table 5.2), the remainder were installed at the 12 o'clock position. Transducers WT01 to WT14 were welded tip, PTFE insulated Type T thermocouples mounted on the outer surface of the pipe wall, under the insulation. The type and manufacturer of the fluid temperature transducers FT01 to FT07 was not specified. In this study they have been assumed to be the same as the wall temperature thermocouples in all respects. They were mounted at 45° to the pressure transducers. All of the instrumentation was calibrated.

Table 5.1: Technical specifications for the instruments mounted on the National Grid shock tube. The fluid temperature transducers have been assumed to be the same make and manufacture as the wall temperature transducers.

Instrument	Range	Sensitivity	Accuracy/resolution	Frequency (KHz)
FP-X – Kulite CT-375M fast response pressure transducers	0.35 – 210 bar; 77.65 – 393.15 K	0.05 – 0.1 MPa	0.05 – 0.1 MPa	150 – 1400
WT-X – Type T thermocouples	-73.15 – 533.15 K	-	± 2.2 K	-
FT-X – Fluid thermocouples	-73.15 – 533.15 K	-	± 2.2 K	-

Table 5.2: A summary of the instruments available on the National Grid shock tube and their locations relative to the open end (Cosham et al., 2011, 2012). (FP = fluid pressure, FT = fluid temperature, WT = wall temperature).

Instrument location	Pressure Transducers	Temperature Transducers	Distance from open end (m)
1	FP01, FP02	-	0.0864
2	FP03, FP04	WT01, FT02	0.34
3	FP05, FP06	-	0.54
4	FP07, FP08	-	0.74
5	FP09, FP10	-	0.94
6	FP11, FP12	-	1.24
7	FP13, FP14	WT02, FT03	1.84
8	FP15, FP16	-	2.44
9	FP17, FP18	-	3.64
10	FP19	-	4.84
11	FP20	WT03	6.04
12	FP21	-	9.04
13	FP22	-	13.54
14	FP23	WT04, FT04	18.04
15	FP24	-	22.54
16	FP25	WT05	30.04
17	FP26	WT06	42.04
18	FP27	WT07, FT05	54.04
19	FP28	WT08	66.04
20	FP29	WT09	77.94
21	FP30	WT10, FT06	89.94
22	FP31	WT11	101.94
23	FP32	WT12	113.94
24	FP33	WT13, FT07	125.94
25	FP34	WT14, FT01	137.94
26	FP35	-	143.775

5.2.2 Experimental methodology and tests conducted

The shock tube was first purged with CO_2 before being charged for each experiment. For experiments using impure CO_2 the shock tube was partially filled with CO_2 before the calculated mass of other gas was added. Additional CO_2 was then added to achieve the desired pressure.

The recirculation loop includes a pump and heat exchangers. While the shock tube is being charged the fluid is circulated through the recirculating loop to encourage mixing. During the final stages of filling the heat exchanger is used to achieve the desired inventory temperature.

For impure inventories samples were taken and tested using gas chromatography. The inventory was considered homogeneously mixed if two consecutive tests performed at least one hour apart yielded essentially the same results.

Once the desired initial test conditions (i.e. temperature, pressure, composition) were achieved the pump in the recirculation loop was shut down and the loop isolated from the shock tube. Inventory temperature and pressure in the shock tube were allowed to equilibrate for typically 10 to 15 minutes. The blowdown experiment was then initiated by explosively cutting the rupture disk.

Various blowdown experiments with different inventory compositions and initial properties were conducted by National Grid (Cosham et al., 2011, 2012). Recorded data from four such experiments is used extensively in this thesis. The inventory compositions and basic test conditions for these experiments are presented in table 5.3.

Table 5.3: Feed composition and initial test conditions for selected CO_2 shock tube experiments (Cosham et al., 2011, 2012).

Experiment	Feed Composition		Feed Temperature (°C)	Feed Pressure (bara)	Ambient Temperature (°C)
	Component	Mole %			
1	CO_2	100	5.1	39.11	17.5
2	CO_2	95.97	5.3	38.91	20.4
	N_2	4.03			
3	CO_2	100	5.2	153.4	10.2
4	CO_2	95.92	20.0	141.41	0.3
	N_2	4.08			

5.2.3 Experimental data recorded

The list of instruments in table 5.2 represents the complete selection of instruments that could be mounted on the shock tube, and their locations. Not all instruments were used in each test and of those that were some did not record useable data. Additionally, only limited experimental data has been shared by National Grid.

For experiments 1 and 2, the available experimental data has been published as plots of the fluid pressure against decompression wave speed (calculated using the data captured from transducers FP03 to FP18). Additionally data for the variation of fluid pressure with time during the first second of decompression has been published for experiment 1 only (Cosham et al., 2011).

Limited experimental data has been published for experiments 3 and 4, see for example Cosham et al. (2012). Further data from experiments 3 and 4 used in this thesis was made available by National Grid as part of the COOLTRANS research programme (UKCCSRC, 2012). Pressure and temperature history data was provided from transducers FP35, FT01 and FT07 for both experiments 3 and 4. Additionally, pressure history data from the first 2 s of discharge was available from transducers FP25, FP28

and FP31 for experiment 3 only. Wall temperature history data from both experiments was available from transducers WT02 to WT14.

5.2.4 Simulating the National Grid experiments

Throughout this thesis the National Grid shock tube experiments described in this section are referred to as "experiment *number*". All simulations are referred to as "Test *number*"; those simulations based on National Grid experiments are clearly indicated.

All simulations assume that the inventory is at rest and homogeneously mixed, with no variation in fluid properties along the length of the shock tube, prior to blowdown. Additionally, it is assumed that there is no longitudinal variation in wall temperature prior to blowdown

5.3 Selection of an Equation of State for modelling outflow

In this section work to identify an appropriate EoS for modelling CO_2 pipeline blowdown is presented. Various EoS are available for use in OUTFLOW to calculate the fluid density, speed of sound and phase split; parameters required for the accurate modelling of rapid transients. The available experimental data from experiments 1 and 2, consisting of plots of recorded pressure vs. decompression wave speed, may therefore be used to assess the accuracy of an EoS in calculating the above parameters, and therefore its suitability for modelling CO_2 pipeline blowdown.

5.3.1 Simulating gas phase shock tube experiments 1 and 2

Simulations of experiments 1 and 2 (see table 5.3) were conducted using OUTFLOW, these are numbered Tests 1 and 2 respectively. A complete list of the simulation parameters is given in table 5.4. Outflow from the shock tube was simulated for 5 s following FBR in each case.

Table 5.4: Simulation parameters used for modelling the National Grid experiments 1 and 2, blowdown of a shock tube containing gas phase CO_2.

	Inputs	Test 1	Test 2
Pipeline characteristics	Upstream fitting	Closed end	Closed end
	Downstream fitting	Rupture disk	Rupture disk
	Pipe length (m)	144	144
	Pipe external diameter (mm)	171.94	171.94
	Pipe wall thickness (mm)	10.97	10.97
	Pipe roughness (mm)	0.0000043	0.0000043
	Pipe orientation to the horizontal plane (°)	0	0
	Heat transfer option	Insulated	Insulated
	Heat transfer coefficient (W/m^2K)	5	5
Inventory and ambient parameters	Feed composition (mole %)	CO_2 100	CO_2 95.97
			N_2 4.03
	Fluid temperature (°K)	278.25	278.45
	Fluid pressure (bara)	39.11	38.91
	Ambient temperature (°K)	290.65	293.55
	Ambient pressure (bara)	1.01	1.01
Failure parameters	Failure mode	FBR	FBR
	Failure location relative to upstream end (m)	144	144
	Discharge coefficient	1	1
Other parameters	Number of pipe grid points	100	100
	Simulation model	HEM	HEM
	Equation of State	SRK, PR, MPR, PRSV-1	SRK, PR, MPR, PRSV-1
	Friction factor correlation	Chen (Equation 3.33)	Chen (Equation 3.33)
	Total depressurisation time (s)	5	5

5.3.2 Equations of State investigated for modelling pipeline blowdown

Tests 1 and 2 were simulated using four cubic EoS:

- Soave Redlich-Kwong (SRK) (Soave, 1972) (equation 3.5, section 3.4)
- Peng-Robinson (PR) (Peng and Robinson, 1976) (equation 3.6, section 3.4)
- modified PR (MPR) of Wu and Chen (1996) (equation 3.7, section 3.4)
- modified PR (PRSV-1) of Stryjek and Vera (1986)

The PRSV-1 EoS retains the basic form of the PR EoS given in section 3.4. However, the κ function used in equation 3.14 is modified by Stryjek and Vera (1986):

$$\kappa = \kappa_0 + \kappa_1(1 + T_r^{0.5})(0.7 - T_r) \quad \textbf{5.1}$$

$$\kappa_0 = 0.378893 + 1.4897153\omega - 0.17131848\omega^2 + 0.0196554\omega^3 \quad \textbf{5.2}$$

The binary interactions parameters used in OUTFLOW have not been calibrated for CO_2 and its mixtures, therefore based on the work of Li and Yan (2009a, 2009b) (see section 2.6.2) both the PR and the SRK EoS are included in this study. It has been reported however that the PR EoS can produce errors in calculated density of up to 15 %, especially at low temperatures (ca. -50 °C) (UCL, 2010). The PRSV-1 EoS has been reported to produce more accurate vapour pressure predictions at reduced temperatures (T_r) ≤ 0.7 for a variety of compounds, including CO_2, compared with the PR EoS (Stryjek and Vera, 1986). Reduced temperature is calculated from T/T_c. For pure CO_2 a T_r of 0.7 corresponds to a fluid temperature of 213 K; 3 K below the triple point temperature. The PRSV-1 therefore has the potential to maintain calculation accuracy in the event that inventory properties pass the triple point during depressurisation. The MPR EoS is included in the present investigation as it has been shown to produce excellent agreement with the SW density predictions for pure CO_2 in the liquid and vapour phases and along the saturation line. The SW EoS may be considered as a bench mark as it is primarily based on fitting to experimental data (Span and Wagner, 1996).

The GERG 2008 EoS (Kunz et al., 2007) was developed for modelling natural gas mixtures and it has since been considered for CCS systems. Its reported accuracy in the temperature/pressure range for CCS is reported to be high (Li et al., 2011). However its use in OUTFLOW resulted in prohibitively long computational run times. As the SW EoS possesses a similar level of complexity to the GERG, its incorporation into OUTFLOW was not attempted.

Cosham et al. (2011) simulated National Grid experiments 1 and 2 using the isentropic decompression model DECOM. This model utilised the Span and Wagner (1996) EoS (SW) for Test 1 and the GERG 2008 EoS (Kunz et al., 2007) for Test 2.

Therefore in this study OUTFLOW results for Tests 1 and 2 generated with the SRK, PR, MPR and PRSV-1 EoS were compared with both the available experimental and DECOM data.

The OUTFLOW predicted decompression wave speed is calculated by subtracting the fluid velocity, u, from the speed of sound, a, (i.e. $a - u$) at the grid point closest (1.44 m) to the rupture plane (referred to as point A hereafter).

5.3.3 Comparison of the performance of selected EoS

Figures 5.2 and 5.3 present the comparisons of the experimental and simulated fluid pressure against decompression wave speed for Tests 1 and 2 respectively. OUTFLOW simulations were conducted using the EoS equations 3.6, 3.7, PRSV-1 (3.6 with 5.1) and 3.5 (PR, MPR, PRSV-1 and SRK respectively). As the raw experimental data was unavailable, it was instead extracted from pressure vs decompression wave speed figures presented in Cosham et al. (2011). As stated above (see table 5.1), the claimed certainty in the measured pressures is ±0.05-0.1 MPa.

Referring to the data in figures 5.2 and 5.3, several trends may be observed. In order of appearance, decreasing fluid pressure is associated with decreasing decompression wave speed in both the experimental and simulated data. Slight plateaux in the fluid pressure (indicated on the figures) resulting from discontinuities in the speed of sound are observed in each curve. These occur due to the transformation of the inventory from vapour to a two-phase mixture. For all cases, the predicted plateaux occur at higher pressures than observed experimentally. This was attributed by Cosham et al. (2011) to delayed nucleation in the inventory which is not accounted for in OUTFLOW.

The simulated and experimental data are in reasonable agreement for two phase fluids at pressures above ca. 16 bara. Below 10 bara the experimental decompression wave speed reaches 0 m/s, indicating the decompression wave has been ejected from the shock tube. In contrast DECOM predicts the decompression wave is ejected from the shock tube as the pressure reaches ca. 14 bara. OUTFLOW, with all the cubic EoS considered, predicts that below 16 bara the decompression wave speed remains relatively constant at ca. 40 m/s. This prediction follows from the equation used to calculate decompression wave speed at point A (1.44 m behind the rupture plane). In practise OUTFLOW predicts the ejection of the decompression wave from the shock tube as the pressure at the rupture plane passes ca. 10 bara.

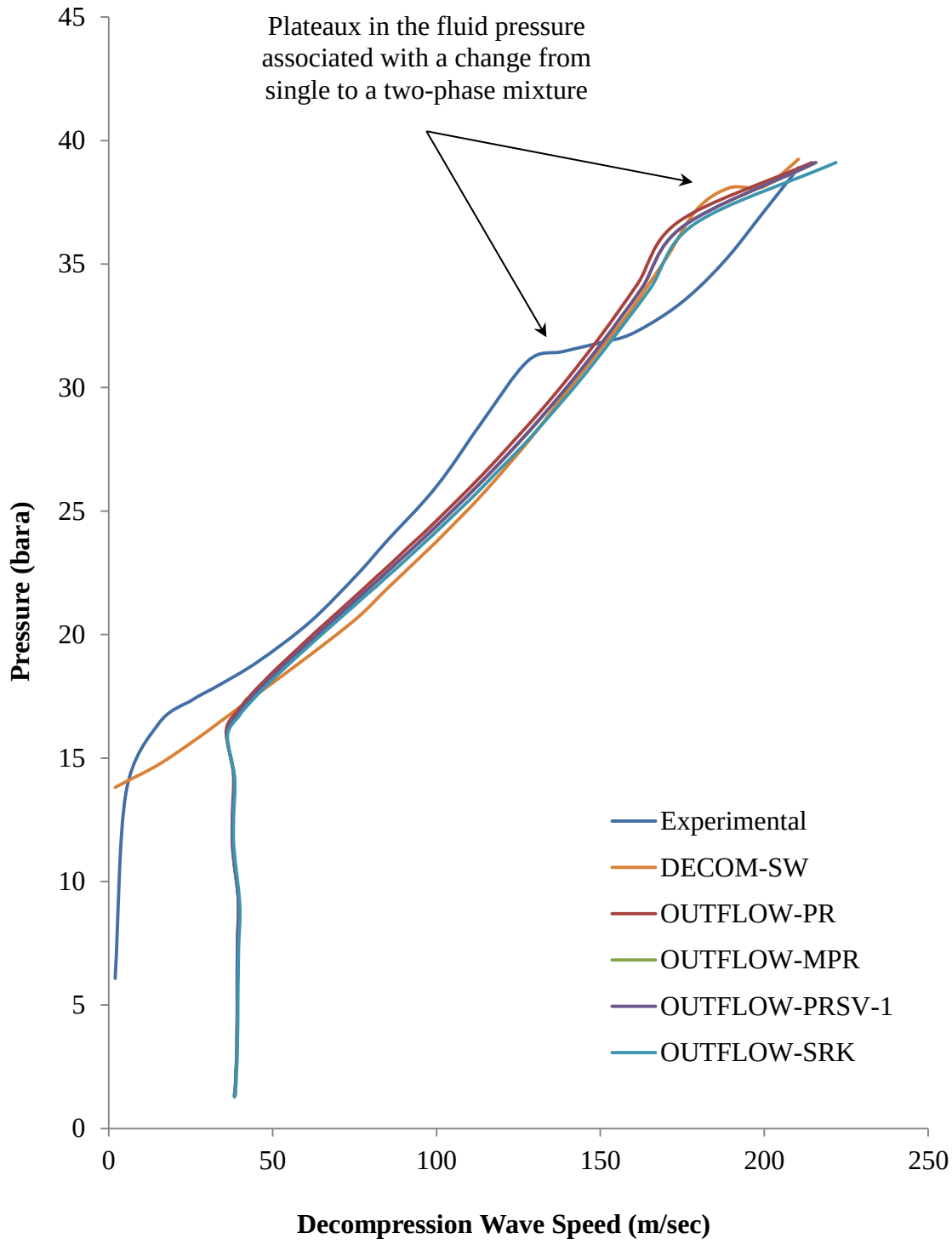

Figure 5.2: Simulated and experimental fluid pressure vs. decompression wave velocity for Test 1 (pure CO_2; see table 5.4).

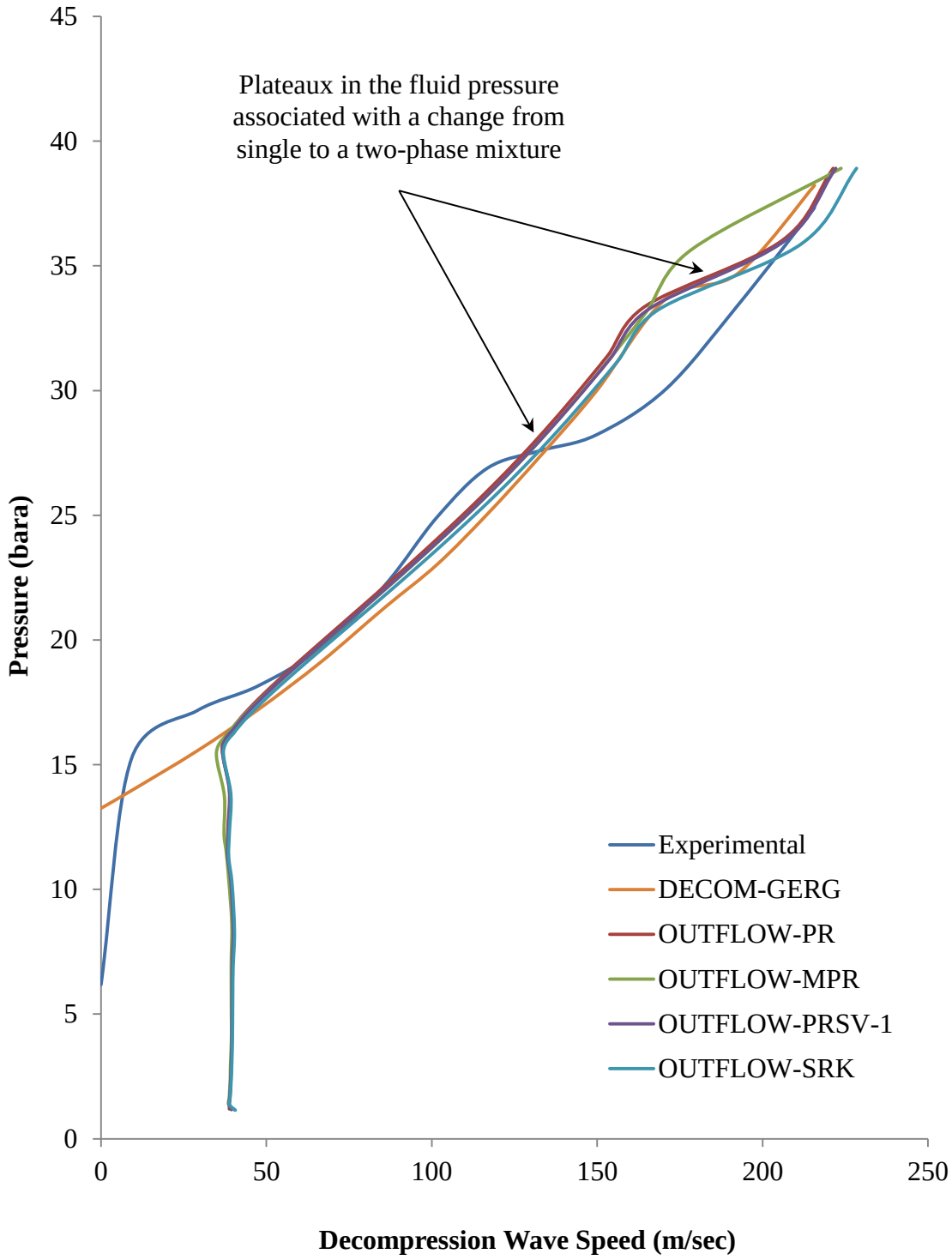

Figure 5.3: Simulated and experimental fluid pressure vs. decompression wave velocity for Test 2 (CO_2 with 4.03 mol% N_2 impurity; see table 5.4).

For Tests 1 and 2, the DECOM data incorporating the SW and GERG EoS slightly over predicts the two-phase decompression wave speed compared with both the experimental

data and the OUTFLOW data generated using all the cubic EoS considered. All the OUTFLOW simulations predict very similar decompression wave speeds, these are in best agreement with the experimental two phase decompression wave speed at pressures between 16 and 25 bara. It may therefore be inferred that when incorporated in OUTFLOW there is little difference in the performance of the cubic EoS considered for calculating fluid density, phase split and speed of sound between ca. 16 to 40 bara. This pressure range is relatively small however, especially in the context of CO_2 pipeline transportation.

Analysis of the available OUTFLOW simulation data indicates that a reduced inventory temperature, T_r, of 0.7 is not reached in either test before the decompression wave is ejected from the shock tube. No experimental temperature data was available to confirm this prediction. Assessing the accuracy of the PRSV-1 at lower temperatures was therefore not possible for Tests 1 and 2.

Figure 5.4 presents the fluid pressure/time histories from transducers FP20, FP22 and FP23 (see table 5.2) for Test 1, together with the corresponding simulated data generated using OUTFLOW incorporating the PR EoS. Experimental data is available for the first 1000 ms following FBR. As may be observed, following test initiation the recorded pressure first increases before dropping sharply, this is due to the explosive cutting of the rupture disk and passage of the decompression wave. After this a short plateau is observed at each transducer, corresponding to the change from single to a two phase mixture. Both phenomena are indicated on figure 5.4. The recorded pressure then continues to decrease.

As may be observed, the predicted pressure histories at each transducer show relatively good agreement with the experimental data during the first 1000 ms of blowdown. In particular there is good agreement in the times at which the simulated and experimental decompression waves reach each transducer position (as indicated by the time at which the pressure changes from the initial pressure). The data demonstrates the ability of the PR EoS to accurately model rapid transients in vapour phase and saturated CO_2 at $T_r > 0.7$.

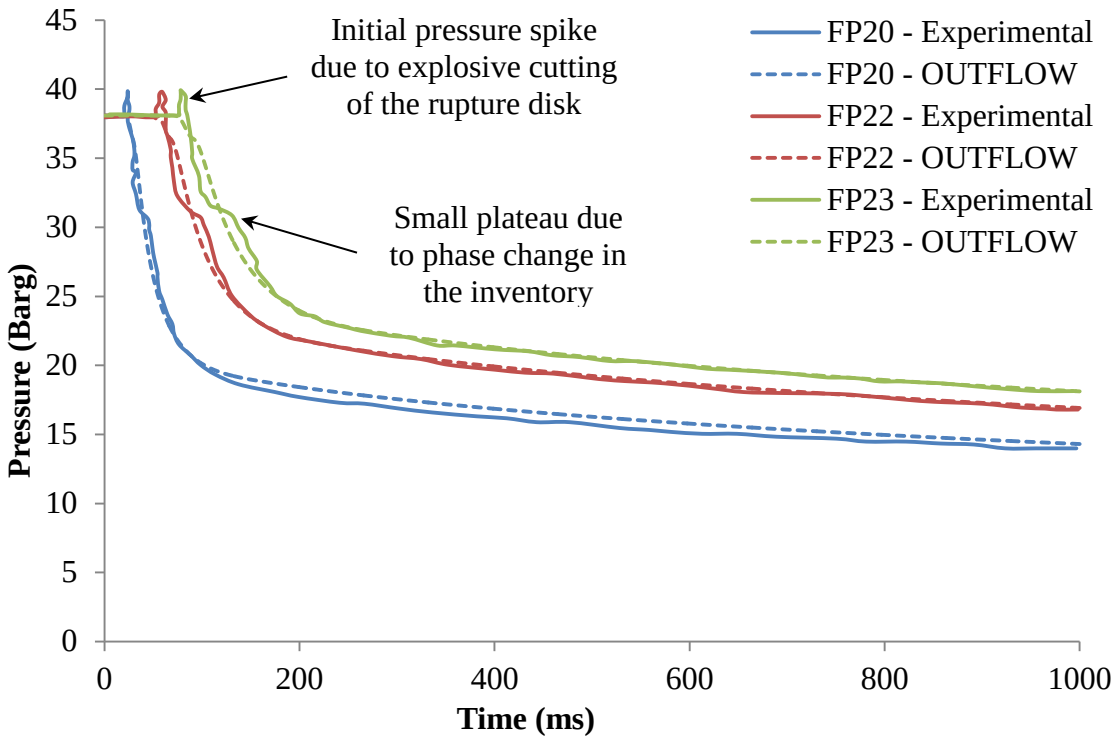

Figure 5.4: Test 1 experimental and PR simulated fluid pressure histories from transducers FP20, FP22 and FP23 during the first 1000 ms of blowdown.

Summary of results

OUTFLOW simulations of Tests 1 and 2 (pure CO_2 and CO_2 with 4.03 % N_2 respectively), with each of the cubic EoS considered, demonstrated marginally better agreement with experimental decompression wave speed between 16 and 25 bara compared to the DECOM data. Insufficient experimental data was available to properly assess the claimed advantages of the MPR and PRSV-1 EoS over the PR EoS. Comparison of Test 1 experimental and simulated pressure histories from various transducers demonstrated that the PR EoS is able to accurately predict depressurisation rate and decompression wave speed in the inventory. The PR EoS has therefore been selected for use in all modelling work in this thesis.

5.4 Validation of the OUTFLOW wall temperature model

In this section experimental pipe wall temperature data recorded from the National Grid shock tube experiments 3 and 4 (see table 5.3) are used to validate OUTFLOW pipe wall temperature predictions.

5.4.1 Description of the simulations conducted

Simulations of experiments 3 and 4 (see table 5.3) were conducted using OUTFLOW, these are numbered Tests 3 and 4 respectively. A complete list of the simulation parameters is given in table 5.5.

A description of experiments 3 and 4, including of the data recorded, has been presented in section 5.2.

Data from wall temperature transducers WT02 to WT14 (see table 5.2) was used to validate the wall temperature predictions of OUTFLOW.

Table 5.5: Simulation parameters for Tests 3 and 4, the blowdown of a shock tube containing dense phase CO_2.

	Inputs	Test 3	Test 4
Pipeline characteristics	Upstream fitting	Closed end	Closed end
	Downstream fitting	Rupture disk	Rupture disk
	Pipe length (m)	144	144
	Pipe external diameter (mm)	171.94	171.94
	Pipe wall thickness (mm)	10.97	10.97
	Pipe roughness (mm)	0.0000043	0.0000043
	Pipe orientation to the horizontal plane (°)	0	0
	Heat transfer option	Insulated	Insulated
	Heat transfer coefficient (W/m^2K)	5	5
Inventory and ambient parameters	Feed composition (mole %)	CO_2 100	CO_2 95.92 N_2 4.08
	Fluid temperature (°K)	278.35	293.15
	Fluid pressure (bara)	153.41	141.41
	Ambient temperature (°K)	283.35	273.45
	Ambient pressure (bara)	1.01	1.01
Failure parameters	Failure mode	FBR	FBR
	Failure location relative to upstream end (m)	144	144
	Discharge coefficient	1	1
Other parameters	Number of pipe grid points	144	144
	Simulation model	HEM	HEM
	Equation of State	PR (equation 3.6)	PR (equation 3.6)
	Friction factor correlation	Chen (Equation 3.33)	Chen (Equation 3.33)
	Total depressurisation time (s)	25	25

5.4.2 OUTFLOW wall temperature validation results

Figure 5.5 presents experimental and OUTFLOW predicted pipe wall temperature profiles for Test 3 at time intervals of 0, 5, 10, 15 and 20 s following rupture. The experimental temperature profiles at each time interval are based on data from transducers WT02 to WT14. Before FBR considerable variation in the experimental pipe wall temperatures was observed; this can be ascribed to instrument calibration. Thermocouples WT05, WT08 and WT10 reported an initial pipe wall temperature closest to the calculated initial wall temperature (281.75 K). Wall temperature histories from these transducers are compared with the corresponding simulated data in figure 5.6. The locations of these instruments are indicated in figure 5.5.

Referring to figures 5.5 and 5.6 it may be observed that the temperature of the pipe wall prior to blowdown is over predicted. Cooling of the pipe wall is predicted to occur immediately upon rupture in contrast to the experimental data which indicates a distinct delay in the onset of cooling. Referring to figure 5.6, a decrease in the predicted rate of cooling, resulting from rapid transients in the inventory, is observed between ca. 3 and 5 s. Cooling of the pipe wall is predicted to cease significantly earlier than observed experimentally (at ca. 15 s), and at significantly colder temperatures.

Figure 5.7 presents the experimental and predicted wall temperature profiles at various times for Test 4. Figure 5.8 presents the corresponding experimental and simulated wall temperature histories at transducers WT04, WT08 and WT11. As may be observed the Test 4 pipe wall temperature predictions display the same trends in behaviour as discussed for Test 3.

In summary, the accuracy of the OUTFLOW predicted wall temperature data was poor. The model OUTFLOW (reviewed in section 2.4.4) is therefore inappropriate for investigating pipe wall cooling in CO_2 pipelines during blowdown.

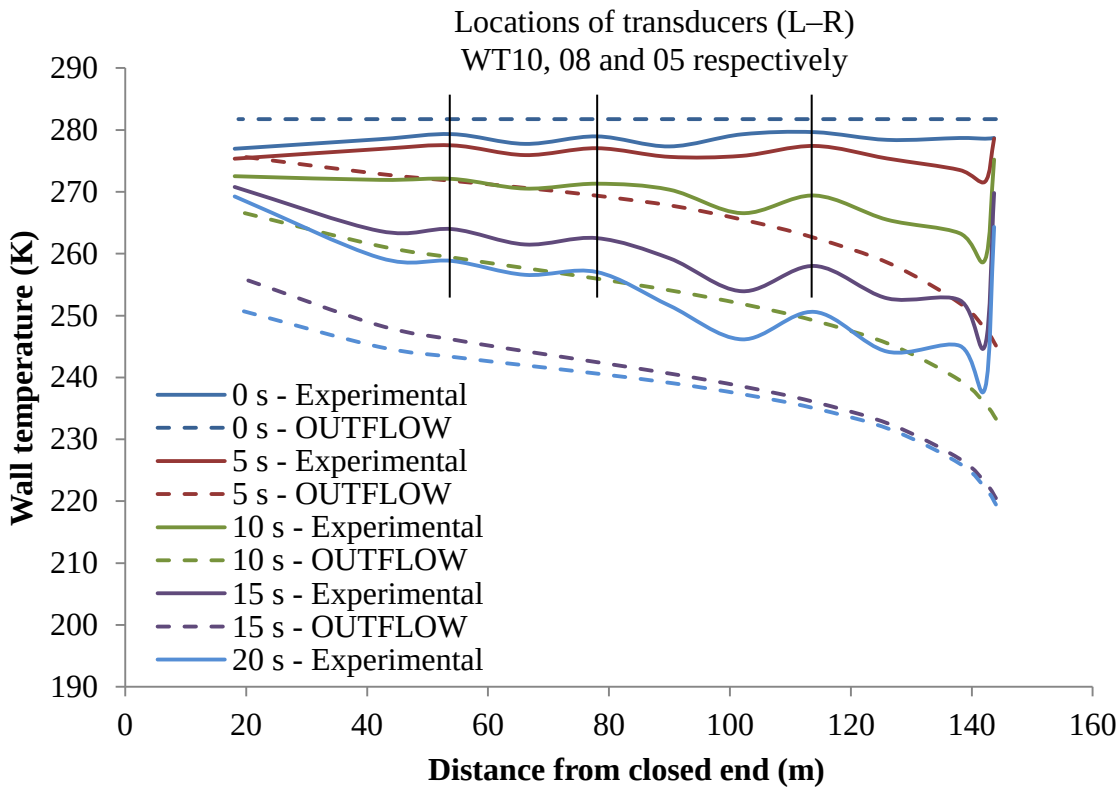

Figure 5.5: Experimental and OUTFLOW predicted pipe wall temperature profiles at various times for Test 3 (pure CO_2; see table 5.5).

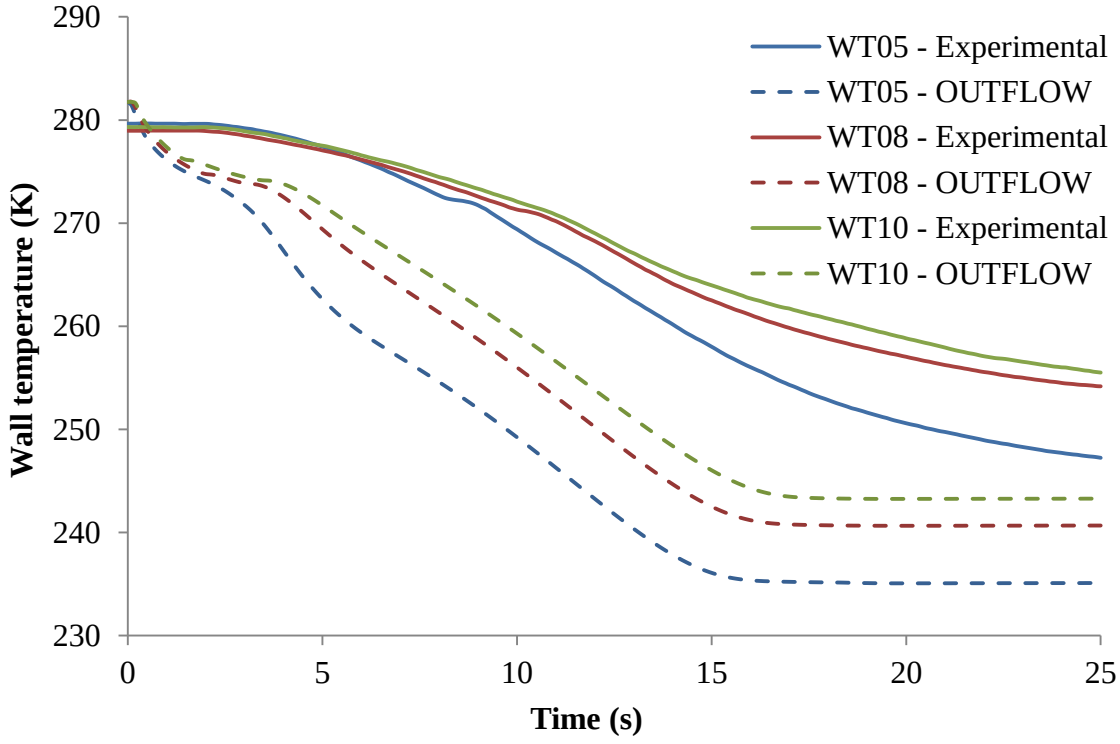

Figure 5.6: Experimental and OUTFLOW predicted pipe wall temperature histories at transducers WT05, 08 and 10 for Test 3 (pure CO_2; see table 5.5).

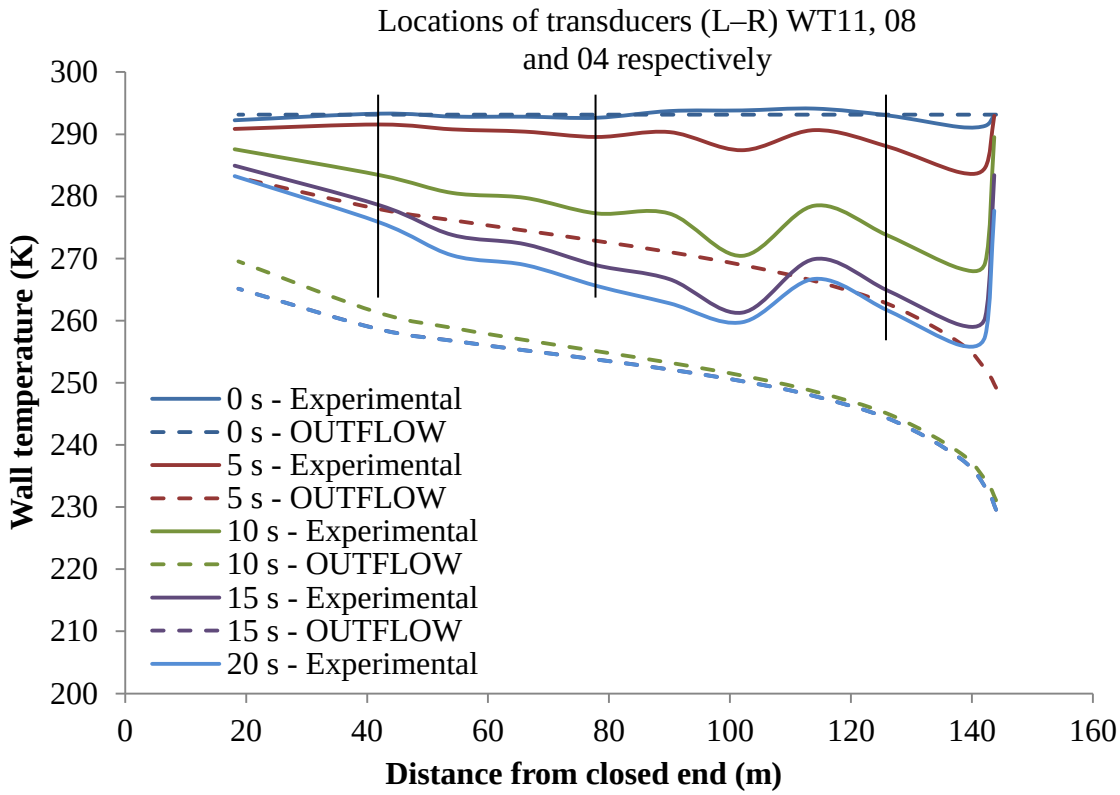

Figure 5.7: Experimental and OUTFLOW predicted pipe wall temperature profiles at various times for Test 4 (CO_2 with 4.08 mol% N_2; see table 5.5).

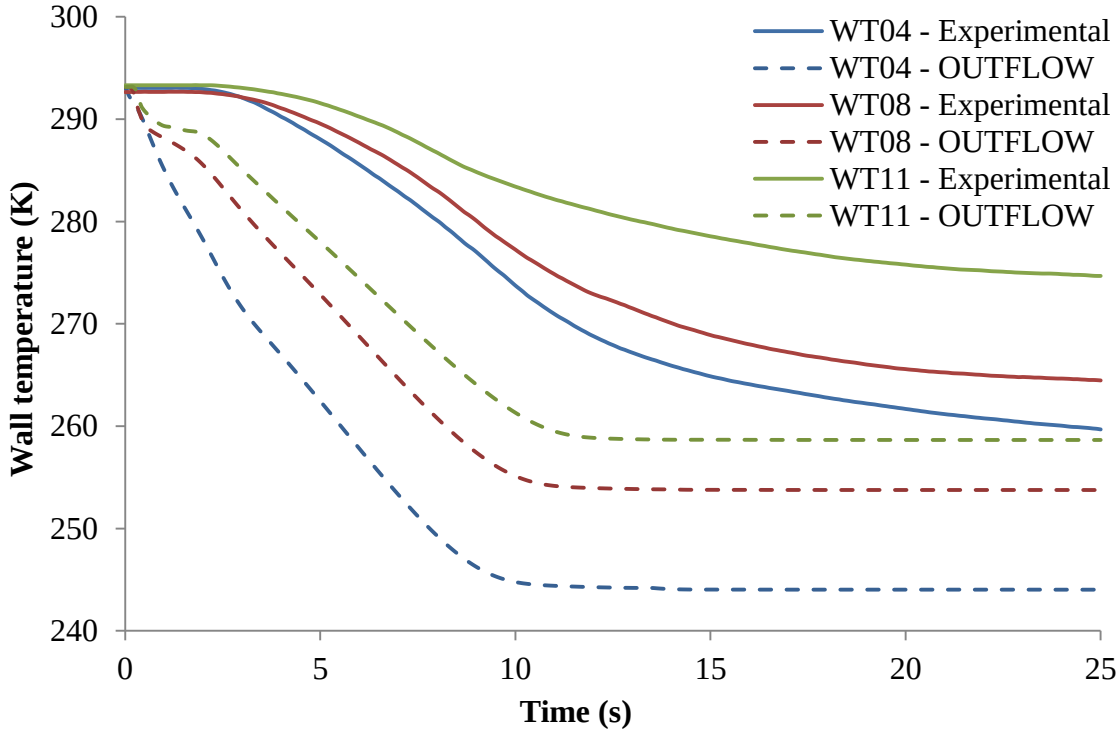

Figure 5.8: Experimental and OUTFLOW predicted pipe wall temperature histories at transducers WT04, 08 and 11 for Test 4 (CO_2 with 4.08 mol% N_2; see table 5.5).

5.5 Conclusion

In this chapter an EoS appropriate for modelling the blowdown of CO_2 pipelines was selected based on a comparison of the performance of various EoS when used to model blowdown of a shock tube using OUTFLOW. Of the EoS considered, the PR EoS was selected for use in this thesis as it was demonstrated to be able to model rapid transients in the gas phase inventory with acceptable accuracy.

The wall temperature predictions of the model OUTFLOW were validated against shock tube decompression data for dense phase CO_2 inventories. Model predictions were seen to significantly over predict the degree of cooling and under predict duration. The OUTFLOW wall temperature model reported in section 3.6 is therefore shown to be inappropriate for modelling CO_2 pipeline venting.

In the next chapter the development of a Finite Element model of heat conduction for use in calculating heat conduction in a pipe wall is presented. The integration of this model with OUTFLOW is described and the new composite model is validated against data from experiments 3 and 4.

Chapter 6: Development and validation of a Finite Element heat conduction model for calculating transient pipe wall temperatures during outflow from pipelines

6.1 Introduction

As discussed in chapter 1, the prediction of the transient discharge rate from a failed pipeline is central to predicting all hazards associated with a release. In the specific case of pipelines carrying CO_2 for CCS an important consequence of pipeline failure is rapid cooling in the pipe wall driven by the depressurisation of the inventory. Thus any discharge model applied to CO_2 pipeline failure modelling must also be capable of predicting transient temperature changes in a pipe wall adjoining an inventory.

The discharge model OUTFLOW was reviewed in chapter 2 and shown to be able to accurately model depressurisation rate, discharge rate and rapid transients in an inventory following pipeline failure. However, the validation of the OUTFLOW wall temperature model, presented in chapter 5, demonstrated that it is not capable of accurately predicting transient wall temperatures following pipeline failure.

In this chapter the development and integration into OUTFLOW of a Finite Element model for heat conduction in a pipe wall is presented. The composite model, referred to as FEM-O, is then validated. The selection of a Finite Element model for modelling wall temperatures is discussed in section 2.5 and a description of the experiments used in the validation of FEM-O is presented in section 5.2.

6.2 A Finite Element Model (FEM) of heat conduction

As discussed in section 2.5, a FEM model of heat conduction was selected for modelling pipe wall temperatures during venting/blowdown of CO_2 pipelines. This model was selected for its flexibility in discretising the solution domain. This flexibility will allow the future extension of the model to simulating transient temperature changes in complex inline infrastructure such as valves or pipeline junctions.

In this section the formulation of the FEM heat conduction model and its integration with OUTFLOW is described. The combined models are referred to as FEM-O.

6.2.1 Discretisation and boundary conditions for the solution domain

In section 3.6.1 it was noted that the OUTFLOW wall temperature model assumes only radial heat transfer through the wall. This assumption may not be suitable for short vent pipes where longitudinal heat conduction may be significant. Given the conservation equations 3.1 to 3.3 are solved for one dimensional, homogeneous equilibrium flow, a two dimensional (axial and radial) heat conduction model for the pipe wall and surrounding material is the most complex the fluid model can exploit.

Axial node coordinates

The rectangular solution domain representing the pipe wall is therefore discretised into a two dimensional mesh of regularly sized triangular elements with nodes located at each element corner, as illustrated in figure 6.1.

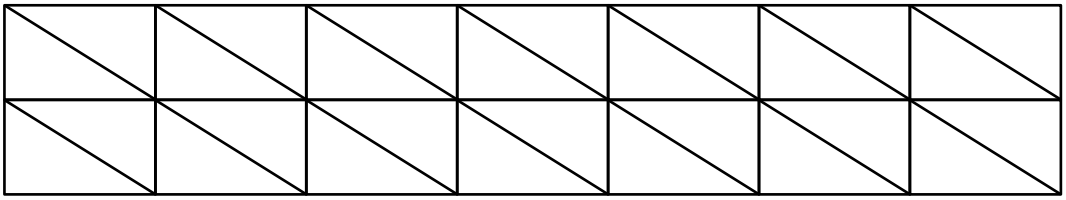

Figure 6.1: An illustration of a Finite Element mesh composed of triangular elements (three rows and eight columns of nodes in this schematic).

When solving the conservation equations, heat flux between the pipe wall and fluid is accounted for by the term Q_h in the energy conservation equation 3.3 only. Thus each fluid grid point is associated with a column of FEM nodes at the same axial coordinate to simplify the calculation of Q_h. The number of fluid grid points, assumed to be evenly distributed in the fluid, is specified by the user. A total of eleven rows of nodes are used in the FEM mesh, their radial coordinates are dependent on the environment in which the pipeline is modelled.

Radial node coordinates

The pipeline may be modelled as exposed to air, insulated or buried. The ten rows of elements in the FEM solution domain are grouped accordingly, as shown in figure 6.2. Permanent boundary conditions applied to the solution domain are also illustrated.

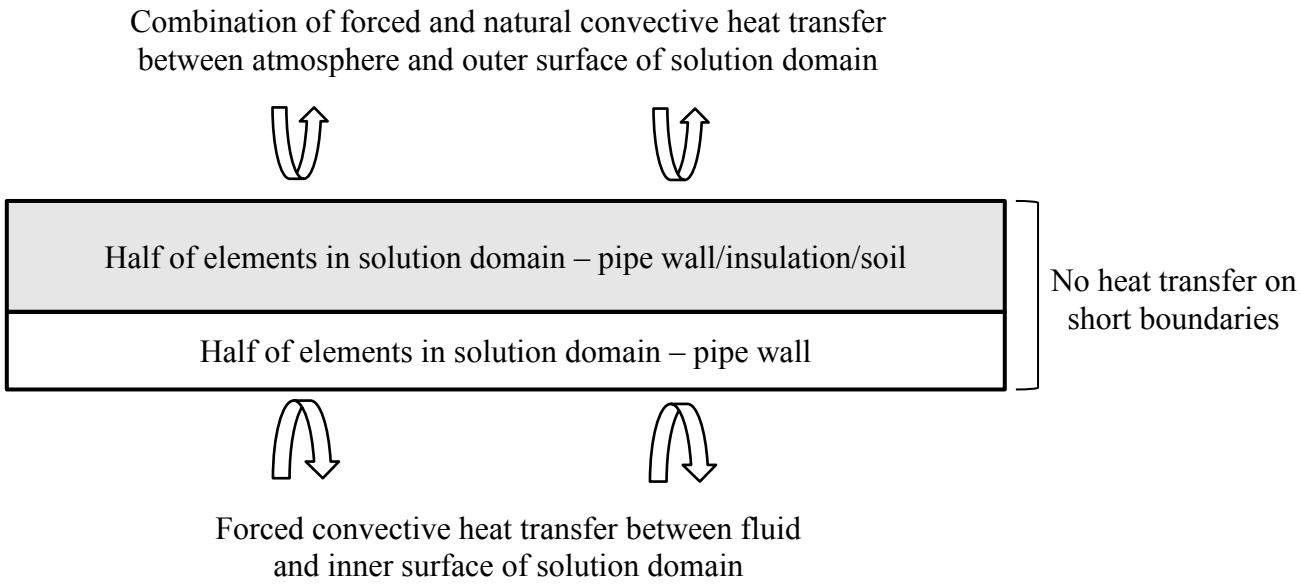

Figure 6.2: Subdivisions of, and boundary conditions applied to, the FEM solution domain to model heat conduction in the pipe wall of pipes exposed to air, insulated or buried.

When modelling as pipe exposed to air all ten rows of elements are used to represent the pipe wall. For insulated or buried pipes five rows of elements are used to represent the

pipe wall and five rows the insulation or soil. The pipe wall thickness is specified by the researcher. The insulation layer thickness is assumed to be two and a half times that of the pipe wall, alternatively the soil burial depth has been assumed to be 1.5 m. Radial coordinates of the FEM nodes are calculated accordingly. Thus elements corresponding to the different materials are different sizes, however all elements corresponding to a particular material are the same size.

With the dimensions of the solution domain specified the coordinates of the nodes within it and the shape function for each node, N_i, may be calculated, where the subscript *i* denotes the node.

Development of a sparse FEM grid

Early testing of FEM-O demonstrated that the FEM model consumed a significant amount of computer memory, resulting in prohibitively long computational run times for longer pipelines. A sparse FEM grid system was therefore developed for use when the number of fluid grid points was greater than 200. In this case, the ratio of fluid grid points to columns of FEM nodes is reduced from 1:1 to 10:1. As discussed previously, it is assumed that fluid grid points remain equally distributed. The columns of FEM nodes remain equally spaced in the solution domain. Flux values at fluid grid points without a corresponding column of FEM nodes are calculated by interpolating values between relevant FEM nodes.

6.2.2 Formulation of the Finite Element heat conduction model

Two dimensional heat conduction in a substance with isotropic thermal conductivity and no heat generation is given by:

$$\frac{\delta}{\delta x}\left(k\frac{\delta T}{\delta x}\right)+\frac{\delta}{\delta y}\left(k\frac{\delta T}{\delta y}\right)=\rho c_p\frac{\delta T}{\delta t} \qquad \textbf{6.1}$$

Where T is the temperature, t the time, x is the axial pipeline coordinate and y the radial coordinate. k, ρ and c_p are the thermal conductivity, density and heat capacity of the pipe wall respectively.

Convective boundary conditions are applied between the pipe wall and fluid and insulation/soil and atmosphere, these are respectively given by:

$$k\frac{\delta T}{\delta x}l + k\frac{\delta T}{\delta y}m + h\left(T_{wall} - T_f\right) = 0 \; on \; \Gamma_{inner} \qquad \textbf{6.2}$$

$$k\frac{\delta T}{\delta x}l + k\frac{\delta T}{\delta y}m + h(T_{ins} - T_{amb}) = 0 \; on \; \Gamma_{outer} \qquad \textbf{6.3}$$

Where h is the convective heat transfer coefficient, T_{amb} the ambient temperature, T_{ins} the temperature of the insulation/soil surface, T_{wall} the temperature of the wall surface and T_f the fluid temperature. l and m are direction cosines normal to the boundary, Γ represents the boundary.

Heat transfer between the short ends of the FEM mesh and the ambient is ignored, as indicated in figure 6.2.

Using the Galerkin Method, the temperature over the solution domain is discretised as follows:

$$T(x,y,t) = \sum_{i=1}^{n} N_i(x,y)T_i(t) \qquad \textbf{6.4}$$

Where N_i are the element shape functions, n is the number of nodes in the element and $T_i(t)$ are the time dependent nodal temperatures.

The Galerkin representation of equation 6.1 is:

$$\int_{\Omega} N_i\left[\frac{\delta}{\delta x}\left(k\frac{\delta T}{\delta x}\right) + \frac{\delta}{\delta y}\left(k\frac{\delta T}{\delta y}\right) - \rho c_p\frac{\delta T}{\delta t}\right]d\Omega = 0 \qquad \textbf{6.5}$$

Where Ω is the two dimensional solution domain. Using Green's Lemma (Lewis et al., 2004), the first two terms of equation 6.5 may be re-written:

$$\int_{\Omega} N_i \frac{\delta}{\delta x}\left(k\frac{\delta T}{\delta x}\right)d\Omega = \int_{\Gamma} N_i k \frac{\delta T}{\delta x} l d\Gamma - \int_{\Omega} \frac{\delta N_i}{\delta x} k \frac{\delta T}{\delta x} d\Omega \qquad \textbf{6.6}$$

$$\int_{\Omega} N_i \frac{\delta}{\delta y}\left(k\frac{\delta T}{\delta y}\right)d\Omega = \int_{\Gamma} N_i k \frac{\delta T}{\delta y} m d\Gamma - \int_{\Omega} \frac{\delta N_i}{\delta y} k \frac{\delta T}{\delta y} d\Omega \qquad \textbf{6.7}$$

Equation 6.5 may therefore be written in the form:

$$-\int_{\Omega} \left[k\frac{\delta N_i}{\delta x}\frac{\delta T}{\delta x} + k\frac{\delta N_i}{\delta y}\frac{\delta T}{\delta y} + N_i \rho c_p \frac{\delta T}{\delta t}\right]d\Omega + \int_{\Gamma} N_i k \frac{\delta T}{\delta x} l d\Gamma + \int_{\Gamma} N_i k \frac{\delta T}{\delta y} m d\Gamma = 0 \qquad \textbf{6.8}$$

By applying the shape function and integrating over the boundary, equation 6.2 may be re-written as:

$$\int_{\Gamma} N_i k \frac{\delta T}{\delta x} l d\Gamma + \int_{\Gamma} N_i k \frac{\delta T}{\delta y} m d\Gamma = -\int_{\Gamma} N_i h\left(T_{wall} - T_f\right) d\Gamma \qquad \textbf{6.9}$$

Equation 6.3 may be manipulated in a similar fashion.

Substituting the spatial approximation given in equation 6.4, and equation 6.9, into equation 6.8 yields:

$$-\int_{\Omega} \left[k\frac{\delta N_i}{\delta x}\frac{\delta N_j}{\delta x} T_j(t) + k\frac{\delta N_i}{\delta y}\frac{\delta N_j}{\delta y} T_j(t) + N_i \rho c_p \frac{\delta N_j}{\delta t} T_j(t)\right]d\Omega - \int_{\Gamma} N_i h\left(T_{wall} - T_f\right) d\Gamma = 0 \qquad \textbf{6.10}$$

Where *i* and *j* represent the nodes. Equation 6.10 may be written in the more convenient form:

$$[C_{ij}]\left\{\frac{\delta T_j}{\delta t}\right\} + [K_{ij}]\{T_j\} = \{f_i\} \quad \textbf{6.11}$$

Where:

$$[C_{ij}] = \int_{\Omega} \rho c_p N_i N_j d\Omega \quad \textbf{6.12}$$

$$[K_{ij}] = \int_{\Omega} \left[k\frac{\delta N_i}{\delta x}\frac{\delta N_j}{\delta x}\{T_j\} + k\frac{\delta N_i}{\delta y}\frac{\delta N_j}{\delta y}\{T_j\}\right] d\Omega + \int_{\Gamma} hN_i N_j d\Gamma \quad \textbf{6.13}$$

$$\{f_i\} = + \int_{\Gamma} N_i h T_a d\Gamma \quad \textbf{6.14}$$

Equation 6.11 may be solved for the nodal temperatures at a given time using simple matrix manipulations.

6.2.3 Integration of the FEM with OUTFLOW

As discussed previously, the composite model of OUTFLOW with the FEM is referred to as FEM-O.

The material properties and thickness of the pipe wall and external environment are assumed to be uniform for each pipeline section. Additionally, the pipe wall thickness may vary between pipe sections, however each section is assumed to have the same external environment. Therefore, when modelling venting of a buried pipeline for example, both the main and vent pipes may have different wall thicknesses but both are modelled assuming they are buried. This limitation to FEM-O is due to limits in the flexibility of the discharge model OUTFLOW. The material properties of the pipe wall, insulation and soil used in FEM-O are presented in table 6.1.

Table 6.1: Material properties of the pipeline, insulation and soil used in the FEM (Almanza et al., 2004).

Material	Density (kg/m^3)	Heat capacity (J/kg.K)	Thermal conductivity ($W/m^2.K$)
Pipe wall	7854.0	434.0	53.65
Foam insulation (polyethylene)	32.5	2906.0	0.0484
Soil (moist clay)	1700.0	1000.0	0.8

The fluid model calculates fluid properties at each grid point in sequence while the FEM calculates wall temperatures at all nodes simultaneously. Thus the fluid model must complete the calculation for each pipe section before the wall temperatures of the section are calculated.

When calculating the fluid properties of the system prior to rupture the pipe wall is assumed to be the same temperature as the ambient. The FEM subsequently calculates the real wall temperature by iterating over short time steps until further iterations result in no significant change ($<1x10^{-3}$ K) in nodal temperatures.

When performing transient fluid property calculations, FEM-O uses the calculated wall temperatures from the previous time interval to calculate fluid properties throughout the pipeline. The wall temperatures are then updated before the calculation advances to the next time interval. The time step size from the fluid model, based on the Courant-Friedrichs-Lewy (CFL) criterion (equation 4.7), is also used in the FEM calculation. The use of a short time step, especially during the early stages blowdown, is used to maintain the accuracy of predictions.

The calculation algorithm illustrating the integration of the FEM conduction model with the outflow model is presented in figures 6.3 and 6.4.

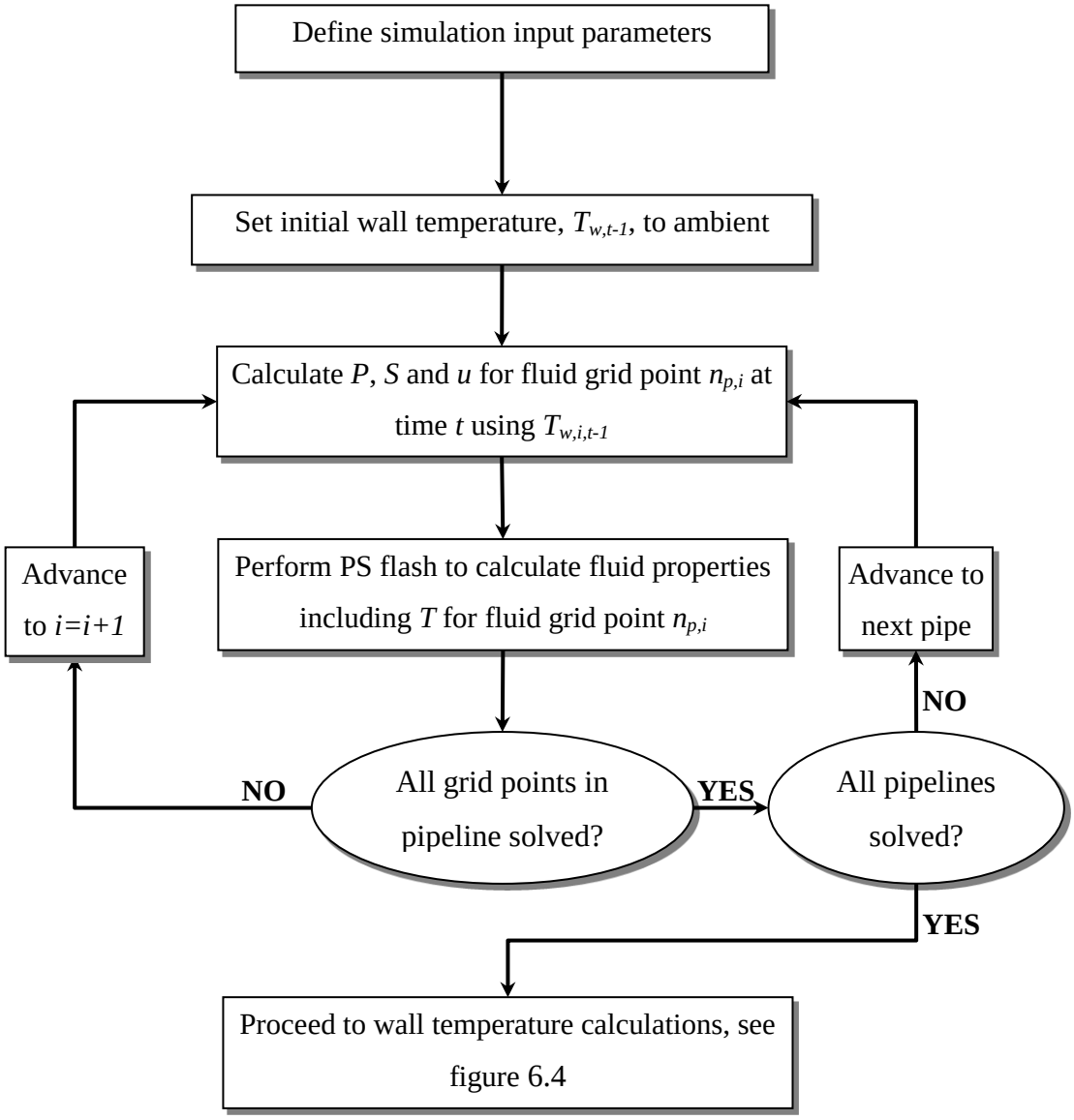

Figure 6.3: Calculation algorithm for obtaining pipe wall temperatures during outflow, part A. The subscripts *w, t, p* and *i* refer to the wall, time, pipe and grid point respectively.

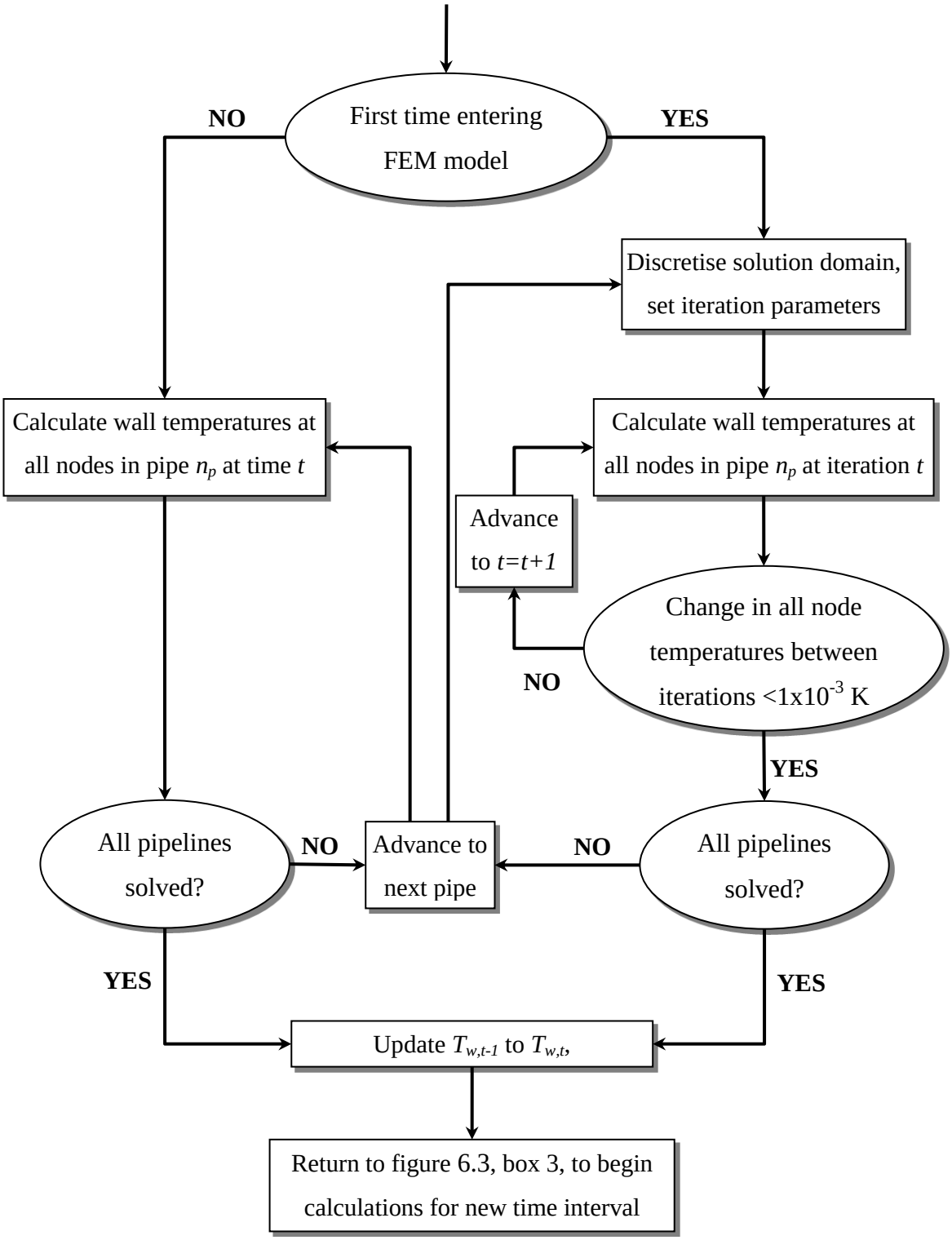

Figure 6.4: Calculation algorithm for obtaining pipe wall temperatures during outflow, part B. *T* represents the temperature, the subscripts *w, t, p* and *i* refer to the wall, time/iteration, pipe and grid point respectively.

6.2.4 Further development of FEM-O for modelling CO_2 pipeline blowdown

As discussed in section 3.6.2, for two phase inventories FEM-O utilises the Steiner and Taborek (1992) correlation for calculating the fluid/pipe wall heat transfer coefficient (FHTC). This correlation modifies the liquid only FHTC using the two phase flow convective factor F_{tp} (equation 3.56). The formulation of equation 3.56 was reported as suitable for fluids with a vapour fraction less than 60 %. This represents a significant limitation to FEM-O as, depending on the nature of a pipeline failure, the proportion of vapour in a CO_2 inventory may evolve above 60 %. Alternatively during venting the proportion of vapour in an inventory will certainly evolve above 60 %.

Steiner and Taborek (1992) presented an extended F_{tp} equation for fluids containing high vapour fractions (i.e. >60 %) and demonstrated its improved performance compared with equation 3.56. This extended equation for F_{tp} is shown in equation 6.15.

$$\frac{h_{FC}}{h_l} = F_{tp} = \left(\left[(1-x)^{1.5} + 1.9x^{0.6}(1-x)^{0.01} \left(\frac{\rho_l}{\rho_v} \right)^{0.35} \right]^{-2.2} + \left[\frac{h_v}{h_l} x^{0.01} \left\{ 1 + 8(1-x)^{0.7} \left(\frac{\rho_l}{\rho_v} \right)^{0.67} \right\} \right]^{-2} \right)^{-0.5} \quad \textbf{6.15}$$

Where h_{FC} is the fluid heat transfer coefficient (adjusted for forced convection) and h_l is the heat transfer coefficient for the liquid phase only (see equation 3.57). x is the inventory vapour fraction, ρ_v and ρ_l are the vapour and liquid densities respectively, h_v and h_l are respectively the pure vapour and liquid heat transfer coefficients and F_{tp} is the two phase flow convective factor.

Equation 6.15 was integrated into FEM-O to calculate the FHTC at fluid nodes where the proportion of vapour exceeded 60 %. At nodes where the vapour fraction is less than 60 % the original formulation for F_{tp} (equation 3.56) is retained.

6.3 Validation of FEM-O

In this section FEM-O fluid pressure, temperature and pipe wall temperature predictions are validated against experimental data recorded during the blowdown of a shock tube containing dense phase CO_2 inventories.

6.3.1 Description of the simulations conducted

Simulations of experiments 3 and 4 (see table 5.3) were conducted using FEM-O, these are numbered Tests 5 and 6 respectively. The simulation parameters for Tests 5 and 6 are the same as used previously for Tests 3 and 4; they are repeated below in table 5.5 for convenience.

A detailed description of experiments 3 and 4, including of the data recorded, has been presented in section 5.2.

The measured experimental data from pressure transducer FP35, fluid temperature transducers FT01 and FT07 and wall temperature transducers WT02 to WT14 was used to validate FEM-O. Additionally, detailed fluid pressure data during the first 500 ms of discharge from transducers FP25, FP28 and FP31 was used for model validation. The locations of the specified instruments on the shock tube are detailed in table 5.2.

Table 6.2: Simulation parameters for Tests 5 and 6, the blowdown of a shock tube containing pure and impure dense phase CO_2 respectively.

	Inputs	Test 5	Test 6
Pipeline characteristics	Upstream fitting	Closed end	Closed end
	Downstream fitting	Rupture disk	Rupture disk
	Pipe length (m)	144	144
	Pipe external diameter (mm)	171.94	171.94
	Pipe wall thickness (mm)	10.97	10.97
	Pipe roughness (mm)	0.0000043	0.0000043
	Pipe orientation to the horizontal plane (°)	0	0
	Heat transfer option	FEM – Insulated	FEM – Insulated
Inventory and ambient parameters	Feed composition (mole %)	CO_2 100	CO_2 95.92
			N_2 4.08
	Fluid temperature (°K)	278.35	293.15
	Fluid pressure (bara)	153.41	141.41
	Ambient temperature (°K)	283.35	273.45
	Ambient pressure (bara)	1.01	1.01
Failure parameters	Failure mode	FBR	FBR
	Failure location relative to upstream end (m)	144	144
	Discharge coefficient	1	1
Other parameters	Number of pipe grid points	144	144
	Simulation model	HEM	HEM
	Equation of State	PR (equation 3.6)	PR (equation 3.6)
	Friction factor correlation	Chen (Equation 3.33)	Chen (Equation 3.33)
	Total depressurisation time (s)	25	25

6.3.2 FEM-O validation results

In this section the validation of the FEM-O wall temperature model is discussed first, the validation of the fluid model is subsequently addressed.

Figure 6.5 presents experimental and FEM-O predicted outer pipe wall temperature profiles for Test 5 at time intervals of 0, 5, 10, 15 and 20 s following rupture. The experimental temperature profiles at each time interval are based on data from transducers WT02 to WT14. As discussed previously for Test 3, a uniform temperature in the pipe wall was not recorded prior to blowdown. Thermocouples WT05, WT08 and WT10 recorded initial temperatures closest to the calculated initial wall temperature (281.0 K). Thus temperature histories from these instruments are compared with the corresponding simulated data in figure 6.6. The corresponding Test 3 OUTFLOW predictions at these transducers are also shown in the figure for comparison.

Referring to figure 6.5, although the recorded wall temperature profiles display considerable fluctuations along the length of the pipe at each time interval, the trends in the profiles are clear. The experimental and predicted wall temperature profiles are generally in good agreement. During the later stages of blowdown a trend may be observed for FEM-O predicted temperatures to be fractionally lower than observed experimentally. This is due to the earlier predicted onset of cooling, discussed in reference to figure 6.6. Unrealistic wall temperatures are predicted at the extreme ends of the shock tube wall at both 5 and 10 s, the cause of which is not known.

Referring to figure 6.6, it may be observed that the experimental pipe wall temperatures remain unchanged until ca. 2 s after blowdown was initiated. This is likely due to boundary layer effects in the accelerating fluid, the mounting of the relevant instruments on the external surface of the pipe may also contribute. From ca. 2 s steady cooling is observed until blowdown nears completion, barring small peaks in the wall temperature histories at ca. 273 K. These are probably due to the formation of water ice on the outer surface of the shock tube.

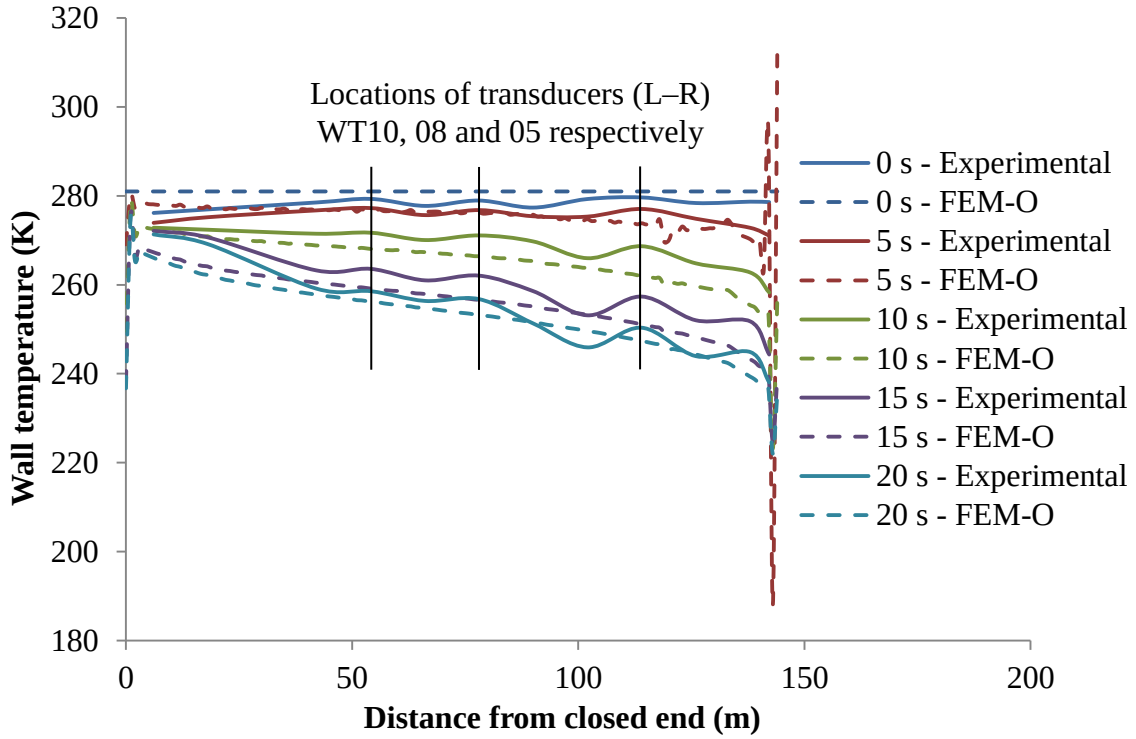

Figure 6.5: Experimental and FEM-O predicted outer pipe wall temperature profiles at various times for Test 5 (pure CO_2, see table 5.5).

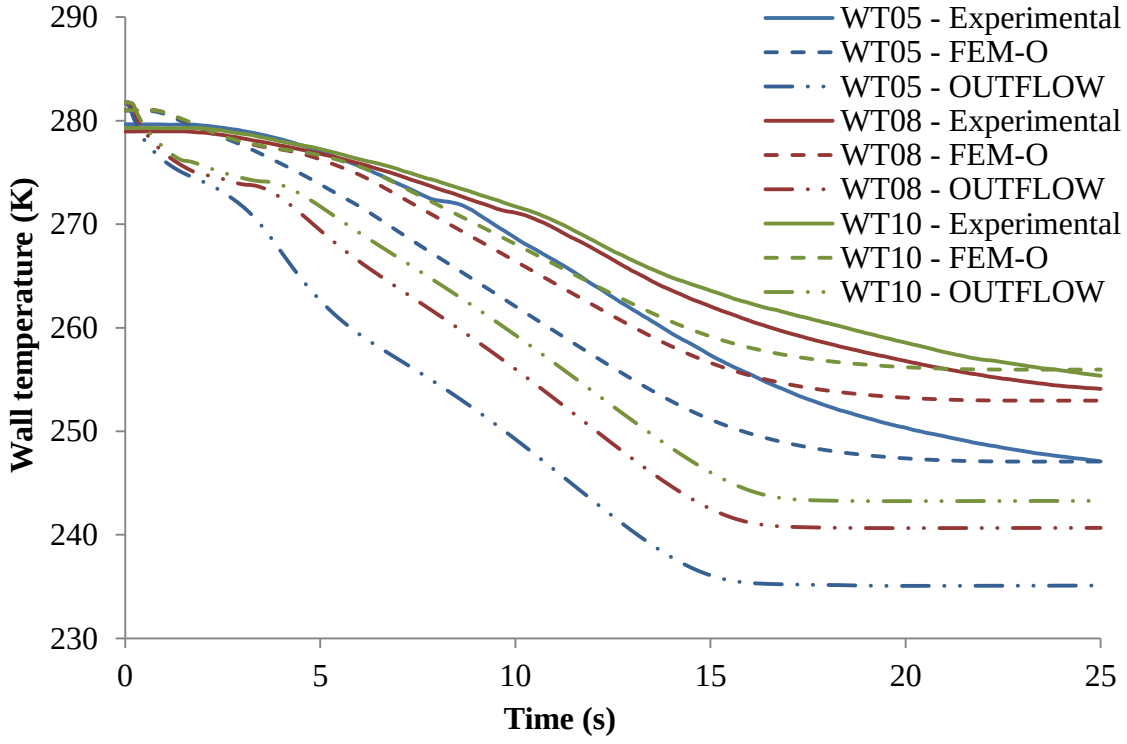

Figure 6.6: Experimental and FEM-O predicted outer pipe wall temperature histories at transducers WT05, 08 and 10 for Test 5 (pure CO_2, see table 5.5).

Comparing the observed and predicted wall temperature data from WT05, WT08 and WT10 in figure 6.6, the predicted initial temperatures are higher than observed experimentally and cooling is predicted to begin earlier (boundary layer effects are not accounted for in FEM-O). Except at WT05 (30 m from the open end), the rate of wall cooling varies during the first ca. 6 s of blowdown. This results from rapid transients in the fluid altering the local depressurisation rate at the closed end of the shock tube during this period. After ca. 6 s no rapid transients exist in the system and the cooling rate generally matches that observed experimentally. The degree and duration of cooling predicted at each transducer closely matches the experimental data. The significant overall improvement of the FEM-O over OUTFLOW predictions is also readily discernible in the data from Tests 3 and 5.

Considering Test 6, the initial simulation of this test failed to accurately predict the pipe wall temperature prior to blowdown. As a result transient wall temperature predictions also showed poor agreement with the experimental data. In order to accurately predict the initial pipe wall temperature the FEM steady state algorithm was altered to ignore heat transfer between the atmosphere and the pipe insulation. No alterations were made to the transient FEM algorithm. This alteration was only used when simulating Test 6.

Test 6 was simulated again with the discussed alteration to the FEM steady state algorithm. Figure 6.7 presents the experimental and FEM-O predicted outer pipe wall temperature profiles for Test 6 at 0, 5, 10, 15 and 20 s following rupture. Experimental temperature profiles at each time interval are based on data from transducers WT02 to WT14. Thermocouples WT04, WT09 and WT11 recorded initial temperatures closest to the calculated initial wall temperature (293.15 K). Thus temperature histories from these instruments are compared with the corresponding simulated data in figure 6.8. The corresponding Test 4 OUTFLOW predictions from these transducers are also shown in the figure for comparison.

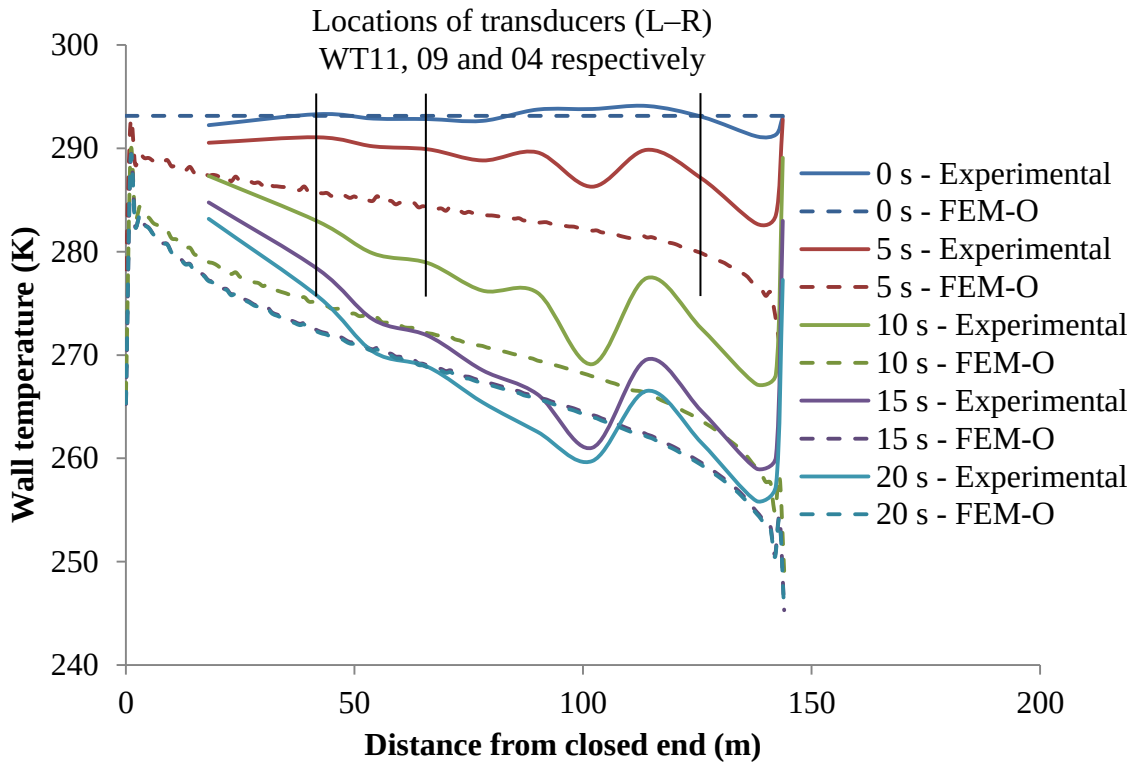

Figure 6.7: Experimental and FEM-O predicted outer pipe wall temperature profiles at various times for Test 6 (CO_2 with 4.08 mol% N_2, see table 5.5).

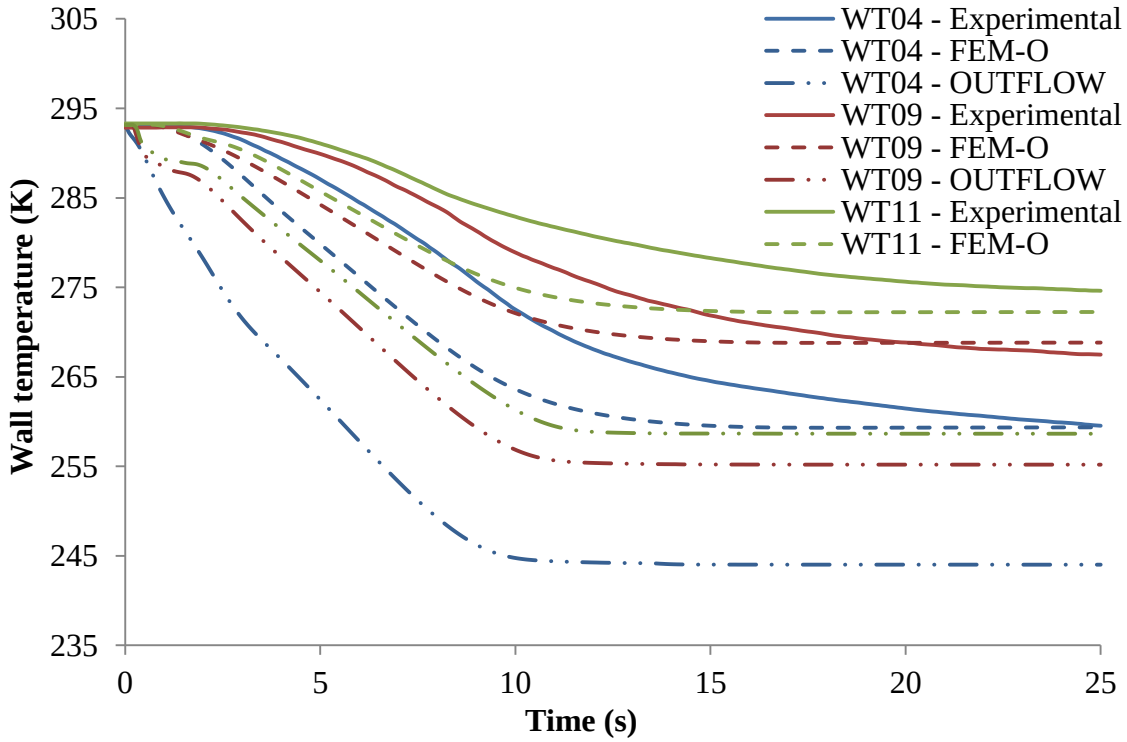

Figure 6.8: Experimental and FEM-O predicted pipe wall temperature histories at transducers WT04, 09 and 11 for Test 6 (CO_2 with 4.08 mol% N_2, see table 5.5).

Referring to figure 6.7, although a uniform pipe wall temperature was not recorded prior to FBR, the calculated initial wall temperature is in good agreement with the experimental data. The recorded wall temperature profiles display increasingly large fluctuations along the length of the pipe up to 10 s after rupture. Nonetheless trends in all wall temperature profiles remain clear. Between 5 and 10 s wall temperatures are predicted to be significantly cooler than observed experimentally due to the earlier onset of cooling predicted by FEM-O (see also figure 6.8). Unrealistic pipe wall temperatures are also predicted at the ends of the pipe wall.

Referring to figure 6.8, steady cooling of the pipe wall was observed experimentally from ca. 2 s after FBR. The rate of cooling was observed to decrease from ca. 15 s as blowdown nears completion. As observed for Test 5, cooling in the pipe wall was predicted to begin earlier than observed experimentally, thus accounting for the difference between the experimental and predicted wall temperature profiles at 5 and 10 s. The predicted rate and range of cooling shows reasonable agreement with the experimental data. The significant overall improvement of the FEM-O over OUTFLOW predictions is also readily discernible in the data from Tests 4 and 6. No effect on the predicted rate of cooling is observed from rapid transients in the inventory.

In summary, FEM-O wall temperature predictions for Tests 5 and 6 show good agreement with the corresponding experimental data and are significantly more accurate than the corresponding OUTFLOW predictions. In both simulations FEM-O was able to predict the wall temperature prior to blowdown with reasonable accuracy. Although the onset of cooling in Tests 5 and 6 was predicted to occur earlier than observed experimentally, the degree and duration of predicted pipe wall cooling was in good agreement with the relevant experimental data in both tests.

Turning to the FEM-O fluid property predictions for Tests 5 and 6, figure 6.9 presents the experimental and predicted fluid pressure histories at FP35 for both tests. Experimental data for the first 500 ms following rupture of Test 5 is available and discussed in reference to figure 6.10. No comparable data is available for Test 6.

Referring to figure 6.9, the predicted and experimental data is generally in good agreement. The FEM-O predicted Test 5 pressure history of fluctuates between ca. 0.5 and 8 s and the Test 6 pressure history between ca. 0.5 and 3 s. These fluctuations are caused by predicted rapid transients in the inventory. Small, brief increases in experimental pressure are recorded at ca. 18 and 14 s for Tests 5 and 6 respectively (indicated in figure 6.9). At comparable times plateaux in the corresponding temperature histories at FT01 were recorded (see figure 6.11). These features coincide with the triple point properties of pure CO_2 (216.6 K and 5.16 bara, calculated in REFPROP (Lemmon et al., 2013) using the PR EoS). The formation of solid CO_2 in the inventory of both Test 5 and 6 is therefore a realistic possibility.

Figure 6.10 presents the Test 5 experimental and predicted fluid pressure histories at transducers FP25, FP28 and FP31 (see table 5.2) during the first 500 ms of blowdown. Pressure spikes in the inventory resulting from the explosive cutting of the rupture disk are indicated on the figure. FEM-O models the failure of a pipeline as an instantaneous event thus the pressure spikes are not mirrored in the simulated data.

The arrival of the explosive and decompression waves at each transducer is very closely matched by the arrival of the predicted decompression wave. The reflected explosive and decompression waves may be observed arriving at each transducer from ca. 290 ms while the reflected predicted decompression wave arrives later. This may be significant when modelling venting as in such events the decompression wave is expected to dissipate in the pipe system over time. Notwithstanding the above, the time difference between the return of the reflected experimental and simulated decompression waves to each transducer is extremely small. The ability of the PR EoS to model rapid transients in pure, dense phase CO_2 is therefore shown to be satisfactory. It may be inferred from this result that for the blowdown scenario simulated (Test 5, based on experiment 3) the PR EoS calculates the properties of dense phase CO_2 with reasonable accuracy, including fluid density.

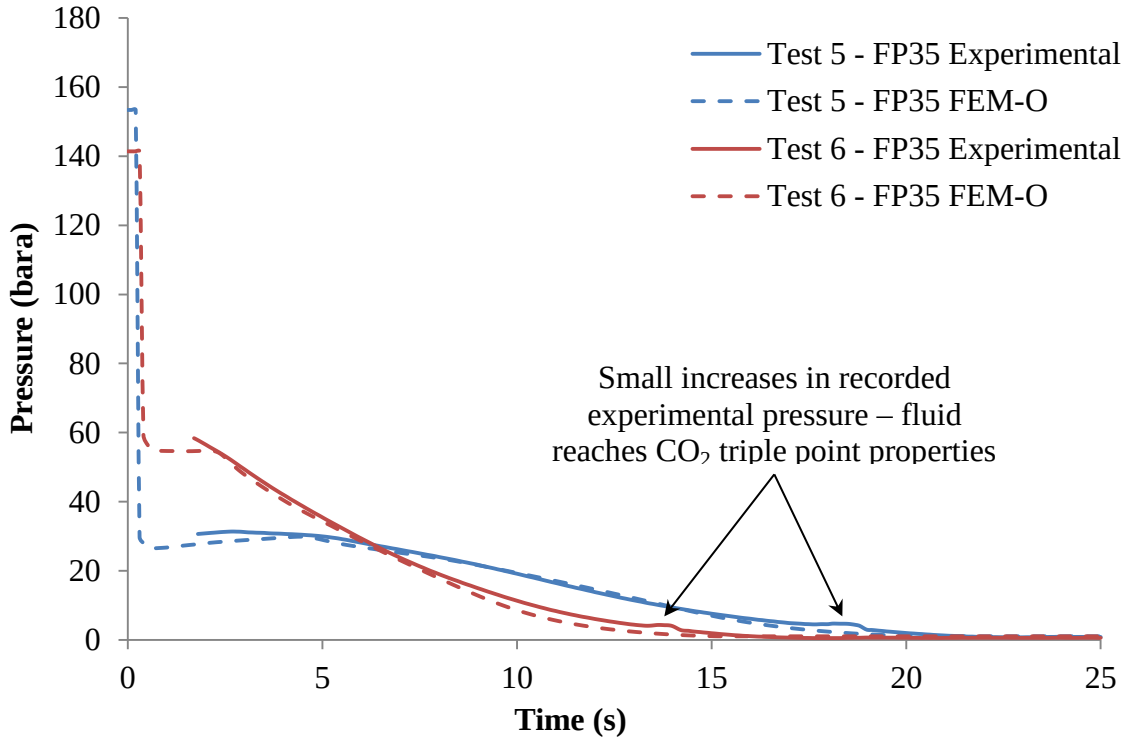

Figure 6.9: Experimental and FEM-O predicted fluid pressure histories at FP35 for Tests 5 (pure CO_2) and 6 (CO_2 with 4.08 mol% N_2, see table 5.5).

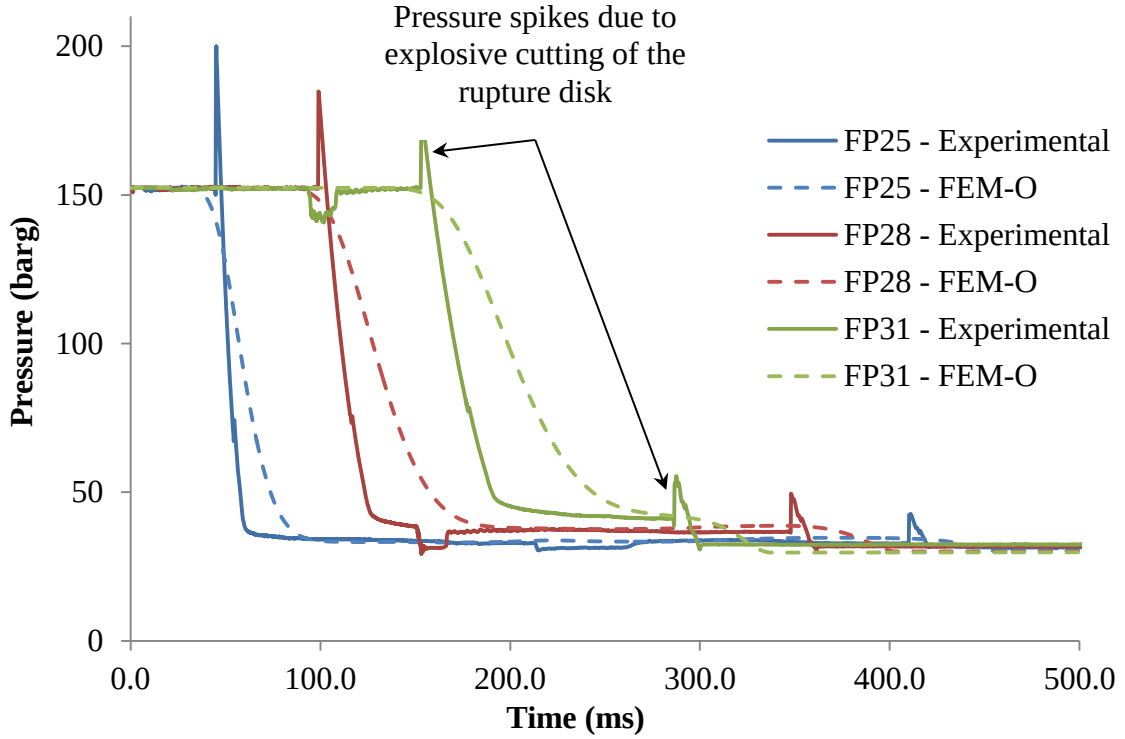

Figure 6.10: Test 5 experimental and FEM-O predicted fluid pressure histories at transducers FP25, 28 and 31 during the first 500 ms of blowdown.

Figures 6.11 and 6.12 present the experimental and predicted fluid temperature histories at transducers FT01 and FT07 respectively for Tests 5 and 6. As may be observed, FEM-O consistently under-predicts the fluid temperature for both tests and at both transducers. The predicted and experimental temperatures diverge from ca. 14 and 9 s for Tests 5 and 6 respectively. The minimum predicted fluid temperatures significantly under-predict the experimental temperatures by the end of blowdown. The FEM-O data presented therefore suggests the two phase flow convective factor equation 6.15 might be increasingly inaccurate when applied to fluids with vapour fractions > 95 %.

Concerning the experimental data reported in figures 6.11 and 6.12, it should be noted that the minimum fluid temperature recorded during blowdown was the same in both tests. The proportion of impurity in the CO_2 inventory for Test 6 (4.08 mole% N_2) is not unrealistic (de Visser et al., 2008). Thus the data suggests that for CO_2 inventories with the expected range of purity; ca. >91 % CO_2 considered by, for example, National Grid UK (Cosham et al., 2011) and ca. >96 % recommended by the DYNAMIS Project (de Visser et al., 2008), the duration of a release is the dominant factor in determining the likely minimum temperature reached by the fluid during blowdown. Thus when simulating very prolonged blowdown events the PRSV-1 EoS (with calibrated binary interaction parameters) may prove to be more appropriate for use than the PR EoS.

Although not presented in chapter 5, the OUTFLOW fluid temperature histories predicted for Tests 3 and 4 at FT01 are almost identical to those shown for FEM-O in figures 6.11 and 6.12. It may therefore be concluded that while the FEM model is sensitive to the predicted fluid temperatures the fluid model is less sensitive to the wall temperature predictions.

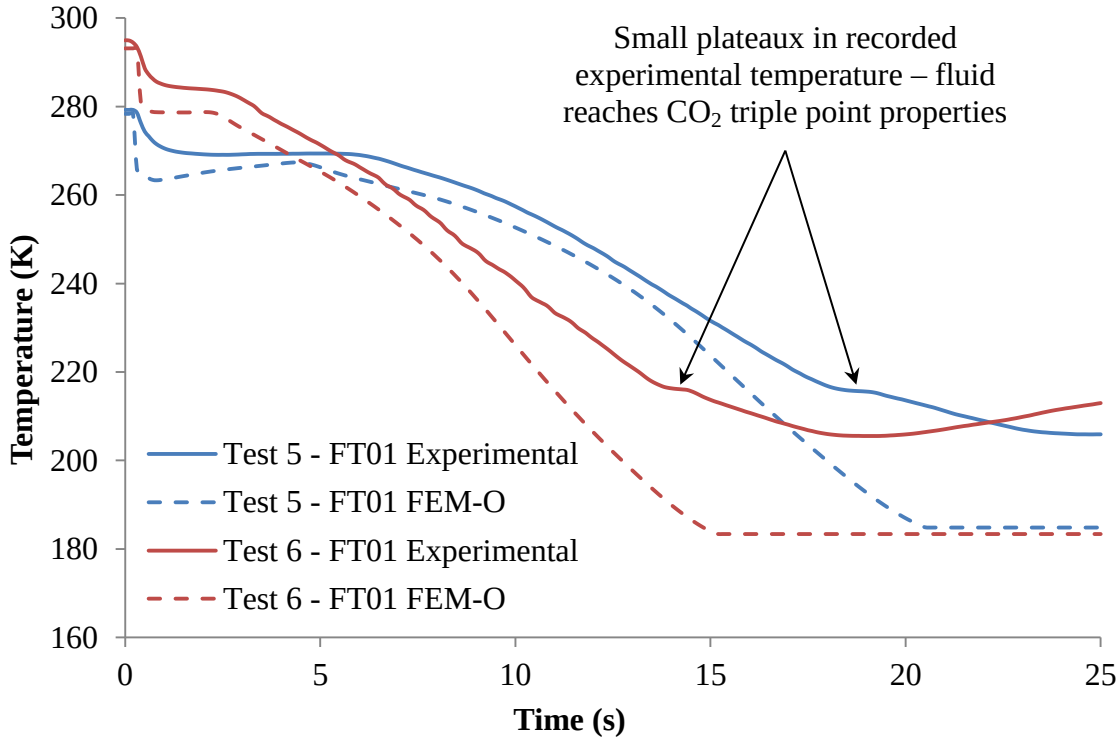

Figure 6.11: Experimental and FEM-O predicted fluid temperature histories at FT01 for Tests 5 (pure CO_2) and 6 (CO_2 with 4.08 mol% N_2, see table 5.5).

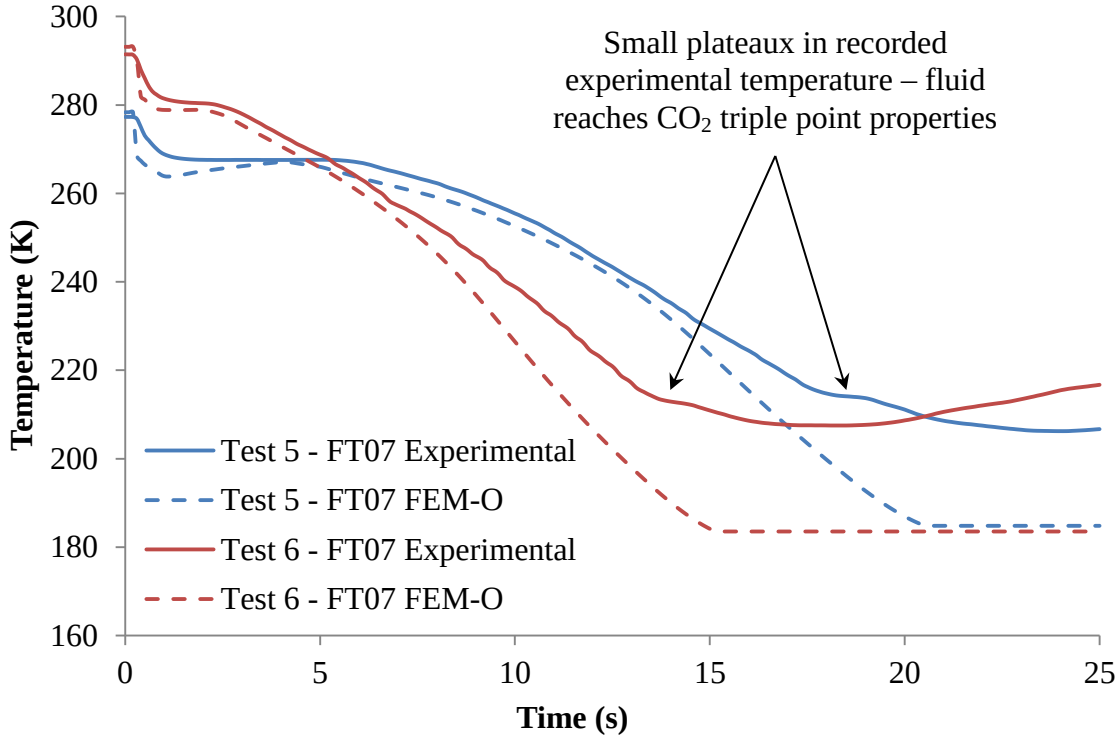

Figure 6.12: Experimental and FEM-O predicted fluid temperature histories at FT07 for Tests 5 (pure CO_2) and 6 (CO_2 with 4.08 mol% N_2, see table 5.5).

It was noted that FEM-O simulation run times were significantly longer than the corresponding OUTFLOW run times, as shown in table 6.3.

Table 6.3: A comparison of simulation run times for Tests 3 to 6.

	OUTFLOW	FEM-O
Test 3/Test 5	14 min. 54 sec.	4 hrs 15 min.
Test 4/Test 6	26 min. 26 sec.	4 hrs 35 min.

This has significant implications for the applicability of FEM-O to simulating systems composed of multiple pipes, such as would be expected during venting or when simulating outflow from networks of pipelines.

6.4 Conclusion

In this chapter a Finite Element model for calculating transient heat conduction in a pipe wall was developed and integrated with the model OUTFLOW. The resulting composite model, referred to as FEM-O, was then validated.

The Finite Element model developed was formulated to calculate pipe wall heat conduction in two dimensions. Boundary conditions of forced convective heat transfer and a mixture of natural and forced convective heat transfer are applied to the inner and outer surfaces of the FEM solution domain respectively. The pipeline may be modelled as exposed to air or insulated/buried. The two dimensional heat conduction equation for the pipe wall, including terms for convective heat transfer at the boundaries, was converted to Finite Element form using the Galerkin Method.

The properties of the inventory are calculated at each fluid grid point in sequence, however properties at each FEM node are calculated simultaneously. Heat flux values at each fluid grid point are therefore calculated using fluid property data from the current time step and wall temperature data from the previous time step. The small time step

used, especially during the early stages of blowdown, minimises any inaccuracy associated with this method. The fluid/pipe wall heat transfer coefficient was also updated to account for the potentially high vapour content of CO_2 inventories during outflow.

FEM-O fluid pressure, temperature and pipe wall temperature predictions were validated against shock tube decompression data for dense phase CO_2 inventories. A detailed description of the experiments and recorded data used in the validation has been presented in section 5.2.

FEM-O demonstrated the ability to accurately model the degree and duration of cooling in the pipe wall during blowdown for both pure (Test 5) and impure (Test 6) CO_2 inventories. In both tests the predicted onset of cooling was earlier than observed experimentally, although uncertainty in the precise start time of the experiment or instrument lag may have contributed to this. Unrealistic pipe wall temperatures were predicted at the extreme ends of the pipe. Their cause is unknown and they do not appear to significantly affect the accuracy of the results. Wall temperature predictions were seen to be sensitive to variations in predicted fluid properties. Fluid pressure predictions showed good agreement corresponding experimental data. Rapid fluid transients in Test 5 were predicted with good accuracy by FEM-O. Fluid temperatures were consistently under-predicted.

Finally, it was observed that although FEM-O produces significantly improved wall temperature predictions compared with OUTFLOW, the simulations run times were also much greater.

Chapter 7: Modelling of fluid flow through pipeline junctions

7.1 Introduction

As discussed in section 2.2, pipelines are the most practical transportation option for large scale CCS operations. Given the geographical spread of CO_2 sources such as power stations, CCS pipelines can be expected to extend over long distances and varying topographies. Given the myriad difficulties in operating multiple smaller pipelines they will be grouped into networks (Chandel et al., 2010).

Given their potential length, sections of a pipe network undergoing venting/with a failure are likely to possess varying inclination; this will affect the overall outflow process and therefore the properties of the dispersing inventory cloud. Additionally, the section may possess a T-junction, further complicating the outflow process. Given that CO_2 is more dense than air, odourless and causes instantaneous unconsciousness and ultimately death at concentrations ≥ 10 % v/v (Kruse and Tekiela, 1996), a proper understanding of the discharge process is therefore vital. This requires an outflow model with the demonstrated ability to model fluid flow through pipeline junctions.

In this chapter the pipeline junction boundary conditions presented in section 4.3.3 are considered for modelling the venting of CO_2 pipelines. In the first part of the chapter potential weaknesses are identified and new formulations for the boundary conditions proposed. In the second and third sections the new two and three pipe junction boundary conditions are respectively validated against available experimental data provided by the UK National Grid. All simulations in this chapter are performed with FEM-O.

7.2 Justification and New Model Description

The boundary conditions for modelling fluid flow through pipeline junctions have been presented in section 4.3.3. Referring to figures 4.5 and 4.6, fluid properties at the terminal node in each pipe connected to the junction are described by one Path line and one Mach line each. Referring to figure 4.3, the position of point *o* is always upstream of node *i* at t_1, and therefore indicates the direction of flow. The boundary conditions should therefore account for variation in the direction of flow. However, their implementation in OUTFLOW is such that the Path line compatibility equations from all nodes are included simultaneously in the calculation at each time step, thus describing a scenario in which fluid flows into the junction from all directions. When combined with the indicated Mach line equations (figures 4.5 and 4.6), this system of equations may not necessarily result in reduced accuracy. Indeed previous tests with OUTFLOW have produced logical and coherent results, although these have not been validated. The computational effort required to obtain a solution, and therefore the simulation run-time, is surely high however.

The Test 5 run-time with FEM-O was 4 hours and 12 minutes; the same test performed with OUTFLOW had a run-time of 14 minutes 54 seconds (see table 6.3). Reduction of the run-time, with a potential increase in accuracy at any pipeline junctions, would represent a significant improvement to FEM-O. In this section new formulations of the junction boundary conditions, intended to reduce run-time and increase accuracy, are presented.

New boundary conditions for an N-pipe junction

Figures 7.1 and 7.2 present schematic representations of the new application of the MOC to the junction of two and three pipes respectively. B_1, B_2 and B_3 represent the boundary planes between fluid and connectors in the two and three way junctions. C_0 represents the Path line and C_+ and C_- the positive and negative Mach lines respectively. P_{jn}, s_{jn} and u_{jn} are the fluid pressure, entropy and velocity at B_n. As may be observed, the Path lines are now only included in the upstream pipes.

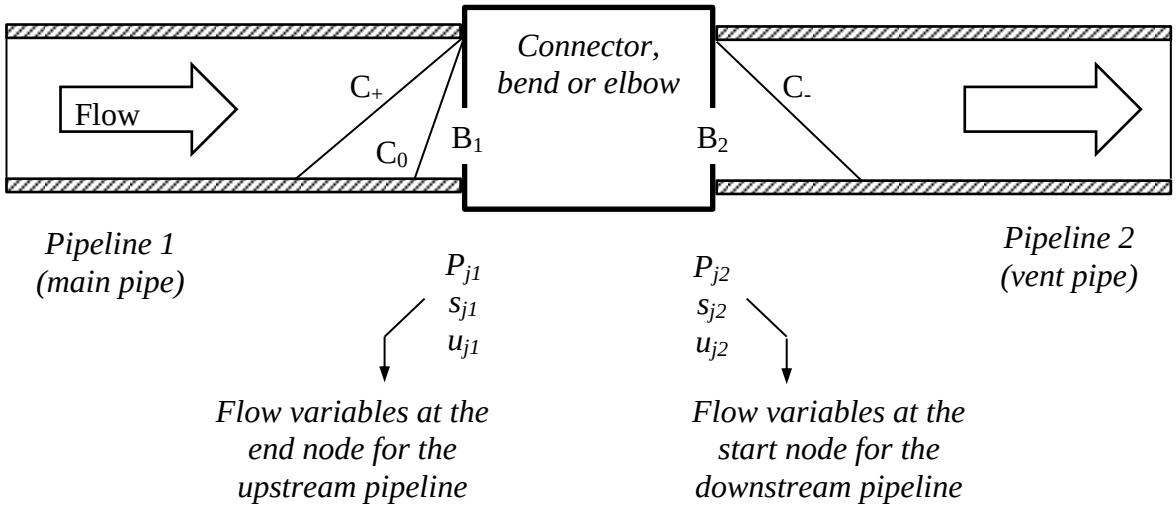

Figure 7.1: Application of the MOC to the simulation of fluid flow across the junction of two pipes.

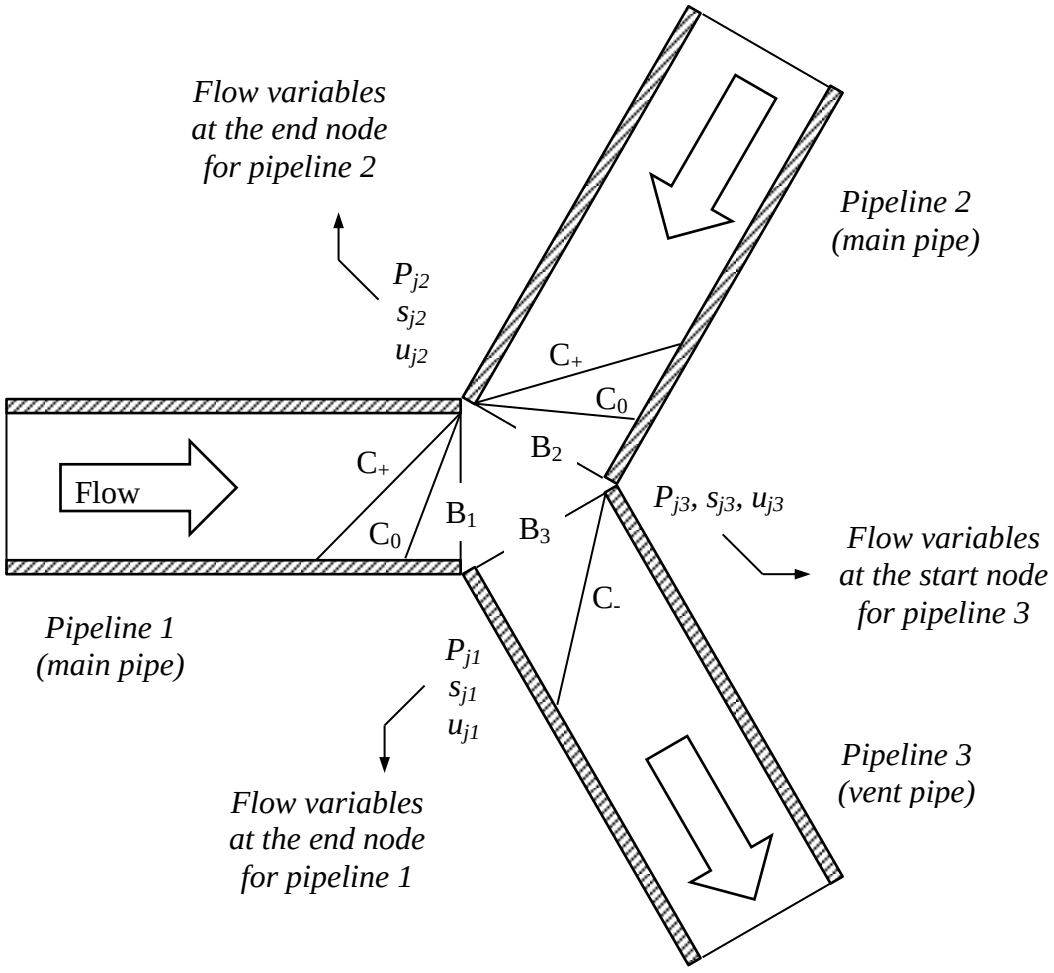

Figure 7.2: Application of the MOC to the simulation of fluid flow across the junction of three pipes assuming a single downstream pipe.

The predictor step of the Euler predictor/corrector algorithm is retained to estimate initial values for *P*, *s* and *u* at each boundary plane. A numerical algorithm (Moré et al., 1980) (referred to hereafter as ZERO_N) based on a modification of the Powell hybrid method (Rabinowitz, 1970) is used to iteratively refine these estimates to meet a pre-defined set of convergence criteria. These criteria are expressed as a number of non-linear functions equal to the number of variables submitted to ZERO_N. The functions are the relevant Mach and Path line equations indicated in figures 7.1 and 7.2 (equations 4.1, 4.3 and 4.5) and a combination of the boundary equations 7.1 to 7.4:

$$P_n = P_v + K_{pl} \quad \textbf{7.1}$$

$$\rho_1 u_1 A_1 = \rho_2 u_2 A_2 \quad \textbf{7.2}$$

$$\rho_3 u_3 A_3 = \frac{\rho_1 u_1 A_1}{x_1} + \frac{\rho_2 u_2 A_2}{x_2} \quad \textbf{7.3}$$

$$2s_v = s_1 + s_2 \quad \textbf{7.4}$$

Where:

$$K_{pl} = 0.5(\rho_2[1+k]u_2|u_2| - \rho_1 u_1|u_1|) \quad \textbf{7.5}$$

$$x_n = 1 + \frac{(V_n/V_T) - 0.5}{0.5} \quad \textbf{7.6}$$

P_n, ρ_n, u_n and A_n represent the fluid pressure, density, velocity and cross sectional area of pipe *n* at B_n respectively. The subscript *v* refers to the junction outlet properties. K_{pl} (Swaffield and Boldy, 1993) is the calculated pressure loss between B_n and B_v for a two pipeline junction. *k* is a constant that depends on the nature of the fitting (elbow, constriction, etc.). Example values of *k* are given in table 7.1 (Perry et al., 2008).

Table 7.1: *k* values for turbulent flow through fittings and valves (Perry et al, 2008).

Type of fitting	*k*
45° elbow (standard)	0.35
90° elbow (standard)	0.75
Coupling/Union	0.04
Tee (standard, branch blanked off)	0.40
Gate valve (open)	0.17
Angle valve (open)	2

When modelling venting through a T-junction the variable K_{pl} is calculated from equation 7.5 based on the fluid properties in the vent and either pipe 1 or 2, whichever has the greater volume. It is then applied to calculate the pressure drop between both main pipe sections and the vent. So long as the dimensions of the two main pipe sections, and by extension the fluid velocities out of them, remain similar this assumption is reasonable.

To ensure mass conservation it has been assumed that the mass of inventory flowing out of each main pipe (i.e. pipes 1 and 2 in a three pipe junction) is proportional to the ratio of their volumes. x_n is a coefficient which accounts for this, and is given by equation 7.6, where V_n and V_T are the volume of pipe n and the total volume of the pipes 1 and 2 respectively.

The new formulations of the boundary conditions presented here have been designed to model venting from pipelines. It is assumed that:

- the pipeline section is isolated and the inventory is at rest prior to venting
- during venting flow through the junction is isentropic
- no backflow occurs between the main pipes
- there is no mass accumulation in the junction

In summary, for a two pipe junction the *n* variables and non-linear functions provided to ZERO_N are:

- P_1, P_2, u_1, u_2, s_1
- C_+ and C_0 from pipe 1, C_- from pipe 2 (equations 4.3, 4.1 and 4.5 respectively), and equations 7.1 and 7.2

For a three pipe junction the *n* variables and non-linear functions provided to ZERO_N are:

- P_1, P_2, P_3, u_1, u_2, u_3, s_1, s_2 and s_3
- C_+, C_0, from pipes 1 and 2, C_- from pipe 3 (equations 4.3, 4.1 and 4.5 respectively), and equations 7.1 (used twice, for $n = 1$ and $n = 2$), 7.3 and 7.4

7.3 Validation of the two pipe junction model

The new two pipe junction boundary condition presented in section 7.2 was validated against a release of pure, dense phase CO_2 through a two pipe system in an experiment designed to mimic steady state venting. The experiment, referred to hereafter as experiment 5, was performed by the UK National Grid as part of the COOLTRANS research programme (UKCCSRC, 2012). The experimental data has not been published.

7.3.1 Description of the two pipe venting experiment

Experiment 5 was designed to mimic the steady state release of pure, dense phase CO_2 through a vent pipe. A schematic of the experimental apparatus is presented in figure 7.3.

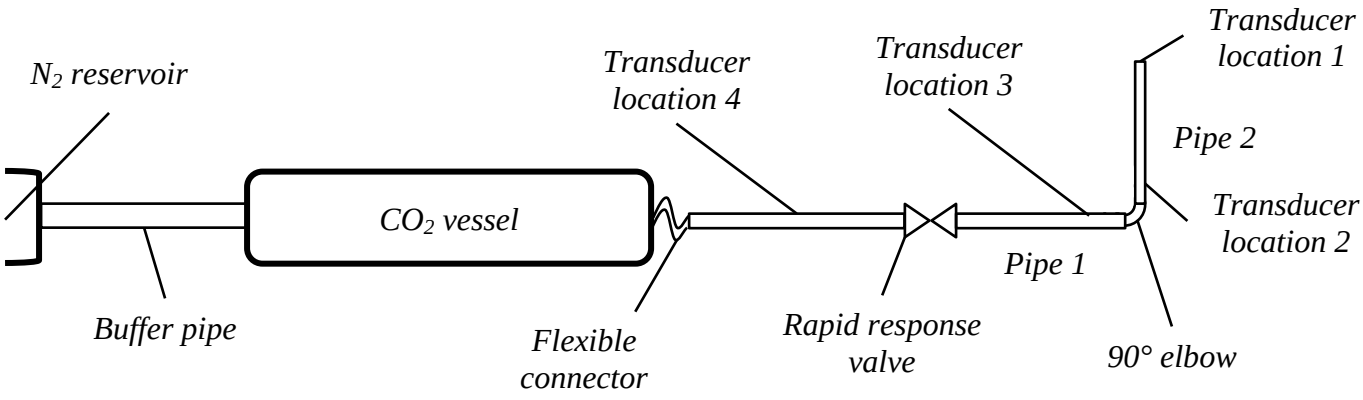

Figure 7.3: A schematic of the pseudo steady state CO_2 release experiment 5.

The vent was built in two sections, referred to as pipe 1 and pipe 2. Pipe 1 is a 12 m long, 49 mm ID horizontal section, pipe 2 is a 1.71 m long vertical section with the same ID; the two are connected using a 90° elbow joint. Neither pipe was insulated against the external environment Opposite the elbow joint pipe 1 was connected to a large, horizontal CO_2 vessel (600 mm ID, 24 m long) via a flexible connector, a precise description of which was not provided by National Grid. The CO_2 vessel was also connected to a high pressure N_2 reservoir via a 132 m long, 150 mm ID buffer pipe. Details of the N_2 reservoir were not provided by National Grid.

Experiments were prepared by charging the CO_2 vessel and buffer pipe with pure CO_2 and allowing the internal conditions to equilibrate. Venting was initiated by opening a rapid response valve installed along pipe 1, the precise location of which was not reported. Pressure was maintained in the CO_2 vessel by allowing N_2 from the reservoir to replace CO_2 released through the vent pipe. The experiment was halted before N_2 could enter the CO_2 vessel.

Pressure and temperature data is available from four transducer locations, detailed in table 7.2 and shown in figure 7.3. The types and technical specifications of the transducers at each location are given in table 7.3. The distance between transducer locations 3 and 4 was reported as 9 m although their precise positions were not

specified. In this work their locations (distance from the open end) have been estimated from photographs and do not account for the length of the elbow joint, which is unknown. Instrument locations 1, 2 and 3 are downstream of the rapid response valve and exposed to the atmosphere prior to test initiation.

The CO_2 properties in the vessel, recorded immediately before venting was initiated, are presented in table 7.4.

Experiment 5 was simulated with FEM-O using both the pipe junction boundary conditions described in section 4.3.3 and those described in section 7.2 (referred to hereafter as the old and new junction models respectively). The simulation is numbered Test 7. To simulate the effect of the CO_2 vessel the reservoir boundary condition was used (see section 4.3.2). An 8 s duration release through the vent was simulated; during the first 4 s the reservoir was modelled as open, after 4 s the reservoir was closed to simulate the effects of closing the rapid response valve on pipe 1. The simulated closure of the reservoir is instantaneous. A complete list of the parameters used in the Test 7 simulations is given in table 7.5.

Table 7.2: Pressure and temperature transducer locations relative to the rupture plane for the pseudo steady state CO_2 release experiment 5. * These distances are estimated from photographs of the experiment.

Transducer location	Fluid Pressure Transducer	Fluid Temperature Transducer	Pipe number	Distance from open end (m)
1	FP01	FT01	2	0.075
2	FP02	FT02	2	1.56
3	FP03	FT03	1	1.91*
4	FP04	FT04	1	10.91*

Table 7.3: The types and technical specifications of the instruments used in the pseudo-steady state release experiment 5.

Instrument type	Range (bar)	Sensitivity	Accuracy/resolution	Frequency (KHz)
FP-X – Kulite CT-375M fast response pressure transducers	0.35 – 210 bar; 77.65 – 393.15 K	0.05 – 0.1 MPa	0.05 – 0.1 MPa	150 – 1400
FT-X – Type T thermocouples	-73.15 – 533.15 K	-	± 2.2 K	-

Table 7.4: Inventory composition and initial fluid conditions for the pseudo steady state release of CO_2 through a vent pipe.

	Feed Composition				
Experiment	Component	Mole %	Feed Temperature (°C)	Feed Pressure (bara)	Ambient Temperature (°C)
5	CO_2	100	8.16	150.71	10.0

Table 7.5: Simulation parameters for the pseudo steady state release of CO_2 from a reservoir through a vent pipe.

	Inputs	Test 7	
		Pipe 1	Pipe 2
Pipeline characteristics	Upstream fitting	Reservoir	2 pipe junction (90° bend)
	Downstream fitting	2 pipe junction (90° bend)	Release plane
	Pipe length (m)	12	1.71
	Pipe external diameter (mm)	60.33	60.33
	Pipe wall thickness (mm)	5.54	5.54
	Pipe roughness (mm)	0.018	0.018
	Pipe orientation to the horizontal plane (°)	0	90
	Heat transfer option	FEM – Exposed to air	FEM – Exposed to air
Inventory and ambient parameters	Feed composition (mole %)	CO_2 – 100	
	Fluid temperature (°K)	281.31	
	Fluid pressure (bara)	150.71	
	Ambient temperature (°K)	283.15	
	Ambient pressure (bara)	1.01	
Failure parameters	Failure mode	FBR	
	Failure location relative to upstream end (m)	13.71	
	Discharge coefficient	1	
	Time of reservoir shutoff (s)	4.0	
Other parameters	Number of pipe grid points	50	50
	Simulation model	HEM	
	Equation of State	PR (equation 3.6)	
	Friction factor correlation	Chen (Equation 3.33)	
	Total depressurisation time (s)	8	

7.3.2 Two pipe junction validation results

The FEM-O simulation run time for Test 7 using the old junction model was 13 hours 52 minutes, in contrast the new junction model run time was 7 hours 51 minutes, a significant improvement.

Experimental data from transducer locations 2 and 3 was used to validate the new two-pipe junction model. Figures 7.4 and 7.5 present the experimental and FEM-O simulated fluid pressure and temperature at FP02 and FT02 (located just after the junction, see table 7.2) respectively. The experimental data is plotted such that the time of valve closure coincides with simulated reservoir closure at 4 s. In all cases, the reported trends in fluid properties at FP02 and FT02 were the same as those upstream of the junction at FP03 and FT03, thus the data from upstream of the junction is not shown.

As may be observed in figure 7.4, the constant experimental pressure at FP02 before valve closure indicates an essentially steady state release was achieved during venting. The experimental pressure loss through the junction was ca. 5.49 bara.

FEM-O predicts steady state outflow at FP02 with both junction models from ca. 0.5 s after initiation of the simulation until reservoir shutdown at 4.0 s. A relatively constant rate of pressure loss is then predicted with both junction models, barring a brief decrease in depressurisation rate caused by fluctuation of the fluid velocity following reservoir closure. This behaviour is more distinct in the predicted data due to the assumption of instantaneous reservoir shutdown. The new junction model predicts a slightly lower steady state pressure compared to the old junction model, both models under-predict the experimental fluid pressure. Steady state pressure losses through the junction are predicted to be ca. 2.19 bara and 3.23 bara when using the old and new junction models respectively.

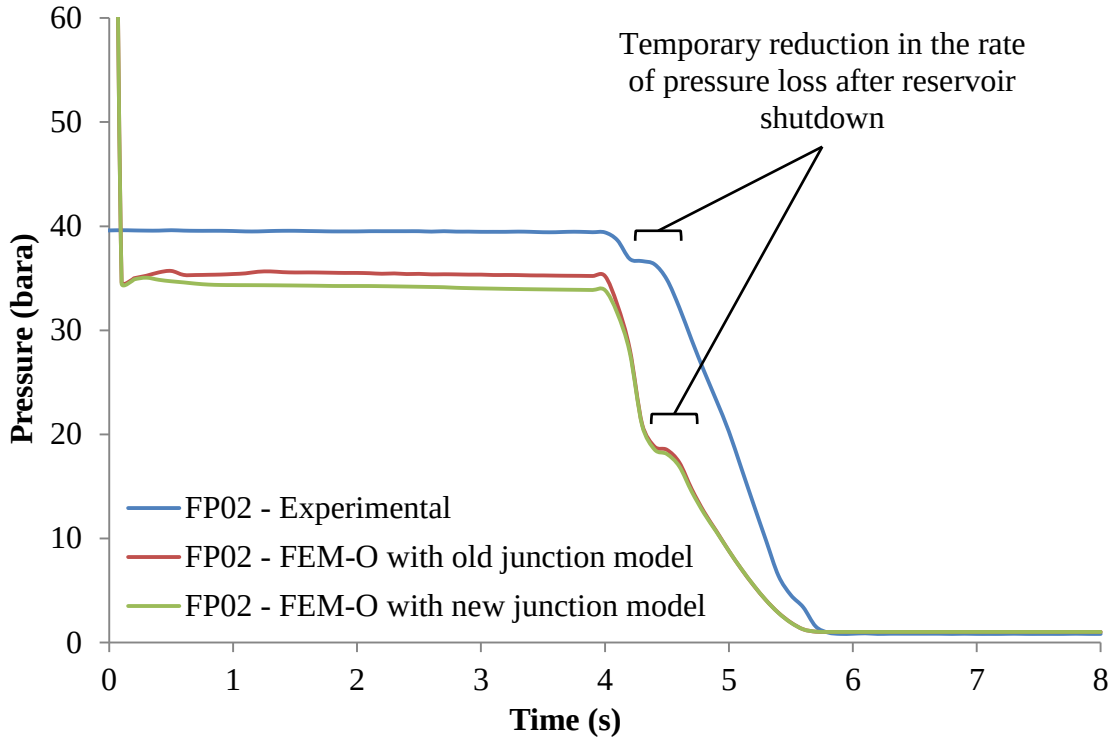

Figure 7.4: A comparison of experimental and FEM-O predicted fluid pressures at FP02 (see table 7.2) for Test 7, reservoir shutdown occurred at 4.0 s.

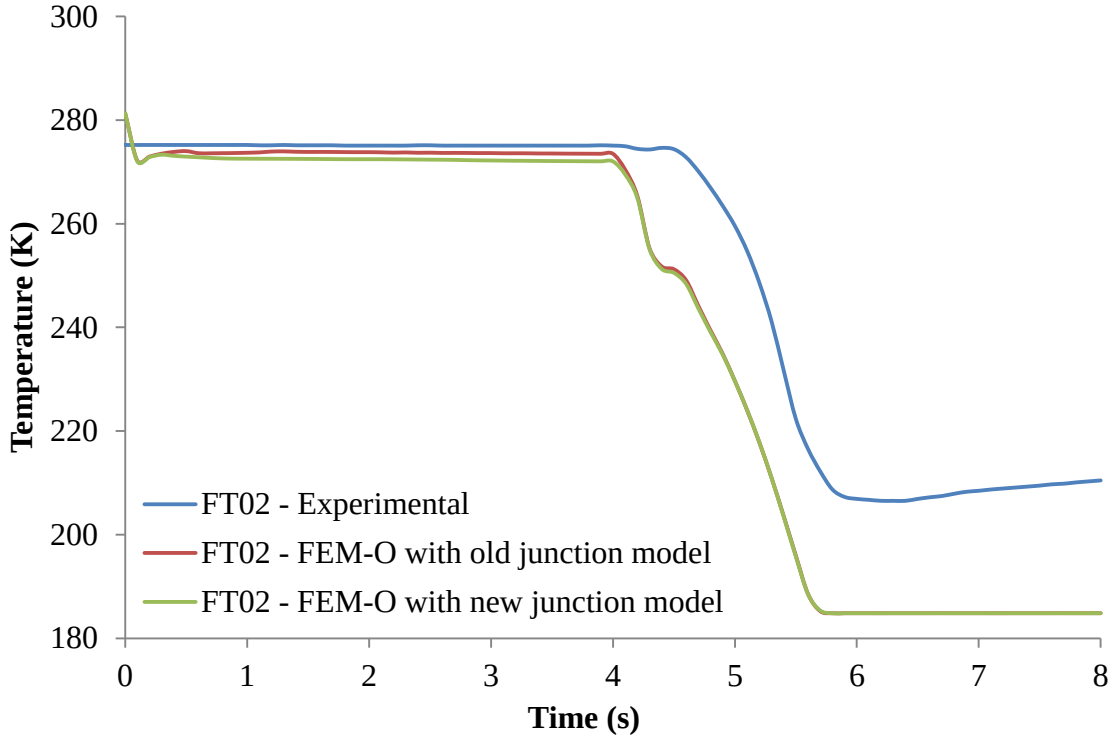

Figure 7.5: A comparison of the Test 7 experimental and FEM-O predicted fluid temperatures at FT02 (see table 7.2), reservoir shutdown occurred at 4.0 s.

Referring to figure 7.5, the experimental data reports a constant steady state temperature, with junction temperature losses of ca. 2°K. Fluid temperature is not observed to change significantly for ca. 0.7 s following reservoir shutdown, this may be due to instrument time lag. Otherwise the trends in the predicted fluid temperature data closely match those in the corresponding pressure data.

Predicted fluid pressure, velocity and entropy data for Test 7, generated using both junction models, was also analysed. No unusual behaviour in the fluid pressure and velocity predictions was observed. However, fluctuations in fluid entropy were discovered in the predicted data. Figure 7.6 presents the predicted fluid entropy profiles for Test 7 at 2.0 s after test initiation, data generated using both the old and new junction models is presented. As may be observed, fluctuations in fluid entropy are predicted at the inlet of pipe 1 and at the release plane by both junction models and in the vicinity of the junction by the old junction model only. The latter fluctuation is associated with the predicted change of the fluid from pure liquid to a liquid-vapour mixture. When using the new junction model this phase transition is predicted to occur at the junction itself rather than in pipe 1. The remaining fluctuations are not associated with any unexplained fluid phenomena and so are assumed to result from the application of the relevant boundary conditions to the system.

Figure 7.7 presents the FEM-O predicted pipe wall temperature profiles for Test 7 at 2.0 s after test initiation using the old and new junction models. As may be observed, fluctuations in the predicted fluid entropy are mirrored by fluctuations in the wall temperature at corresponding locations.

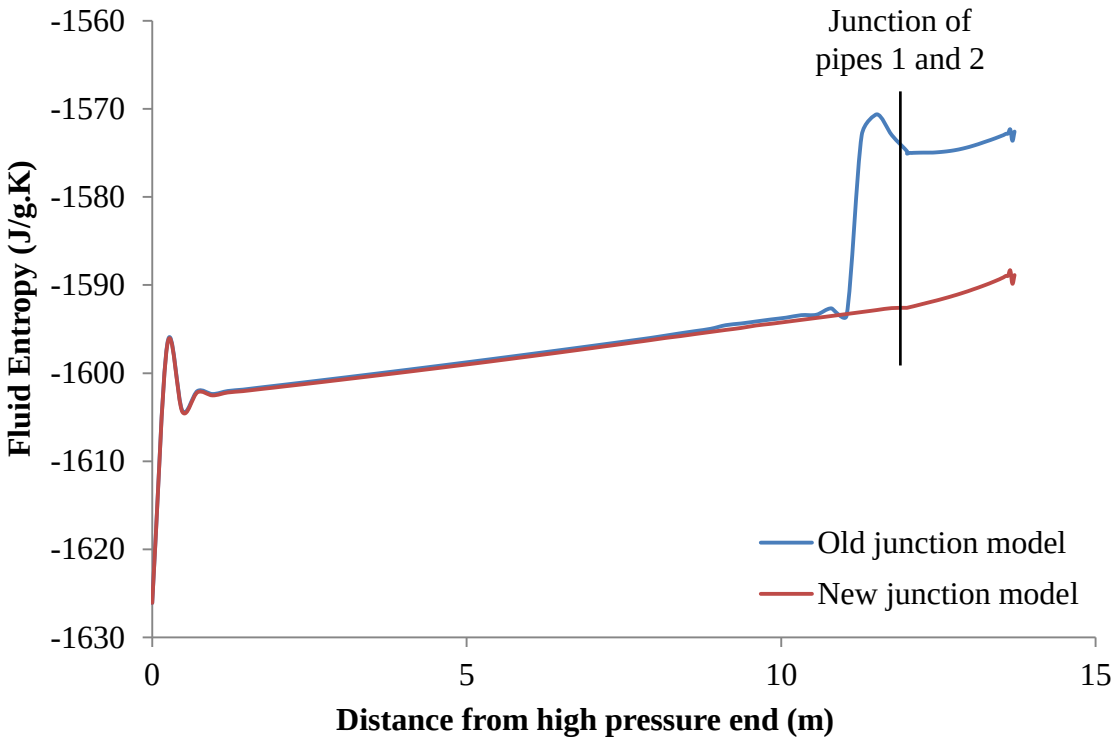

Figure 7.6: A comparison of the FEM-O predicted fluid entropy profiles in the pipe system 2 s after the initiation of Test 7.

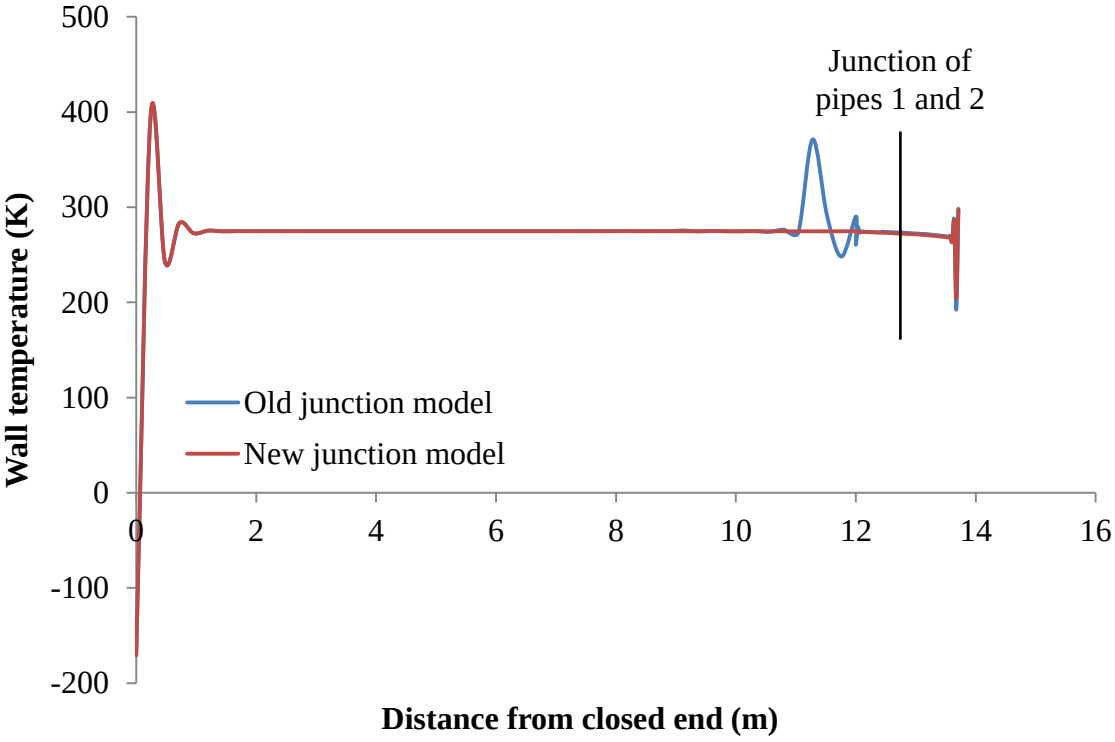

Figure 7.7: FEM-O predicted pipe wall temperatures 2 s after simulation initiation for Test 7.

Referring to figure 7.4, the trends in experimental and FEM-O predicted fluid pressures are the same, however the differences in steady state pressures are significant. Table 7.6 presents the Test 7 experimental and FEM-O predicted (new junction model) steady state fluid pressures at each transducer location 2.0 s after test initiation.

Table 7.6: Test 7 experimental and FEM-O predicted (new junction model) fluid pressures 2.0 s after test initiation. * Distances estimated from photographs of the experiment.

Transducer	Distance from open end (m)	Experimental pressure (bara)	FEM-O pressure (bara)	% difference
FP01	0.075	32.79	26.79	-18.2
FP02	1.56	39.47	34.25	-13.2
FP03	1.91*	44.95	37.47	-16.6
FP04	10.91*	79.7	45.57	-43

As may be observed there is a significant, although relatively consistent, percentage difference between the experimental and predicted pressures at transducers FP01 to FP03. At FP04 the FEM-O predicted pressure is 43 % smaller than that observed experimentally. The implementation of the reservoir boundary condition (see section 4.3.2) may have contributed to this difference. This boundary condition assumes the reservoir is infinite and net fluid movement within it is nil, thus the fluid velocity at the inlet to pipe 1 is assumed to be 0 m/s. However, given the size of the CO_2 vessel used in Test 7 (600 mm ID, 24 m long) this assumption is unlikely to remain valid. To test this conclusion, as well as investigate further the relationship between fluid entropy and pipe wall temperature, the reservoir boundary condition was modified to allow for fluid velocities greater than 0 m/s at the pipe inlet. The modified boundary condition holds the pressure and entropy at the pipe inlet at their initial values while updating the velocity at each time interval. Velocity at the inlet was therefore calculated from the negative Mach line compatibility equation 4.5.

Using the modified reservoir boundary condition and the new junction model Test 7 was simulated with FEM-O (simulation parameters are given in table 7.5). Fluid pressures were significantly over-predicted compared to the available experimental data at all transducer locations. Fluid temperatures were also over-predicted with increasing severity as distance from the reservoir increased. The infinite reservoir assumption is therefore more appropriate for modelling fluid outflow for Test 7.

The predicted fluid pressure, velocity and entropy data was analysed. No unexplained trends in the pressure and velocity predictions were discovered. No fluctuations in fluid entropy were predicted at the inlet if pipe 1. Figure 7.8 shows the pipe wall temperature profiles 2.0 s after initiation of Test 7 using the original and modified reservoir boundary conditions. As may be observed, fluctuations in the wall temperature predicted at the inlet of pipe 1 were also eliminated with the modified reservoir boundary condition.

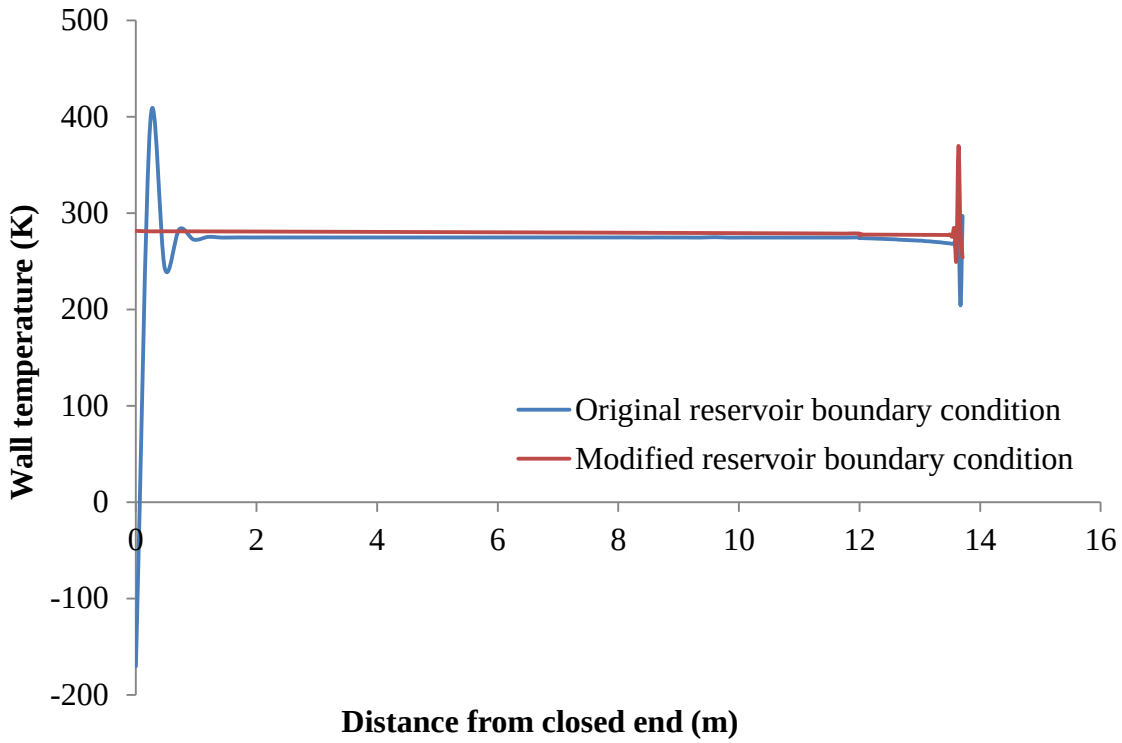

Figure 7.8: FEM-O predicted pipe wall temperature profiles 2 s after initiation of Test 7 using the original and modified reservoir boundary conditions.

A clear relationship between fluctuations in the predicted fluid entropy (figure 7.6) and unrealistic pipe wall temperature predictions (figures 7.7 and 7.8) at the inlet to pipe 1 is therefore demonstrated. Re-examination of the Test 5 and 6 results revealed the same relationship when the closed end and rupture plane boundary conditions are used. The likely mechanism is for the fluid entropy fluctuations to produce numerical instability in the finite element model, resulting in unrealistic wall temperature predictions.

Re-examination of the Tests 3 and 4 OUTFLOW results revealed similar, although less severe, fluctuations in predicted fluid entropy compared to those observed in the FEM-O predictions. The cause of these fluctuations is not known with certainty; they may result from the correct function of the model following the formulation and implementation of the relevant boundary conditions. Alternatively an unidentified issue in the formulation of the boundary conditions or implementation of the MOC may produce them.

In summary, significant savings in computational run time (ca. 45 %) have been achieved without significant loss of accuracy by using the new two pipe junction boundary condition presented in section 7.2. Fluctuations in predicted fluid entropy, resulting from the application of boundary conditions, have also been shown to result in fluctuating/unrealistic wall temperature predictions. Based on the data presented, all such fluctuations occur in close proximity to the ends of the pipes and do not appear to affect the overall quality of the wall temperature or fluid model predictions or the stability of the simulations.

7.4 Validation of the three pipe junction model

In this section the three pipe junction boundary condition presented in section 7.2 is validated against experimental data gathered from the venting of a large CO_2 pipeline system through a T-junction (referred to hereafter as experiment 6).

Experimental 6 was conducted by the UK National Grid as part of the COOLTRANS research programme (UKCCSRC, 2012). Experimental data recorded from this experiment has not been published:

7.4.1 Description of a three pipe junction venting experiment

In this experiment the re-circulation loop of a large scale CO_2 release experiment was vented through an instrumented, vertical vent pipe mounted on its top side. The re-circulation loop incorporated a pump and heat exchanger. Data was recorded by the UK National Grid. A schematic of the pipe layout is shown in figure 7.9 and the dimensions of the pipes are presented in table 7.7.

It was not possible to simulate this system exactly using FEM-O, therefore the pipe layout was simplified and the pump and heat exchanger removed, as shown in figure 7.10. Pipes *c*, *d* and *e* (figure 7.9) have been combined into a single pipe (pipe 5, figure 7.10) with the same ID as pipe *c* and a volume equal to that of pipes *c*, *d* and *e* combined. Pipe *b* was first subdivided into two sections in order to simulate the T-junction, however this resulted in prohibitively long run time. Pipe *b* was therefore subdivided into three pipes (pipes 2, 3 and 4) as shown in figure 7.10, which presents the final schematic of the simulated system. The dimensions of the simulated pipe layout are given in table 7.10.

Fluid property data is only available from instruments placed in the vent pipe, the locations of these are presented in table 7.8. The types and technical specifications of the instruments used at each location are given in table 7.9.

Experimental method

Before venting the re-circulation loop was isolated from the main experiment using valves located at the ends of pipes *a* and *f* (figure 7.9), the pump and heat exchangers were also shut down. Venting was initiated by opening a valve at the base of the vent pipe. This valve was kept open for 300 s before being closed.

Experiment 6 was simulated for 300 s using FEM-O, details of the finalised simulation inputs are given in tables 7.10 and 7.11. The simulation is numbered Test 8.

Table 7.7: Pipe dimensions of the re-circulating loop shown in figure 7.9.

Pipe	Length (m)	Internal diameter (mm)	Orientation relative to horizontal (°)
a	12	323	0
b	370	609	0
c	10	430	0
d	3	377	0
e	10	323	0
f (vent)	5.88	80.75	90

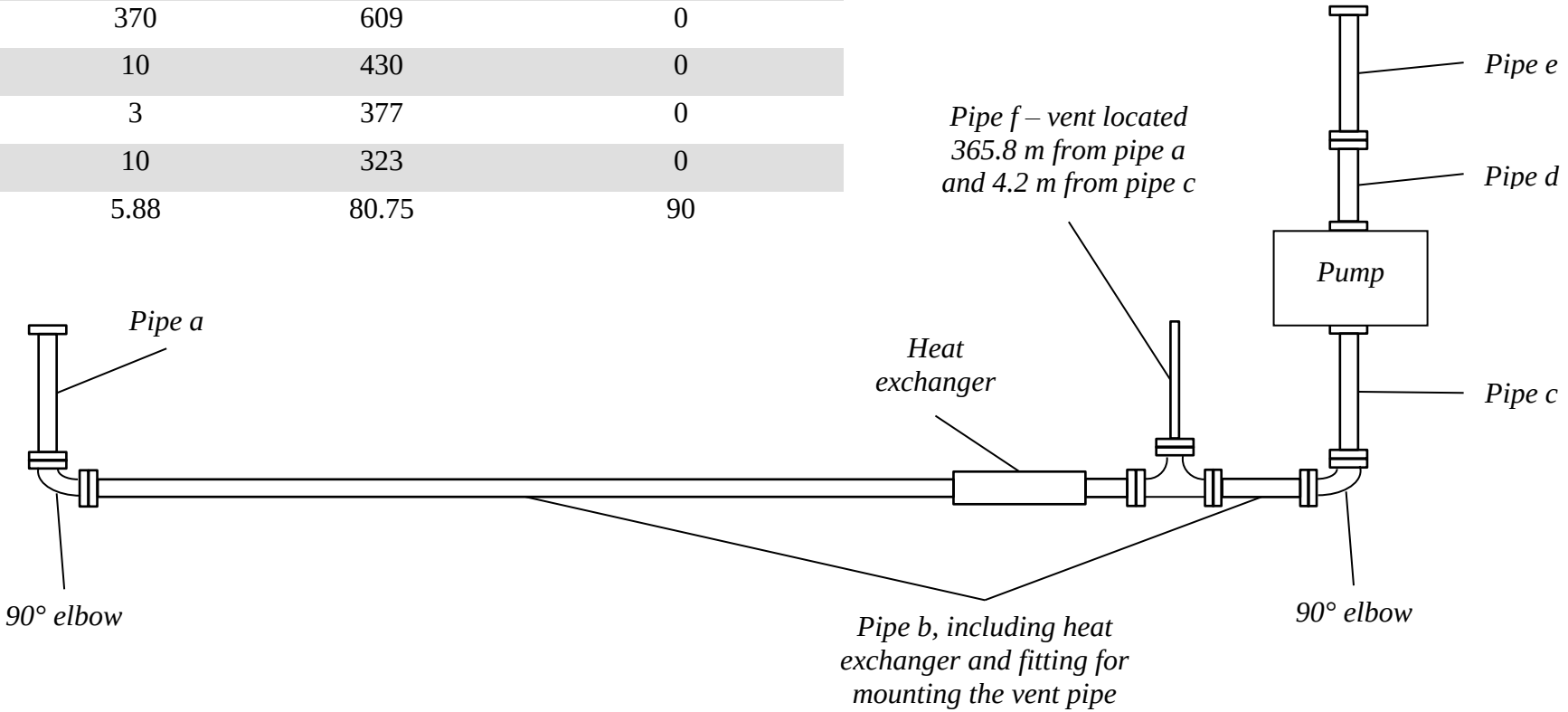

Figure 7.9: A diagram of the re-circulating loop layout.

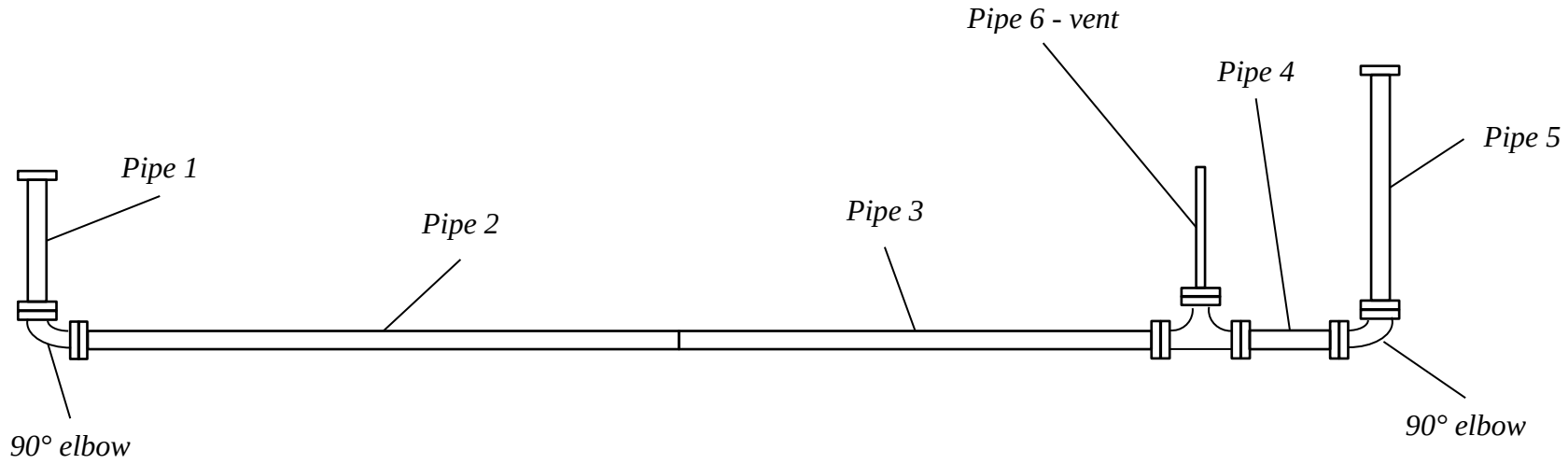

Figure 7.10: A diagram of the simplified re-circulating loop used in the simulation of Test 8. (Pipes 2 and 3 were initially simulated as a single pipe before being subdivided to reduce the run time).

Table 7.8: Types and locations of the instruments installed on the vent pipe of the re-circulating loop (pipe 6, figure 7.10).

Transducer location	Fluid Pressure Transducer	Fluid Temperature Transducer	Wall Temperature Transducer	Distance from open end (m)
1	FP01	FT01	WT01	0.08
2	FP02	FT02	WT02	1.74
3	FP03	FT03	WT03	3.4

Table 7.9: The types and technical specifications of the instruments installed on the vent pipe of the re-circulating loop (pipe 6, figure 7.10).

Instrument type	Range	Sensitivity	Accuracy	Response (frequency)
FP-X – Kulite CT-375M fast response pressure transducers	0.35 – 210 bar; 77.65 – 393.15 K	0.05 – 0.1 MPa	0.05 – 0.1 MPa	150 – 1400
FT-X – Type T thermocouples	-73.15 – 533.15 K	-	± 2.2 K	-
WT-X – Type T thermocouples	-73.15 – 533.15 K	-	± 2.2 K	-

Table 7.10: Simulation parameters (pipe dimensions) used in the simulation of experiment 6, venting through a T-junction.

		Inputs	Test 8
Pipeline Characteristics	Pipe 1	Pipeline Length (m)	12
		Pipe External Diameter (mm)	355
		Pipe Wall Thickness (mm)	16
		Pipe Orientation to the Horizontal Plane (°)	0
	Pipe 2	Pipeline Length (m)	200
		Pipe External Diameter (mm)	641
		Pipe Wall Thickness (mm)	16
		Pipe Orientation to the Horizontal Plane (°)	0
	Pipe 3	Pipeline Length (m)	165.8
		Pipe External Diameter (mm)	641
		Pipe Wall Thickness (mm)	16
		Pipe Orientation to the Horizontal Plane (°)	0
	Pipe 4	Pipeline Length (m)	4.2
		Pipe External Diameter (mm)	641
		Pipe Wall Thickness (mm)	16
		Pipe Orientation to the Horizontal Plane (°)	0
	Pipe 5	Pipeline Length (m)	17.98
		Pipe External Diameter (mm)	462
		Pipe Wall Thickness (mm)	16
		Pipe Orientation to the Horizontal Plane (°)	0
	Pipe 6 (vent pipe)	Pipeline Length (m)	5.88
		Pipe External Diameter (mm)	100.75
		Pipe Wall Thickness (mm)	10
		Pipe Orientation to the Horizontal Plane (°)	90
		Heat Transfer Option	FEM – Exposed to air
		Pipeline Roughness (mm)	0.05

Table 7.11: Simulation parameters (fluid, rupture and numerical) used in the simulation of experiment 6, venting through a T-junction.

		Inputs	Test 8
Inlet Parameters		Feed Composition (mole %)	CO_2 93.69
			H_2 1.07
			N_2 3.36
			O_2 1.88
		Feed Inlet Temperature (°K)	279.75
		Feed Inlet Pressure (bara)	95.5
		Ambient Temperature (°K)	276.72
		Ambient Pressure (bara)	1.01
Failure Conditions		Failure Mode	FBR (pipe 6)
		Failure Location Relative to High Pressure end (m)	383.68
		Discharge Coefficient	1
Other Parameters	**Pipe 1**	Number of Pipeline Grid Points	12
	Pipe 2	Number of Pipeline Grid Points	200
	Pipe 3	Number of Pipeline Grid Points	170
	Pipe 4	Number of Pipeline Grid Points	4
	Pipe 5	Number of Pipeline Grid Points	18
	Pipe 6	Number of Pipeline Grid Points	30
		Simulation Model	HEM
		Equation of State	PR (equation 3.6)
		Friction Factor Correlation	Chen (Equation 3.33)
		Total Depressurisation Time (s)	300

7.4.2 Early T-junction simulations and refinements to FEM-O

The first simulation of Test 8 with FEM-O was not successful using the new three pipe boundary condition described in section 7.2. Unrealistic wall temperature predictions near the T-junction (figure 7.10) resulted in the failure of the simulation at ca. 100 s; these were caused by fluctuations in the predicted fluid entropy at the corresponding locations. The implementation in code of the new three pipe boundary condition appeared to contribute to these fluctuations by not enforcing the assumption of isentropic flow effectively. The new three pipe junction boundary condition was therefore refined to rigidly enforce the assumption of isentropic flow. Equation 7.4 was replaced in the ZERO_N algorithm by two simpler functions:

$$s_1 = s_2 \qquad \textbf{7.7}$$

$$s_2 = s_v \qquad \textbf{7.8}$$

In order to add equations 7.7 and 7.8 to ZERO_N a second non-linear function had to be removed; the Path line equation for the smaller of the two main pipes attached to the T-junction was selected (in the case of Test 8 this was the Path line for pipe 4). The refined variables and non-linear functions provided to the ZERO_N algorithm are therefore:

- P_1, P_2, P_3, u_1, u_2, u_3, s_1, s_2 and s_3
- C_+ and C_0 from pipe 1, C_+ from pipe 2, C_- from pipe 3 (equations 4.3, 4.1 and 4.5 respectively), and equations 7.1 (used twice, for n = 1 and n = 2), 7.3, 7.7 and 7.8

The pipeline system modelled in Test 8 was the first of sufficient size to utilise the sparse grid system described in section 6.2.1. This grid system contributed to the prediction of unrealistic wall temperatures and ultimately the failure of the Test 8 simulation, it was therefore rejected in favour of the standard grid system. In order to maintain the lower run times associated with the sparse grid system the number of rows

of nodes in the FEM mesh was reduced to three rows for a pipeline exposed to air and five rows for an insulated or buried pipeline (see section 8.4). Tests 5, 6 and 7 were repeated with the three and five row FEM meshes, the results demonstrated no loss of accuracy when compared with the experimental data or the simulation data presented in this thesis.

With the refinements to ZERO_N and the FEM mesh Test 8 was successfully simulated in 125 hours 43 minutes. No run-time comparison was possible with the original three pipe junction boundary condition presented in section 4.3.3 as the relevant computer code was not available for use with FEM-O.

7.4.3 Three pipe junction validation results

Simulation data from Test 8 is compared with the corresponding experimental fluid pressure, fluid temperature and wall temperature data from FP03, FT03 and WT03 (towards the base of the vent pipe) in figures 7.11, 7.12 and 7.13 respectively.

Referring to figure 7.11, a peak in the experimental fluid pressure is observed as blowdown begins due to an initially high proportion of liquid entering the vent pipe (NB the real vent pipe was open to the atmosphere prior to venting). From ca. 15 s a steady rate of decompression is recorded until venting is halted at 300 s. FEM-O predicts a steady depressurisation rate from ca. 5 s. As may be observed, from this time onward the fluid pressure is consistently under predicted at FP03.

Stratification of a CO_2 inventory in a shock tube subjected to a puncture at one end has been observed experimentally (CO2PipeHaz, 2012), as discussed in section 2.4.7. Based on the available experimental data for Test 8 and the known parameters of the system, it is likely that the inventory has stratified by 15 s after rupture, resulting in predominantly vapour entering the vent pipe. FEM-O cannot account for stratification as it assumes a homogeneous equilibrium in the inventory. As a result the proportion of liquid predicted

to enter the vent, and therefore the depressurisation rate, will be over predicted, as is observed for Test 8.

Referring to figure 7.12, following test initiation the predicted fluid temperature increases by ca. 17 K in the first 1 s of blowdown. After this time the trend in cooling is as expected given the predicted pressure profile presented in figure 7.11. Similar behaviour is observed in the predicted wall temperatures at WT03 (as shown in figure 7.13) where the temperature increases by ca. 10 K before cooling occurs.

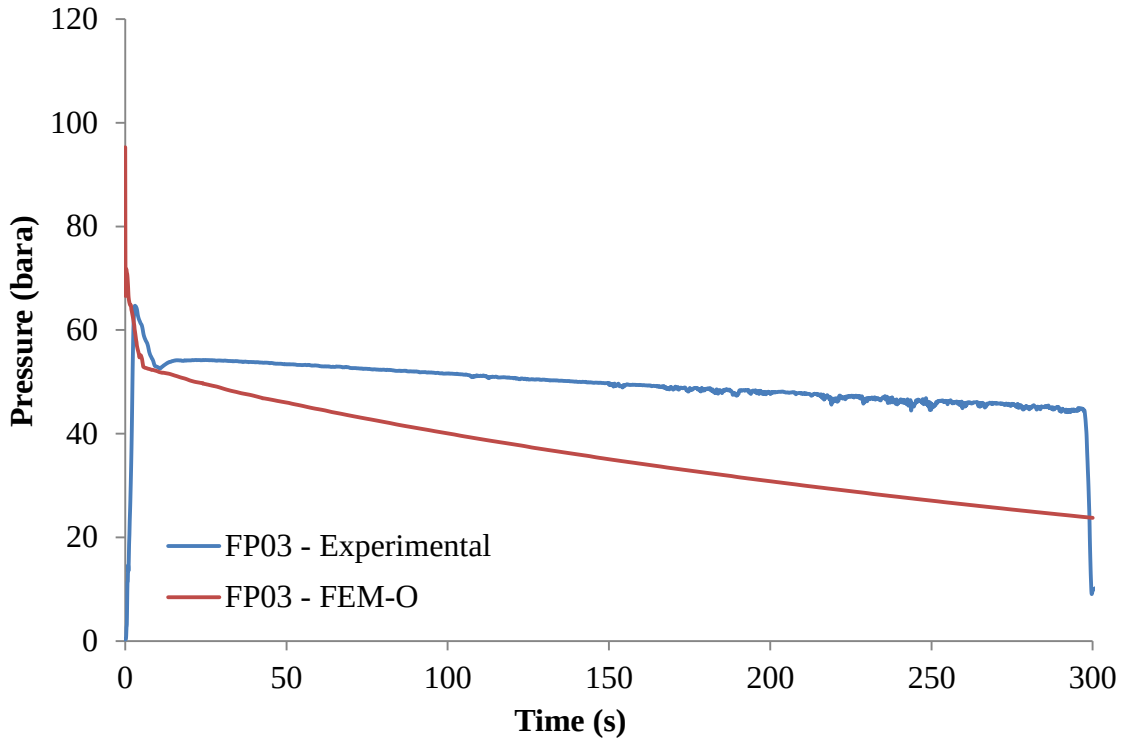

Figure 7.11: A comparison of the Test 8 experimental and FEM-O predicted fluid pressure at FP03.

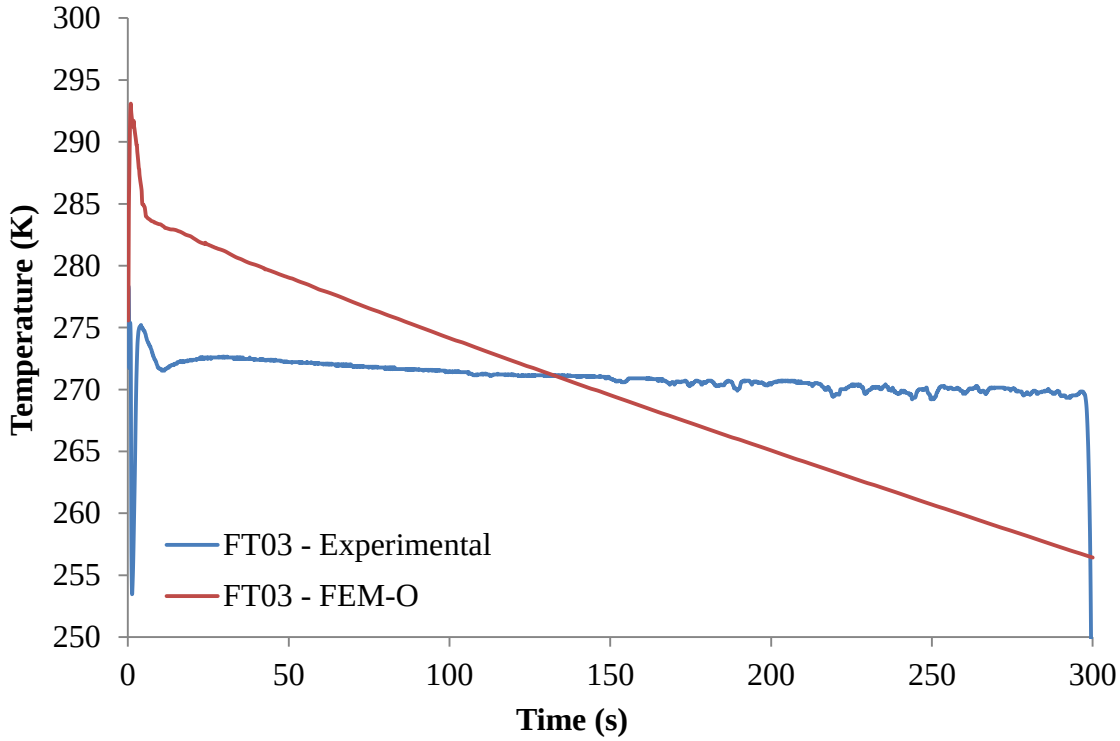

Figure 7.12: A comparison of the Test 8 experimental and FEM-O predicted fluid temperature at FT03.

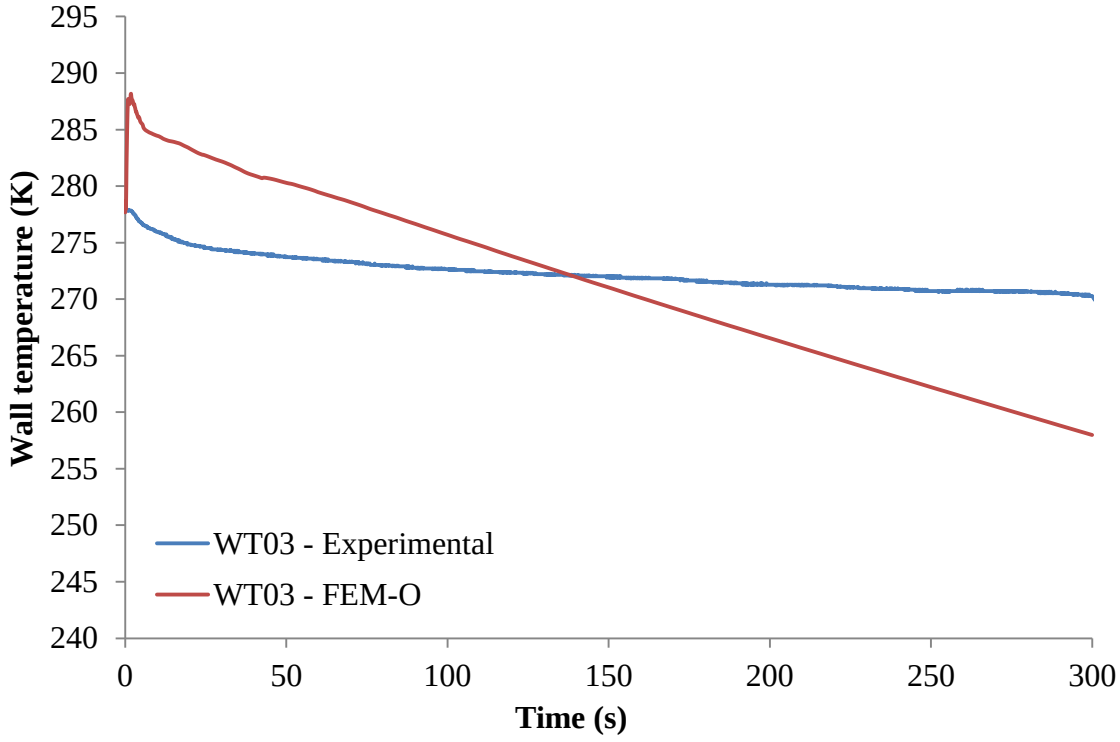

Figure 7.13: A comparison of the Test 8 experimental and FEM-O predicted vent pipe wall temperatures at WT03.

The initial increase in predicted fluid temperature results from the enforcement of isentropic flow through the T-junction. Figure 7.14 presents the fluid entropy profiles in the vicinity of the T-junction from pipes 3 to 6, 6 s after venting begins. As may be observed the predicted fluid entropy at both inlets and the outlet to the junction are the same, indicating that the ZERO_N algorithm is successfully converging to a solution. However the solution calculated is unrealistic compared to the entropy profiles in pipes 3 and 4. The calculation of unrealistic solutions in ZERO_N continues for the entire Test 8 simulation, with cumulative effects on all fluid properties calculated from the EoS. The over prediction of fluid and pipe wall temperatures has been discussed in reference to figures 7.12 and 7.13. Fluid density predictions are also affected and as a result mass is no longer conserved in the simulation. From an initial inventory of 93.7 tonnes, by 300 s 18.7 tonnes is predicted to have been ejected and 33.7 tonnes remains in the recirculation loop. This corresponds to a mass conservation index of 3.2.

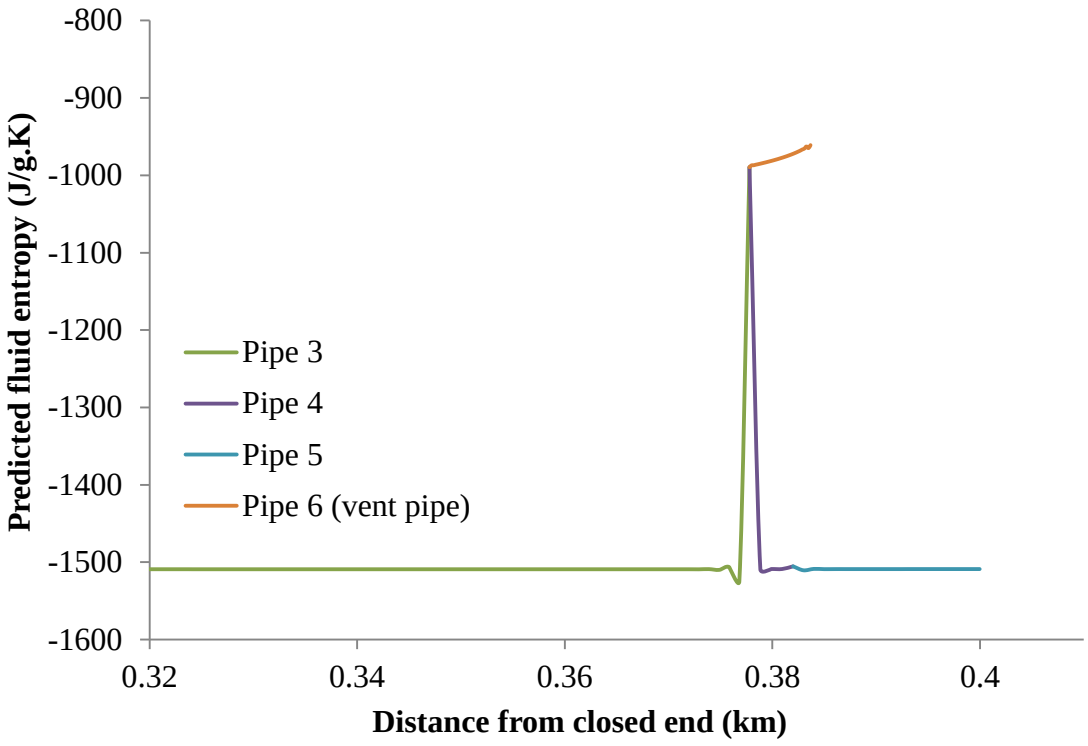

Figure 7.14: FEM-O predicted fluid entropy profiles in the vicinity of the T-junction 6 s after initiation of Test 8.

The choice of Path line retained as a convergence criterion in ZERO_N also affects the solution. As discussed previously, in order to include both equations 7.7 and 7.8 in the ZERO_N algorithm the Path line equation from the smaller of the two main pipes (for Test 8 this was pipe 4) was removed from the algorithm. When Test 8 was simulated with the other Path line retained the higher temperatures predicted in the vent pipe were eliminated, however the simulation did not run to completion.

Summary of results

In summary, FEM-O significantly over predicted the depressurisation rate in Test 8 compared to the experimental data. Analysis of the Test 8 results suggests the assumption of isentropic flow in a junction is inappropriate for modelling venting, resulting in unrealistic calculation results from all calculations carried out using the PR EoS. Importantly, the simulation failed to conserve mass. The evidence also suggests the application of the HEM model to modelling this venting experiment is inappropriate.

The flexibility afforded by the ability to choose the convergence criteria in the ZERO_N subroutine provides the opportunity to develop the three pipe boundary condition further in order to correctly model venting. Additionally, the potential exists to model more complex pipeline infrastructure such as closing or opening valves.

7.5 Conclusion

In this chapter new formulations for two and three pipe junction boundary conditions were presented. These were validated against experimental pressure, fluid and wall temperature data from two dense phase CO_2 release experiments; a pseudo steady state release and venting of a long pipeline through a T-junction.

When simulating the pseudo steady state experiment (Test 7) the new junction model demonstrated a significantly reduced run time (ca. 45 %) and acceptable agreement with the experimental data. Neither the new or old junction model predictions were

significantly more accurate compared to the other. Alteration of the reservoir boundary condition demonstrated the sensitivity of the Finite Element conduction model to fluctuations in fluid entropy.

Blowdown through a T-junction (Test 8) was simulated using the new junction model only. The depressurisation rate was significantly over-predicted in this experiment, partly due to the assumption of homogeneous equilibrium in the fluid. The assumption of isentropic flow in the T-junction resulted in the over-prediction of fluid and pipe wall temperatures in the vent pipe and the failure of FEM-O to conserve mass. The significant changes in fluid pressure and velocity inside the T-junction suggest that the assumption of isentropic flow is inappropriate for modelling venting.

Significant improvements in FEM-O run time were also achieved by reducing the number of rows of nodes in the Finite Element mesh. In the case of Test 8 this also allowed for the use of a standard, rather than sparse FEM grid, which contributed to the successful completion of the Test 8 simulation.

Chapter 8: FEM-O verification studies

8.1 Introduction

In chapters 6 and 7 FEM-O was validated against a range of experimental data for CO_2 releases from various pipe configurations. During this validation work various refinements to FEM-O were implemented, these included:

- an extended heat transfer coefficient (Steiner and Taborek, 1992) for calculating fluid/wall heat transfer when the vapour fraction of the inventory is > 60 %;
- the development of new formulations for two and three pipe junction boundary conditions;
- the reduction of the number of rows of nodes in the FEM mesh from 11 to 5 for an insulated/buried pipe and 3 for a pipe exposed to air in order to reduce simulation run time.

Additionally, the sparse grid system was identified as a possible source of instability in FEM-O during the work simulating Test 8 (see section 7.4.2).

In this chapter a verification study of the refined FEM-O is performed. Wherever possible the simulations conducted are based on the National Grid shock tube experiment 3 (described in section 5.2). This facilitates the analysis of verification data shown in this chapter as well as allowing easy comparison with the experimental and simulation data presented in chapter 6.

In section 8.2 the pipe wall steady state temperature calculation algorithm is investigated by simulating heat transfer in the wall of a shock tube prior to blowdown.

In section 8.3 the effect of the external pipeline environment (buried, insulated or exposed to air) on the transient pipe wall temperatures during blowdown is investigated.

Data recorded from experiment 3 is used for reference when analysing the simulation results.

In section 8.4 the sensitivity of FEM-O predicted wall temperature results to the number of rows of nodes in the Finite Element mesh is investigated. Scenarios which include a pipeline exposed to air, insulated and buried pipelines are considered.

In section 8.5 the sparse FEM grid approximation is tested. In the specific case of Test 8 (see section 7.4.2) fluctuations in the pipe wall temperatures near the T-junction caused the initial simulation to fail. It was concluded that the sparse FEM grid (see section 6.2.1) exacerbated the effect of these fluctuations on the simulation. In this section the sparse FEM grid is tested by simulating blowdown of a 300 m long, single section pipe. Pipe wall temperature predictions for this pipeline, generated using a sparse and standard FEM mesh are compared.

In section 8.6 a verification study of the two pipe junction model developed in chapter 7 is presented. The analysis considers fluid flow through the junction only.

In section 8.7 the three pipe junction model developed in chapter 7 is considered. Blowdown of a pipeline system consisting of three pipes with different volumes connected at a junction is simulated. The analysis of this test considers fluid flow through the junction only.

In section 8.8 the complete venting of a 250 m long horizontal pipeline is simulated with FEM-O. Based on the simulation data the transient fluid flow regime in the main pipe is assessed and the applicability of the HEM assumption to modelling venting discussed in light of the results.

In section 8.9 conclusions for the chapter are presented.

8.2 FEM-O steady state wall temperature model

In this section the FEM-O steady state pipe wall temperature calculation algorithm (see figure 6.4) is tested for a pipe containing an inventory of air at 1.01 bara.

The dimensions of the pipe simulated are the same as those used when simulating experiment 3. An inventory of air is modelled. Inventory temperatures less than, the same as and warmer than the ambient air, to which the pipe is exposed, are considered. The pipe simulation parameters are detailed in table 8.1.

The pipeline was simulated until the steady state wall temperatures had been successfully calculated. It was assumed that the inventory was at rest and homogeneously mixed prior to blowdown, with no variation in fluid properties along the length of the shock tube.

Table 8.1: Simulation parameters used to investigate the FEM-O steady state model (pipe parameters and feed composition are common between tests).

	Inputs	Test 9	Test 10	Test 11
Pipeline characteristics	Upstream fitting	Closed end		
	Downstream fitting	Rupture disk		
	Pipe length (m)	144		
	Pipe external diameter (mm)	171.94		
	Pipe wall thickness (mm)	10.97		
	Pipe roughness (mm)	0.0000043		
	Pipe orientation to the horizontal plane (°)	0		
	Heat transfer option	FEM – exposed to air		
Inventory and ambient parameters	Feed composition (mole %)	N_2 – 79.0143 %, O_2 – 20.946 %, CO_2 – 0.0397 %		
	Fluid temperature (°K)	283.35	283.35	303.35
	Fluid pressure (bara)	1.01	1.01	1.01
	Ambient temperature (°K)	283.35	303.35	283.35
	Ambient pressure (bara)	1.01	1.01	1.01
Failure parameters	Failure mode	FBR		
	Failure location relative to upstream end (m)	144		
	Discharge coefficient	1		
Other parameters	Number of pipe grid points	144		
	Simulation model	HEM		
	Equation of State	PR (equation 3.6)		
	Friction factor correlation	Chen (Equation 3.33)		
	Total depressurisation time (s)	n/a		

Figure 8.1 presents the FEM-O predicted steady state wall temperatures for Tests 9 to 11. In these simulations the FEM mesh was modelled with eleven rows of nodes, the data presented is for the middle row. No significant temperature gradient was predicted through the pipe wall.

As may be observed the data displays the expected trends: when the inventory and ambient are at 283.35 K the wall has the same temperature, when the inventory or ambient is warmer than the other the wall is proportionally warmer. The wall temperature is always closer to the ambient temperature when the ambient and inventory temperatures are different. This is due to the use of different heat transfer correlations on the inner and outer surfaces of the pipe wall and to the velocities of the inventory (0 m/s) and the ambient air (5 m/s).

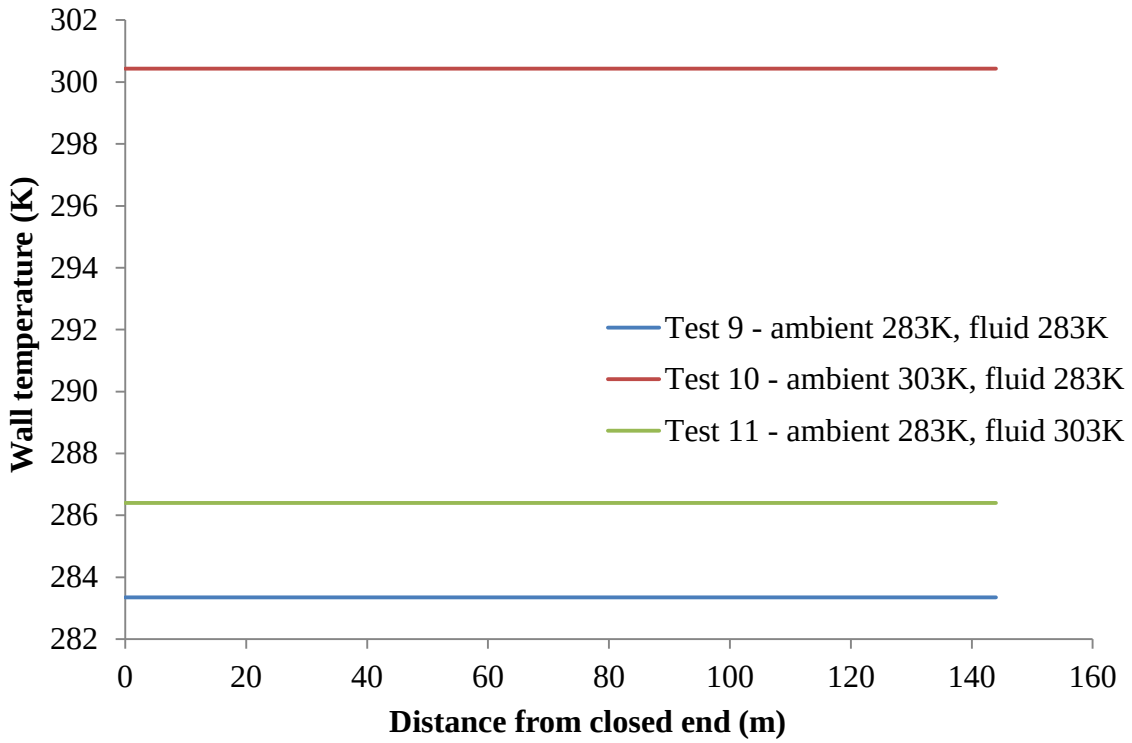

Figure 8.1: Steady state pipe wall temperature profiles for Tests 9 to 11.

The steady state wall temperature algorithm implemented in FEM-O therefore displays the expected behaviour.

8.3 Effects of the external pipeline environment on blowdown

In this section blowdown of a shock tube containing dense phase CO_2 is simulated with FEM-O in order to investigate the effect of different external pipeline environments on the predicted wall temperatures. The shock tube, inventory and other simulation parameters are based on the National Grid shock tube experiment 3 (see section 5.2), with the exception that the pipe is simulated in three environments; buried, insulated and exposed to air (uninsulated). Simulations conducted in this section used five rows of nodes in the FEM mesh.

Details of the simulation parameters are given in table 8.2.

A detailed comparison and discussion of the available experimental and FEM-O predicted Test 5 data was presented in section 6.3. Therefore in this section only the steady state wall temperature predictions and relative trends in the simulated wall temperature data are discussed for Tests 5, 12 and 13.

The simulated outer pipe wall temperatures 54 and 114 m from the closed end of the pipe are compared in figures 8.2 and 8.3 respectively for Tests 5, 12 and 13. Corresponding experimental data from the same locations (recorded by transducers WT10 and WT05 respectively, see table 5.2, section 5.2.1) is shown in figures 8.2 and 8.3 for comparison.

Table 8.2: Summary of the simulation parameters used when investigating the impact of pipe external environment on blowdown.

	Inputs	Test 5	Test 12	Test 13
Pipeline characteristics	Upstream fitting		Closed end	
	Downstream fitting		Rupture disk	
	Pipe length (m)		144	
	Pipe external diameter (mm)		171.94	
	Pipe wall thickness (mm)		10.97	
	Pipe roughness (mm)		0.0000043	
	Pipe orientation to the horizontal plane (°)		0	
	Heat transfer option	FEM – insulated	FEM – buried	FEM – exposed to air
Inventory and ambient parameters	Feed composition (mole %)		CO_2 – 100 %,	
	Fluid temperature (°K)		278.35	
	Fluid pressure (bara)		153.41	
	Ambient temperature (°K)		283.35	
	Ambient pressure (bara)		1.01	
Rupture parameters	Failure mode		FBR	
	Failure location relative to upstream end (m)		144	
	Discharge coefficient		1	
Other parameters	Number of pipe grid points		144	
	Simulation model		HEM	
	Equation of State		PR (equation 3.6)	
	Friction factor correlation		Chen (Equation 3.33)	
	Total depressurisation time (s)		25	

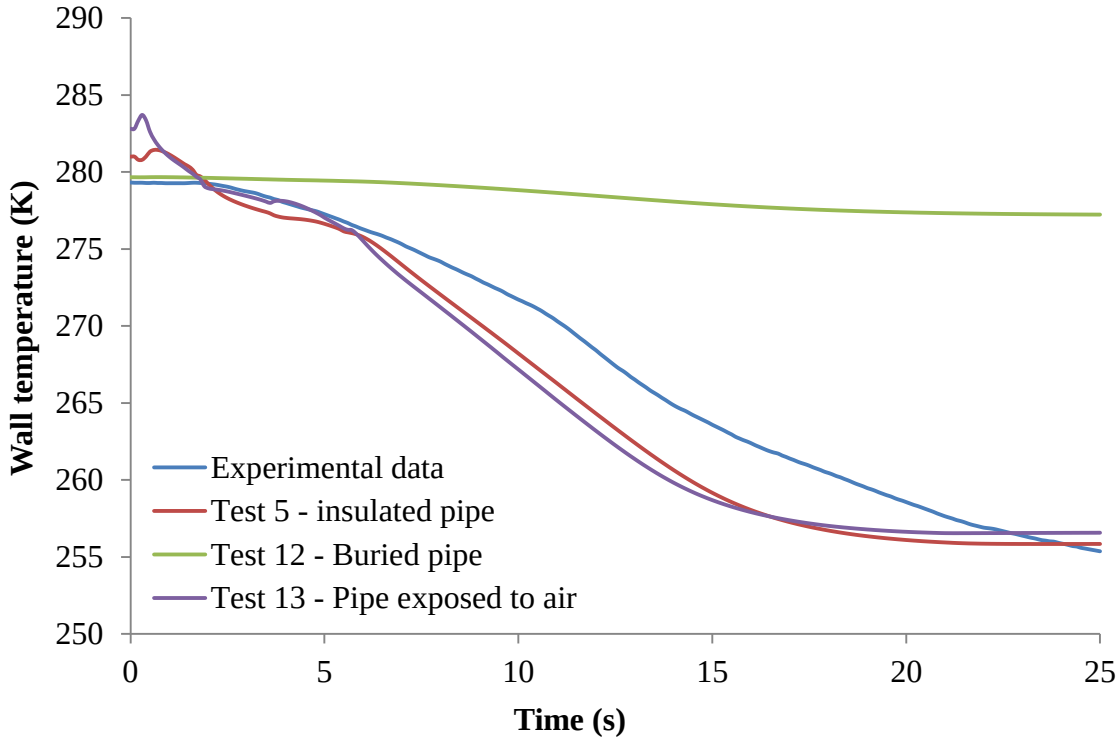

Figure 8.2: Transient outer pipe wall temperatures 54 m from the closed end of a shock tube in various environments during blowdown.

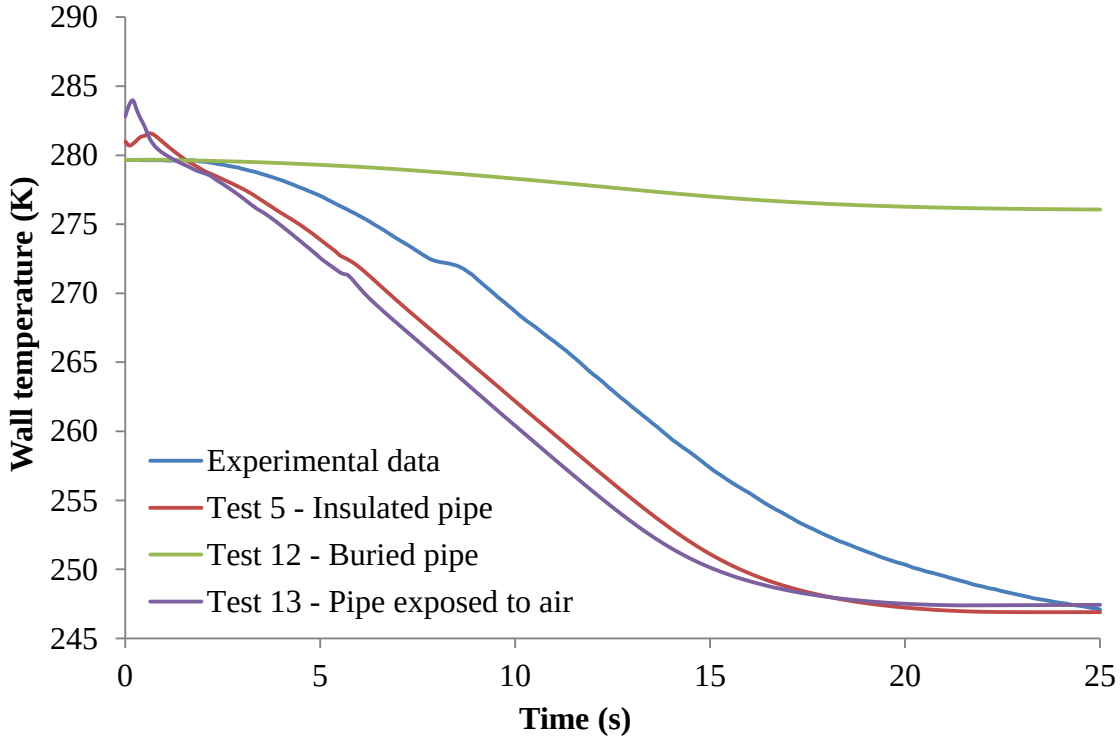

Figure 8.3: Transient outer pipe wall temperatures 114 m from the closed end of a shock tube in various environments during blowdown.

Referring to both figures, as expected the initial (i.e. steady state) predicted pipe wall temperature is greatest when the pipe is exposed to air and lowest when buried. This follows from the relative thicknesses and conductive properties of the insulation and soil layers in the FEM mesh (see table 6.1, section 6.2.3).

Referring to the Test 12 (buried pipe) data, very limited cooling is predicted in the pipe wall. Due to its thickness (1.5 m) and capacity to store energy (see table 6.1) the soil layer acts as an effective reservoir of heat that is transferred to the pipe wall during blowdown.

Referring to the Test 5 and 13 predictions in figures 8.2 and 8.3, the trends in pipe wall cooling are the same. Additionally and unexpectedly, the degree of cooling predicted is essentially the same for both Tests. In the scenario considered the wall of the insulated pipe (Test 5) would be expected to undergo more significant cooling than the uninsulated one (Test 13). Given the demonstrated accuracy of the Test 5 predictions (see section 6.3) the predicted minimum pipe wall temperatures for Test 13 must be considered unreliable.

In summary, blowdown simulations of insulated and buried shock tubes exhibit the expected behaviour relative to each other. The accuracy of the predictions for an insulated pipe has been discussed in detail in section 6.3. Predictions for an uninsulated pipe display the expected trends in cooling, however the degree of cooling is greater than expected. Therefore, while the uninsulated pipe FEM boundary condition may still be used to verify model performance, predictions made with it should be validated as a priority.

8.4 Finite Element mesh – rows of nodes

In this section the sensitivity of FEM-O pipe wall temperature predictions to the number of rows of nodes in the FEM mesh is investigated. The impact of the pipeline external environment (buried, insulated or exposed to air) on the size of the FEM mesh needed for realistic wall temperature predictions is also considered.

To perform the above analysis Test 5 (based on experiment 3, the blowdown of a foam insulated shock tube containing dense phase CO_2), which was previously simulated with 11 rows of nodes in the FEM mesh (see section 6.3), was simulated again with 5 and 3 rows of nodes in the mesh. Simulation parameters have been presented previously in table 8.2. In this section only the trends in predicted wall temperatures between different FEM mesh sizes are discussed.

Figures 8.4 and 8.5 respectively present the FEM-O predicted outer pipe wall temperatures (middle row of nodes in the respective FEM meshes) 54 and 114 m from the closed end of the shock tube following FBR. The corresponding experimental data from transducers WT10 and WT05 (see table 5.2, section 5.2.1) is shown in the figures for comparison.

Referring to both figures, it may be observed that all the FEM-O wall temperature predictions display the same trends in cooling for each of the mesh sizes considered. Barring some small numerical instability in the 5 row mesh predictions during the first 1 s of blowdown (due to rapid transients in the fluid), only very small differences in the wall temperature predictions are observed between the 11 and 5 row FEM meshes. For modelling pipe wall cooling during blowdown these mesh sizes may thus be considered equally accurate.

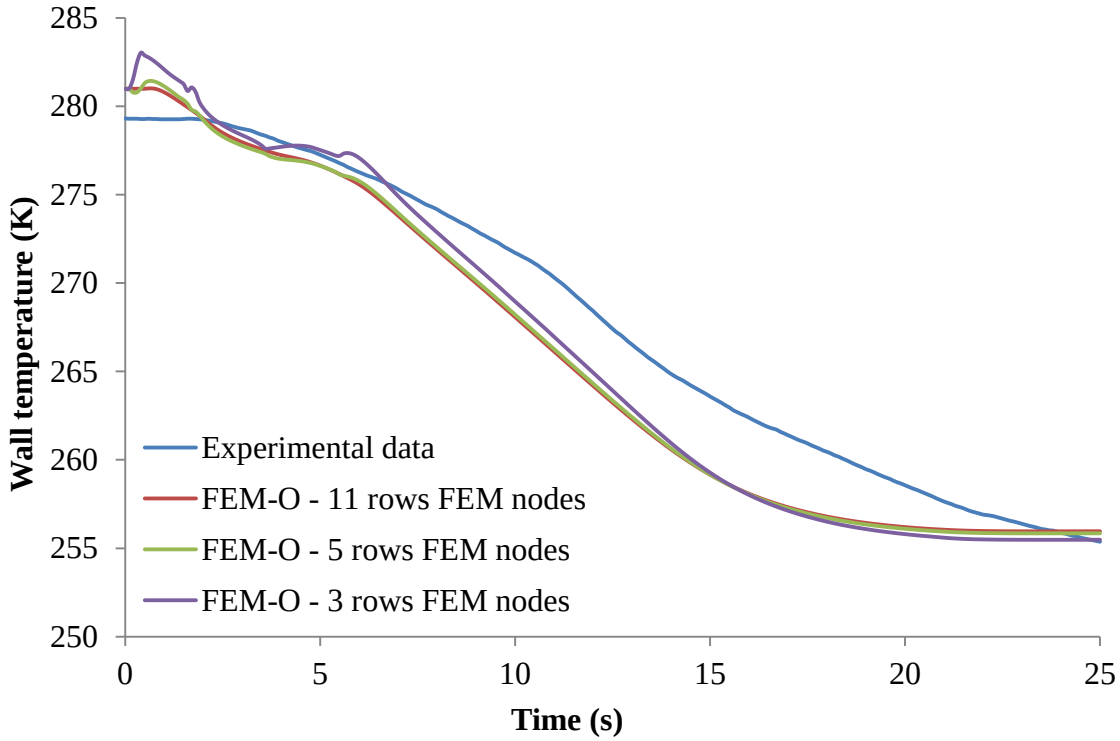

Figure 8.4: Experimental and predicted outer pipe wall temperatures at transducer WT10 (54 m from the closed end of the shock tube) for Test 5.

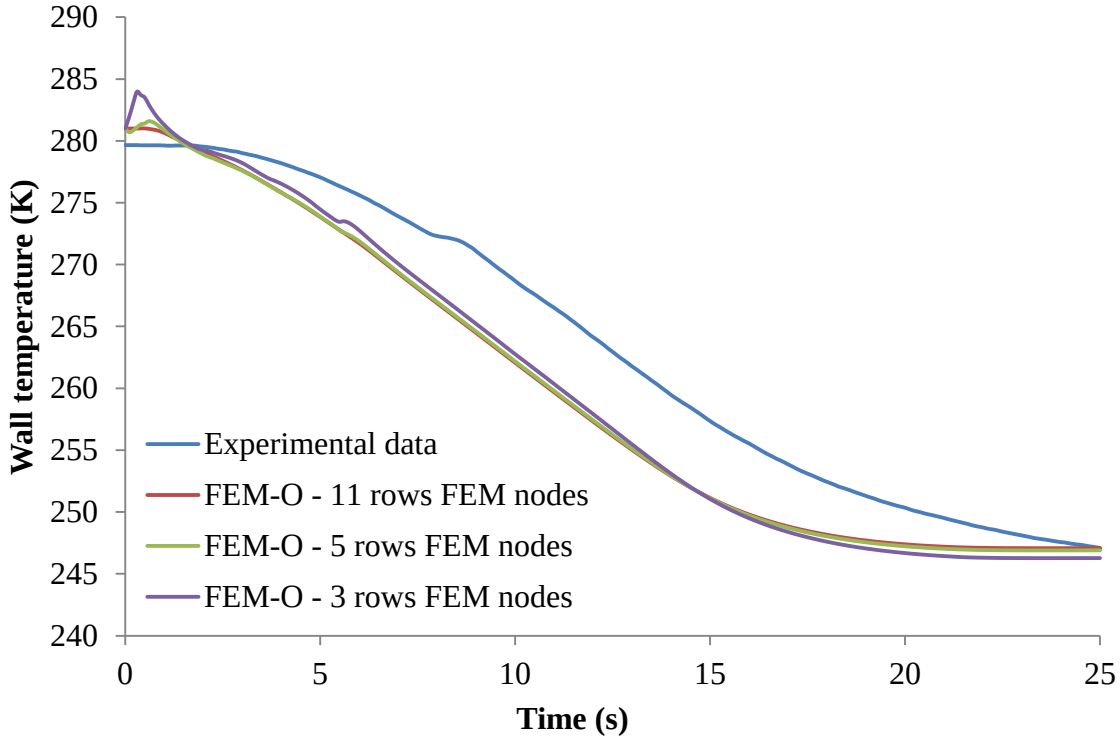

Figure 8.5: Experimental and predicted outer pipe wall temperatures at transducer WT05 (114 m from the closed end of the shock tube) for Test 5.

Wall temperature predictions from the 3 row FEM mesh show some evidence of more prolonged instability in the calculations, especially towards the closed end of the pipe (c.f. figure 8.4 before ca. 6 s). In this simulation the instability is not due exclusively to rapid transients in the inventory. Shown in figure 8.6 is the variation in node temperature during blowdown for the column of nodes in the FEM mesh located 54 m from the closed end of the pipe. Also shown are node temperature predictions at the same location for a Test 5 simulation using three rows of nodes with the pipe exposed to air (uninsulated). As may be observed for the insulated pipe, at the outer surface node (corresponding to the outer insulation surface) the temperature increases significantly as blowdown progresses. This increase in outer surface temperature is predicted along the full length of the pipe. In contrast, when the pipe is modelled as uninsulated the expected cooling is predicted throughout the FEM mesh.

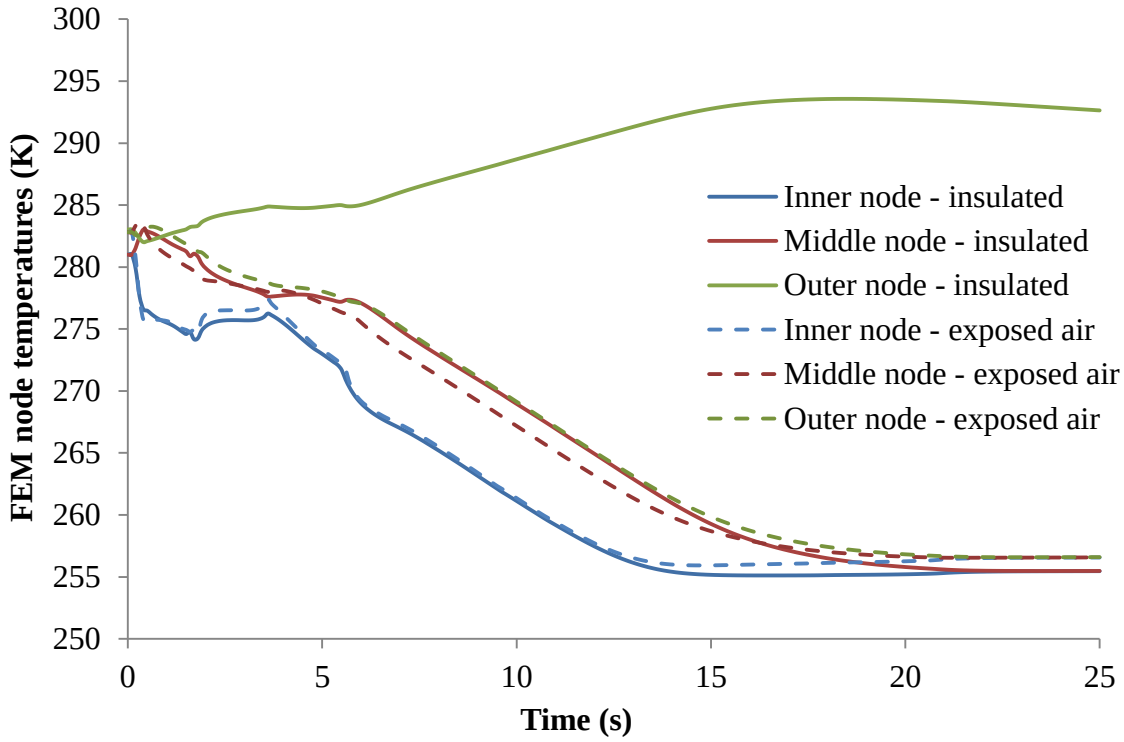

Figure 8.6: Temperature variation of the inner, middle and outer FEM nodes 54 m from the closed end of the pipe during blowdown. Data from the simulation of Test 5 with 3 rows of nodes in the FEM mesh and the pipe modelled as insulated and uninsulated.

In summary, when simulating an insulated pipe using 11 and 5 rows of nodes in the FEM mesh the expected cooling was predicted for all nodes. When using 3 rows of nodes unrealistic temperatures were predicted in the nodes corresponding to the outer insulation surface. The same behaviour may be extrapolated to the simulation of a buried pipeline. For an uninsulated pipe however 3 rows of nodes in the FEM mesh was sufficient to produce realistic transient wall temperature predictions. Therefore when simulating an insulated or buried pipe a minimum of 5 rows of nodes should be used in the FEM mesh. For an uninsulated pipe the evidence suggests 3 rows of nodes are sufficient.

8.5 Finite Element mesh – columns of nodes and the sparse grid

In this section the effect of using a sparse FEM grid on pipe wall temperature predictions during blowdown is assessed. The sparse grid computer code was prepared to overcome the high computational demand of the FEM code and so allow for the modelling of long pipelines. However, as discussed in reference to Test 8 (venting through a T-junction, see section 7.4), its use was identified as contributing to the early simulation failures for that test.

To test the sparse grid computer code a pipeline short enough that it may be simulated with the standard code, but long enough for the sparse grid approximation to be appropriate, must be simulated. Thus in this section blowdown of a 300 m horizontal pipeline containing dense phase CO_2 is simulated. The pipeline is modelled as uninsulated; therefore 3 rows of nodes are used in the FEM grid. FBR at the pipe end is assumed. A complete description of the simulation parameters is presented in table 8.3.

As discussed in section 6.2.1, the sparse grid reduced the number of columns of nodes in the FEM mesh by a factor of 10 compared to the number of fluid grid points. Thus for Test 14 there are 300 fluid grid points, 300 columns of nodes in the standard FEM

mesh and 30 columns of nodes in the sparse FEM grid. For both the standard and sparse FEM meshes columns of nodes are uniformly spread along the length of the pipe.

Table 8.3: Details of the simulation parameters used to investigate the performance of the sparse grid FEM code.

	Inputs	Test 14
Pipeline characteristics	Upstream fitting	Closed end
	Downstream fitting	Bursting disk
	Pipe length (m)	300
	Pipe external diameter (mm)	170
	Pipe wall thickness (mm)	10
	Pipe roughness (mm)	0.05
	Pipe orientation to the horizontal plane (°)	0
	Heat transfer option	FEM – exposed to air
Inventory and ambient parameters	Feed composition (mole %)	CO_2 – 100 %
	Fluid temperature (°K)	298.15
	Fluid pressure (bara)	101
	Ambient temperature (°K)	293.15
	Ambient pressure (bara)	1.01
Failure parameters	Failure mode	FBR
	Failure location relative to upstream end (m)	300
	Discharge coefficient	1
Other parameters	Number of pipe grid points	300
	Simulation model	HEM
	Equation of State	PR (equation 3.6)
	Friction factor correlation	Chen (Equation 3.33)
	Total depressurisation time (s)	60

Figure 8.7 presents the Test 14 outer pipe wall temperature profiles from 3.0 and 30.0 s after rupture calculated with FEM-O using both standard and sparse FEM meshes. Referring to the data calculated using the full mesh, fluctuations in the wall temperature

at the open and closed ends of the pipe (at 3.0 and 30.0 s respectively) derive from the application of the relevant boundary conditions as discussed previously in section 7.3.2. Corresponding fluctuations are predicted in the sparse mesh wall temperature profiles. However when using the sparse mesh these fluctuations extend much further along the pipe wall and thus have a greater effect on the calculation of fluid properties at the next time step. Additionally, pipe wall temperatures predicted using the sparse FEM mesh are significantly lower than those predicted with the full mesh along the whole length of the pipe and over the duration of the simulation. The resulting effect on the discharge rate is significant, as discussed in reference to figure 8.8 below.

Figure 8.8 presents the predicted cumulative mass discharge for the Test 14 simulation, calculated using both the standard and sparse FEM meshes. It may be observed that ca. 10 s after rupture the cumulative discharge between the different FEM meshes begins to diverge. This derives from the prediction of lower fluid exit velocities during blowdown when using FEM-O with the sparse FEM mesh. This results in a lower transient discharge rate and the cumulative discharge profile reported in figure 8.8.

In summary, use of the sparse FEM mesh results in significantly different predictions for pipe wall temperature and inventory discharge rate compared to predictions made using the standard FEM mesh. This may be expected to have significant implications for any hazard assessment of a CO_2 pipeline. Bearing in mind the results of the validation of FEM-O presented in chapter 6, the results presented in this section suggest the sparse FEM mesh is not suitable for modelling the blowdown of long CO_2 pipelines.

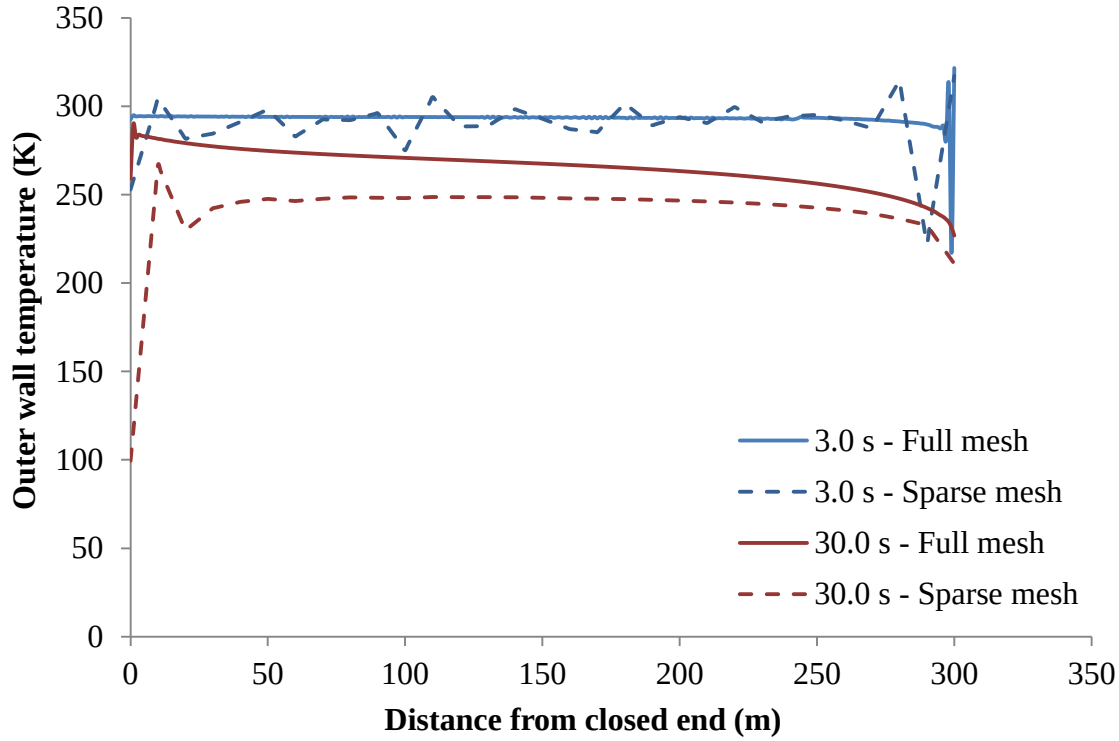

Figure 8.7: Test 14 outer pipe wall temperature profiles 3.0 and 30.0 s after FBR calculated using both standard and sparse FEM meshes.

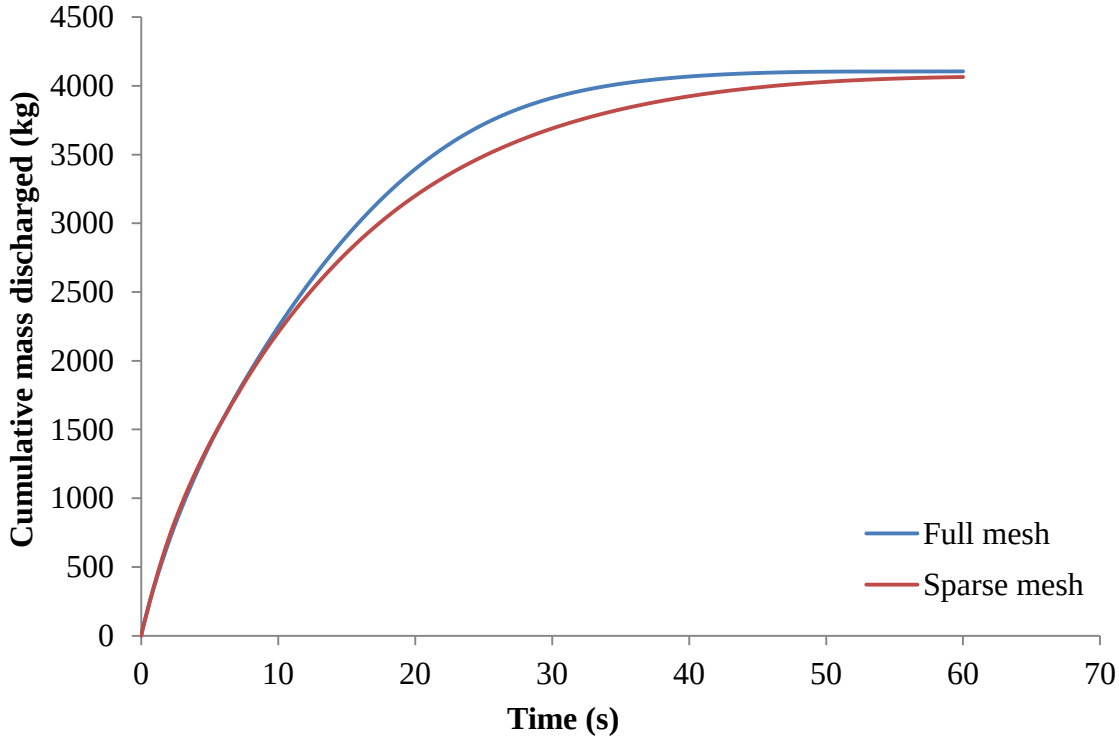

Figure 8.8: Test 14 cumulative mass discharged with time, calculated with FEM-O using both the standard and sparse FEM meshes.

8.6 Two pipe junction model verification

The two pipe junction model proposed in section 7.2 was validated in section 7.3, where it was demonstrated that it could be used to model fluid flow with acceptable accuracy.

In this section the performance of the two pipe junction model proposed in section 7.2 is verified by simulating the blowdown of a hypothetical shock tube with a 45° bend at its midpoint. The simulation parameters are detailed in table 8.4. The shock tube was subject to FBR at its end. The inventory was assumed to be at rest and homogeneously mixed prior to blowdown with no variation in fluid properties along the length of the shock tube.

Predicted fluid pressure, velocity and entropy at the inlet and outlet of the junction during blowdown are presented in figures 8.9, 8.10 and 8.11 respectively.

Referring to figure 8.9, the expected trends in the pressure histories at both the inlet and outlet of the junction are predicted. Between ca. 0.5 and 6 s decay in the fluid pressure appears to occur in a stepwise fashion. This is due to the movement of rapid transients in the fluid, which pass through the junction travelling in both directions. These disappear from the system by ca. 6 s, from which time the expected smooth decay in fluid pressure is predicted. Small fluid pressure losses (< 0.2 bara) are predicted as inventory passes through the junction. This results from the uniform pipe diameter in the system and the small angle of the junction.

Referring to figure 8.10, the expected fluid velocity histories at the inlet and outlet of the junction are predicted. Fluctuations in velocity during the first ca. 6 s of blowdown are due to the propagation of rapid transients in the inventory. Small differences between the pipe 1 outlet and pipe 2 inlet velocities result from small decreases in fluid pressure through the junction.

Table 8.4: Simulation parameters for the two pipe junction verification test.

	Inputs	Test 15	
		Pipe 1	**Pipe 2**
Pipeline characteristics	Upstream fitting	Closed end	2 pipe junction (45° bend)
	Downstream fitting	2 pipe junction (45° bend)	Rupture disk
	Pipe length (m)	72	72
	Pipe external diameter (mm)	171.94	171.94
	Pipe wall thickness (mm)	10.97	10.97
	Pipe roughness (mm)	0.0000043	0.0000043
	Pipe orientation to the horizontal plane (°)	0	0
	Heat transfer option	FEM – insulated	FEM – insulated
Inventory and ambient parameters	Feed composition (mole %)	CO_2 – 100	
	Fluid temperature (°K)	278.35	
	Fluid pressure (bara)	153.4	
	Ambient temperature (°K)	283.35	
	Ambient pressure (bara)	1.01	
Failure parameters	Failure mode	FBR	
	Failure location relative to upstream end (m)	144	
	Discharge coefficient	1	
Other parameters	Number of pipe grid points	72	72
	Simulation model	HEM	
	Equation of State	PR (equation 3.6)	
	Friction factor correlation	Chen (Equation 3.33)	
	Total depressurisation time (s)	30	

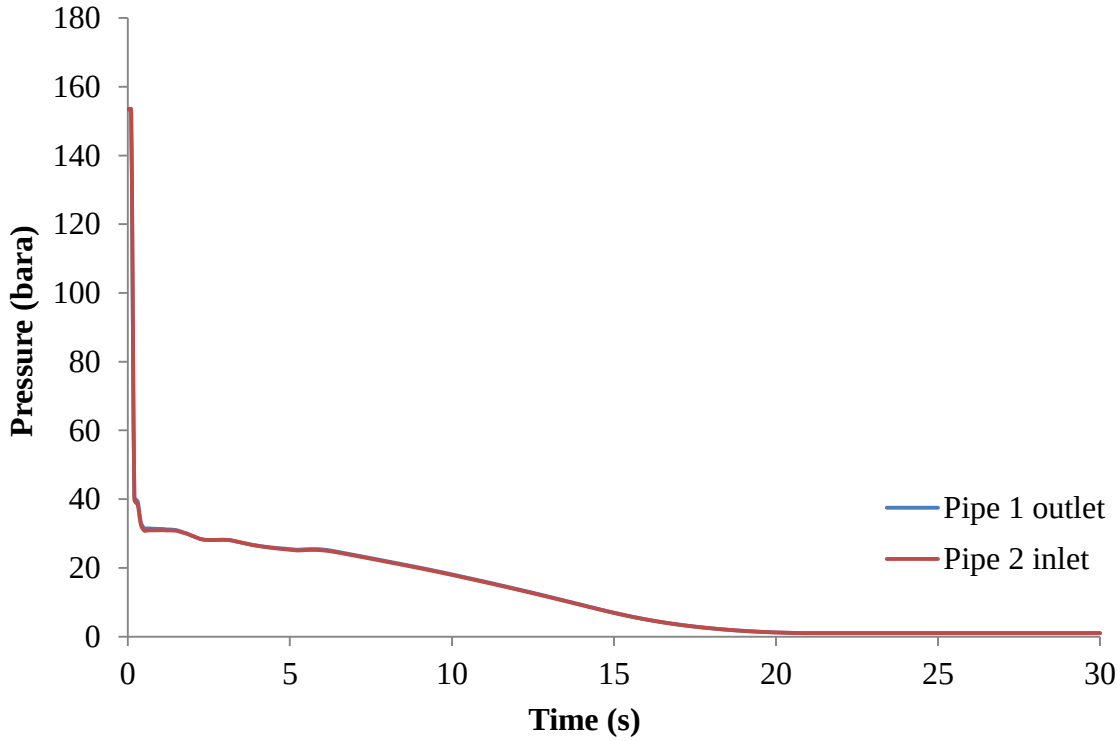

Figure 8.9: FEM-O predicted fluid pressure at the inlet and outlet of the pipeline junction for Test 15.

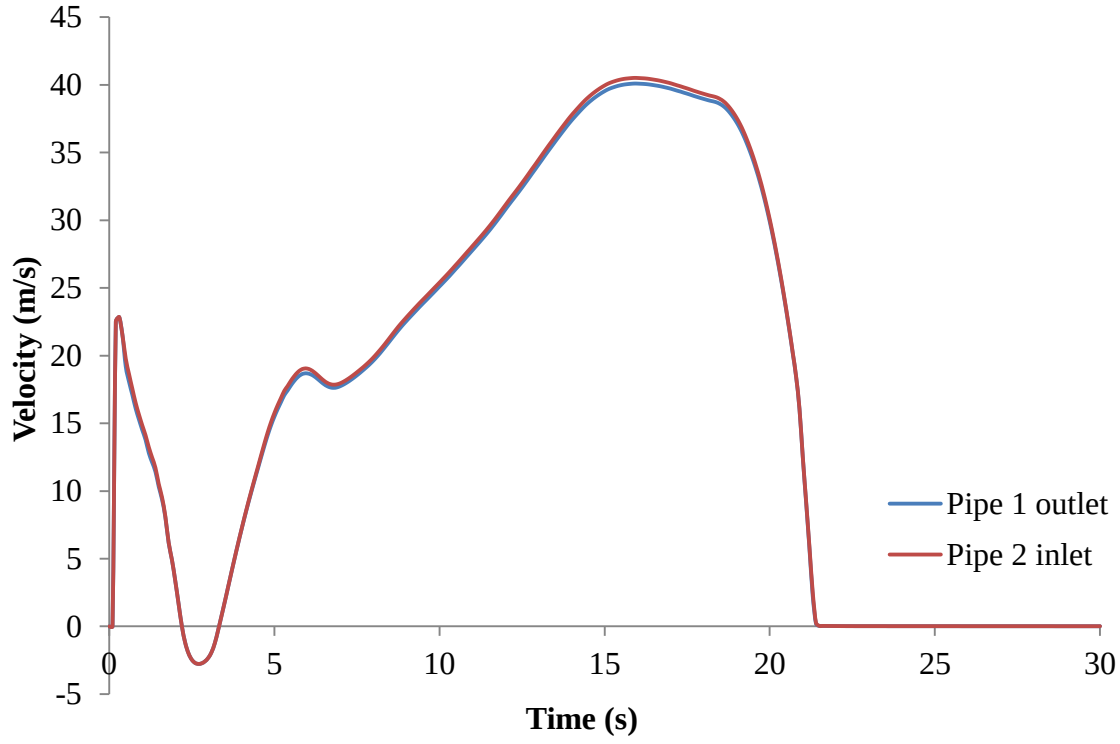

Figure 8.10: FEM-O predicted fluid velocity at the inlet and outlet of the pipeline junction for Test 15.

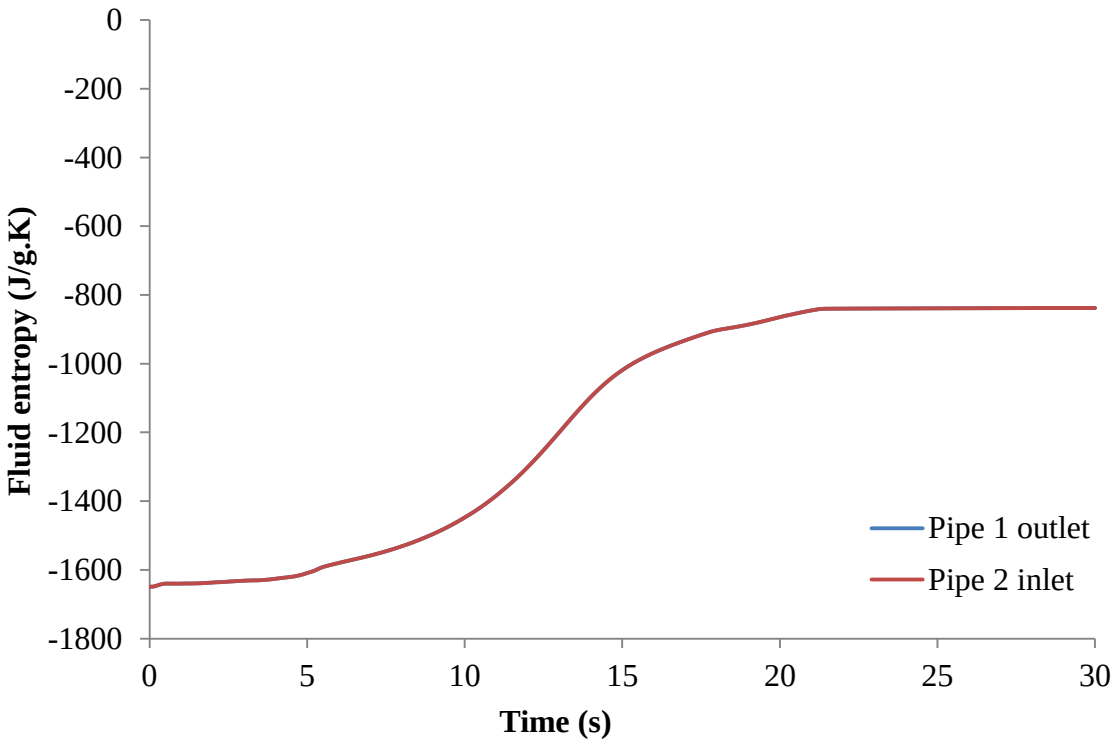

Figure 8.11: FEM-O predicted fluid entropy at the inlet and outlet of the pipeline junction for Test 15.

Referring to figure 8.11 it may be observed that there is no difference in predicted fluid entropy between the inlet and outlet of the junction over the duration of the simulation. Additionally, realistic fluid entropy profiles were calculated during blowdown. Thus the assumption of isentropic fluid flow through the junction is observed to be successfully implemented and appropriate when the pipes connected to the junction have the same ID. The application of the new two pipe junction model to simulating venting, and the impact of the isentropic flow assumption on fluid entropy predictions, is considered for Test 17 in section 8.8.

The two pipe junction model proposed in section 7.2 has therefore been shown to display the expected behaviour when simulating the blowdown of two pipes connected in series. The model has also been shown to remain stable and to produce realistic fluid property predictions when backflow occurs through the junction. This was unexpected given that the model was not designed to model backflow.

8.7 Three pipe junction model verification

In section 7.4 the three pipe junction model proposed in section 7.2 was used to simulate the venting of an isolated pipeline through a vertical vent pipe (Test 8). Simulation results from this experiment suggest the assumption of isentropic flow through the junction is inappropriate when modelling venting, leading to inaccurate predictions and a failure to conserve mass.

In this section FEM-O is applied to simulating the blowdown of a hypothetical pipeline system following accidental FBR of a main pipe. The pipe system consists of three pipes of varying length and internal diameter connected at a T-junction. The three pipe junction model proposed in section 7.2, with the refinements discussed in section 7.4.2, is used to model fluid flow in the junction. Complete details of the pipeline system and simulation parameters are given in table 8.5. The FBR is located at the end of pipe 3. The inventory was assumed to be at rest and homogeneously mixed prior to blowdown with no variation in fluid properties along the length of the shock tube.

Figures 8.12 to 8.15 respectively present the simulated fluid pressures, velocities, flow rates and entropies at the inlets and outlet of the junction for Test 16.

Referring to figure 8.12 the expected decrease in fluid pressure during decompression is observed, with pressure at the inlet of pipe 3 slightly lower than at the outlet of pipes 1 and 2. Some small fluctuations in the predicted pressures can be observed in the first ca. 10 s of blowdown, these are caused by rapid transients in the inventory. Additionally, as pipe 2 has a greater internal diameter than pipes 1 and 3, it was observed that when rapid transients inside pipe 2 arrived at the junction they both propagated through into the connecting pipes while also reflecting off the junction and back along pipe 2. This contributed significantly to the fluctuations in predicted fluid velocity and flow rate at the junction, as may be observed in figures 8.13 and 8.14 below.

Table 8.5: Simulation parameters for the three pipe junction verification test.

	Inputs	Test 16		
		Pipe 1	Pipe 2	Pipe 3
Pipeline characteristics	Upstream fitting	Closed end	3 pipe junction (120° bend)	3 pipe junction (120° bend)
	Downstream fitting	3 pipe junction (120° bend)	Closed end	FBR
	Pipe length (m)	300	100	100
	Pipe external diameter (mm)	170	220	150
	Pipe wall thickness (mm)	10	10	10
	Pipe roughness (mm)	0.05	0.05	0.05
	Pipe orientation to the horizontal plane (°)	0	0	0
	Heat transfer option	FEM – exposed to air		
Inventory and ambient parameters	Feed composition (mole %)	CO_2 – 100		
	Fluid temperature (°K)	298.15		
	Fluid pressure (bara)	101		
	Ambient temperature (°K)	293.15		
	Ambient pressure (bara)	1.01		
Failure parameters	Failure mode	FBR		
	Failure location relative to upstream end (m)	400		
	Discharge coefficient	1		
Other parameters	Number of pipe grid points	300	100	100
	Simulation model	HEM		
	Equation of State	PR (equation 3.6)		
	Friction factor correlation	Chen (Equation 3.33)		
	Total depressurisation time (s)	120		

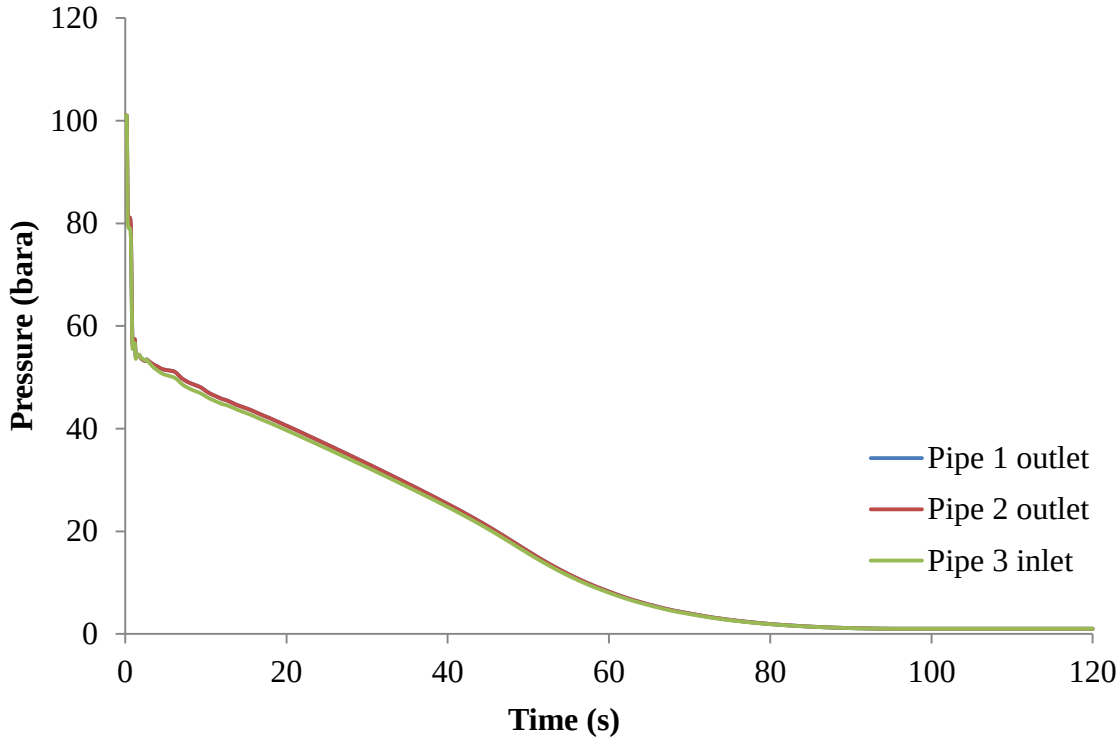

Figure 8.12: FEM-O predicted fluid pressures at the inlets and outlet of the pipeline junction for Test 16.

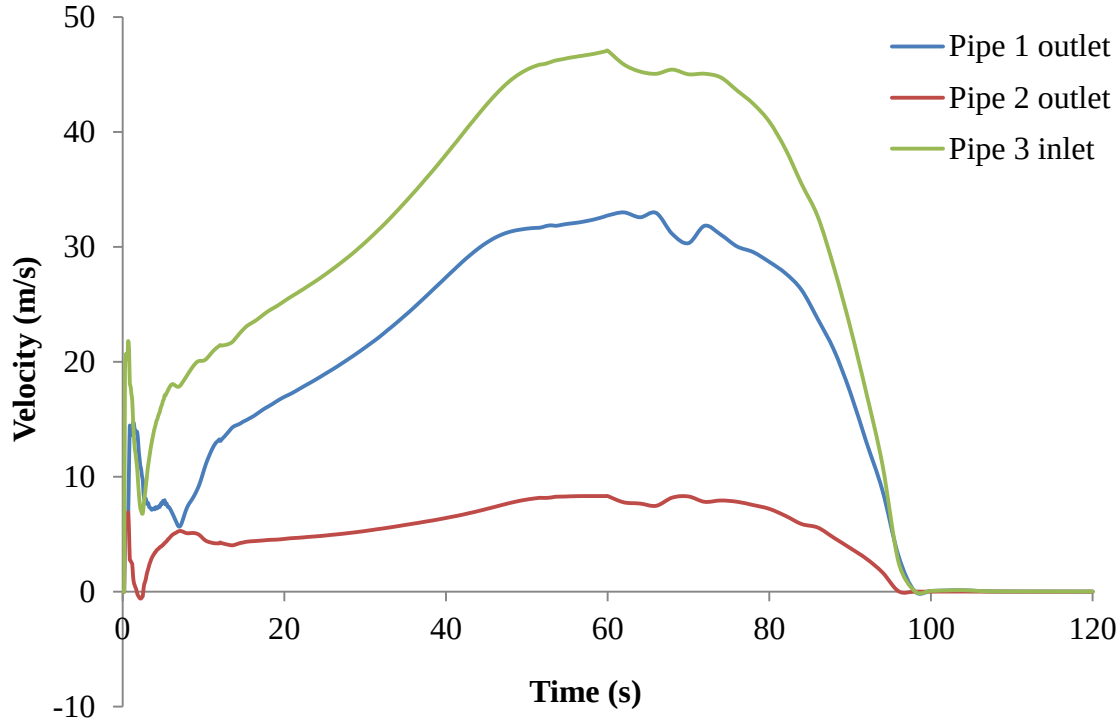

Figure 8.13: FEM-O predicted fluid velocity at the inlets and outlet of the pipeline junction for Test 16.

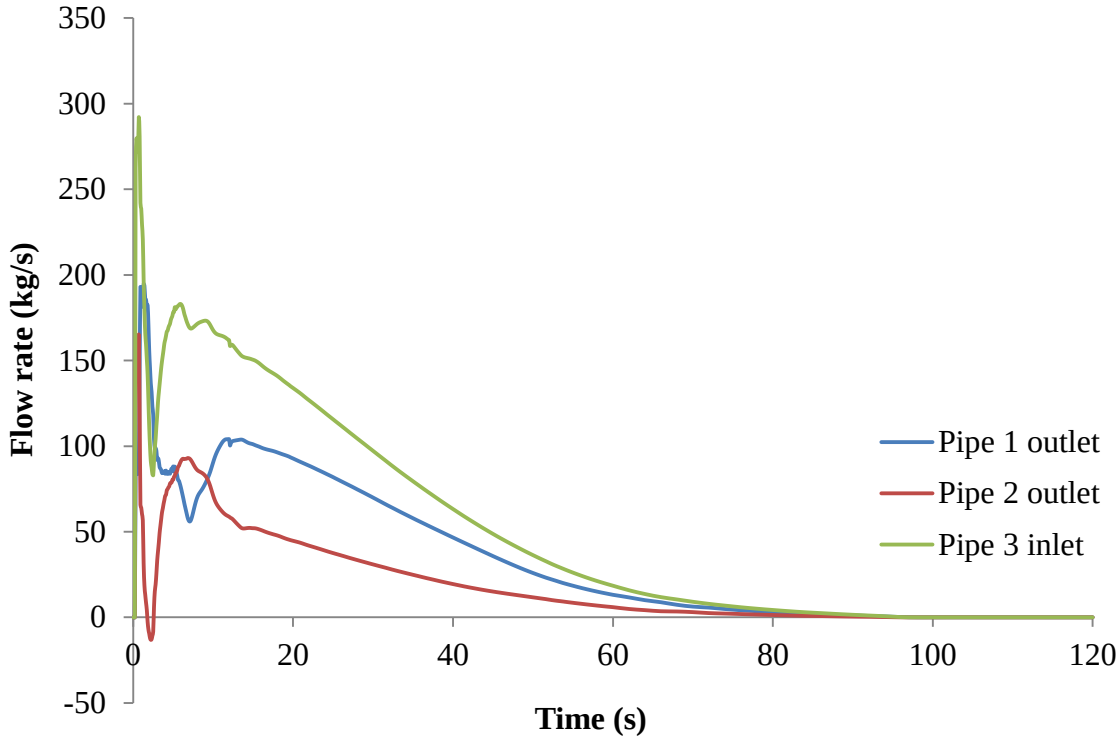

Figure 8.14: FEM-O predicted inventory mass flow rates at the inlets and outlet of the pipeline junction for Test 16.

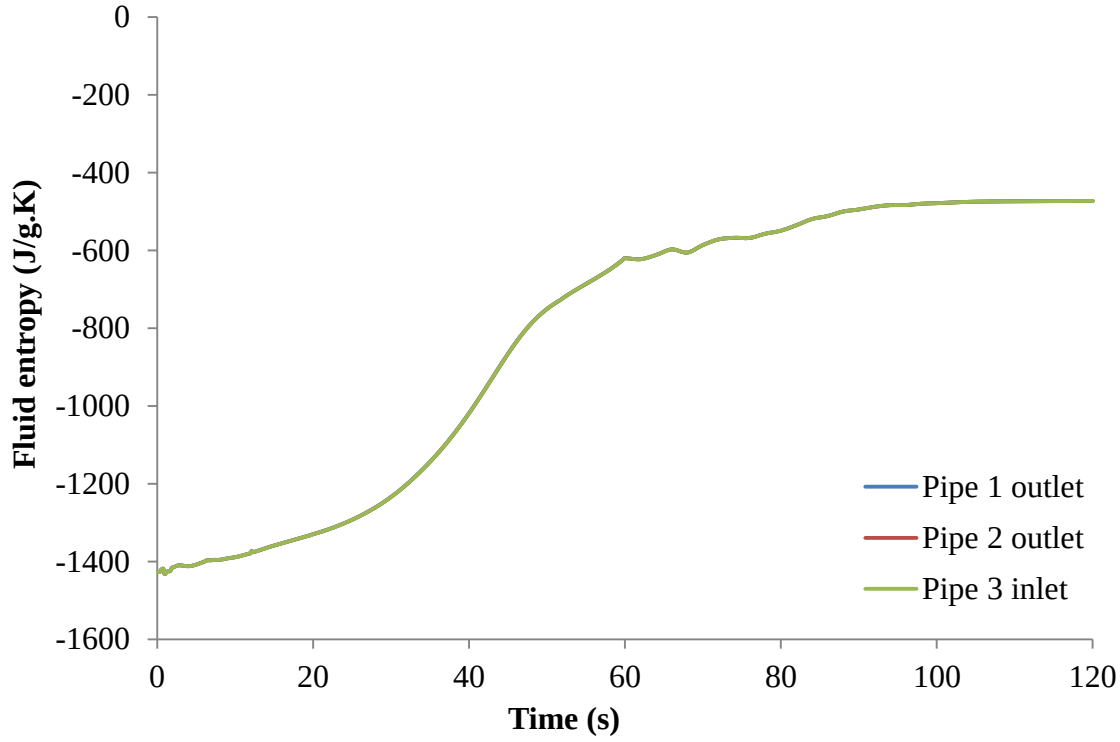

Figure 8.15: FEM-O predicted fluid entropies at the inlets and outlet of the pipeline junction for Test 16.

Referring to figure 8.13, fluctuations in the fluid velocity at the two inlets and outlet of the junction are clearly visible during the first ca. 10 s of blowdown. These result from the propagation of rapid transients in the inventory. Further, smaller fluctuations in fluid velocity are predicted at ca. 70 s, the cause of which is unknown. The latter are not considered significant as by this stage of blowdown the discharge rate has fallen below 10 kg/s. The general trends in the predicted fluid velocities are as expected for each pipe.

Figure 8.14 presents the mass flow rates at the inlets and outlet of the pipe junction for Test 16. The fluctuations in the predicted flow rate during the first ca. 10 s of blowdown are consistent with the variations in pressure and velocity discussed previously.

It may be observed that both the fluid velocity and mass flow rates out of pipes 1 and 2 (see figures 8.13 and 8.14) are significantly different. These differences arise from the different volumes of the two pipes (accounted for in the junction model by equation 7.3) and are of the expected magnitude. The mass conservation index for Test 16 was calculated as 1.067. Thus the use of only one Path line and the assumption of isentropic flow in the three pipe junction boundary condition does not appear to adversely affect the accuracy of the simulation when the pipes connected to the junction are of similar diameter.

Referring to figure 8.15, which presents the variation of predicted fluid entropy at the inlets and outlet of the junction, the expected trends are observed. Isentropic flow through the junction is achieved.

In summary, the new three pipe junction model (proposed and refined in sections 7.2 and 7.4.2 respectively) has been shown to be able to realistically model fluid flow through the junction of three pipes when the pipes have similar internal diameters. The expected trends in the data were observed during blowdown of the pipe system. Mass was conserved.

8.8 Predicted flow regimes and pipe wall temperatures during prolonged venting

Two phase flow is expected during blowdown of an initially dense phase CO_2 pipeline due to vaporisation of the inventory. As demonstrated during the CO2PipeHaz project ("CO2PipeHaz," 2012; see section 2.4.7), when outflow occurs through a sufficiently small orifice, such as a puncture, a CO_2 inventory will stratify as there is insufficient turbulence in the inventory to drive mixing of the phases. Conversely, significant turbulence is expected in longer pipelines (>100 m) subject to FBR, making approximations such as the Homogeneous Equilibrium assumption (see section 3.5) used in FEM-O acceptable when modelling such failure scenarios.

A degree of turbulence in the inventory is to be expected during venting as the rate of release will be significantly higher than that from a puncture. However, whether this is sufficient to drive mixing of the phases and render the HEM assumption acceptable when modelling venting is unconfirmed. Analysis of the Test 8 experimental and simulation data suggests that it is not. In the absence of experimental data the fluid flow regime may be calculated from simulation data using an appropriate model, such as that developed by Cheng et al. (2008) for CO_2. Other flow regime models available in the literature do not account for the significant effect that high reduced pressures and low surface tensions can have on the two phase fluid flow characteristics of CO_2. A review of the literature found no other flow pattern models developed specifically for CO_2.

In this section the venting of a long pipeline containing dense phase CO_2 is simulated using FEM-O. The flow regime in the inventory is calculated at various times during venting using the flow pattern model of Cheng et al. (2008). Additionally, the variation in pipe wall temperatures during the venting process and the applicability of the new two pipe junction model to simulating venting scenarios are investigated. The simulation parameters are presented in table 8.6.

Table 8.6: Simulation parameters for Test 17, investigating a prolonged venting operation.

	Inputs	Test 17	
		Pipe 1 (main)	**Pipe 2 (vent)**
Pipeline characteristics	Upstream fitting	Closed end	2 pipe junction
	Downstream fitting	2 pipe junction	Open end
	Pipe length (m)	250	10
	Pipe external diameter (mm)	610	120
	Pipe wall thickness (mm)	20	10
	Pipe roughness (mm)	0.005	0.005
	Pipe orientation to the horizontal plane (°)	0	90
	Heat transfer option	FEM – exposed air	
Inventory and ambient parameters	Feed composition (mole %)	CO_2 – 100 %	
	Fluid temperature (°K)	285.15	
	Fluid pressure (bara)	151	
	Ambient temperature (°K)	283.15	
	Ambient pressure (bara)	1.01	
Failure parameters	Failure mode	FBR	
	Failure location relative to upstream end (m)	260	
	Discharge coefficient	1	
Other parameters	Number of pipe grid points	250	10
	Simulation model	HEM	
	Equation of State	PR (equation 3.6)	
	Friction factor correlation	Chen (Equation 3.33)	
	Total depressurisation time (s)	1500	

Figure 8.16 presents the variation of predicted fluid pressure at the release plane for Test 17. As may be observed the pressure follows the expected trend during venting; saturation conditions are reached by ca. 10 s and the triple point pressure by ca. 660 s after venting begins. Two unexpected features in the pressure history are indicated on the figure, neither of which has a significant effect on the overall simulation results. The first, occurring from ca. 10 to 75 s, results from fluctuations in predicted fluid entropy near the release plane. The second, a small increase in fluid pressure occurring at ca. 850 s, is predicted throughout the inventory and is especially discernible at the junction. It is discussed in reference to figure 8.17, which presents the fluid properties at the inlet and outlet of the pipe junction plotted on the CO_2 phase diagram (calculated using the PR EoS).

Referring to figure 8.17, the predicted fluid properties display the expected behaviour between the beginning of venting and reaching the triple point. Below triple point conditions the fluid pressure and temperature decrease to a minimum before increasing again. The pressure then drops rapidly to ambient while the temperature falls to a minimum of ca. 185 K. The latter increase in pressure is reported at ca. 850 s in figure 8.16. Below the triple point predictions diverge from the sublimation line as the PR EoS (Peng and Robinson, 1976) is calibrated for vapour-liquid mixtures only.

The fluid flow regime in the inventory is calculated in the main pipe (pipe 1, see table 8.6) at a location 5 m from the junction of the main and vent pipes. Calculated following the method of Cheng et al. (2008), figure 8.18 presents the flow regime map 15 s after venting begins. At this time the inventory has a predicted vapour quality of 0.06 % and a mass velocity of 544 kg/m^2s (see figure 8.18). The flow regime is therefore a mixture of slug and stratified-wavy flow; there is insufficient vapour to create a single continuous vapour volume in the main pipe and the fluid is moving with sufficient velocity to create waves at the liquid/vapour interface. The flow regime was also calculated at 240 s, 480 s and 720 s (data not shown). The flow regimes at these times were stratified-wavy, stratified and stratified respectively.

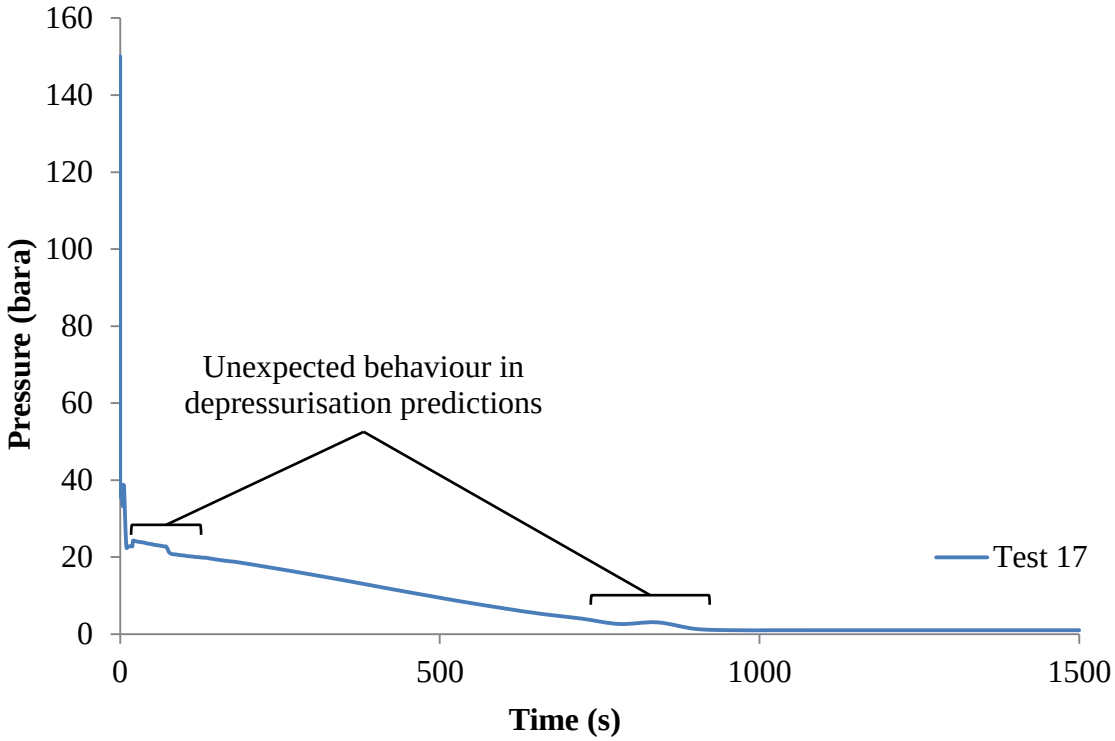

Figure 8.16: Variation of fluid pressure at the release plane for Test 17.

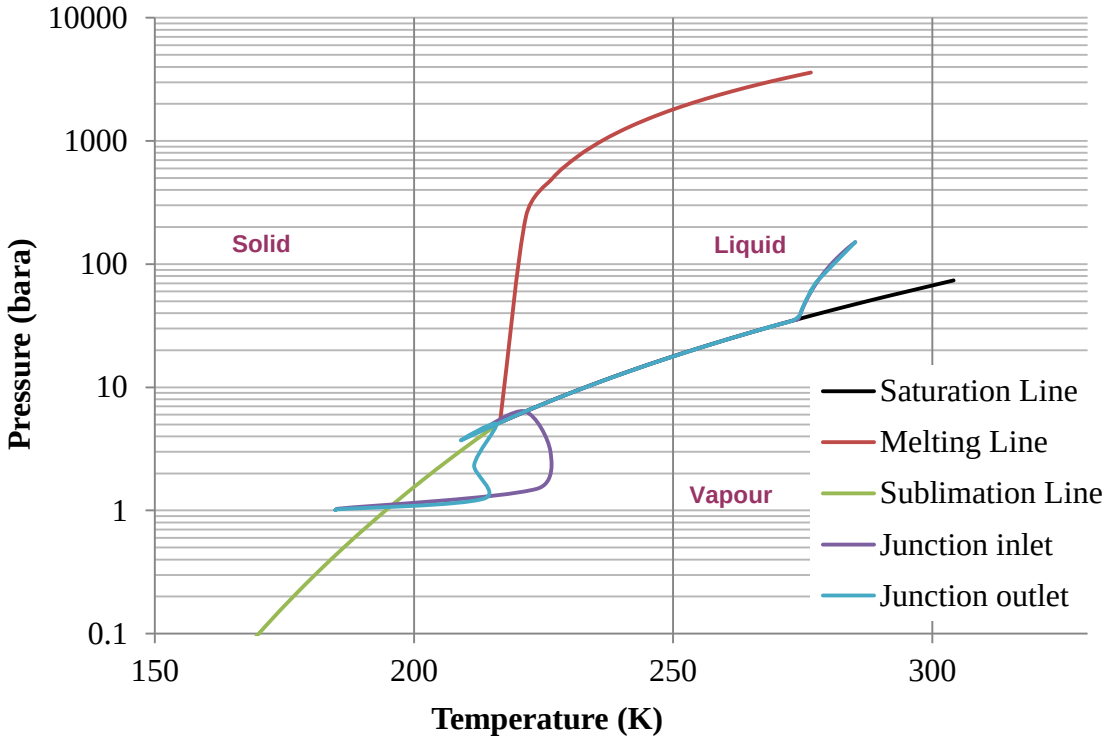

Figure 8.17: Variation of fluid properties at the inlet and outlet of the junction for Test 17, plotted on the CO_2 phase diagram (calculated using the PR EoS).

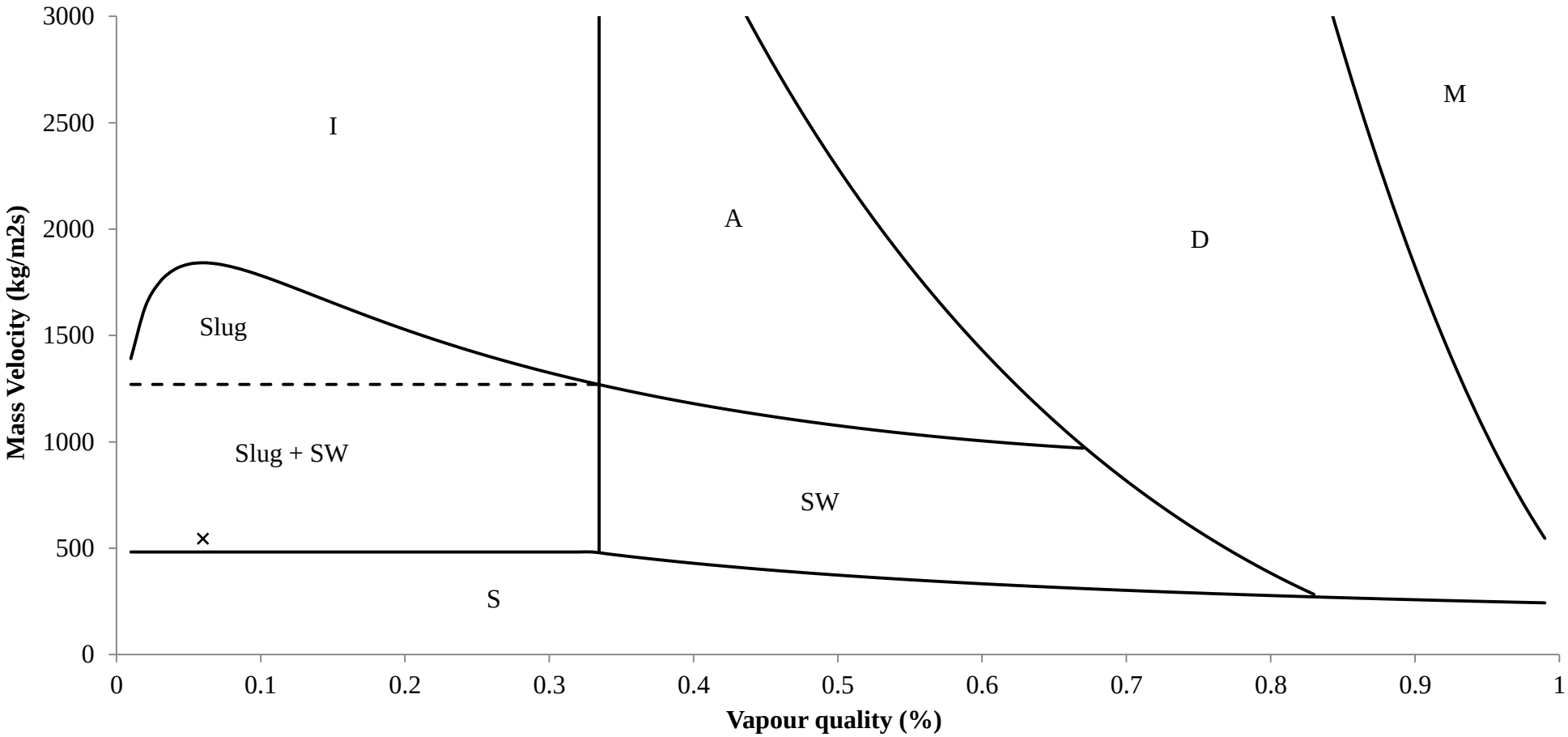

Figure 8.18: Flow regime map for Test 17 at 15 s after venting begins (S is stratified flow, SW is stratified-wavy flow, Slug is slug flow, I is intermittent or plug flow, A is annular flow, D is the dryout region and M is mist flow).

The modelling work presented suggests that the HEM assumption is inappropriate for modelling pipeline venting and thus that FEM-O should not be used in such scenarios. However this conclusion reasonably supposes that the vent pipe is connected to the top of the main pipe and therefore that the proportion of liquid entering it, and therefore the discharge rate, is over predicted by FEM-O. In practise, the venting of any pipeline will be conducted as quickly as is safely possible. For CO_2 pipelines the process might be accelerated by preferentially venting the liquid inventory. This may be achieved by connecting the vent to the bottom of the main pipe section. Assuming the pipeline has a constant horizontal inclination and that blowdown is overwhelmingly dependent on flow in the vent pipe; from the modelling perspective the problem would then become one of turbulent flashing liquid flowing in a pipe, a scenario for which FEM-O is of proven accuracy (see chapter 6). Fluid flow through venting infrastructure of the type outlined might then be modelled using an appropriately calibrated value of k (see equation 7.5). Therefore, while the work presented in this section does not support the use of FEM-O for modelling venting of CO_2 pipelines, further developments in the design of CO_2 pipelines may render the model more widely useful to modelling CO_2 pipeline blowdown.

Predicted pipe wall temperatures were also considered for Test 17. Figure 8.19 presents the variation of outer pipe wall temperature 245 m from the closed end of the main pipe (i.e. 5 m from the junction) and 5 m along the vent pipe (i.e. half way along). These locations are expected to experience the coldest temperatures without calculations being affected by the application of boundary conditions in the fluid model (discussed previously in section 7.3.2).

As may be observed, in the main pipe the wall experiences a continuous rate of cooling and reaches a minimum temperature of 245 K at ca. 720 s. In the vent pipe the wall cools to significantly lower temperatures (a minimum of 206 K at 840 s). The fluctuations in calculated fluid properties below the triple point, discussed in reference to figures 8.16 and 8.17 above, are also reflected in the main and vent pipe wall temperature predictions. Additionally, as discussed in section 8.3 above, wall

temperature predictions for uninsulated pipes may be under predicted by FEM-O. Thus the predicted pipe wall temperatures should be considered subject to a degree of error, especially after ca. 660 s. However it may be reasonably concluded that the vent pipe is at far greater risk of cooling below its DBTT and may be expected to do so significantly earlier than the adjoining main pipe section.

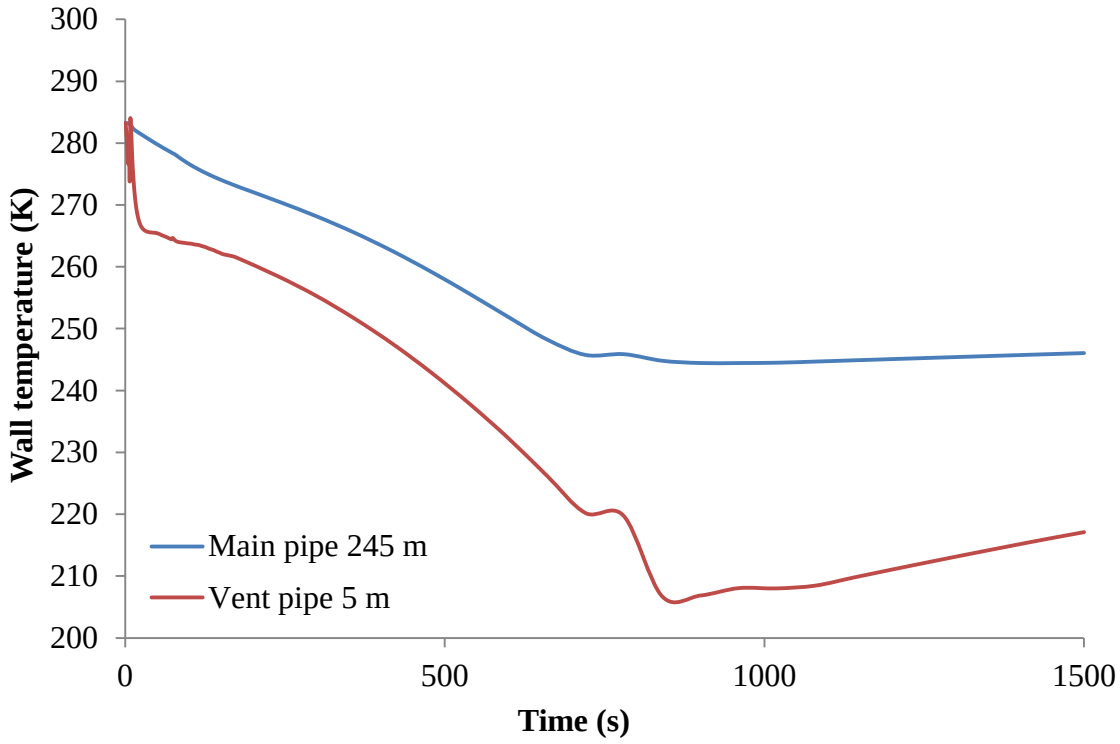

Figure 8.19: Outer pipe wall temperature histories in the main and vent pipes for Test 17. Data from locations 5 m either side of the pipeline junction.

Test 17 is the first application of the new two pipe junction model to a venting scenario. In this simulation the ZERO_N algorithm converged to a realistic solution for fluid entropy at the inlet of the junction, thus predicted fluid temperatures and densities in the main pipe were realistic and mass was conserved during venting (discussed below).

Significant acceleration of the fluid was predicted as it passed through the junction however. Due to the assumption of isentropic flow, an expected increase in fluid entropy at the junction outlet associated with such acceleration was not predicted. This has implications for the accurate prediction of fluid temperature, density and phase split

in the vent pipe. Therefore while the new two pipe junction model produces more realistic venting results compared with the three pipe junction model (see section 7.4.3), their accuracy remains uncertain due to the assumption of isentropic flow in the junction.

In summary, in this section it has been demonstrated that during the venting of a long pipeline containing initially dense phase CO_2 the inventory quickly stratifies. As a result FEM-O results for transient and cumulative discharge rate are over predicted as the model assumes homogeneous equilibrium in the inventory. FEM-O might still be useful in future for modelling venting of CO_2 pipelines; a plausible scenario was discussed to support this assertion. The application of the new two pipe junction model to the Test 17 venting scenario produced realistic results. However the assumption of isentropic flow in the junction is expected to lead to some inaccuracy in predicted fluid properties and pipe wall temperatures in the vent pipe. Fluid properties in the main and vent pipes were predicted to pass the triple point during outflow, at which point unrealistic behaviour was predicted. These unrealistic predictions did not significantly affect the simulation; a mass conservation index of 1.00 was calculated for Test 17 using the method discussed in Denton (2009). Minimum vent pipe wall temperatures were predicted to fall below 210 K.

8.9 Conclusion

This chapter builds on the validation work of the preceding chapters by carrying out verification studies of the FEM heat conduction model and the new two and three pipe junction models. Additionally the venting of a long pipeline was modelled and the applicability of FEM-O, based on the HEM, for modelling such scenarios was assessed.

To verify the performance of the Finite Element model key components were investigated individually. These included:

- the steady state wall temperature calculation algorithm;
- the discretisation of the FEM solution domain;

- the application of external boundary conditions to the FEM mesh;
- the sparse mesh approximation for long pipelines.

Of the model components listed, the steady state model performed as expected. FEM-O wall temperature predictions also displayed the expected trends when the different external boundary conditions were applied to the solution domain. However for uninsulated pipes the degree of cooling predicted was greater than expected.

The accuracy of the FEM calculations were shown to be dependent on the discretisation of the solution domain. Additionally, the external boundary condition applied also informed the nature of the discretisation applied to the solution domain. It was discovered that when the FEM mesh was modelled using uniform heat transfer properties a minimum of three rows of nodes was required for accurate calculations. When the solution domain contained non-uniform heat transfer properties, i.e. the pipe was buried or insulated, a minimum of five rows of nodes was required for accurate calculations. The sparse mesh approximation was shown to produce unacceptable inaccuracies in predicted wall temperature and pipeline discharge data.

The performance of the two and three pipe junction models (see sections 7.2 and 7.4.2) was also investigated by simulating outflow from hypothetical pipelines. Both junction models behaved as expected: trends in the variation of fluid pressure and velocity through the junctions were successfully modelled, isentropic flow was achieved without loss of stability, finally mass was conserved. Passage of rapid fluid transients through the junction was also successfully modelled. The available evidence from Tests 8, 15, 16 and 17 suggests the assumption of isentropic flow through a pipeline junction is acceptable when the variation in diameter between the pipes connected to the junction is not large.

Lastly the venting of a large, hypothetical CO_2 pipeline was modelled using FEM-O. The fluid flow regime was predicted to be a mixture of slug and stratified wavy flow from 15 s after venting begins before transitioning to stratified flow for the bulk of the decompression. The assumption of homogeneous equilibrium in the inventory is

therefore not appropriate when modelling CO_2 pipeline venting. However a plausible pipeline design scenario was discussed which might allow the future use of FEM-O for modelling venting. This study also indicates the vent pipe is at far greater risk of falling below its DBTT during venting compared with the main pipe. The vent pipe was predicted to experience a minimum temperature of 206 K although this prediction is subject to a degree of error as discussed in section 8.8. Lastly, analysis of predicted fluid properties at the junction of the main and vent pipes

Chapter 9: Conclusions and future work

9.1 Conclusions

Various hazards are associated with the release of CO_2 from a high pressure CCS pipeline including cooling in the pipe wall, solids formation and the atmospheric dispersion of the inventory (Bilio et al., 2009). An essential part of the hazard assessment for a CO_2 pipeline is the prediction of the transient discharge rate and pipe wall temperature during a release of inventory. Many mathematical models for predicting transient discharge rate have been reported. However, heat transfer between the pipeline and ambient is not always accounted for in these models. Where it is, any validation work on the heat conduction models has not been reported. Additionally, in many cases these models are applicable to single pipelines only.

This thesis addressed the modelling of transient pipe wall temperatures and of fluid flow in pipeline junctions during blowdown of CO_2 pipelines. The main contributions are:

- a review of the literature concerning pipeline outflow models and their methods of addressing heat transfer between the ambient and inventory;
- the development of a two dimensional Finite Element heat conduction model and its integration with a validated pipeline outflow model;
- validation of this conjugate model (FEM-O) against experimental pipe wall and fluid data during pipeline blowdown;
- the formulation and validation against experimental data of pipeline junction boundary conditions for modelling fluid flow between pipes.

A summary of the main findings of this work is described below.

The review of the literature presented in chapter 2 identified the discharge and depressurisation rates, propagation of rapid transients and pipe wall temperature

variation as key parameters in the process of CO_2 pipeline blowdown. This informed the subsequent review of the reported pipeline outflow models, resulting in the selection of the model OUTFLOW (see section 2.4.4) for use in this thesis based on its demonstrated ability to accurately model the above phenomena, except for transient pipe wall temperatures. Indeed none of the outflow models reviewed described pipe wall heat conduction or fluid/wall heat transfer in detail, nor were the results of these calculations validated against appropriate experimental data.

The popularity of FDM and FVM methods for modelling heat conduction in the pipe wall was discussed. The requirement of regular solution domain discretisation with these numerical methods limits their use to simple pipeline geometries. The Finite Element method, which has no requirement for regular solution domain discretisation and so can be used to model structures with complex geometry, was selected for modelling pipe wall temperatures in this work. While the flexibility of the method was not exploited in this work, it allows for extensive future development.

OUTFLOW is dependent on an EoS for calculating the thermodynamic properties of the inventory. Thus a review of work investigating the accuracy of various cubic EoS for calculating the properties of CO_2 and its mixtures was conducted. This indicated no cubic EoS was consistently more accurate than the others tested when calculating a range of pure fluid and mixture properties. The importance of using a calibrated binary interaction parameter for the accuracy of the EoS was also highlighted. In the absence of a calibrated binary interaction parameter the PR or PT EoS were identified as more likely to produce accurate calculation results. It was also observed that no study had investigated the accuracy of any EoS under pipeline blowdown scenarios.

A detailed summary of the formulation of the model OUTFLOW, based on the mass, momentum and energy conservation equations for transient fluid flow in a pipeline, was presented in chapter 3. These equations were expressed in terms of pressure, entropy and velocity and were shown to be quasilinear and hyperbolic.

In the same chapter the main features of the lumped body approach for modelling heat transfer effects between the fluid/pipe wall and pipe wall/ambient were also presented together with the relevant heat transfer correlations.

The formulation of the Method of Characteristics based on the Method of Specified Time intervals was subsequently presented in chapter 4. The governing conservation equations were converted into compatibility and characteristic equations. These were then discretised using the Euler predictor-corrector technique. Boundary conditions to describe various pipeline features such as closed and open ends, junctions and reservoirs were also presented.

With its formulation described and the accuracy of the fluid model discussed in chapter 2, OUTFLOW was applied to the modelling of CO_2 pipeline blowdown and the results were presented in chapter 5. First the accuracy of various EoS for calculating CO_2 inventory properties during blowdown of a large scale shock tube was assessed. OUTFLOW pipe wall temperature predictions were then validated against appropriate experimental data.

Based on comparisons with the available experimental data the PR EoS (Peng and Robinson, 1976) was selected for modelling work in this thesis. The limited availability of experimental data was noted. Validation of the OUTFLOW wall temperature model revealed its accuracy to be poor when compared against experimental shock tube wall temperature data for pure and impure CO_2 inventories.

To address the weakness of the OUTFLOW wall temperature calculations a two dimensional Finite Element heat conduction model was developed to calculate pipe wall temperatures and heat transfer between the fluid and ambient. Details of its formulation, together with the appropriate boundary conditions, were presented in chapter 6. The conjugation of the fluid and FEM models to create the new model FEM-O was discussed. The fluid/pipe wall heat transfer correlation used in OUTFLOW was identified as inappropriate for CO_2 inventories as its accuracy decreases when the proportion of vapour in a fluid increases above 60 %. Thus a refinement to the

correlation (Steiner and Taborek, 1992) was implemented in FEM-O to account for inventories with a high (> 60 %) proportion of vapour.

The validation of FEM-O was then addressed. Both the FEM wall temperature model and fluid model predictions were compared against experimental shock tube decompression data. Pure and impure dense phase CO_2 inventories were investigated. FEM-O pipe wall temperature predictions were shown to be accurate representations of the experimental data, both in terms of range of temperatures predicted and rate of cooling. The significantly increased simulation run time of FEM-O compared with OUTFLOW was noted.

When modelling CO_2 pipeline networks using FEM-O, the formulation of the junction boundary conditions was identified as increasing the simulation run time and potentially reducing calculation accuracy. Given the significantly greater run time of FEM-O compared with OUTFLOW, the development of more computationally efficient junction boundary conditions was undertaken.

In chapter 7 new formulations for two and three pipe junction boundary conditions for FEM-O were presented and validated against experimental data. For the two pipe junction model fluid flow data between two pipes of equal internal diameter was used. For the three pipe junction model experimental data for venting through a T-junction was available.

With the new two-pipe junction boundary condition significant reductions in runtime (ca. 45 %) were achieved. Given the nature of the experiment against which simulation results were validated, the results from both the old and new two pipe junction boundary conditions showed acceptable agreement with the experimental data. Differences between the predictions from each boundary condition were small.

For the three pipe junction boundary condition, agreement between the predicted and experimental data was shown to be poor. Given the large acceleration of the inventory through the junction, which was not seen in the two pipe junction experiment, the

assumption of isentropic flow was not appropriate and lead to the calculation of unrealistic flow behaviour. Additionally, although unproven it is believed the inventory stratified during the venting experiment. In such a scenario the HEM assumption used in FEM-O would also contribute to the divergence between experimental and simulated data.

With the FEM-O fluid and wall temperature predictions validated against a range of experimental data a verification study of the model was performed, the results of which were presented in chapter 8. Predictions from the steady state wall temperature calculation algorithm displayed the expected trends. The number of rows of nodes in the FEM mesh needed for accurate calculations was shown to be dependent on the external environment of the pipe; for buried or insulated pipelines five rows of nodes are required, for an uninsulated pipe three rows is sufficient. The sparse mesh approximation was developed to reduce the computational load associated with modelling of very long pipelines. It was shown to introduce significant inaccuracies into FEM-O simulation results.

The performance of the two and three pipe junctions proposed in chapter 7 was also investigated. Outflow from pipeline systems composed of pipes of similar diameters and subject to FBR was modelled. Both junction models produced the expected trends in the variation of fluid pressure and velocity during outflow, isentropic flow was achieved without loss of stability, lastly mass was conserved. The available evidence from simulations suggests isentropic flow through a junction may be assumed when the pipes connected to the junction have similar diameters.

The final study presented in chapter 8 addressed the evidence for possible stratification of a CO_2 inventory during venting. Blowdown of a hypothetical pipeline through a vertical vent was modelled and the inventory flow regime calculated at various times. The flow regime was predicted to be stratified flow for the bulk of the decompression. The assumption of homogeneous equilibrium in the inventory therefore renders FEM-O inappropriate for modelling CO_2 pipeline venting.

In summary, the outflow model FEM-O has been developed to simulate the variation in transient pipe wall temperatures during blowdown of CO_2 pipelines. FEM-O was created by integrating the previously reported model OUTFLOW with a Finite Element model of heat conduction for calculating pipe wall temperatures. New boundary conditions for modelling fluid flow in pipeline junctions were developed for FEM-O. FEM-O pipe wall temperature and fluid property predictions have been successfully validated against a range of experimental data. Based on the literature review presented in chapter 2, this is the first time a pipe wall temperature model has been validated against large scale experimental data. Testing of the new junction boundary conditions, including by comparison with experimental data, demonstrated they were limited in their application to scenarios where isentropic flow in the junction may be assumed. The scenario simulated in Test 7 was one such, here simulation results showed reasonable agreement with the experimental data. The accumulated evidence presented in this thesis indicates FEM-O is inappropriate for modelling CO_2 pipeline venting or punctures due to the HEM assumption.

FEM-O has the potential to make significant contributions to the safe design and operation of CO_2 pipelines for CCS by helping illustrate the consequences and hazards associated with releases from such pipelines. However the use of the HEM assumption renders FEM-O unsuitable for modelling venting and punctures, the two most common types of release event. Thus there exists significant scope for further work; suggestions are presented in the next section.

9.2 Suggestions for future work

9.2.1 Extend FEM-O to model two phase flow

The experimental and simulation data presented in this thesis indicates a CO_2 pipeline inventory will stratify during venting or outflow from a puncture. In this situation the HEM has been shown to be inappropriate. FEM-O may be extended to modelling two phase flow including thermal and mechanical non-equilibrium effects. Such work would significantly extend the range of applicability of FEM-O, including to venting or outflow from punctures (the most common types of release).

9.2.2 Extend the Finite Element heat conduction model to three dimensions (axial, radial and circumferential)

Should a CO_2 pipeline inventory stratify during outflow sections of the pipe wall will be in contact with either vapour or liquid phases for prolonged periods of time. Given the significant differences expected between wall-vapour and wall-liquid heat transfer coefficients, as well as different liquid and vapour phase temperatures, different rates of circumferential cooling in the pipe wall may result. Thus different sides of the pipe wall may be at greater risk of falling below their DBTT as outflow progresses.

To assess the hazards associated with such behaviour the Finite Element heat conduction model presented in this thesis may be extended to calculating heat conduction in three dimensions (axial, radial and circumferential). It should be integrated with a two phase flow model, such as that described in section 9.2.1, to properly exploit its capability.

9.2.3 Modelling of heat conduction in valves

Numerous pipeline scenarios exist in which fluid flows through an inline valve, including venting. However, the extreme inventory cooling associated with CO_2 venting may be detrimental to a valve and should be avoided if possible (ElementEnergy, 2010). The flexible grid discretisation method used in the Finite Element method may be exploited to model transient temperature changes in the materials making up a valve. Such information will contribute to the development of protocols to minimise the exposure of the valve to extreme temperatures.

9.2.4 Modelling of solids deposition on internal pipeline surfaces

During blowdown of a CO_2 pipeline it has been shown that the inventory properties may pass the CO_2 triple point (see section 6.3), thus leading to the formation of solid CO_2. Deposition of solid CO_2 on the internal surface of a straight pipe does not necessarily increase the risks associated with blowdown, although it may be expected to alter the rate of heat transfer between the inventory and pipe wall. However, deposition on pipeline infrastructure such as valve surfaces may impair function and so increase the risks associated with blowdown. Modelling of such phenomena during blowdown should therefore be considered.

9.2.5 Improving the numerical efficiency of the FEM computer code

The current two dimensional implementation of the FEM in computer code utilises square matrices extensively. Useful data is concentrated in a single diagonal band within each matrix. The remaining space is populated by irrelevant data.

It was observed during the development of FEM-O that for longer pipelines the size of the FEM matrices became extremely large, resulting in the use of large volumes of

computer memory and prohibitively increasing runtime. Extension of the FEM conduction model to three dimensions will exacerbate such problems.

The development of the sparse FEM mesh approximation was one attempt to address this issue. As discussed previously, the attempt failed. Further efforts to improve the computational efficiency of the FEM computer code may nonetheless be expected to yield considerable practical benefits to FEM-O.

9.2.6 Refinement of the three pipe junction boundary condition for modelling venting

As demonstrated in sections 7.4 and 8.7, the proposed three pipe junction boundary condition may be used to model fluid flow in pipelines but is currently inappropriate for modelling venting due to the large acceleration of the inventory through the junction in such scenarios. The assumption of isentropic flow during venting was identified as one cause of the observed poor simulation accuracy. Scope therefore exists for further development of this boundary condition, possibly with a more fundamental investigation of fluid flow into a vent pipe located at a T-junction.

References

Almanza, O., Rodriguez-Perez, M. A., & de Saja, J. A. (2004). Measurement of the thermal diffusivity and specific heat capacity of polyethylene foams using the transient plane source technique. *Polymer International*, *53*, 2038–2044. doi:10.1002/pi.1624

Al-Zaharnah, I. T., Yilbas, B. S., & Hashmi, M. S. J. (2000). Conjugate heat transfer in fully developed laminar pipe flow and thermally induced stresses. *Computer Methods in Applied Mechanics and Engineering*, *190*, 1091–1104.

Ansys. (n.d.). FLUENT CFD Software. Retrieved January 26, 2015, from http://www.ansys.com/Products/Simulation+Technology/Fluid+Dynamics/Fluid+Dynamics+Products/ANSYS+Fluent

Assael, M. J., Trusler, J. P. M., & Tsolakis, T. F. (1996). *Thermophysical Properties of Fluids: An Introduction to Their Prediction*. London: Imperial College Press.

Atti, O. (2006). *Modelling outflow and low temperature induced crack propagation in pressurised pipelines.* University College London.

Bachu, S., Bonijoly, D., Bradshaw, J., Burruss, R., Holloway, S., Christensen, N., & Mathiassen, O. (2007). CO2 storage capacity estimation: Methodology and gaps. *International Journal of Greenhouse Gas Control*, *1*(4), 430–443. doi:10.1016/S1750-5836(07)00086-2

Bendiksen, K., Maines, D., Moe, R., & Nuland, S. (1991). The Dynamic Two-Fluid Model OLGA: Theory and Application. *SPE Production Engineering*, *6*(2). Retrieved from http://www.onepetro.org/mslib/servlet/onepetropreview?id=00019451&soc=SPE

Bhatti, M. S., & Shah, R. K. (1987). Turbulent and transition flow convective heat transfer in ducts. In S. Kakac, R. K. Shah, & W. Aung (Eds.), *Handbook of Single-Phase Convective Heat Transfer*. New York: Wiley Interscience.

Bilio, M., Brown, S., Fairweather, M., & Mahgerefteh, H. (2009). CO2 pipelines material and safety considerations. In *IChemE Symposium Series: HAZARDS XXI Process Safety and Environmental Protection* (Vol. 155, pp. 423–429). Manchester: IChemE. Retrieved from http://eprints.ucl.ac.uk/80288/

Botros, K., Geerligs, J., Zhou, J., & Glover, a. (2007). Measurements of flow parameters and decompression wave speed following rupture of rich gas pipelines, and comparison with GASDECOM. *International Journal of Pressure Vessels and Piping*, *84*(6), 358–367. doi:10.1016/j.ijpvp.2007.01.005

Botros, K. K., Carlson, L., & Reed, M. (2013). Extension of the semi-empirical correlation for the effects of pipe diameter and internal surface roughness on the decompression wave speed to include High Heating Value Processed Gas mixtures. *International Journal of Pressure Vessels and Piping*, *107*, 12–19. doi:10.1016/j.ijpvp.2013.03.004

Botros, K. K., Geerligs, J., & Eiber, R. J. (2010). Measurement of Decompression Wave Speed in Rich Gas Mixtures at High Pressures (370 bars) Using a Specialized Rupture Tube. *Journal of Pressure Vessel Technology*, *132*(5), 051303. doi:10.1115/1.4001438

Botros, K. K., Geerligs, J., Rothwell, B., Carlson, L., Fletcher, L., & Venton, P. (2010). Transferability of decompression wave speed measured by a small-diameter shock tube to full size pipelines and implications for determining required fracture propagation resistance. *International Journal of Pressure Vessels and Piping*, *87*(12), 681–695. doi:10.1016/j.ijpvp.2010.10.006

Botros, K. K., Studzinski, W., Geerligs, J., & Glover, A. (2004). Determination of Decompression Wave Speed in Rich Gas Mixtures. *The Canadian Journal of Chemical Engineering*, *82*, 880–891.

Brent, R. P. (2002). *Algorithms for minimization without derivatives*.

Brown, S. F. (2011). *CFD Modelling of Outflow and Ductile Fracture Propagation in Pressurised Pipelines*. *University College London*. University College London.

Brown, S., Martynov, S., Mahgerefteh, H., Chen, S., & Zhang, Y. (2014). Modelling the non-equilibrium two-phase flow during depressurisation of CO2 pipelines. *International Journal of Greenhouse Gas Control*, *30*, 9–18. doi:10.1016/j.ijggc.2014.08.013

Brown, S., Martynov, S., Mahgerefteh, H., & Proust, C. (2013). A homogeneous relaxation flow model for the full bore rupture of dense phase CO2 pipelines. *International Journal of Greenhouse Gas Control*, *17*, 349–356. doi:10.1016/j.ijggc.2013.05.020

Burlutskiy, E. (2013). Mathematical modelling on rapid decompression in base natural gas mixtures under rupturing. *Chemical Engineering Research and Design*, *91*(1), 63–69. doi:10.1016/j.cherd.2012.06.017

Burlutskiy, E. (2014). Numerical analysis of phase behavior during rapid decompression of rich natural gases. *Process Safety and Environmental Protection*, *92*(6), 555–564. doi:10.1016/j.psep.2013.03.001

Chandel, M. K., Pratson, L. F., & Williams, E. (2010). Potential economies of scale in CO2 transport through use of a trunk pipeline. *Energy Conversion and Management*, *51*(12), 2825–2834. doi:10.1016/j.enconman.2010.06.020

Chen, J. R., Richardson, S. M., & Saville, G. (1995). Modelling of two-phase blowdown from pipelines - I. A hyperbolic model based on variational principles. *Chemical Engineering Science*, *50*(4), 695–713. doi:10.1016/0009-2509(94)00246-N

Chen, N. H. (1979). An explicit equation for friction factor in pipe. *Industrial and Engineering Chemistry Fundamentals*, *18*(3), 296–297.

Cheng, L., Ribatski, G., Moreno Quibén, J., & Thome, J. R. (2008). New prediction methods for CO2 evaporation inside tubes: Part I - A two-phase flow pattern map and a flow pattern based phenomenological model for two-phase flow frictional pressure drops. *International Journal of Heat and Mass Transfer*, *51*(1-2), 111–124. doi:10.1016/j.ijheatmasstransfer.2007.04.002

Churchill, S. W., & Bernstein, M. (1977). A correlating equation for forced convection from gases and liquids to a circular cylinder in cross-flow. *Journal of Heat Transfer*, *99*, 300.

Churchill, S. W., & Chu, H. H. S. (1975). Correlating equations for laminar and turbulent free convection from a horizontal cylinder. *International Journal of Heat and Mass Transfer*, *18*(9), 1049–1053.

Cleaver, R., Cumber, P. S., & Halford, A. (2003). Modelling outflow from a ruptured pipeline transporting compressed volatile liquids. *Journal of Loss Prevention in the Process Industries*, *16*(6), 533–543. doi:10.1016/j.jlp.2003.08.004

CO2PipeHaz. (2012). Retrieved from http://www.co2pipehaz.eu/index.php

Cosham, A., Jones, D., Armstrong, K., Allason, D., & Barnett, J. (2011). The decompression behaviour of CO2 in the gas phase. In *International Forum on the Transportation of CO2 by Pipeline*. Newcastle.

Cosham, A., Jones, D. G., Armstrong, K., Allason, D., & Barnett, J. (2012). The Decompression Behaviour of Carbon Dioxide in the Dense Phase. In *Proceedings of the 2012 9th International Pipeline Conference*. Calgary.

Courant, R., Friedrichs, K., & Lewy, H. (1967). On the partial difference equations of mathematical physics. *IBM Journal of Research and Development*, *11*(2), 215–234.

Cumber, P. (2007). Outflow from fractured pipelines transporting supercritical ethylene. *Journal of Loss Prevention in the Process Industries*, *20*(1), 26–37. doi:10.1016/j.jlp.2006.08.007

Daubert, T. E., & Danner, R. P. (1990). Data Compilation - Physical and Thermodynamic Properties of Pure Compounds. *Taylor and Francis (Extant)*.

De Visser, E., Hendriks, C., Barrio, M., Molnvik, M., Dekoeijer, G., Liljemark, S., & Legallo, Y. (2008). Dynamis CO2 quality recommendations. *International Journal of Greenhouse Gas Control*, *2*(4), 478–484. doi:10.1016/j.ijggc.2008.04.006

Demetriades, T. A., Drage, T. C., & Graham, R. S. (2013). Developing a new equation of state for carbon capture and storage pipeline transport. *Proceedings of the Institution of Mechanical Engineers, Part E: Journal of Process Mechanical Engineering*, *227*(2), 117–124. doi:10.1177/0954408913481552

Denton, G. S. (2009). *CFD Simulation of Highly Transient Flows*. University College London.

Dittus, F. W., & Boelter, L. M. K. (1985). Heat transfer in automobile radiators of the tubular type. *Int. Comm. Heat Mass Transfer*, *12*, 3–22.

ElementEnergy. (2010). *CO2 Pipeline Infrastructure : An analysis of global challenges and opportunities*. Cambridge.

Ely, J. F., & Hanley, H. J. M. (1981). Prediction of transport properties. 1. Viscosity of fluids and mixtures. *Industrial & Engineering Chemistry Fundamentals*, *20*(4), 323–332.

Ely, J. F., & Hanley, H. J. M. (1983). Prediction of transport properties. 2. Thermal conductivity of pure fluids and mixtures. *Industrial & Engineering Chemistry Fundamentals*, *22*(1), 90–97.

Fairuzov, Y. V. (1998a). Blowdown of pipelines carrying flashing liquids. *AIChE Journal*, *44*(2), 245–254. doi:10.1002/aic.690440203

Fairuzov, Y. V. (1998b). Numerical Solution for Blowdown of Pipeline Containing Flashing Liquid. *AIChE Journal*, *44*(9), 2124–2128.

Fairuzov, Y. V. (1999). Transient Conjugate Heat Transfer During Flashing of Liquids in Pipes. *Chemical Engineering & Technology*, *22*(8), 713–717. doi:10.1002/(SICI)1521-4125(199908)22:8<713::AID-CEAT713>3.3.CO;2-0

Fairuzov, Y. V. (2000). Modeling of Conjugate Two- Phase Heat Transfer During Depressurization of Pipelines, *122*(February).

Flatt, R. (1986). Unsteady compressible flow in long pipelines following a rupture. *International Journal for Numerical Methods in Fluids*, *6*(2), 83–100. doi:10.1002/fld.1650060204

Gale, J. (2004). Transmission of CO2 - safety and economic considerations. *Energy*, *29*(9-10), 1319–1328. doi:10.1016/j.energy.2004.03.090

Gear, C. W. (1971). *Numerical initial value problems in ordinary differential equations*. Englewood Cliffs, NJ: Prentice-Hall.

Godunov, S., Zabrodine, A., Ivanov, M., Kraiko, A., & Prokopov, G. (1979). *Resolution numerique des problemes multidimensionnels de la dynamique des gaz* (editions M.). Moscow, Russia.

Golomb, D. (1993). Ocean Disposal of CO2; Feasibility, Economics and Effects. *Energy Conversion and Management*, *34*(9), 967–976.

Golomb, D. (1997). Transport systems for ocean disposal of CO2 and their environmental effects. *Energy Conversion and Management*, *38*, 279–286.

HSE. (1996). A guide to the Pipelines Safety and Regulations 1996. *Interpretation A, Journal of Bible and Theology*.

Ikeda, M. K., & Schaefer, L. a. (2011). Examining the effect of binary interaction parameters on VLE modelling using cubic equations of state. *Fluid Phase Equilibria*, *305*(2), 233–237. doi:10.1016/j.fluid.2011.03.029

Incropera, F. P., & DeWitt, D. P. (1996). *Fundamentals of heat and mass transfer* (4th Ed.). New York: John Wiley & Sons.

International Energy Agency (IEA). (2013). *World Energy Outlook 2013 Factsheet*.

International Energy Agency (IEA). (2014). *World Energy Outlook 2014 Factsheet*.

IPCC. (2005). *Carbon Dioxide Capture and Storage*. (B. Metz, O. Davidson, H. de Coninck, M. Loos, & L. Meyer, Eds.). New York: Cambridge University Press.

IPCC. (2014). *Climate Change 2014: Synthesis Report*.

Ji, W., & Lempe, D. A. (1997). Density improvement of the SRK equation of state. *Fluid Phase Equilibria*, *130*(12), 49–63.

Ji, X., Tan, S. P., Adidharma, H., & Radosz, M. (2005). SAFT1-RPM Approximation Extended to Phase Equilibria and Densities of CO2 -H2O and CO2 -H2O-NaCl Systems. *Industrial & Engineering Chemistry Research*, *44*, 8419–8427.

Keenan, J. H., & Neumann, E. P. (1946). Measurements of friction in a pipe for subsonic and supersonic flow of air. *Journal of Applied Mechanics*, *13*(2). Retrieved from http://hdl.handle.net/2060/19930093691

Kruse, H., & Tekiela, M. (1996). Calculating the consequences of a CO2 pipeline rupture. *Energy Conversion and Management*, *37*(6-8), 1013–1018.

Kunz, O., Klimeck, R., & Wagner, W. (2007). *The GERG-2004 Wide-Range Equation of State for Natural Gases and Other Mixtures*.

Lemmon, E. W., Huber, M. L., & McLinden, M. O. (2013). NIST Standard Reference Database 23: Reference Fluid Thermodynamic and Transport Properties-

REFPROP, Version 9.1. Gaithersburg: National Institute of Standards and Technology, Standard Reference Data Program.

Leveque, R. J. (2002). *Finite volume methods for hyperbolic problems*. Cambridge University Press.

Lewis, R. W., Nithiarasu, P., & Seetharamu, K. N. (2004). *Fundamentals of the Finite Element Method for heat and fluid flow* (1st Editio.). Wiley-Blackwell.

Lewis, R. W., Nithiarasu, P., & Seetharamu, K. N. (2004). *Fundamentals of the Finite Element Method for Heat and Fluid Flow*. Wiley-Blackwell.

Li, H., Jakobsen, J., Wilhelmsen, Ø., & Yan, J. (2011). PVTxy properties of CO2 mixtures relevant for CO2 capture, transport and storage: Review of available experimental data and theoretical models. *Applied Energy*, *88*(11), 3567–3579. doi:10.1016/j.apenergy.2011.03.052

Li, H., & Yan, J. (2009a). Evaluating cubic equations of state for calculation of vapor–liquid equilibrium of CO2 and CO2-mixtures for CO2 capture and storage processes. *Applied Energy*, *86*(6), 826–836. doi:10.1016/j.apenergy.2008.05.018

Li, H., & Yan, J. (2009b). Impacts of equations of state (EOS) and impurities on the volume calculation of CO2 mixtures in the applications of CO2 capture and storage (CCS) processes. *Applied Energy*, *86*(12), 2760–2770. doi:10.1016/j.apenergy.2009.04.013

Li, H., Yan, J., & Anheden, M. (2007). *Evaluation of existing methods for the thermodynamic properties calculation of CO2 mixtures.*

Mahgerefteh, H., & Atti, O. (2006). Modeling low-temperature–induced failure of pressurized pipelines. *AIChE Journal*, *52*(3), 1248–1256. doi:10.1002/aic.10719

Mahgerefteh, H., Atti, O., & Denton, G. (2007). An Interpolation Technique for Rapid CFD Simulation of Turbulent Two-Phase Flows. *Process Safety and Environmental Protection*, *85*(1), 45–50. doi:10.1205/psep.05118

Mahgerefteh, H., Brown, S., & Denton, G. (2012a). Modelling the impact of stream impurities on ductile fractures in CO2 pipelines. *Chemical Engineering Science*, *74*, 200–210. doi:10.1016/j.ces.2012.02.037

Mahgerefteh, H., Brown, S., & Martynov, S. (2012b). A study of the effects of friction, heat transfer, and stream impurities on the decompression behavior in CO2 pipelines. *Modeling and Analysis*, *2*, 369–379. doi:10.1002/ghg

Mahgerefteh, H., Oke, a, & Atti, O. (2006a). Modelling outflow following rupture in pipeline networks. *Chemical Engineering Science*, *61*(6), 1811–1818. doi:10.1016/j.ces.2005.10.013

Mahgerefteh, H., Oke, a, & Rykov, Y. (2006b). Efficient numerical solution for highly transient flows. *Chemical Engineering Science*, *61*(15), 5049–5056. doi:10.1016/j.ces.2006.03.012

Mahgerefteh, H., Rykov, Y., & Denton, G. (2009). Courant, Friedrichs and Lewy (CFL) impact on numerical convergence of highly transient flows. *Chemical Engineering Science*, *64*(23), 4969–4975. doi:10.1016/j.ces.2009.08.002

Mahgerefteh, H., Saha, P., & Economou, I. G. (1999). Fast numerical simulation for full bore rupture of pressurized pipelines. *AIChE Journal*, *45*(6), 1191–1201. doi:10.1002/aic.690450605

Mahgerefteh, H., Saha, P., & Economou, I. G. (2000). Modeling fluid phase transition effects on dynamic behavior of ESDV. *AIChE Journal*, *46*(5), 997–1006. doi:10.1002/aic.690460512

Mahgerefteh, H., & Wong, S. M. A. (1999). A numerical blowdown simulation incorporating cubic equations of state. *Computers & Chemical Engineering*, *23*(9), 1309–1317. doi:10.1016/S0098-1354(99)00296-3

Martynov, S., Brown, S., & Mahgerefteh, H. (2013). An extended Peng-Robinson equation of state for carbon dioxide solid-vapor equilibrium. *Greenhouse Gases Science and Technology*, (2), 1–12. doi:10.1002/ghg

Martynov, S., Brown, S., Mahgerefteh, H., Sundara, V., Chen, S., & Zhang, Y. (2014). Modelling three-phase releases of carbon dioxide from high-pressure pipelines. *Process Safety and Environmental Protection*, *92*(1), 36–46. doi:10.1016/j.psep.2013.10.004

McCoy, S., & Rubin, E. (2008). An engineering-economic model of pipeline transport of CO2 with application to carbon capture and storage. *International Journal of Greenhouse Gas Control*, *2*(2), 219–229. doi:10.1016/S1750-5836(07)00119-3

More, J. J., Garbow, B. S., & Hillstrom, K. E. (1980). *User guide for MINPACK-1*. Argonne, IL, USA.

Myers, G. E. (1987). *Analytical Methods in Conduction Heat Transfer*. Genium.

Nikuradse, J. (1933). Stromungsgesetze in rauhen Rohren. *Forsch. Arb. Ing.-Wes.*

Nordsveen, & Haerdig. (1997). Simulations of severe slugging during depressurization of an oil/gas pipeline. *Modeling, Identification and Control*, *18*(1), 61–73.

Oke, A. (2004). *An efficient numerical simulation for modelling outflow following rupture or puncture of pressurised pipeline networks.* University College London.

Oke, A., Mahgerefteh, H., Economou, I., & Rykov, Y. (2003). A transient outflow model for pipeline puncture. *Chemical Engineering Science*, *58*, 4591–4604.

Patel, N. C., & Teja, A. S. (1982). A new cubic equation of state for fluids and fluid mixtures. *Chemical Engineering Science*, *37*(3), 463–473.

Peneloux, A., & Rauzy, A. (1982). A consistent correction for Redlich-Kwong-Soave volumes. *Fluid Phase Equilibria*, *8*, 7–23.

Peng, D.-Y., & Robinson, D. B. (1976). A New Two-Constant Equation of State. *Industrial & Engineering Chemistry Fundamentals*, *15*(1), 59–64. doi:10.1021/i160057a011

Perry, R. H., Green, D. W., & Maloney, J. O. (Eds.). (2008). *Perry's Chemical Engineers' Handbook* (8th Ed.). New York: McGraw-Hill.

Picard, D. J., & Bishnoi, P. R. (1987). Calculation of the thermodynamic sound velocity in two-phase multicomponent fluids. *International Journal of Multiphase Flow*, *13*(3), 295–308.

Picard, D. J., & Bishnoi, P. R. (1988). The Importance of Real-Fluid Behaviour and Non-Isentropic Effects in Modeling Decompression Characteristics of Pipeline Fluids for Application in Ductile Fracture Propagation Analysis. *Canadian Journal of Chemical Engineering*, *66*(1), 3–12.

Prasad, P., & Ravindran, R. (1985). *Partial Differential Equations*. New Delhi: Wiley Eastern Ltd.

Rabinowitz, P. (Ed.). (1970). *Numerical methods for non-linear algebraic equations*. London: Gordon and Breach.

Ransom, V. H., & Trapp, J. A. (1978). *RELAP5 progress summary*.

Redlich, O., & Kwong, N. J. S. (1949). On the thermodynamics of solutions. *Chemical Review*, *44*, 233–244.

Richardson, S., & Saville, G. (1996). Blowdown of LPG Pipelines. *Process Safety and Environmental Protection*, *74*(4), 235–244. doi:10.1205/095758296528581

Rohsenow, W. M., Hartnett, J. P., & Cho, Y. I. (Eds.). (1998). *Handbook of heat transfer* (3rd ed.). New York: McGraw-Hill.

Shafeen, A., Croiset, E., Douglas, P. L., & Chatzis, I. (2004). CO2 sequestration in Ontario, Canada. Part II: cost estimation. *Energy Conversion and Management*, *45*(20), 3207–3217. doi:10.1016/j.enconman.2003.12.018

Shoup, G., Xiao, J. J., & Romma, J. O. (1998). *Multiphase pipeline blowdown simulation and comparison to field data*.

Shuter, D., Bilio, M., Wilday, J., Murray, L., & Whitbread, R. (2011). Safety issues and research priorities for CCS systems and infrastructure. *Energy Procedia*, *4*, 2261–2268. doi:10.1016/j.egypro.2011.02.115

SIMULIA. (2011). ABAQUS FEA. Dassault Systemes.

Sinnott, R. K. (1999). *Coulson and Richardson's Chemical Engineering, Volume 6, Chemical Engineering Design* (3rd Ed.). Oxford: Butterworth-Heinemann.

Skovholt, O. (1993). CO2 TRANSPORTATION SYSTEM. *Energy Convers.*, *34*(9), 1095–1103.

Soave, G. (1972). Equilibrium constants from a modified Redlich-Kwong equation of state. *Chemical Engineering Science*, *27*(6), 1197–1203.

Solorzano, M., Barragan, F., & Bazua, E. R. (1996). Comparative study of mixing rules for cubic equations of state in the prediction of multicomponent vapor-liquid equilibria. *Phase Equilibria*, *122*(99).

Span, R., & Wagner, W. (1996). A New Equation of State for Carbon Dioxide Covering the Fluid Region from the Triple-Point Temperature to 1100 K at Pressures up to 800 MPa. *Journal of Physical and Chemical Reference Data*, *25*(6), 1509–1596.

Steiner, D., & Taborek, J. (1992). Flow Boiling Heat Transfer in Vertical Tubes Correlated by an Asymptotic Model. *Heat Transfer Engineering*, *13*(2), 43–69. doi:10.1080/01457639208939774

Stewart, H., & Wendroff, B. (1984). Two-Phase Flow: Models and Methods. *Journal of Computational Physics*, *56*, 363–409.

Stroud, K. A. (1995). *Engineering mathematics: programmes and problems* (4th Ed.). London: Macmillan.

Stryjek, R., & Vera, J. H. (1986). PRSV: An improved Peng-Robinson equation of state for pure compounds and mixtures. *The Canadian Journal of Chemical Engineering*, *64*(2), 323–333. doi:10.1002/cjce.5450640224

Svensson, R., Odenberger, M., Johnsson, F., & Stromberg, L. (2004). Transportation systems for CO2 - application to carbon capture and storage. *Energy Conversion and Management*, *45*(15-16), 2343–2353. doi:10.1016/j.enconman.2003.11.022

Swaffield, J. A., & Boldy, A. P. (1993). *Pressure surge in pipe and duct systems*. Vermont: Ashgate Publishing Limited.

Tam, V. H. Y., & Cowley, L. T. (1988). Consequences of pressurized LPG releases: the Isle of Grain full scale experiments. In *Proc. Gastech 88. 13th Int LNG/LPG Conf.* Kuala Lumpur.

Tannehill, J. C., Anderson, D. A., & Pletcher, R. H. (1997). *Computational fluid mechanics and heat transfer* (2nd Editio.). London: Taylor and Francis.

Techo, R. (1965). An accurate equation for the computation of the friction factor for smooth pipes from the Reynolds number. *Journal of Applied Mechanics*, *32*, 443.

Terenzi, A. (2005). Influence of Real-Fluid Properties in Modeling Decompression Wave Interacting with Ductile Fracture Propagation. *Oil & Gas Science and Technology*, *60*(4), 711–719. doi:10.2516/ogst:2005050

Toro, E. F. (2009). *Riemann solvers and numerical methods for fluid dynamics* (3rd ed.). Springer - Verlag.

UCL. (2010). *Private Communication - Gas phase CO2 pipeline hazard analysis*.

UKCCSRC. (2012). COOLTRANS. Retrieved from https://ukccsrc.ac.uk/resources/ccs-projects-directory/dense-phase-carbon-dioxide-pipeline-transportation-cooltrans

United Nations. (2014a). United Nations Framework Convention on Climate Change. Feeling the Heat: Climate Science and the Basis of the Convention. Retrieved February 11, 2015, from http://unfccc.int/essential_background/the_science/items/6064.php

United Nations. (2014b). United Nations Framework Convention on Climate Change. First steps to a safer future: Introducing The United Nations Framework Convention on Climate Change. Retrieved February 11, 2015, from http://unfccc.int/essential_background/convention/items/6036.php

Walas, S. (1985). *Phase equilibria in chemical engineering*. Boston: Butterworth.

Webber, D. M., Fannelop, T. K., & Witlox, H. W. M. (1999). *Source terms from two-phase flow in long pipelines following an accidental breach*. *Science*.

Wu, D., & Chen, S. (1996). A modified Peng-Robinson equation of state. *Chemical Engineering Communications*, *156*(1), 215–225.

Wylie, E. B., & Streeter, V. L. (1993). *Fluid transients in systems*. Engelwood, NJ.: Prentice-Hall.

Xu, B. P., Jie, H. E., & Wen, J. X. (2014). A pipeline depressurization model for fast decompression and slow blowdown. *International Journal of Pressure Vessels and Piping*, *123-124*, 60–69. doi:10.1016/j.ijpvp.2014.07.003

Yapıcı, H., & Albayrak, B. (2004). Numerical solutions of conjugate heat transfer and thermal stresses in a circular pipe externally heated with non-uniform heat flux. *Energy Conversion and Management*, *45*(6), 927–937. doi:10.1016/S0196-8904(03)00195-X

Yu, J.-M., Lu, B. C. Y., & Iwai, Y. (1987). Simultaneous calculations of VLE and saturated liquid and vapor volumes by means of a 3P1T cubic EOS. *Fluid Phase Equilibria*, *37*, 207–222.

Zhang, P. (2014). *Modelling Brittle Fracture Propagation in the Next Generation CO2 Pipelines*. University College London.

Zhang, Z., Wang, G., Massarotto, P., & Rudolph, V. (2006). Optimization of pipeline transport for CO2 sequestration. *Energy Conversion and Management*, *47*(6), 702–715. doi:10.1016/j.enconman.2005.06.001

Zhu, H., Yang, X., Li, J., & Li, N. (2013). Simulation analysis of thermal influential factors on crude oil temperature when double pipelines are laid in one ditch. *Advances in Engineering Software*, *65*, 23–31. doi:10.1016/j.advengsoft.2013.04.016

Zucrow, M. J., & Hoffman, J. D. (1975). *Gas Dynamics*. New York: Wiley.